Whiter than white: interactions between optical brighteners and surfactants in detergents

RAMSEY, HELEN,ELIZABETH

"Whiter than white": interactions between optical brighteners and surfactants in detergents

Helen Elizabeth Ramsey

In partial fulfilment of the requirement for the degree of Doctor of Philosophy

Department of Chemistry, Durham University

March 2016

"Whiter than white": interactions between optical brighteners and surfactants in detergents

The interactions between an optical brightener and surfactants commonly found in laundry detergents were studied. Three techniques were used; fluorescence spectroscopy was used to determine the effect of the addition of surfactants on the rate of brightener deposition, while small-angle X-ray scattering (SAXS) and molecular dynamics (MD) simulations were used to determine the effect of the brightener on the micellar structure pre-deposition. In addition, the effect of calcium ions on micellar structure was studied using these techniques. The effect of surfactant addition on $CaCO_3$ crystallisation was also studied.

It was found that the addition of nonionic surfactants inhibited the deposition of brightener onto fabric surfaces, whereas the addition of anionic surfactants aided this deposition process. This was correlated to the micellar structures found using SAXS and MD simulations; the anionic surfactant system formed ellipsoidal structures, in which the brightener was incorporated onto the surface of the hydrocarbon core, whereas the nonionic surfactant formed spherical structures where the brightener was held within the outer shell, which appeared to hamper its ability to be deposited. In addition, the brightener was shown to affect micellar radius and aggregation number of the nonionic surfactant, in a manner similar to the addition of anionic surfactant to nonionic surfactant.

The addition of calcium ions at concentrations up to 0.36 g L^{-1} Ca^{2+} (for SAXS) and 0.77 g L^{-1} Ca^{2+} (for MD simulations) to nonionic and anionic surfactant systems was not seen to significantly affect their micellar structure, although a greater affinity was seen between the calcium and the anionic surfactant than between the calcium and the nonionic surfactant. The effect of the addition of surfactants on the rate of $CaCO_3$ crystallisation and the polymorphs produced was determined.

Table of Contents

Table of Figures

Table of Tables

List of abbreviations

AE, AE7	Alcohol ethoxylate
AES, AE1S	Alcohol ether sulfate
AOT	Dioctyl sodium sulfosuccinate
B15, Bri 15	Brightener 15
B49, Bri 49	Brightener 49
CIE	International Commission on Illumination (*Commission internationale de l'éclairage*)
CMC	Critical Micelle Concentration
CNT	Classical Nucleation Theory
CTAC	Cetyl trimethylammonium chloride
DEEDMAC	Diethyl ester dimethyl ammonium chloride
DMSO	Dimethyl sulfoxide
EM	Energy Minimisation
FORTRAN	Formula Translating System
FTIR	Fourier Transform Infrared
FWA	Fluorescent whitening agent
GIFT	Generalised Indirect Fourier Transform
GROMACS	Groningen Machine for Chemical Simulation
HOMO	Highest Occupied Molecular Orbital
IFI	Integrated Fluorescence Intensity
IFT	Indirect Fourier Transform
LAS	Linear alkyl benzene sulfonate
LUMO	Lowest Unoccupied Molecular Orbital

MD	Molecular Dynamics
o/w	Oil in water
OZ	Ornstein-Zernike
P&G	Procter & Gamble
PET	Polyethylene terephthalate
SAXS	Small Angle X-ray Scattering
SDS	Sodium dodecyl sulfate
UHQ	Ultra-high quality
WAXS	Wide Angle X-ray Scattering
w/o	Water in oil

Statement of copyright

Acknowledgements

Firstly, I would like to thank my supervisor, Dr. Sharon Cooper, and my industrial supervisors, Dr Euan Magennis and Dr Michelle Jackson, for their guidance and support during this project. I would also like to thank Procter & Gamble for funding this project through the CEMENT program.

I'd like to thank all members of the Cooper Group who have supported me: Dr Kate Nicholson, Dr Cen Chen, Natasha Hargreaves, Dr Chris Herron, Helen Riggs, Dr Oliver Cook, Dr Isaac Odiase, Dr Mehrin Chowdhury, Mike Paton, Janet Berry, Dr Reduwan Billah, Jenny Kermode, Charlie Lunn, Luke Tucker, Philippa Matthews, Benjamin Deviliers, Ben Hodgkiss, Stephen Dufton, Dr Stephanie Freitag-Pohl, Jennifer Fowler, and Harriet Forsyth.

For assistance with photochemistry, I would like to thank Prof Andy Beeby, and his group, particularly Andrew Duckworth and Valentina Manici.

For their help with simulation work, I would like to thank Prof Mark Wilson, Dr Martin Walker, and Jim Madge.

I would like to thank Steven Charlton (Department of Mathematics, Durham University) for insightful discussions on graph theory and algorithm building.

For his assistance with X-ray crystallography, I would like to thank Dr Dmitry Yufit.

Finally, I would like to thank Mum, Dad, Steve, Peter and Doug, for all of their support.

1. Introduction

In this project, the deposition of brighteners in laundry detergents, and their interactions with surfactant micelles, was studied. This is a topic of importance in the detergent industry.

Section 1.1 of the literature review will introduce the topic of laundry detergents, giving a brief history of the subject and the composition of an average detergent. Section 1.2 will cover the main component of detergents, surfactant molecules. Section 1.3 will cover the laundry process itself, including fabrics, types of soil, and the various methods of laundering fabrics. Section 1.4 will cover fluorescence, and Section 1.5 will cover the optical brightener. Section 1.6 will set out the aims of this project.

1.1. Detergents

Since ancient times, humans have used detergents to wash themselves and their clothes. Evidence for soaps has been found in texts from ancient Babylon (2200 BC) and Egypt (1550 BC), and a soap manufacturer was discovered in Pompeii (79 AD)[1]. This soap was made by mixing animal fats with an alkali such as lye. Until recently, bars of soap were used for all household cleaning.

The first major development came at the turn of the 20th century, when soap began to be sold as flakes or powder. This made it easier for the soap to dissolve, allowing the clothes to be soaked in solution rather than scrubbed with a bar.[2] The next major development came in 1916, when, in order to combat the shortage of fats for soap manufacture during the First World War, artificial surfactants were first manufactured. Finally, products containing builders were first produced in the USA in 1947.[3] This marks the first time that a recognisable modern laundry detergent was produced.

The purpose of a detergent is primarily to remove dirt; however, it also provides several other functions. A typical laundry detergent will contain the following ingredients:[4]

1.1.1. Surfactants

Surfactants provide the primary cleaning function of the detergent formulation by lowering the surface tension between oily soils and the wash solution. They will be covered in more detail in Section 1.2.

1.1.2. Builders

Many surfactants are highly sensitive to the presence of ions in solution, in particular those ions present in hard water. Anionic surfactants are the most susceptible; they contain negatively charged head groups balanced by a positive counterion such as Na^+. If hard water ions such as Ca^{2+} or Mg^{2+} are present in solution, they can form complexes with the surfactant monomers of the form Ca(*surfactant*)$_2$ or Mg(*surfactant*)$_2$. These complexes have a very low solubility and will precipitate out of solution to form lime soap or 'soap scum'.[5,6] The effects of surfactant and cation concentration on this process are illustrated in Figure 1-1 below.

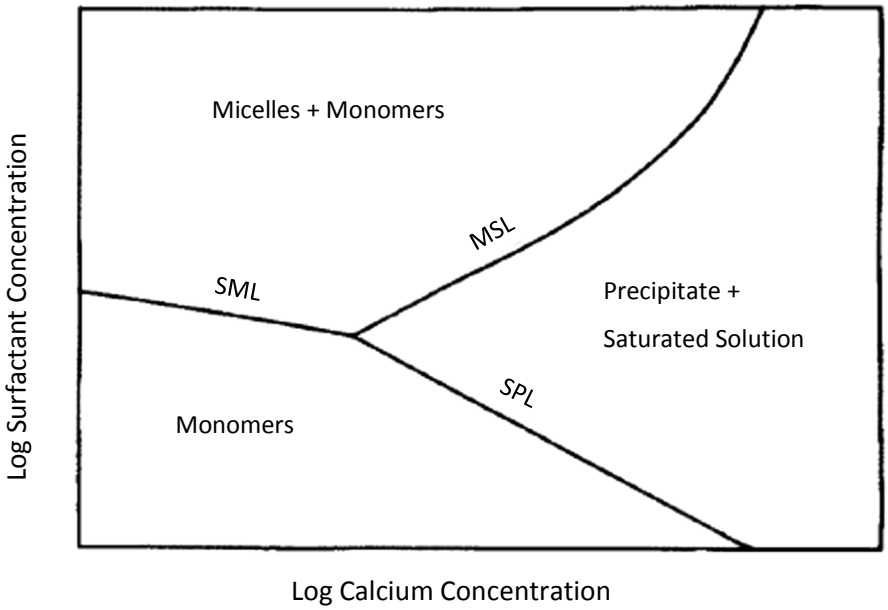

Figure 1-1: Effect of calcium ion concentration and surfactant concentration on the formation of Ca(*surfactant*)$_2$ complexes. Line SML (surfactant micellisation line) shows the effect of Ca^{2+} on the CMC (critical micelle concentration). Line SPL (surfactant precipitation line) shows the region where increasing Ca^{2+} concentration causes precipitation of Ca(*surfactant*)$_2$. Line MSL (micelle solubilisation line) shows the region where the surfactant concentration is high enough to form micelles, which can resolubilise the Ca(*surfactant*)$_2$.Used with permission. Copyright 1985 Journal of the American Oil Chemists' Society ([6])

As shown in the figure above, the effect of these ions in solution can be reduced by increasing the surfactant concentration. This is because the cations will only form insoluble complexes with surfactant monomers. Above the CMC, the cations can bind to the surface of the micelle, and thus be effectively removed from solution.[7]

In order to combat the effect of hard water, builders are used in detergents; these substances will remove the ions from solution, allowing the surfactants to function correctly.

Traditionally, sodium triphosphate (also known as sodium tripolyphosphate) is used as the builder in detergents; however, this compound has raised environmental concerns over eutrophication. As a result, its use is banned in several European countries and phased out in others. Zeolites are often used as a replacement; these minerals consist of tetrahedra of $(SiO_4)^{4-}$ and $(AlO_4)^{5-}$ in a cage-like structure, with Group 1 or 2 cations (typically Na^+) held loosely within the openings in the cage or 'pores'.[8] These minerals can remove Ca^{2+} or Mg^{2+} ions from detergent solutions by exchanging them with these ions.[9] They can be found in nature or artificially synthesised.

1.1.3. Polymers

Polymers in detergents have three main uses. Firstly, polymers can be used to add to the cleaning action of the detergent by removing soils directly. Secondly, some polymers (soil release polymers) bind directly to hydrophobic fabrics such as synthetic fibres, and increase the hydrophilicity of the fabric. This means that oily soil will not be able to 'soak into' the fabric as easily, reducing the amount of cleaning that the garment will require in the future.[10] Finally, polymers are also used to bind dye released by the fabric, preventing it from redepositing and staining other items in the wash.

1.1.4. Enzymes

Enzymes are proteins produced by biological organisms that act as catalysts for a reaction. In laundry detergents, they will aid stain removal by breaking down biological molecules. Three types can be found in detergents: amylases will break down starch, proteases will break down protein and lipases will break down fats. They are most effective in lower-temperature washes, as they will denature at high temperatures and cease to function.

Currently, most of the enzymes used in detergents are obtained from bacteria; however, it has been shown that a suitable protease for laundry applications could be obtained from waste fish intestines produced by the fishing industry. This would be an effective way to recycle a material that is otherwise discarded, contributing to pollution.[11]

Recently, there has been controversy over the use of enzymes in detergents, with many users claiming that they have become sensitized or suffered skin irritation. However, dermatologists have concluded that there is no evidence of enzymes in detergents causing damage to the skin of consumers.[12]

1.1.5. Bleach and bleach enhancers

Bleaches are also used to break down soil chemically, allowing easier removal. Typically, oxygen bleaches such as persalts are used in detergents; these release peroxide ions. Oxygen bleaches will only have a noticeable effect on stains when used at high temperatures; if used at room temperature, they would take 24 hours to act noticeably on a stain. To improve bleaching activity, bleach activators such as tetra acetyl ethylene diamine (TAED) are used. These react with the peroxide ion to produce peracetic anions (CH_3COOO^-) which are far more effective bleaches than peroxide ions.[13]

1.1.6. Optical brighteners and hueing dyes

Over time, white clothing will start to oxidise, causing it to absorb blue light more. As a result, the clothing will appear yellower. Both optical brighteners and hueing dyes will provide a blue tint to the clothes, making them appear whiter. Both the yellowing of fabric and the action of optical brighteners and hueing dyes will be discussed in more depth in Section 1.5.

1.1.7. Perfumes

Perfumes are used for two purposes: to mask the 'chemical' smell of the detergent itself, and to leave clothes smelling pleasant after washing.

1.2. Surfactants

The term 'surfactant' is short for 'surface active agent'. Surfactants are molecules with a hydrophilic, polar 'head' group and a hydrophobic, non-polar 'tail' group. They can exist at interfaces between immiscible liquid phases, or liquid/air interfaces, and thus lower the interfacial tension between them. Because they have polar and non-polar groups, they are referred to as amphiphilic. A schematic of a surfactant is shown in Figure 1-2 below.

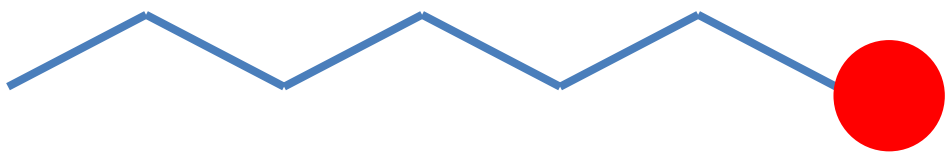

Figure 1-2: A surfactant molecule

Generally, the tail group will be a hydrocarbon chain; the head group will depend on the type of surfactant used.

1.2.1. Types of surfactant

1.2.1.1. Anionic surfactants

Anionic surfactants have a negatively charged head group. One example would be sodium dodecyl sulfate, or SDS, which has a sulfate (SO_3^-) head group. These surfactants are used as the 'workhorse' cleaners in the detergent industry; however, they are susceptible to the presence of ions such as those found in hard water, and thus are rarely used alone.

1.2.1.2. Cationic surfactants

These surfactants have positively charged head groups (e.g. NH_3^+ groups). Due to this head group, they are attracted to negatively charged fabrics and are typically used as fabric softeners and conditioners, rather than for soil removal.

1.2.1.3. Nonionic surfactants

The head groups of these surfactants carry no charge – instead, they are polar. Examples include long-chain alcohols. They are generally less soluble than anionic surfactants, but are unaffected by the presence of ions in solution. They are often used as a cosurfactant.

1.2.1.4. Zwitterionic surfactants

These surfactants have head groups carrying both positive and negative charges. They are not widely used in detergents.

1.2.2. Interfacial tension

Consider a liquid such as water at room temperature. A water molecule in the bulk will experience attractive forces from all directions, whereas a molecule at the surface will only experience the same attractive forces from beneath the surface and from other surface molecules around it, as the attraction to air molecules will be very weak. This means that the water molecules at the surface of the solution will have a higher potential energy than those in the bulk. For this reason, it takes work to create a surface or interface.[14]

Interfacial tension is defined as the change in Gibbs free energy with the change in area as an interface is created, with constant pressure and temperature:

$$\gamma = \left(\frac{\delta G}{\delta A}\right)_{T,P}$$

Equation 1-1

where *γ* is the surface tension, *G* is the Gibbs free energy, and *A* is the surface area. Interfacial tension is always positive, as it takes work to create a surface. (The term 'surface tension' is only used in the case of an interface with a gas; for two liquids, a solid and a liquid, or two solids, the term 'interfacial tension' is used instead.)

For this reason, when oil and water are mixed, they will separate into one oil layer and one water layer, to minimize the interface between them. As surfactants have both hydrophobic and hydrophilic parts, they can exist at the interface between the two, and lower the interfacial tension.

1.2.3. Aggregation of surfactant molecules

When a low concentration of surfactant is added to water, it will initially form a monolayer on the surface, with the hydrophilic head groups pointing down towards the water, and the hydrophobic tails pointing outwards. In addition, some surfactant molecules will enter the water as individual molecules. There will be two sets of forces acting on the surfactant molecules in solution. Attractive hydrogen-bonding and dipole-dipole or dipole-ion interactions will exist between the water molecules and the hydrophilic head group, but not between the water molecules and the hydrophobic tail group. The water molecules will form a cage-like structure around the tail group to maximise its interactions with other water molecules; this will be entropically unfavourable as the water configurations will be limited. As the concentration of surfactant is increased, the amount of water required to form the cage-like structures increases, thus reducing further the entropy of the system. Eventually, once the critical micelle concentration (CMC) is reached, it becomes more favourable for the surfactant molecules to form micelles so that the hydrocarbon tails are effectively removed from the water and the water can adopt its unperturbed bulk structure. These micelles are (usually) spherical structures where the surfactant molecules cluster with the tail groups in the centre and the head groups facing outward towards the water. If oil is used as the solvent instead of water, then the surfactant tails will face outward and the head groups inward, to form a reverse micelle.

1.2.3.1. Packing Parameter

Not all surfactants can form a micelle, and not all can form a reverse micelle. This is due to steric factors. Surfactants with bulky tail groups and narrow head groups will be able to efficiently pack together as a reverse micelle, but not as a micelle, and vice versa. This steric factor is referred to as the **packing parameter**. This was first described in 1975 by Israelachvili et al[15], and is used to predict the most favourable shape that a surfactant will aggregate to form. The packing parameter is given by $\frac{v}{a_0 l_c}$, where v is the volume of the hydrocarbon tail, l_c is the length of the tail, and a_0 is the surface area per surfactant at the surface of the structure. The structures that surfactants can form, and the maximum packing parameter required for each, can be seen in Table 1-1 below.

Table 1-1: Packing parameters for various structures

Structure	Maximum packing parameter
Spherical micelle	0.33
Globular micelle	0.38
Toroid	0.44
Cylinder	0.50
Bilayer	1

This theory is widely used today, although it has been criticized for ignoring the contribution of the tail group – as the volume of the chain is directly proportional to its length, $\frac{v}{l_c}$ will be effectively constant, and increasing the chain length will not affect the packing parameter.[16]

1.2.3.2. Mixed micelles

For solutions containing two surfactants, the CMC will vary according to the composition of the mixture and the CMCs of the two surfactants. Assuming ideal mixing, the CMC of the resulting mixture will be given by the equation

$$\frac{1}{C^*} = \frac{\alpha}{C_1} + \frac{(1-\alpha)}{C_2}$$

Equation 1-2

where C^* is the CMC of the mixture, C_1 and C_2 are the CMCs of surfactants 1 and 2 respectively, and α is the mole fraction of surfactant 1 in the mixture (excluding solvent).[17,18] Four points must be noted regarding this model; firstly, the proportion of each surfactant in solution may not be the same as the proportion within the micelles. Secondly, Clint's initial study[18] only used two very similar nonionic surfactants, as such they will have a similar limiting surface tension; if they had very different surface tensions, the assumption of ideal mixing may break down. In addition, while the model was used to successfully predict the CMC in the case studied, it proved less accurate in predicting the surface tension for mixtures above the CMC; again, this is attributed to the solution not behaving ideally. Finally, this model cannot be used for a surfactant with a low aggregation number. This is because Clint uses the phase separation model for his calculation, which cannot be applied to such systems.

1.2.4. Cloud point and Krafft point

The cloud point is a key phenomenon for nonionic surfactants (although cationic surfactants may also show clouding). It provides an upper bound for the temperature of a surfactant system; as the temperature increases to the cloud point, the micelles start to attract each other, with the attraction increasing with increasing temperature. At the cloud point, the micelles will clump together, causing the mixture to phase-separate into a surfactant-rich phase and a surfactant-poor phase.[19] The cloud point arises due to the decreased strength of the hydrogen-bonding between the water and the nonionic headgroup as the temperature increases.

Conversely, the Krafft point is the minimum temperature at which an ionic surfactant can exist in solution. Below the Krafft point, the surfactant will exist as a solid, whereas above it, the surfactant will either form micelles or exist as monomers. For this reason, the Krafft point has been described as the melting point of the surfactant in solution.[20]

1.2.5. Emulsions and microemulsions

An emulsion consists of two immiscible liquids such as oil and water, with one dispersed within the other. These liquids are referred to as the dispersed phase and the continuous phase.

Because of interfacial tension, emulsions are thermodynamically unstable. However, they can be stabilized by reducing the interfacial tension and thereby droplet size, and adding cosurfactants, producing microemulsions. This works because, to spontaneously form a

stable mixture, the Gibbs free energy of mixing must be negative. This Gibbs free energy is given by:

$$\Delta G_m = -T\Delta S_m + A_v\gamma$$

Equation 1-3

where ΔG_m is the change in Gibbs free energy, T is the temperature, ΔS_m is the change in entropy upon mixing, A_v is the area of the interface per unit volume, and γ is the surface tension.

For a standard emulsion, ΔG_m will be positive. This means that the mixture will not form spontaneously, and will not be thermodynamically stable. However, to create a microemulsion, additional surfactant and often a cosurfactant are added, reducing the interfacial tension. This significantly reduced interfacial tension (~ 10^{-3} mN m^{-1}) means that forming smaller droplets and creating additional interfaces costs far less energy and is compensated by the increased entropy. Hence, although A_v will increase as the droplet size decreases, the reduction in γ, and increase in ΔS_m, will compensate for this. This allows the positive term to reduce until $T\Delta S_m > A_v\gamma$. At this point, $\Delta G_m < 0$, and so the mixture will be thermodynamically stable.[21]

Microemulsions can be classified using the Winsor system. This divides microemulsions into 4 types:[22] Winsor I microemulsions are oil-in-water (o/w) microemulsions, with a layer of excess oil. Winsor II microemulsions are water-in-oil (w/o) microemulsions, with a layer of excess water. Winsor III microemulsions contain a free layer of excess oil, a free layer of excess water, and a single bicontinuous microemulsion containing oil, water and surfactant. Winsor IV microemulsions consist of a single microemulsion containing oil, water, and surfactant. They contain no excess layers.

These microemulsions are shown in Figure 1-3.

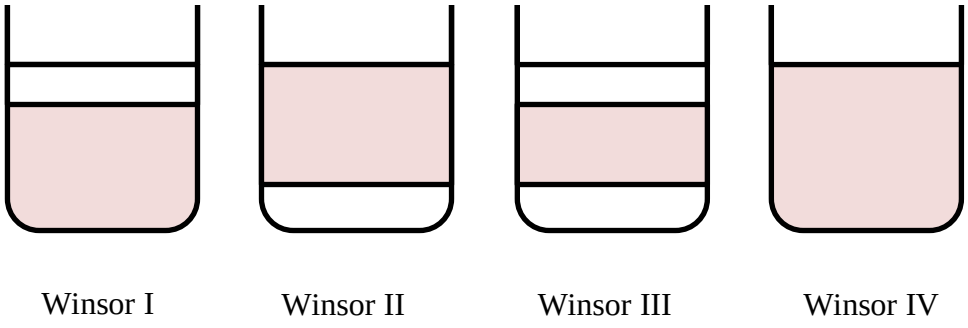

Figure 1-3: Winsor microemulsions

Ternary phase diagrams can be used to show the effect of composition on a system containing three components (usually an aqueous phase, an oil phase and a surfactant). An example is shown in Figure 1-4.

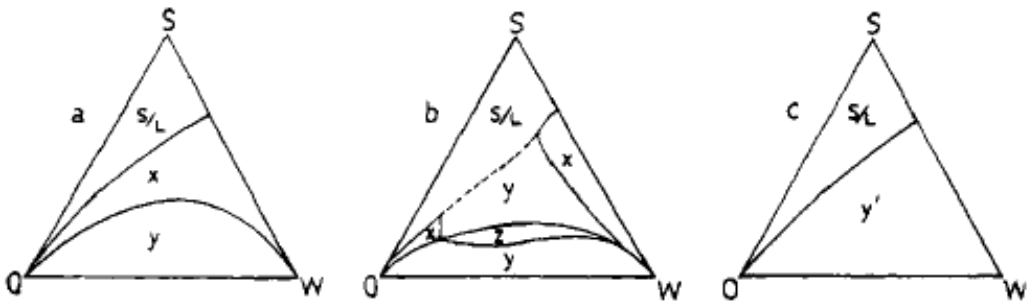

Figure 1-4: Ternary phase diagrams of cyclohexane/SDS + 1-propanol/water system at various NaCl concentrations: (a) 0.5; (b) 1.0; 9c) 3.0 M. S/L indicates a solid/liquid two-phase region, y indicates a Winsor I solution, y' indicates a Winsor II solution, z indicates a Winsor III solution and x indicates a Winsor IV solution (see Section 1.2.5.1). Reprinted with permission from ([23]). Copyright 1994.

1.2.6. Surfactants used in this study

Four surfactants were used in this study: LAS, AE1S (example of AES), AE7 (example of AE), and DEEDMAC. These surfactant groups will be discussed in turn.

1.2.6.1. LAS

Linear alkyl benzene sulfonates (LAS) are a class of anionic surfactants, with an isomeric proportion that depends on their method of synthesis. They have an average chain length of 11.6,[24] a CMC of 0.34 mM (although this will depend on the isomer)[17], a micelle radius of 1.61 nm and an aggregation number of 20-40 (increasing with increased addition of cosurfactant).[25] A sample structure can be seen in Figure 1-5.

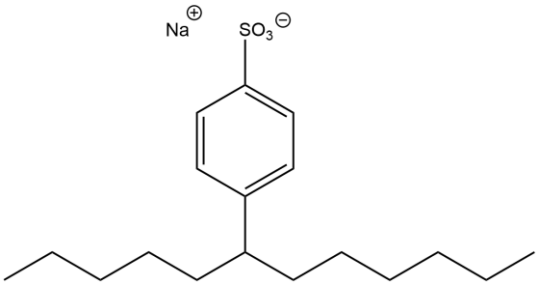

Figure 1-5: Structure of LAS [24]

They have a packing parameter of ~0.56 (with or without the phenyl ring)[25], which would suggest that they form cylindrical micelles or lamellar sheets; however, small-angle neutron scattering (SANS) experiments have shown the presence of globular micelles as well.[17,25] This has been attributed to the conformational changes that the surfactant undergoes at micellisation; ^{1}H NMR studies have shown that, during micellisation, the shorter hydrocarbon chain will 'loop back' towards the aromatic ring.[26] This is illustrated in Figure 1-6 below.

Figure 1-6: The 'looping back' of the hydrocarbon chain of LAS during micellisation. The hydrocarbon chain is represented by the blue line and the hydrophilic 'head' is represented by the red circle.

LAS is ultimately derived from kerosene. From the kerosene, linear paraffins with between 10 and 13 carbon atoms are extracted. These are then used to alkylate benzene, with $AlCl_3$, HF or Detal used as a catalyst. This produces linear alkylbenzene, or LAB. LAB is then reacted with H_2SO_4, oleum, SO_3 gas, $ClSO_3H$ or sulfamic acid to give LAS.[27]

LAS is known to fluoresce, due to its phenyl ring. It shows two peaks in its fluorescence emission spectrum, at 289 nm and 350 nm (within the UV range). For this reason, micelles of LAS can be used in fluorescence studies without the use of fluorescent probes.[28]

1.2.6.2. AE

Alcohol ethoxylates are nonionic surfactants consisting of an alcohol group with between 3 and 9 ethoxy groups, and a hydrocarbon chain of 14-15 carbon atoms. An example is shown in Figure 1-7 below. They are not affected by water hardness.

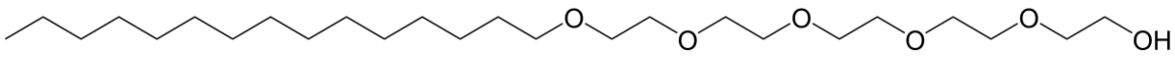

Figure 1-7: Alcohol ethoxylate, AE7

Studies have shown that several factors will affect the performance of AE; the more linear the alcohol from which the AE is synthesized, the lower the CMC and higher the surface tension at the CMC will be, whereas the higher the degree of substitution at the second carbon of the chain, the lower the cloud point, foam stability and wetting time will be.[29] The alcohol ethoxylate used in this study, AE7, has approximately 7 ethoxy groups, and a CMC of 0.1 g L^{-1}.[30]

1.2.6.3. AES

Alcohol ethoxylates (AE) and alcohol ether sulfates (AES) are closely linked; AES is produced by the sulfonation of AE. They are anionic surfactants. An example[24] is shown in Figure 1-8 below.

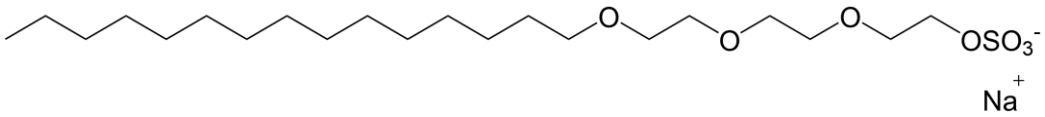

Figure 1-8: Alcohol ether sulfate

Typically, hydrocarbon chain lengths of 12-15 carbon atoms will be used; these will have a CMC of ~ 0.1 – 0.4 mM,[31] i.e. 0.035 – 0.14 g L^{-1}, and a recorded aggregation number of between 43-80.[32,33]

1.2.6.4. DEEDMAC

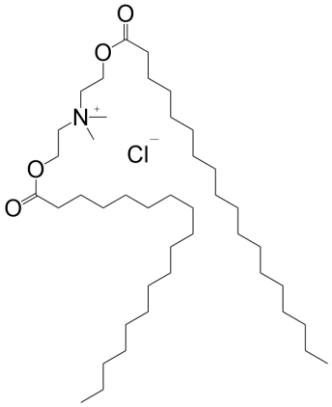

Figure 1-9: DEEDMAC

Diethyl ester dimethyl ammonium chloride (DEEDMAC) is a cationic surfactant commonly used as a fabric softener, developed as a highly biodegradable replacement for ditallow dimethyl ammonium chloride (DTDMAC), from which it differs by the addition of two ester groups. It is considered to be highly insoluble,[34] with a solubility of less than 1 g L^{-1}.[35] Its small head group and two-tailed nature make this surfactant a poor choice to form micelles; however, with addition of ethanol, this surfactant has been used to produce vesicles.[36]

1.3. The laundry process

This section will cover three main points: firstly, the types of fabric available will be discussed and their interactions with water and soil considered. Secondly, the process of removal of soil by surfactants will be considered. Finally, laundry techniques and consumer behavior will be discussed.

1.3.1. Types of fabric

There are two main groups into which fabrics can be organized: natural and synthetic. Natural fibres are those which are found in nature, such as cotton, wool and silk. Synthetic fibres are those which are produced chemically, such as polyester.

1.3.1.1. Cotton

The seeds of a cotton plant are surrounded by white 'hairs', each consisting of a single cell. These cells have cell walls composed of cellulose, a polysaccharide with the formula $(C_6H_{12}O_6)_n$. It can be seen in Figure 1-10. As the cotton plant matures, these cells dry out, removing their cell contents, leaving only the cellulose cell walls remaining (a process that

is completed manually in the bleaching stages of production). These cell walls are harvested, and provide the fibres seen in cotton.[37]

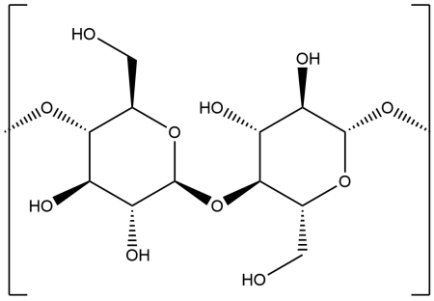

Figure 1-10: Cellulose

Cellulose contains a lot of primary and secondary alcohol groups; this makes it highly hydrophilic and thus easily wettable. It has long been a popular choice of fibre for clothing.

1.3.1.2. Wool

Wool consists of spun hairs from the fleece of sheep; like all hair, it is mainly composed of keratin, a protein. However, unlike the hair of other mammals, the hairs of sheep are crimped. This allows the hairs to 'grab' one another, allowing them to be spun together.

Proteins such as keratin consist of polymers of amino acids, shown in Figure 1-11 below. Wool readily absorbs moisture from air, with the release of heat as the gaseous water condenses into liquid water.

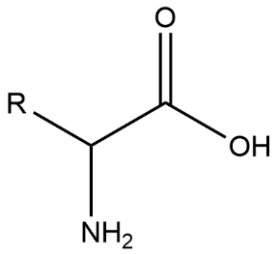

Figure 1-11: An amino acid. R represents a variable group

Much research has been done into the source of wool's unusual properties. One early paper calculated the number of sites that bound to water molecules per measure of wool, and noted that it matched the number of C=O groups from the keratin per measure of wool. Thus, the author concluded that these groups are responsible for the absorption of water vapour. However, while this theory would be plausible, the work presented no

chemical evidence to support this claim; therefore, this work must be regarded with caution.[38]

Later groups attributed the uptake of water at low humidity to binding with the NH_3^+ and (to a lesser extent) COO^- groups associated with the side chains of the keratin; it was found that removing these groups greatly reduced the sorption of water into the wool fibre.[39–41] At higher humidities, water was said to associate with the peptide bonds along the main chain of the protein, swelling the fibre and allowing the strands to rearrange.[39]

Wool fibres are coated in a waxy lipid layer; when these lipids are removed, the absorbency of the wool fibres increases.[42] These lipids prevent water easily accessing the hydrophilic keratin in the core of the wool fibre.

Other factors which affect the absorbency of wool include ion concentration; this is referred to as the Hofmeister phenomenon, in which addition of ions will increase or decrease the absorption of water, depending on the positions of the ions added in the Hofmeister series. (It should be noted that there is no single Hofmeister series; the order of ions in the series will depend on the system used.)[43] At present, this phenomenon is not fully understood, but it is speculated that it may be due to the dispersion forces in solution.[44]

1.3.1.3. Silk

Silk is a natural fibre found in the cocoons of silkworms. It consists of the proteins fibroin and sericin, both of which contain only the amino acids glycine, alanine, tyrosine and serine.

1.3.1.4. Polyester

Polyester is a man-made fibre, consisting of polymers containing ester groups. The most commonly used polyester is polyethylene terephthalate (PET), which has the repeating structure seen below.

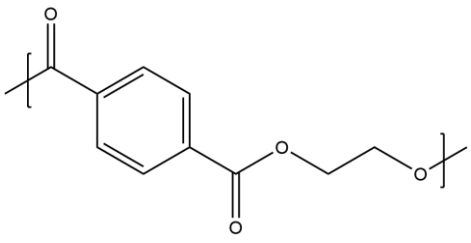

Figure 1-12: Structure of PET

Despite the presence of the carbonyl groups, polyester is highly hydrophobic. This makes it a difficult fabric to dye and clean. However, it is possible to increase the hydrophilicity of the fabric through the addition of hydrophilic polymers. As many polyesters are anionic, most success has been achieved using cationic polymers such as cationic starch.[45]

1.3.2. Removal of dirt

Most problematic soils on clothes are hydrophobic. These include food stains, mud, and sebum produced by the skin. As these soils are not soluble in water, they cannot be removed by rinsing with water alone; therefore, surfactants must be added to improve the process.

The shape of an oil droplet on fabric, in water or in air, can be described using Young's equation:

$$\gamma_{SW} = \gamma_{SO} + \gamma_{OW} cos\theta$$

Equation 1-4

In this equation, γ_{SW} is the interfacial tension between the solid and the water, γ_{SO} is the interfacial tension between the solid and the oil droplet, γ_{OW} is the interfacial tension between the oil droplet and the water, and θ is the contact angle between the drop and the surface. This is illustrated in Figure 1-13.

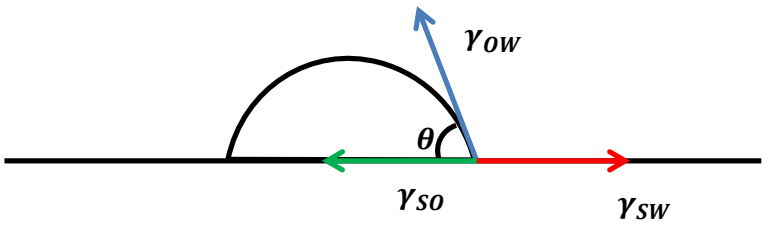

Figure 1-13: Parameters of Young's equation

When a fabric containing an oily stain is submerged in water, γ_{OW} will be high. However, when surfactants are added to the water, they will adsorb to the interface between the oil droplet and the water. This will lower the interfacial tension between the oil droplet and the water. The effect of this can be seen by rearranging Young's equation:

$$\cos\theta = \frac{\gamma_{SW} - \gamma_{SO}}{\gamma_{OW}}$$

Equation 1-5

At the start of the process, γ_{OW} is very high. However, when a surfactant is added, γ_{OW} will decrease. The process which follows will depend on the magnitude of γ_{SW}.

If γ_{SW} is low (i.e. the fabric is hydrophilic), or can be made low through the adsorption of surfactants, then $\gamma_{SW} - \gamma_{SO}$ will be (or will become) negative, resulting in an initial contact angle greater than 90°. As the surfactant is added to the oil-water interface, γ_{OW} decreases further, increasing the contact angle. Eventually a point may be reached where $\gamma_{OW} = \gamma_{SO} - \gamma_{SW}$, with cos θ = -1 and θ = 180°. Thus, the drop will be completely lifted off the surface.[3] This process is referred to as the roll-up of soil, and is illustrated in Figure 1-14 below. Even if $\theta \neq 180°$, mechanical agitation in the wash process can still lift and remove the oil droplet.

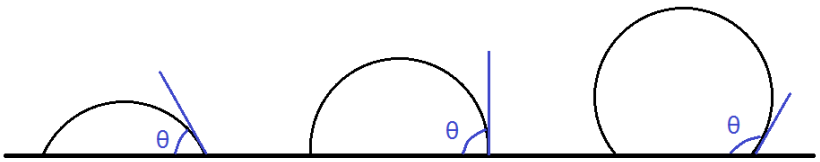

Figure 1-14: Mechanism of dirt roll-up

If $\gamma_{SW} - \gamma_{SO}$ cannot be made negative (for example, if the surface is highly hydrophobic, resulting in a very low value for γ_{SO}), then this process cannot occur. However, oil removal can still occur by emulsification, if the interfacial tension between oil and water is lowered sufficiently. In this process, the contact angle will increase to about 90°. Then, hydraulic currents will cause 'necking' of the droplet, causing part of it to bud off.[46] This process can then be repeated until the soil is removed. This process is shown in Figure 1-15 below.

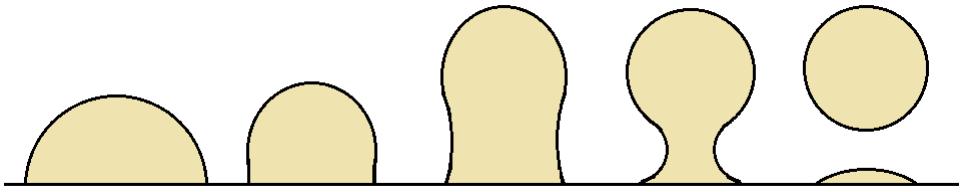

Figure 1-15: Emulsification of oily soil

The third method of oil removal, solubilisation, will remove oil by uptake of the oil molecules into surfactant micelles. Therefore, this method is only effective when the concentration of surfactant is above the CMC. It is not believed to provide a major contribution to soil removal.

1.3.3. Washing machines & technology

Worldwide, laundry is done in one of three ways: by hand, by automated washing machines, or by a half-automated process.

Two types of automatic washing machines are seen: horizontal axis machines where the clothes are loaded from the front (as seen in European countries), and vertical axis machines where the clothes are loaded from above (as seen in North America, Australia, and Asia). However, much of the new stock is shifting towards horizontal axis machines; as the clothes can be rotated vertically in these machines, only half of the drum needs to be filled, whereas vertical axis machines need to be filled completely to ensure all clothes are covered.[47]

North American, Australian, and Asian households are, however, using less energy to heat the water in their washes; the average American wash cycle is run at 30°C, whereas the average European cycle is both run at a hotter temperature, and for longer.[47] There are signs, however, that European consumers are moving to more energy-efficient washing habits over time.[48]

1.4. Fluorescence

In a molecule, electrons will exist in orbitals. These orbitals can be bonding orbitals (i.e. they will increase the bond order), non-bonding orbitals (no effect on bond order), or antibonding orbitals (will decrease the bond order). An example is shown in Figure 1-16.

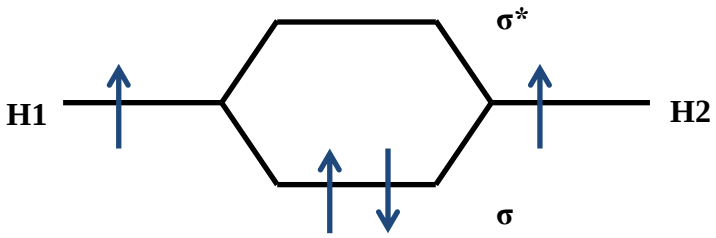

Figure 1-16: A molecular orbital diagram for a hydrogen molecule. The hydrogen atoms are marked H1 and H2. The bond creates an antibonding orbital (σ*) and a bonding orbital (σ).

Normally, the molecule will be in its ground state (termed S_0). However, if excited, one electron of a bonding pair can move to a higher electronic energy level (a molecular electronic transition). Each electronic energy level has an associated set of vibrational energy levels; these are termed $v = 0$ (the lowest), $v = 1$, $v = 2$ etc. In the case of the hydrogen molecule above, this would lead to one electron moving from the σ orbital to

σ^* orbital. These electronic and vibrational energy levels can be seen in Jablonski diagrams (such as Figure 1-17).

When the electron moves to a higher orbital, its spin can be either the same (parallel) or opposite (antiparallel) to that of the electron left behind. If the spins are antiparallel, then the overall spin of the molecule will be 0 and the electron will be in a singlet excited state (S_1, S_2 etc.). If the spins are parallel, then the overall spin of the molecule will be 1 and the electron will be in a triplet excited state (T_1, T_2 etc.). Two points must be noted about singlet and triplet excited states; firstly, each T_n state is lower in energy than the corresponding S_n state. Secondly, transitions from S_n to T_n states, and vice versa, are forbidden. (However, they may occur at slow rates under certain conditions.)

The process of fluorescence starts when an electron is excited, usually by electromagnetic radiation, from the ground state into a singlet excited state. Typically, it will also have a higher vibrational energy ($v > 0$). The electron will transfer to the lowest vibrational energy state via a series of non-radiative processes (e.g. by transfer of heat to the solvent). Once it has reached the level where v=0, it will move back to the ground state, releasing the excess energy in the form of electromagnetic radiation. This process is shown in Figure 1-17.

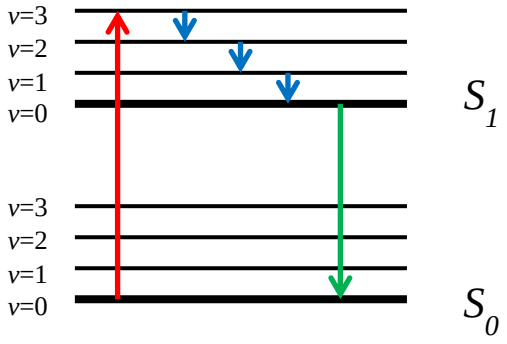

Figure 1-17: Jablonski diagram showing the process of fluorescence. The initial absorption of radiation is shown in red, non-radiative processes are shown in blue, and the movement of the electron to the ground state, with the release of electromagnetic radiation, is shown in green.

The process of phosphorescence starts in a similar way; radiation is absorbed, moving the electron to a singlet excited electronic state. The electron will move down the vibrational energy levels until it reaches $v = 0$. However, instead of relaxing to the ground state immediately, it will undergo an intersystem crossing to a triplet state. If $v > 0$, it will then move further down the vibrational energy levels until $v = 0$. The electron will then

undergo the transition $S_0 \leftarrow T_n$. This transition is forbidden, and will thus have a far longer lifetime than fluorescence. This process is shown in Figure 1-18 below.

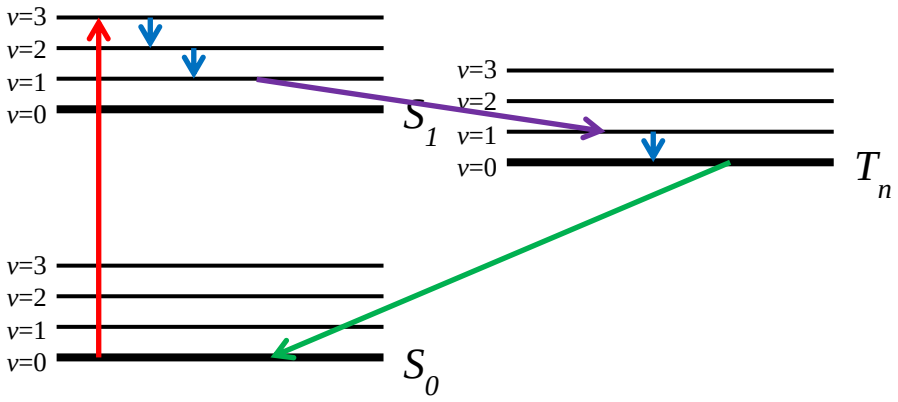

Figure 1-18: Jablonski diagram showing the process of phosphorescence. Initial absorption is shown in red, non-radiative transitions are shown in blue, intersystem crossing is shown in purple and emission of radiation is shown in green.

1.5. Optical brighteners and hueing dyes

Over time, white clothes will start to absorb light in the blue visible region; this will cause them to appear yellow. This will make the fabric appear dingy to the consumer. Whitecare technology in detergents aims to correct this. There are two main components to Whitecare: optical brighteners and hueing dyes. Optical brighteners will absorb light in the UV region and emit it in the blue region, making the fabric appear both brighter and less yellow, whereas hueing dyes will absorb light in the yellow region, making the fabric appear less yellow, but also less bright. For best results, a combination of the two is required.

1.5.1. Fabric yellowing

The yellowing of fabric has been attributed to the formation of aldehyde, ketone or carboxyl groups. In cotton, they are formed through the oxidation of hydroxyl groups found in cellulose fibres by various chemicals. The aldehyde groups are considered to have the greatest impact on the discolouration of fabric, although carboxyl groups can also affect colour.[49–51] Some of the products of oxidation reactions seen in cotton are shown in Figure 1-19 overleaf.

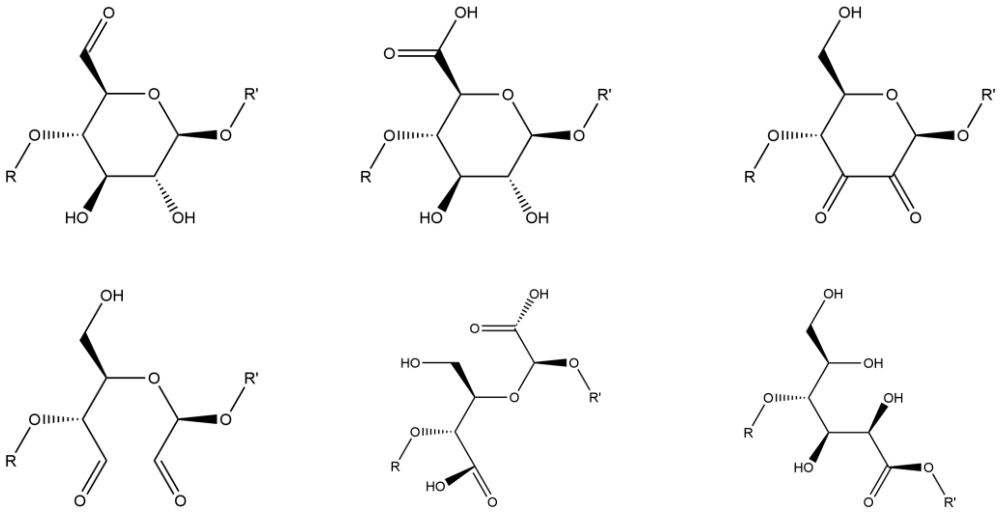

Figure 1-19: Oxidation products of cellulose, including products formed with and without ring opening. Adapted with permission. Copyright 2002 Elsevier ([52]).

Aldehyde groups may absorb visible light due to their π-bonds. When a chemical bond absorbs a photon, it will use the energy within that bond to move an electron from the highest occupied molecular orbital (HOMO) to the lowest unoccupied molecular orbital (LUMO). The greater the HOMO-LUMO gap, the more energy will be used and the lower the wavelength of photon needed to excite the electron across the gap. Therefore, the molecule will absorb photons with wavelengths corresponding to their HOMO-LUMO gap.

Most transitions will be in the UV region ($\lambda < 400$ nm). As the C=O bond contains a π-bond, it will have electrons in its π-orbitals; therefore it can undergo a $\pi^* \leftarrow \pi$ phase transition. As this represents a comparatively low HOMO-LUMO gap, the radiation absorbed will have a comparatively high wavelength. If the molecule has a large degree of π-conjugation, this will reduce the HOMO-LUMO gap further. This may lead to the molecule absorbing within the blue visible region, giving it a yellow appearance.

Several causes of fabric oxidation have been suggested. Perincek *et al*[51] attribute some fabric yellowing to the effects of ozonation; fabrics whitened with ozone rather than bleach may contain residual free radicals, which will continue to act on the cotton over time. However, as evidence of fabric yellowing predates the use of ozone to whiten fabric, this is unlikely to be the sole cause of yellowing.

Another cause of fabric yellowing is photo-oxidation. In this process, UV light acts on atmospheric oxygen to create free radicals that will oxidise the fabric. It has been suggested that these radicals are generated in a Bolland-Gee auto-oxidation reaction.[53] A generic reaction scheme is shown in Figure 1-20 overleaf.

$$Initiation \begin{cases} Polymer \xrightarrow{initiator} R^{\bullet} \\ R^{\bullet} \rightarrow R_X^{\bullet} \end{cases}$$

$$Propagation \begin{cases} R^{\bullet} + O_2 \rightarrow RO_2^{\bullet} \\ RO_2^{\bullet} + RH \rightarrow ROOH + R^{\bullet} \end{cases}$$

$$Chain\ branching \begin{cases} ROOH \rightarrow RO^{\bullet} + HO^{\bullet} \\ 2ROOH \rightarrow RO_2^{\bullet} + RO^{\bullet} + H_2O \\ RO^{\bullet} + RH \rightarrow ROH + R^{\bullet} \\ HO^{\bullet} + RH \rightarrow R^{\bullet} + H_2O \end{cases}$$

$$Termination \begin{cases} 2RO_2^{\bullet} \rightarrow Inert\ products \\ RO_2^{\bullet} + R^{\bullet} \rightarrow ROOR \\ 2R^{\bullet} \rightarrow RR \end{cases}$$

Figure 1-20: Generic Bolland-Gee auto-oxidation reaction scheme. Adapted from ([54]) with permission from the Royal Society of Chemistry.

Ironically, some fabric yellowing has been attributed to optical brighteners. The presence of brighteners on the fabric has been shown to accelerate the oxidation process of the fabric through the formation of superoxide, O_2^-, and peroxides.[55]

Other sources of fabric yellowing have been identified; Bangee *et al*[56] attribute yellowing in stored fabrics to NO_2 reacting with the antioxidant 2,6-di-*tert*-butyl-4-methyl-phenol (BHT), found in polyethylene and polypropylene packaging. However, as most consumers do not store their clothing in plastic packaging, this is unlikely to be a major cause of fabric yellowing over time.

1.5.2. Optical brighteners

The most common optical brighteners (also known as fluorescent whitening agents or FWA) used today are based on 1,1'-[1,2-Ethenediyl]dibenzene, known as stilbene. These compounds are naturally occurring in nature, particularly in plants.

The fluorescence of stilbenes depend on their C=C bonds and bond conjugation. They can exist as cis- and trans- isomers. When exposed to ultraviolet light, trans-stilbene will enter an excited energy state. Trans-stilbene has planar geometry,[57] whereas the excited state has perpendicular geometry rather than planar,[58] and so can return to either the cis- or the trans- form. If it re-forms the trans isomer, the excess energy will be released as electromagnetic radiation (with a fluorescence quantum yield of 0.05 for stilbene itself)[59].

Otherwise, it will form the cis-isomer in a non-radiative transition.[60] For this reason, only trans-stilbenes are useful in Whitecare.

When cis-stilbene is excited, it can also reach an excited state; however, this is a different excited state from excited trans-stilbene, although both are perpendicular. From this state, it can either form cis-stilbene with a probability of 71.7%, trans-stilbene with a probability of 20.3%, or react to form dihydrophenanthrene with a probability of 8.0%.[61]

Stilbenes have the greatest affinity for cotton fabrics. As, historically, cotton has been the most used clothing fibre, this has brought stilbenes into wide use. However, synthetic fibres are increasingly used in clothing manufacture. Therefore, other brighteners have been developed to brighten these fibres, such as coumarins. These are based on the heterocyclic molecule coumarin (2H-chromen-2-one). This molecule is shown in Figure 1-21 below.

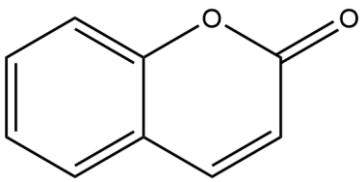

Figure 1-21: Coumarin

In this system, there is conjugation between the two oxygen atoms within the molecule. This reduces the HOMO-LUMO gap as discussed previously, allowing the molecule to fluoresce.[62] These compounds can be synthesized using starting materials derived from plants, such as 6,7-dihydroxycoumarin (also known as esculetin or aesculetin).[63]

1.5.3. Interactions with detergent ingredients

Many brighteners will be broken down by bleaches in detergents. This is more problematic for some brighteners than others; Brightener 49 is considered 'bleach stable', whereas Brightener 15 is 'bleach unstable'. Brightener 49 is also considered superior to Brightener 15 in terms of solubility and fluorescence efficiency.[64]

Brighteners which contain sulfonate groups are also affected by ions – in particular, heavy metal ions and those from Group 2. Ca^{2+} and Mg^{2+} ions will be present in samples of hard water; therefore, water hardness should affect brightener stability, and may cause it to precipitate out of solution.[65]

1.5.4. Dye-surfactant interactions

Surfactants and dye molecules are known to interact in many ways. If the dye and surfactant molecules have the same charge, then the surfactant will compete with the dye to adsorb onto the surface of the fabric. If, however, the surfactant is oppositely charged, or carries a neutral charge, then aggregates between the surfactant and dye molecule will form.[66] (There has been at least one case where a surfactant was thought to be interacting with a like-charged dye; however, this was later shown to be an interaction between the surfactant and an impurity in solution.)[67]

If the surfactant is used at concentrations below its CMC, then dye-surfactant aggregates will form. These can either be ion pairs or pre-micellar complexes. If the surfactant is used above its CMC, then the dye may be incorporated into the micelle itself, either in the hydrophobic 'tail' region or adsorbed onto the surface of the micelle. The use of co-solvents is known to inhibit the formation of these structures.[68]

1.5.4.1. Theory

The strength of the dye-surfactant interaction can be given by the **binding constant**, K_b.

$$K_b = \frac{[SD]}{[S][D]}$$

Equation 1-6

Here, [*SD*] is the concentration of the surfactant-dye dimers, [*S*] is the concentration of free surfactant, and [*D*] is the concentration of free dye molecules.[69] The more hydrophobic the dye molecule is, the higher K_b will be.[66]

The number of surfactant molecules bound to each dye molecule will be given by the **degree of binding**, β.

$$\beta = \frac{m_S - m_{SF}}{m_D}$$

Equation 1-7

In this equation, m_S is the total concentration of surfactant, m_{SF} is the total concentration of free surfactant, and m_D is the concentration of dye.[70]

For one surfactant-dye system, formation of dye-surfactant aggregates was found to proceed in three stages as the surfactant concentration is increased (assuming that it

remains below its CMC).[70] In the first stage, surfactant and dye monomers are attracted by electrostatic and dispersive forces.

$$D^- + S^+ \rightarrow (DS)$$

Equation 1-8

In the next stage, additional surfactant monomers join to the aggregates formed in the first step. This is thought to be due to hydrophobic interactions.

$$S^+ + (DS) \rightarrow (DS_2)^+$$

Equation 1-9

In the final step, further addition of surfactant monomers does not occur. Instead, the dimers formed in the first step will start to aggregate.

$$2(DS) \rightarrow (DS)_2$$

Equation 1-10

1.5.4.2. H- and J- aggregates

When large numbers of dye molecules aggregate, H- and J-aggregates can form. In these systems, the interactions between the molecules cause the absorption peak of the dye to shift. For H-aggregates, the peak is **hypsochromically** shifted (shifted to a shorter wavelength), whereas for J-aggregates, the peak is **bathochromically** shifted (shifted to a longer wavelength).

The main difference between these aggregates physically is the way in which they are stacked. H-aggregates are often referred to as being stacked in 'sandwich' or 'deck-of-cards' structures, forming vertical stacks with little deviation. (Here, π-π interactions will form between the molecules and support the stack)[69]. J-aggregates will line up head-to-tail, to form 'ladder' or 'brick wall' structures.[71] These are shown in Figure 1-22 overleaf.

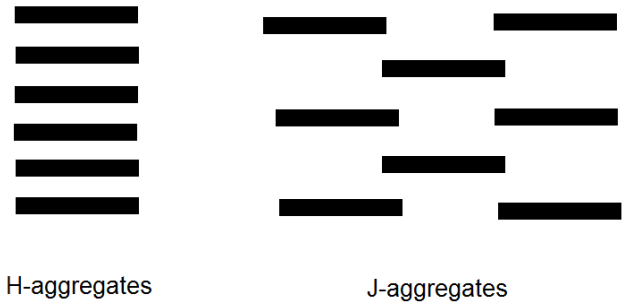

Figure 1-22: H- and J-aggregates. ('Brick wall' structure shown for J-aggregates)

1.5.5. Interactions with fabric

In 2010, Miljković *et al* determined the effect of addition of optical brighteners on the whiteness of fabric, as determined by its CIE index (see Section 1.5.6). It was found that as the concentration of brightener was increased, the whiteness increased up to a maximum, after which it decreased. It was suggested that this was due to excess brightener 'quenching' the fluorescence.[72]

Iamazaki and Atvars tested the effect of anionic surfactants, cationic surfactants and NaCl on the brightness of a fabric treated with Brightener 49. Whiteness was again determined using CIE indices. It was found that adding cationic surfactants increased the uptake of optical brightener until its CMC was reached, whereas anionic surfactants caused the uptake to drop relative to when a cationic surfactant was used (independent of concentration). Adding salt did not affect the fabric treated with the cationic surfactant, but increased the uptake for the fabric treated with the anionic surfactant.[73]

The same research group also imaged fibres treated with Brightener 49 using AFM (atomic force microscopy), SEM (scanning electron microscopy) and TEM (transmission electron microscopy). It was found that, while the brightener deposited evenly on the macro scale, it had formed aggregates on the surface of the fibre.[74]

In 2009, Was-Gubala studied the effect of soaking of fabric in detergent solution on the intensity of colour of dyed fabrics. Several detergent solutions were used, including an Ariel detergent containing optical brighteners. It was shown that, when cotton fabric was soaked in this detergent, it appeared lighter both under natural light and UV light.[75] This suggests that the brightener was depositing in quantities large enough to release enough photons to replace those absorbed by the dye molecules. However, there are three problems with this work; firstly, human volunteers were used to determine the colour change visually, on a scale from 1 ("No change in colour") to 5 ("Change in shade of

colour"). Both this scale, and the overall method used, were highly subjective and are open to error. Secondly, while the author raised the possibility that some dye was lost in solution due to the interruption of ionic bonding between the fabric and the dye, the change in colour due to addition of optical brighteners and loss of dye molecules were not treated separately. Finally, the conditions used (soaking fabric in detergent for 14 days) would not accurately reflect the effect of laundering. Therefore, while this work presented a confirmation that optical brighteners can affect the colour of dyed fabric, it did not provide any quantitative information about the rate, mechanism or efficiency of this process.

(The author continued this work in 2010, using spectrophotometric analysis to determine the change in colour. The maxima of the absorbance spectra, and the transmittance of the sample, were used to measure the change in colour quantitatively. This helps to remedy the first, and most serious, problem with the previous work; however, the latter two remain.)[76]

In 2005, Maseka studied the effect of optical brighteners (presumed to be stilbenes, although the brighteners used were not stated) on absorption and fluorescence emission spectra of both undyed and dyed cotton. This paper had three main findings: firstly, that increasing optical brightener concentration increased the fluorescence of the fabric, up to a maximum value, after which increasing the concentration provided no further increase in fluorescence. Secondly, the fluorescence of the fabric was lower in the dyed cotton. Finally, the addition of brightener did not cause the colour of the fabric to change, with the exception of the yellow fabric, which appeared to have a stronger yellow hue. This was attributed to the brightener acting as a yellow dye once its fluorescence is quenched.[77]

This paper provided evidence that studies of fluorescence of brighteners on fabrics can provide useful data; however, this study is limited in scope for several reasons. Firstly, a standard detergent mixture was used throughout, to which the brighteners were added. While this method did provide consistency throughout the experiment, it introduced a factor that is not addressed – namely, whether other components in the detergent affected either the deposition of the brightener, or its fluorescence. In addition, this paper presented several possible causes for phenomena seen, but did not attempt to determine which is the cause.

1.5.6. Methods to determine whiteness of fabric

Many methods have been used to determine the whiteness of fabrics treated with optical brighteners. One of the simplest methods is visual comparison; two or more fabrics are placed together and compared. This method has been used since the early development of brighteners,[78,79] and is still in use today.

Degree of whiteness can also be calculated objectively, using values such as the CIE index. This will provide the colour of the fabric in terms of *L** (the lightness of the colour), *a** (amount of green and red) and *b** (amount of yellow and blue).[80] These values can be determined using a spectrophotometer, reducing the human error in determining whiteness visually.

UV-vis and fluorescence spectroscopy have also been used[81–83], as the cis- and trans-forms of stilbene brighteners have separate peaks in the emission and absorption spectra.[82] The fluorescent quantum yield can also be determined. The absorption and emission peak height (and sometimes area underneath the peak) may also be used to determine the amount of fluorescent radiation emitted by the sample, and thus the amount of brightener present.[81,83]

The amount of optical brightener present in a fabric has also been determined by extraction. This was done by soaking the fabric sample in water at 80°C (to release the brightener into the water), then adding an ion-pair agent, performing reverse-phase chromatography using a C-18 SPE (silica column containing bound 18-carbon chains) to trap the hydrophobic species, and washing with methanol. Ion-pair HPLC (high performance liquid chromatography) analysis was then performed to separate the species present, and their fluorescence measured.[84]

1.5.7. Brighteners in society

Contamination of rivers and other freshwater sources with human sewage is a major problem. However, optical brighteners can offer a way to determine when this has occurred. Generally, 'blackwater' (sewage) and 'greywater' (waste water from laundry, bathing and other uses) are mixed upon removal, although this is changing. This means that the sewage content of a water sample is proportional to its content of waste water from laundry, and thus the optical brightener concentration. This concentration can be determined by extracting the optical brightener, as described in Section 1.5.6.[85]

However, optical brighteners in rivers and lakes can also have adverse effects on wildlife. It has been shown that stilbene-based optical brighteners can bind to the oestrogen receptors of fish and humans *in vitro*, and thus act as an inhibitor. *In vivo* studies on fish have proved inconclusive.[86]

Another area in which optical brighteners have proved problematic is in forensic science. Semen stains on fabric are usually identified by irradiation with UV light; as fabric treated with brighteners will also fluoresce, this can lead to a false positive result. This can be remedied by narrowing the wavelength of the light source; cotton treated with brighteners will be excited at wavelengths of 340-410 nm, and emit radiation at 440-470 nm, whereas semen has a far broader spectrum.[87]

Optical brighteners have been shown to increase the ultraviolet protection factor of fabrics. This would have applications in the manufacture of protective fabrics for conditions where UV damage is likely to be a problem, such as beach clothing.[88]

1.6. Aims of this project

In this project, I will discuss how optical brighteners and surfactants in washing powder interact. This was investigated in four ways.

In Chapter 3, the deposition of brightener onto the fabric was measured using fluorescence methods. The amount of brightener deposited, and its deposition rate, will be determined. The effect of anionic and nonionic surfactant addition will be measured.

In Chapter 4, the crystal structure of the brightener was studied. Both bulk crystallisations and microemulsion methods were used. A crystal structure was determined for a brightener methanol solvate, and its configuration was compared to that seen elsewhere in the project.

In Chapter 5, the interaction between the surfactant micelle and the brightener molecule was measured using SAXS methods. The change in electron density contrast and micellar radius with the addition of brightener was determined, allowing the position of the brightener within the micelle to be studied.

In Chapter 6, molecular dynamics simulations were run on surfactant systems with and without brightener. The change in micellar radius and aggregation number with changing brightener concentration and type of surfactant was determined.

The effect of calcium carbonate, as seen in hard water systems, was also measured using the same methods, and is presented alongside the data obtained from the brightener systems. In Chapter 4, the effect of the surfactants found in detergents on calcium carbonate precipitation was measured. In Chapter 5, the effect of the addition of calcium ions on the electron density contrast and micellar radius of surfactant micelles was determined. In Chapter 6, molecular dynamics simulations were used to show the positions of calcium ions relative to surfactant micelles.

2. Experimental methods

In this chapter, I will examine the theoretical backgrounds and experimental techniques of the methods used in this project.

2.1. Spectroscopic methods

In this study, two types of spectroscopy were used: absorbance spectroscopy and fluorescence spectroscopy. Both techniques used the fluorescent properties of molecules (as discussed in Chapter 1).

In an absorbance experiment, light of a series of wavelengths is passed through the sample. When the wavelength of light corresponding to an energy transition is passed to the sample, the molecule uses the energy of that photon to undergo an $E_1 \leftarrow E_0$ transition. Therefore, some of the light of that wavelength will be absorbed.

In comparison, fluorescence spectroscopy measures the amount of light released by the $E_0 \leftarrow E_1$ transition. There are two main types of fluorescence spectroscopy – emission and excitation spectroscopy. In fluorescence emission spectroscopy, the wavelength of the radiation used to excite the sample is kept constant. A monochromator is used to ensure that radiation of a single wavelength is emitted into the sample. The intensity and wavelength of the radiation emitted by the sample after excitation can then be measured. This technique is useful to determine the wavelengths of light that the sample will emit upon excitation.

In fluorescence excitation spectroscopy, the intensity of radiation of a given wavelength emitted from the sample will be measured. The wavelength of the radiation passed into the sample will be gradually increased using a monochromator. Thus, the intensity of the radiation released can be compared to the wavelength of the radiation used to excite the sample. This technique is useful to determine the wavelengths of light that cause the greatest excitation of the sample.

In this project, absorbance spectra were taken using a Unicam UV/Vis spectrometer. Emission and excitation spectra were taken using a Fluorolog® spectrophotometer, produced by Horiba, using a 450 W xenon lamp as its light source.

2.2. Small-angle X-ray scattering (SAXS)

2.2.1. Fourier series and Fourier transforms

When the magnitude of a wave (such as a light wave) is plotted against time, it will appear as a sine wave. The frequency of the wave, *f*, is related to the period, T, by the relation $f = \frac{1}{T}$.

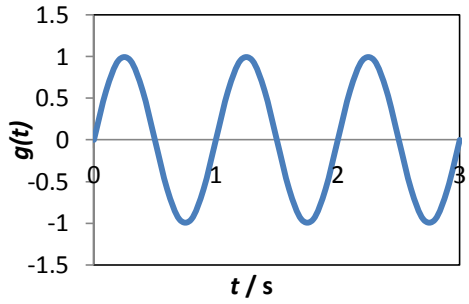

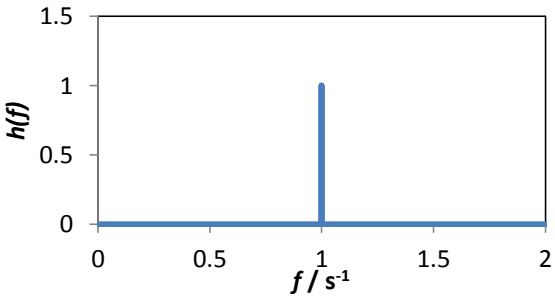

Figure 2-1: A wave *g(t)* with magnitude 1 and period 1 s (shown left)

Figure 2-2: The wave *g(t)* represented in the frequency domain by the function *h(f)* (shown right)

Figure 2-1 shows one such wave, *g(t)*, with a magnitude of 1 and a time period of 1 s. This wave is represented in the time domain; however, it is also possible to represent this wave in terms of frequency. As its period is 1 s, its frequency will be 1 s^{-1}, or 1 Hz. This is shown in Figure 2-2 above. Note that in Figure 2-2 the function is no longer dependent on *t*, but on *f*; the function *g(t)* is now represented by another function, *h(f)*, which appears completely different, but contains the same data.

When two waves are present, $w_1(t)$ and $w_2(t)$, they will combine to form one overall wave, *w(t)*. Let $w_1(t)$ have an amplitude of 2 and a period of 2 s, and let $w_2(t)$ have an amplitude of 1 and a period of 3 s. This is shown in Figure 2-3.

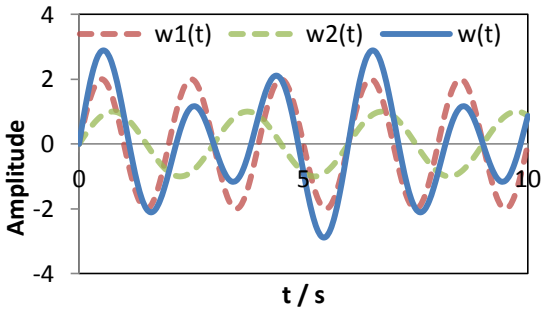

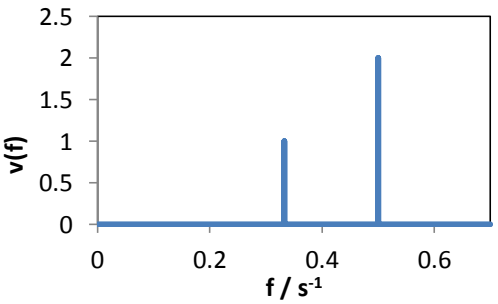

Figure 2-3: The waves $w_1(t)$, $w_2(t)$, and *w(t)* (left)

Figure 2-4: The function *v(f)* (right)

The two waves combine to form a new wave with period 6 s. It is not possible to determine the component waves by examining *w(t)*; however, we can gain this information by representing *w(t)* in the frequency domain as the function *v(f)* (shown in Figure 2-4).

In this manner, it is possible to separate any periodic function into an infinite sum of sine and cosine functions by using its Fourier series. Assume the function *g(x)* is periodic with a period of 2*L*. Then:[89]

$$g(x) = \frac{a_0}{2} + \sum_{n=1}^{\infty} a_n \cos\frac{n\pi x}{L} + b_n \sin\frac{n\pi x}{L}$$

Equation 2-1

Where

$$a_n = \frac{1}{L}\int_{-L}^{L} g(x)\cos\frac{n\pi x}{L}dx$$

Equation 2-2

$$b_n = \frac{1}{L}\int_{-L}^{L} g(x)\sin\frac{n\pi x}{L}dx$$

Equation 2-3

$$\frac{a_0}{2} = \frac{1}{2L}\int_{-L}^{L} g(x)dx$$

Equation 2-4

An example of this is shown in Figure 2-5 overleaf. (While Fourier series can be applied to any function, they can be given physical meaning easily using time and frequency).

A saw function *g(t)* has the equation

$$g(t) = t; \qquad -1 \leq t < 1$$

Equation 2-5

It can be described using the Fourier expansion

$$g(t) = 2\sum_{n=1}^{\infty}\left(\frac{(-1)^{n-1}}{n\pi}\sin n\pi t\right)$$

Equation 2-6

Below, an approximation is given for *g(t)* by calculating its Fourier series up to *n*=5.

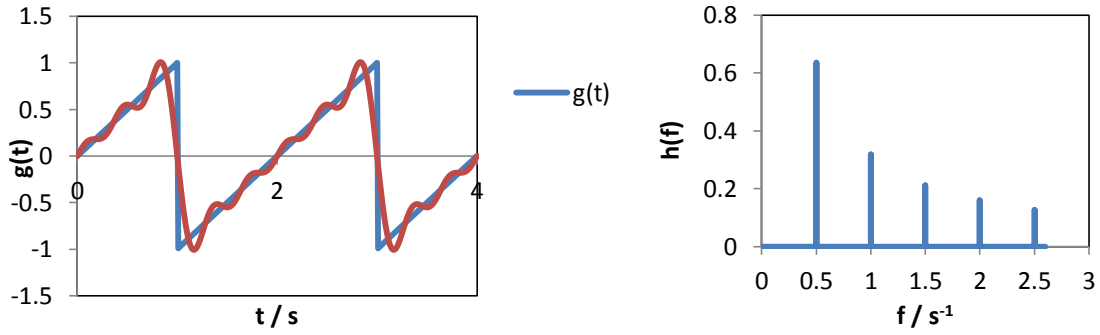

Figure 2-5: A saw function g(t) and its approximation using the first 5 terms of its Fourier expansion (LEFT); g(t) represented in the frequency domain by the function h(f) (RIGHT).

Again, we can plot the amplitude and frequency of the function. It should be noted at this point that the distance between the lines in this domain is inversely proportional to the period of the function *g(t)*; as *L* increases, the lines pack more closely together.

Not all functions are periodic, however. In this case, we consider that $L \to \infty$ and the Fourier Integral is obtained:[90]

$$g(t) = \int_{-\infty}^{\infty} G(f)\, e^{2i\pi f t} df$$

Equation 2-7

In this equation, the terms a_n and b_n have been replaced by a single function *G(f)*, representing *g(t)* in the frequency domain, and the sine and cosine terms have been represented in their complex form using Euler's formulae:

$$\cos\theta = \frac{e^{i\theta} + e^{-i\theta}}{2}$$

Equation 2-8

$$\sin\theta = \frac{e^{i\theta} - e^{-i\theta}}{2i}$$

Equation 2-9

G(f) can be calculated similarly to a_n and b_n using the formula:

$$G(f) = \int_{-\infty}^{\infty} g(t) e^{-2i\pi f t} dt$$

Equation 2-10

G(f) is referred to as the ***Fourier transform*** of *g(t)*, whereas *g(t)* is referred to as ***the inverse Fourier transform*** of *G(f)*. The domain of *g(t)* is sometimes referred to as the 'real domain', whereas the domain of *G(f)* is referred to as the 'reciprocal domain'. One way to think of *G(f)* is as the peaks in the frequency domain, as seen before; however, as *L* tends to infinity, 1/*L* tends to 0. Therefore, the peaks will be infinitely close together and *G(f)* will appear as a curve.

The Fourier transform can be demonstrated using a simple function: consider a square wave with the equation

$$g(t) = \begin{cases} 1 & -1 \leq t \leq 1 \\ 0 & else \end{cases}$$

Equation 2-11

Using the formulae above, its Fourier transform can be calculated as

$$G(f) = \frac{\sin(2\pi f)}{\pi f}$$

Equation 2-12

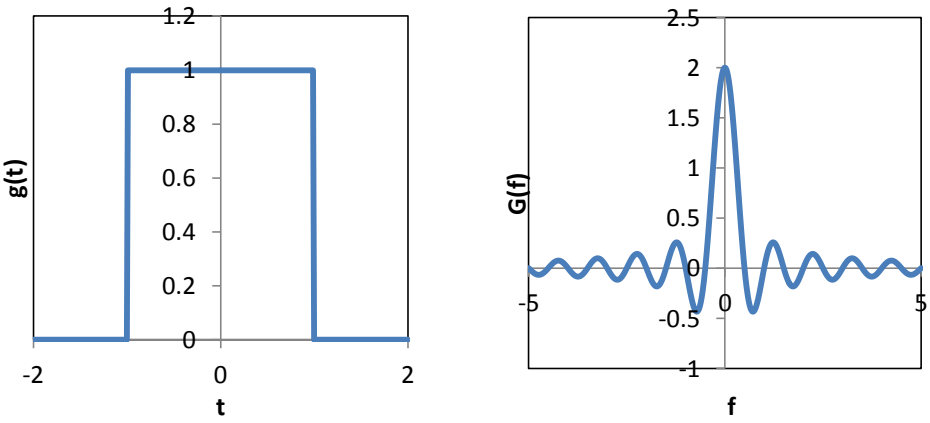

Figure 2-6: Square pulse (left); Fourier transform of a square pulse (right)

2.2.2. X-ray scattering

This section describes a derivation of a simple expression for scattering intensity as given by Porod in 1982:[91]

Assume that a sample contains particles of fixed size and constant electron density. These particles are dissolved in a solution with a different electron density. When X-rays are fired at the sample, the X-rays will be scattered by the sample's electrons. (This occurs when the incident X-ray is absorbed and re-emitted by the electron; adjacent electrons emitting X-rays will experience interference.) This will cause the direction of the beam to change. The angle between the initial direction of travel and the new direction of travel is denoted as 2θ.

Consider an electron in the sample, at a distance *r* from an arbitrary origin. Assume that the electron has diffracted an X-ray by an angle 2θ. This is shown in Figure 2-7 below.

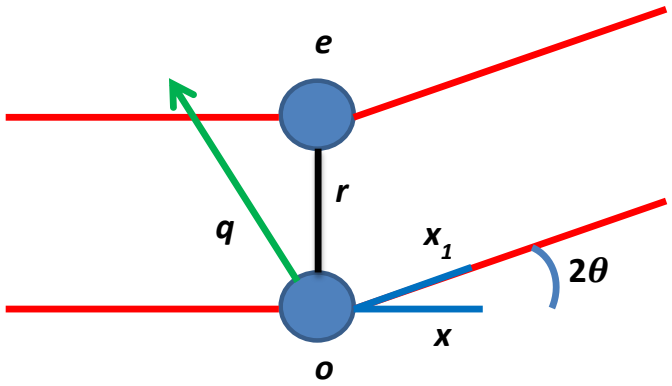

Figure 2-7: An electron (e) diffracting X-rays

The vector ***x*** represents the initial X-ray, whereas $\boldsymbol{x_1}$ represents the scattered beam, as if they were scattered by an origin, *o*. The beam ***x*** is parallel to the wave striking the electron, whereas $\boldsymbol{x_1}$ is parallel to the scattered radiation. The vector *q* then represents the scattering; it has a magnitude of:

$$q = \frac{4\pi}{\lambda}\sin\theta$$

Equation 2-13

This magnitude of *q* defines the 'window' studied:

$$d = \frac{2\pi}{q}$$

Equation 2-14

The maximum distance covered is given by *d*. At low *q*, *d* will be large, corresponding to a large 'window'; interactions between multiple particles can thus be studied. At high *q*, *d* will be low; therefore, sharp detail such as interfaces can be studied. Intermediate values of *q* are used to study the structure of individual particles.

The path difference between the wave scattered at the electron *e* and the beam x_1 is given by

$$path\ difference = -\boldsymbol{r}(\boldsymbol{x} - \boldsymbol{x_1})$$

Equation 2-15

Note that ***r*** (the vector displacement of *e* from *o*) may not be perpendicular to ***x***.

The phase of the radiation scattered by the electron *e*, in relation to *x*, is given by φ.

$$\varphi = -\frac{2\pi}{\lambda}\boldsymbol{r}(\boldsymbol{x} - \boldsymbol{x_1}) = -\boldsymbol{rq}$$

Equation 2-16

The scattered wave can be given as $e^{i\varphi}$, and therefore as e^{-irq}.

To calculate the amplitude of the diffraction, the sum of all waves coming from the sample needs to be found. This is done by considering the electron density, $\rho(r)$. The amplitude of scattered radiation will equal the amplitude of radiation per electron multiplied by the number of electrons present. Hence we can find the amplitude of radiation scattered as a function of *r* and *q*:

$$F(\boldsymbol{q}) = \iiint dV \cdot \rho(\boldsymbol{r}) e^{-i\boldsymbol{rq}}$$

Equation 2-17

This takes exactly the same form as the Fourier transform shown in Equation 2-10; the electron density is in the space domain of *r*, whereas $F(q)$ is in the reciprocal domain.

To find the intensity of the radiation as a function of *q*, the magnitude of $F(q)$ must be found. (As Equation 2-17 is a summation of a set of complex numbers, its magnitude is

taken to ensure that its value is real, not complex.) This is done by multiplying it by its complex conjugate [if $f = x + iy$, then its complex conjugate will be $f^* = x - iy$, and $f \cdot f^* = x^2 + y^2$]:

$$I(\boldsymbol{q}) = F(q)F^*(q) = \iiint \iiint dV_1 \cdot dV_2 \cdot \rho(\boldsymbol{r_1})\rho(\boldsymbol{r_2})e^{-i\boldsymbol{q}(\boldsymbol{r_1}-\boldsymbol{r_2})}$$

Equation 2-18

I(*q*) is therefore a function representing electron density in terms of distance between two points, r_1 and r_2.

Porod[91] recommends breaking the expression *I*(*q*) into two separate steps, first creating a function to find the electron density of two points in terms of the distance between them (i.e. moving from a domain of pure distance to one of 'distance differences'), then integrating this function over the whole volume, calculating the electron density of paired points over all separation distances.

The function used to represent electron densities of paired functions is $\tilde{\rho}^2$, and is given by

$$\tilde{\rho}^2(\boldsymbol{r}) = \iiint dV_1 \rho(\boldsymbol{r_1})\, \rho(\boldsymbol{r_2})$$

Equation 2-19

The intensity is then given by

$$I(\boldsymbol{q}) = \iiint dV \cdot \tilde{\rho}^2(\boldsymbol{r}) \cdot e^{-i\boldsymbol{q}\boldsymbol{r}}$$

Equation 2-20

This is essentially a Fourier transform of the previous function, taking it from the domain of 'distance difference' to the reciprocal domain. This clearly demonstrates the link between *I*(*q*) and the structure of the sample.

The average of e^{-iqr} is taken to get $\frac{\sin qr}{qr}$, and $\tilde{\rho}^2(\boldsymbol{r})$ replaced with the correlation function $\gamma(r)$, which gives the change in electron density fluctuation between two particles at a distance *r* apart[91]. This is defined by Debye and Bueche as "the extensions of the inhomogeneities"[92], and corresponds to the equation $\gamma(r)r^2 = p(r)$, where p(r) is the pair distribution function of the particle, i.e. the probability of finding two electrons at a

distance *r* apart, weighted by the electron density contrast between the particle and solution. Porod gives the most general form of the equation as

$$I(q) = V \int_0^\infty 4\pi \boldsymbol{r}^2 d\boldsymbol{r} \cdot \gamma(r) \frac{\sin \boldsymbol{qr}}{\boldsymbol{qr}}$$

Equation 2-21

However, in most works, the most general form of $I(q)$ is found by substituting the correlation function for the pair distribution function, p(r):

$$\gamma(r) r^2 = p(r)$$

Equation 2-22

$$I(q) = 4\pi \int_0^\infty p(r) \frac{\sin qr}{qr} dr$$

Equation 2-23

This expression has been refined for many different structures and applications; however, all expressions for $I(q)$ rely on the Fourier transformation of an expression for the electronic distribution in real space. Some of these expressions will be discussed in the following section. Expressions for the electronic structure itself, as represented by its pair distribution function $p(r)$, will be discussed later.

Note that this expression assumes that all scattering intensity is caused by scattering from isolated objects, which in our case will be the micelles themselves, and that there is no interference between scattering from neighbouring micelles. In practice, there will be scattering from both sources; scattering from the particles themselves is described by the form factor, $P(q)$, and scattering caused by interference between micelles is described by the structure factor, $S(q)$. These forms of scattering will be discussed in turn.

2.2.3. Form factor, $P(q)$

The form factor, $P(q)$, represents the portion of scattering caused by the individual micelles themselves, as described previously. In most cases, $P(q)$ is given as a Fourier transform of some function of the electron density of the particle, as in Equation 2-17 and Equation 2-18.

By remembering that Equation 2-23 considered only intraparticle scattering (i.e. $S(q) = 1$), we can re-write this equation to give:[93]

$$P(q) = 4\pi \int_0^\infty p(r) \frac{\sin qr}{qr} dr$$

Equation 2-24

emphasizing that $p(r)$ can be obtained from the Fourier transform of $P(q)$ and vice versa.

2.2.4. Pair distribution function, $p(r)$

As previously described, the pair distribution function $p(r)$ describes the probability that one element within a particle will be found at a distance between r and $(r+dr)$ from another. In the case of SAXS, the elements involved are electrons within the micelle.

In all pair distribution functions, a few trends can be seen. Firstly, $p(r)$ will tend to 0 at the maximum diameter of the particle, D. Secondly, any minima in the $p(r)$ indicate regions of different electron density contrast; the number of minima is equal to the number of boundaries between regions of electron density contrast of opposite sign, for example, an electron deficient micelle core and its electron rich outer shell; see Figure 2-8. Finally, the heights of the peaks in $p(r)$ reflect the magnitude of the electron density contrast between the particle and the solution.

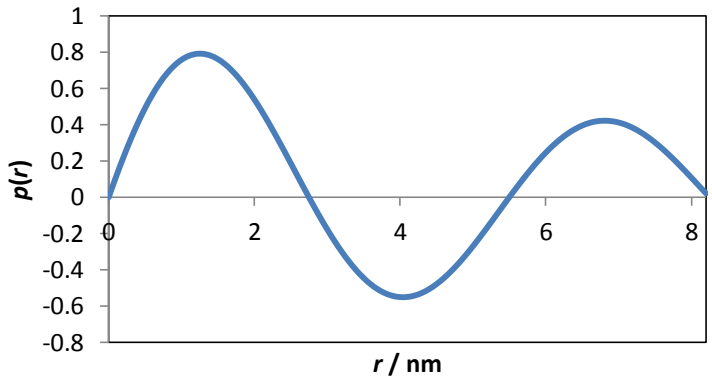

Figure 2-8: A typical $p(r)$ for a particle containing an electron-rich region and an electron-dense region (e.g. a micelle)

In most cases, the pair distribution function has to be calculated numerically. However, in a few cases, the pair distribution can be described mathematically; examples of these will be given as follows.

2.2.4.1. Globular particles

A monodisperse distribution of spheres can be described by the equation:[94]

$$p(r) = 12x^2(2 - 3x + x^3)$$

Equation 2-25

In this equation $x = \frac{r}{D}$ where *D* is the diameter of the sphere and *r* is the distance between the scattering electrons. The particle will have a maximum *p*(*r*) at $x \cong 0.525$.

Figure 2-9 shows the effect of the particle diameter on the pair distribution function for a sphere.

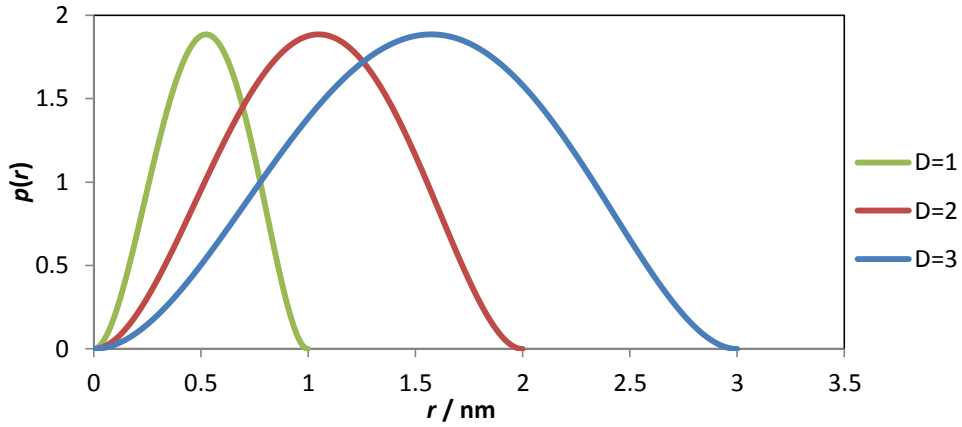

Figure 2-9: Effect of particle diameter on its p(r)

2.2.4.2. Rod-like particles

The pair distribution function for a rod with cross-sectional area *A*, length *L*, and electron density *ρ* can be described by the equation:[94]

$$p(r) = \begin{cases} p(r) = 12x^2(2 - 3x + x^3) & r < L \\ \frac{1}{2\pi}\rho^2 A^2(L - r) & r > L \end{cases}$$

Equation 2-26

The parameter *x* is defined as $x = \frac{r}{D}$ as in Section 2.2.4.1.

2.2.4.3. Hollow spheres

Consider a hollow sphere. This is modelled as a homogeneous sphere of radius R_a and an electron density of *ρ*, with a sphere removed from the centre with a radius R_i. This particle will have a *p*(*r*) as modelled by:[94]

$$p(r) = \begin{cases} \rho^2\left[\frac{4\pi}{3}\left(R_a^3 - R_i^3\right)r^2 - \left(R_a^2 + R_i^2\right)\pi \cdot r^3 + \frac{\pi}{6} \cdot r^5\right] & 0 \le r \le (R_a - R_i) \\ \rho^2\left[\frac{\pi}{2}\left(R_a^2 - R_i^2\right)^2 r\right] & (R_a - R_i) \le r \le 2R_i \\ \rho^2\left[\frac{\pi}{2}\left(R_a^2 - R_i^2\right)^2 \cdot r - \frac{4\pi}{3}R_i^3 \cdot r^2 + \pi R_i^2 \cdot r^3 - \frac{\pi}{12}r^5\right] & 2R_i \le r \le (R_a + R_i) \\ \rho^2\left[\frac{4\pi}{3}R_a^3 \cdot r^2 - R_a^2\pi \cdot r^3 + \frac{\pi}{12} \cdot r^5\right] & (R_a + R_i) \le r \le 2R_a \end{cases}$$

Equation 2-27

Figure 2-10 shows $p(r)$ for various hollow spheres. In each case, the outer radius is assumed to be 1 nm; the electron density is assumed to be the same for all. The $p(r)$ is plotted for various hollow sphere radii. As the inner radius increases, $p(r)$ decreases and becomes more linear.

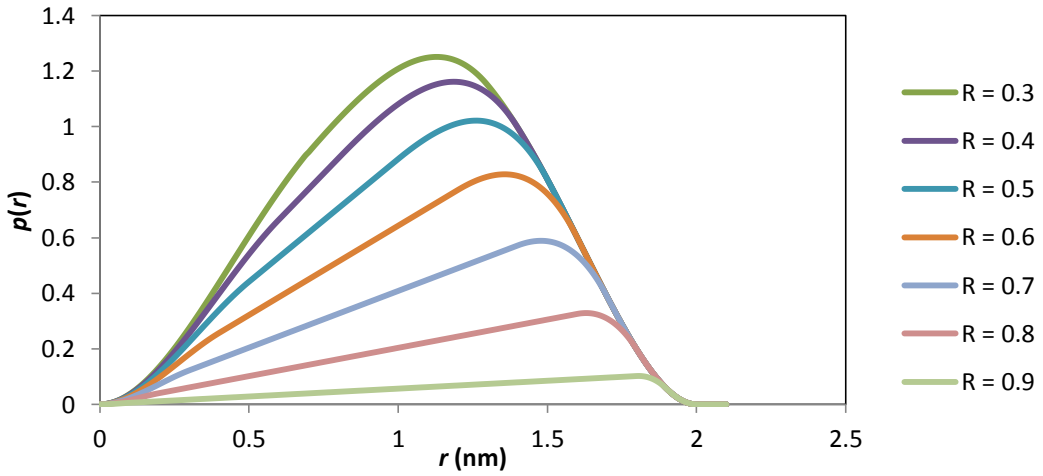

Figure 2-10: Effect of hollow sphere radius on $p(r)$

2.2.4.4. Micelles

In general, surfactant micelles are modelled as a two-layer structure, with an inner core and outer shell. For a standard micelle in water, the hydrophobic tail groups will form the inner core, and will have an electron density lower than that of the solvent (i.e. a negative electron density contrast), and the hydrophilic head groups will form the outer shell, with an electron density that is often higher than that of the solvent (i.e. a positive electron density contrast). Therefore, $p(r)$ of a micelle in water will show three regions; two maxima with positive $p(r)$, (one at low r and one at high r, corresponding to electron pairs both in the inner core or outer shell, respectively) and a minimum with negative $p(r)$, (corresponding to paired electrons where one is in the outer shell and one is in the inner core).

However, other models exist. Vass *et al.* compared the standard, two-layer model with a three-layer model and a four-layer model.[95] In the three-layer model, the tail groups and head groups of the surfactants are again treated as two layers, with the counterions forming a third shell around the micelle. The four-layer model splits the tail groups into the terminal carbon groups, $-CH_3$, and the inner carbon groups, $-CH_2-$. It was found that the most accurate results were obtained using the four-layer model (see Figure 2-12); however, the two-layer model continues to be the most used. In particular, the effect of counterions is often ignored due to their small size and low electron density contrast; typically, scattering due to counterions is 1/100th that of scattering due to the rest of the micelle.[96]

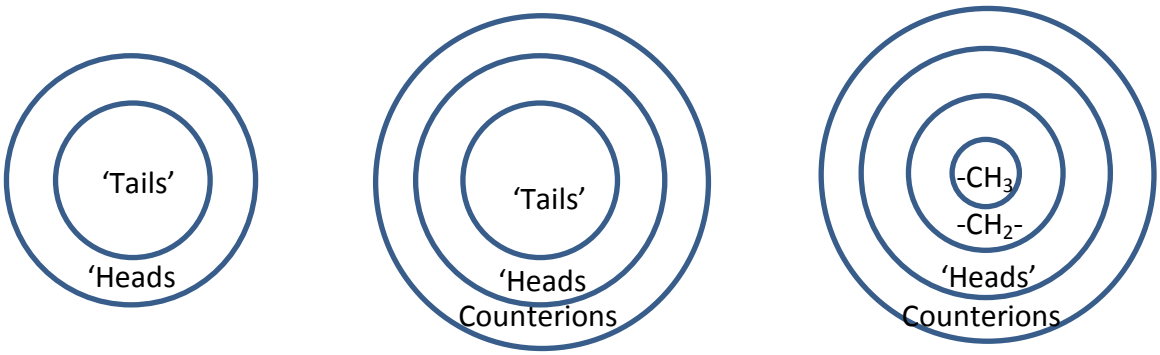

Figure 2-11: The 2, 3 and 4 layer model

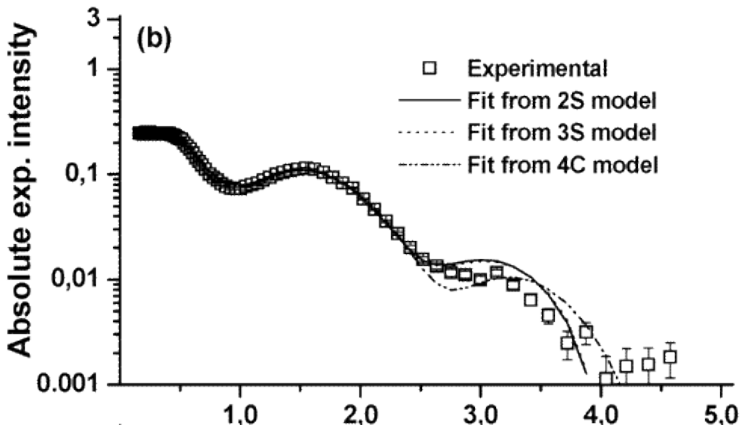

Figure 2-12: Fitting 2-layer, 3-layer and 4-layer models to experimental data for a micelle. Reprinted with permission from (S. Vass, J. Plestil, P. Laggner, T. Gilanyi, S. Borbely, M. Kriechbaum, G. Jakli, Z. Decsy and P. M. Abuja, *Journal of Physical Chemistry B*, 2003, 107, 12752-12761)[95] Copyright (2003) American Chemical Society.

Unlike many particles, surfactants cannot be studied at multiple dilutions to remove the effect of the structure factor, as this will cause the micelles to dissociate below the CMC. For this reason, it is particularly important to compensate for the structure factor while calculating $p(r)$.[97]

2.2.5. Examples of P(q)

2.2.5.1. Spherical particles

The model assumes that the spheres are all identical and homogeneous (i.e. all spheres have a radius *R* and a constant electron density). Let the electron density difference between the spheres and the solvent (aka the electron density contrast) be $\Delta\rho$. Then:[91]

$$P(q) = (\Delta\rho)^2 V^2 \left[3\frac{\sin qR - qR\cos qR}{(qR)^3}\right]^2$$

Equation 2-28

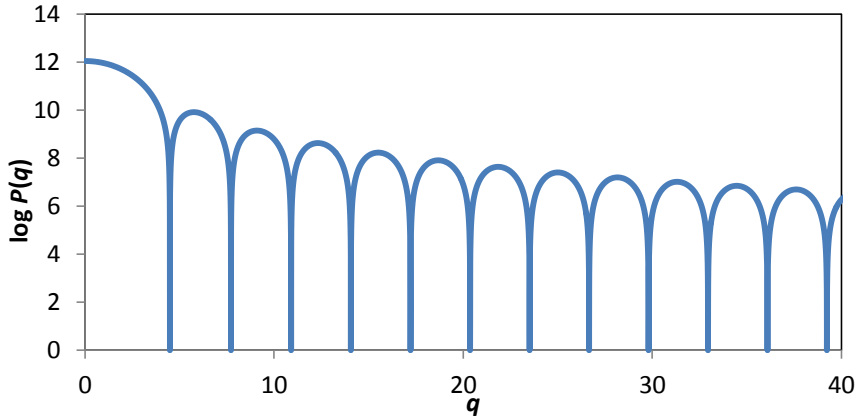

Figure 2-13: Theoretical scattering curve for homogeneous spheres

The curve given by Equation 2-28 is shown in Figure 2-13 above; however, the curve seen in practice would not show these sharp 'dips'. This is because the X-rays produced by the source will not be of one single wavelength, and typically the spheres will not be monodisperse; both effects cause smearing. Often, only the first dip will be discernible.

2.2.5.2. Ellipsoidal particles

This model assumes, again, that the particles are of constant size and electron density. The ellipsoids have axes of length *a*, *b*, and *c*, and an electron density contrast of $\Delta\rho$. Then:[98]

$$P(q) = (\Delta\rho)^2 V^2 \int_0^1 \int_0^1 \left[3\frac{\sin qR_{eff} - qR_{eff}\cos qR_{eff}}{\left(qR_{eff}\right)^3}\right]^2 dxdy$$

Equation 2-29

$$R_{eff} = \sqrt{a^2 \cos^2\left(\frac{1}{2}\pi x\right) + b^2 \sin^2\left(\frac{1}{2}\pi x\right)(1 - y^2) + c^2 y^2}$$

Equation 2-30

R_{eff} represents an average value for the radius of the particle, at the orientation defined by x and y. Integrating over x and y therefore provides an average over all orientations.

If $a=b\neq c$, then Equation 2-30 can be simplified:

$$R_{eff} = \sqrt{a^2\left[1 + y^2\left(\frac{c^2}{a^2} - 1\right)\right]}$$

Equation 2-31

2.2.5.3. *Core-shell particles*

$P(q)$ for core-shell particles (i.e. those that can be modelled by a homogeneous sphere within a larger sphere of a different electron density, such as micelles) can be given by the equation:

$$P(q) = V_c^2(\rho_c - \rho_s)^2\Psi_c^2 + 2V_cV_s(\rho_c - \rho_s)(\rho_s - \rho_{solv})\Psi_c\Psi_s + V_s^2(\rho_s - \rho_{solv})^2\Psi_s^2$$

Equation 2-32

$$\Psi_x = 3\frac{\sin(qR_x) - qR_x\cos(qR_x)}{(qR_x)^3}$$

Equation 2-33

where R_c and R_s are the radius of the inner core and outer shell respectively, V_c and V_s are the volumes of the inner core and outer shell, and ρ_c, ρ_s and ρ_{solv} are the electron densities of the core, shell and solvent respectively.

2.2.6. Structure factor, $S(q)$

The structure factor, $S(q)$, describes all scattering caused by interactions between particles (such as micelles) in solution. It scales with concentration; at very low concentrations, interactions between particles will be minimal, and so $S(q)$ will equal 1 for all values of q. As the concentration increases, the particles will move closer together in space, and so interparticle interactions will increase. As the interaction between the particles will depend on the distance between them, the structure factor will depend heavily on r, and thus q. This section will discuss the origin of the structure factor and its mathematical models.

2.2.7. Correlation functions - the Ornstein-Zernike (OZ) equation

The Ornstein-Zernike (OZ) equation was first proposed in 1914 by Leonard Ornstein and Frits Zernike.

Consider particles in solution. One particle can interact with another in two ways, as shown in Figure 2-14 below.

Figure 2-14: Interparticular interactions

On the left, a particle is shown directly interacting with another. On the right, a particle is interacting with another through a third particle.

In statistical mechanics, the influence of one particle on another can be described using a correlation function. The OZ equation allows the total correlation function, $h(r)$ between two particles to be calculated:[25]

$$h(r) = c(r) + \rho \int h(|r - r'|)c(r')dr'$$

Equation 2-34

The first term, $c(r)$, is the direct correlation function between the particles at a distance r apart, whereas the second term, the integral, represents the sum of all indirect interactions (where the particles are interacting through a third particle at a distance r'). The constant ρ is the density of the solution.

The total correlation function, $h(r)$, is related to the radial distribution function, $g(r)$ through the expression:

$$h(r) = g(r) - 1$$

Equation 2-35

The radial distribution represents the probability that there will be a particle at a distance r from another particle. It will tend to 1 at large values of r, showing that the short-range ordering of the system has been lost.

In order to solve the OZ equation, the mean spherical approximation is used. This treats the particles as hard spheres of radius *R* which cannot intersect each other, and which will repel each other. This allows the following conditions to be set:[99]

$$c(r) = -\beta v(r) \qquad r > R$$

Equation 2-36

$$h(r) = -1 \qquad r < R$$

Equation 2-37

2.2.7.1. S(q)

The structure factor is found by taking a Fourier transform of *g*(*r*), as given by the OZ equation:[95]

$$S(q) = \int g(r) e^{-iqr}\, dr$$

Equation 2-38

One common model used to find *S*(*q*) is the Hayter-Penfold model. This model derives a structure factor as follows:[100]

An existing solution for the OZ equation is used to find *c*(*r*) within the particle (here given as the rescaled parameter *c*(*x*), where $x = {}^{r}/_{\sigma}$, with *σ* as the radius of the particle):

$$c(x) = A + Bx + \frac{1}{2}\eta A x^3 + \frac{C \sinh kx}{x} + \frac{F(\cosh kx - 1)}{x}$$

Equation 2-39

The constants *η* and *k* are the volume fraction and a rescaled Debye screening length respectively. The parameters *A*, *B*, *C*, and *F* are given by the following expressions:

$$A = a_1 + a_2 C + a_3 F$$

Equation 2-40

$$B = b_1 + b_2 C + b_3 F$$

Equation 2-41

$$C = -\frac{\omega_{16} F^2 + \omega_{15} F + \omega_{14}}{\omega_{13} F + \omega_{12}}$$

Equation 2-42

$$w_4F^4 + w_3F^3 + w_2F^2 + w_1F + w_0 = 0$$

Equation 2-43

The parameters a_1, a_2, a_3, b_1, b_2, b_3, ω_{12}, ω_{13}, ω_{14}, ω_{15}, ω_{16}, w_0, w_1, w_2, w_3 and w_4 are derived from physical properties of the system including the surface potential, electronic charge and dielectric constant; their derivation is lengthy and will not be included here.

Solving Equation 2-43 gives multiple values for *F*; for each value, *S*(*K*) can be calculated (with *K* as a rescaled equivalent to *q*, $K = q\sigma$):

$$S(K) = \frac{1}{1 - 24\eta a(K)}$$

Equation 2-44

$$\begin{aligned} a(K) = A\frac{\sin K - K\cos K}{K^3} + B\frac{\left(\frac{2}{K^2} - 1\right)K\cos K + 2\sin K - \frac{2}{K}}{K^3} \\ + \eta A\frac{\frac{24}{K^3} + 4\left(1 - \frac{6}{K^2}\right)\sin K - \left(1 - \frac{12}{K^2} + \frac{24}{K^4}\right)K\cos K}{2K^3} \\ + C\frac{k\cosh k\sin K - K\sinh k\cos K}{K(K^2 + k^2)} \\ + F\frac{k\sinh k\sin K - K(\cosh k\cos K - 1)}{K(K^2 + k^2)} + F\frac{\cos K - 1}{K^2} \\ - \gamma e^{-k}\frac{k\sin K + K\cos K}{K(K^2 + k^2)} \end{aligned}$$

Equation 2-45

The parameter *γ* is related to the contact potential of the particles. All other parameters are as previously given.

For each value of *F*, *S*(*K*) is calculated; the corresponding *g*(*x*) can then be calculated:

$$g(x) = 1 + \frac{1}{12\pi\eta x}\int_0^\infty [S(K) - 1]K\sin Kx\, dK$$

Equation 2-46

If the structure factor calculated gives a solution to *g*(*x*) fulfilling Equation 2-36 and Equation 2-37, then that structure factor is taken to be correct.

Although this model is useful, it makes assumptions about the system that may not be accurate. In practice, most systems are not completely monodisperse, with perfectly homogeneous hard spheres. However, this model provides a useful approximation and a basis for more sophisticated calculations.

2.2.8. Other expressions for *I(q)*

The simplest form of $I(q)$ is given by:[101]

$$I(q) \approx P(q)S(q)$$

Equation 2-47

This equation uses the Born approximation, which consists of taking the incident field, instead of the total field, as the driving field at each point in the scatterer. It is accurate if the scattered field is small compared to the incident field.

As the concentration of the solution is decreased, then the influence of $S(q)$ will decrease. In some situations, at very low concentrations, it can be assumed that $S(q) = 1$ for all q, and thus

$$I(q) = cP(q)$$

Equation 2-48

where c is a constant, and is related to the number of scattering particles in solution, and thus the concentration.

Many other more complicated expressions are available, using some combination of the form and structure factor. One such equation is that given by Aswal and Goyal:[102–104]

$$\frac{d\Sigma}{d\Omega} = n(\rho_m - \rho_s)^2 V^2 [\langle F(q)^2 \rangle + \langle F(q) \rangle^2 (S(q) - 1)] + B$$

Equation 2-49

This equation considers SANS (small-angle neutron scattering) caused by ionic micelles in solution. Here, $I(q)$ is given by $\frac{d\Sigma}{d\Omega}$, the differential scattering per unit volume. $F(q)$ is described as the scattering caused by a single micelle in solution (i.e. the form factor for a single particle) as given by Equation 2-17, $S(q)$ is the structure factor as before, ρ_m and ρ_s are the scattering length densities of the particle and the solvent respectively, n is the number density of micelles in solution, V is the volume, and B is the background.

$\langle F(q)^2 \rangle$ and $\langle F(q) \rangle^2$ are related to *F*(*q*) through the relations

$$\langle F^2(q) \rangle = \int_0^1 [F(q,\mu)^2 d\mu]$$

Equation 2-50

$$\langle F(q) \rangle^2 = \left[\int_0^1 F(q,\mu) d\mu \right]^2$$

Equation 2-51

To calculate *F*(*q*), it is assumed that the micelle is an ellipsoid with one axis elongated; if the length of the elongated axis and shorter axes are termed *a* and *b* respectively, and the cosine of the angle between them is given by μ, then *F*(*q*) can be given by the expressions

$$F(Q,\mu) = \frac{3(\sin x - x cos x)}{x^3}$$

Equation 2-52

$$x = Q[a^2\mu^2 + b^2(1-\mu^2)]^{1/2}$$

Equation 2-53

While this system is useful for modelling spherical, ellipsoid and rod-like micelles, it is limited in use to these geometries and cannot be used for other structures such as bilayers.

A similar expression for *I*(*q*) was used by Vass et al in 2003 (and used again in a different notation in 2008):[95,105]

$$\frac{d\Sigma}{d\Omega} = n_{mic} \cdot \left(\langle |A(q)|^2 \rangle - \langle |A(q)| \rangle^2 + \langle |A(q)| \rangle^2 \cdot \langle \sum_{j,k} \exp\left(-i \cdot q \cdot \left(r_j - r_k \right) \right) \rangle \right)$$

Equation 2-54

A(*q*) is the normalized scattering amplitude from a single particle; this is analogous to *F*(*q*). It should be noted that $\langle |A(q)| \rangle^2$ is equal to the form factor *P*(*q*), $\langle \sum_{j,k} \exp\left(-i \cdot q \cdot \left(r_j - r_k \right) \right) \rangle$ is used as an expression for *S*(*q*), and $\langle |A(q)|^2 \rangle - \langle |A(q)| \rangle^2$ equals the

fluctuation in *P*(*q*). $\langle|A(q)|\rangle$ itself represents the amplitude of the scattering. This expression thus rearranges to give:

$$\frac{d\Sigma}{d\Omega} = n_{mic} \cdot (\langle|A(q)|^2\rangle + \langle|A(q)|\rangle^2(S(q) - 1))$$

Equation 2-55

This is clearly analogous to Aswal and Goyal's expression above, and can be rearranged further to give:

$$\frac{d\Sigma}{d\Omega} = n_{mic} \cdot (\Delta P(q) + P(q)S(q))$$

Equation 2-56

The above model assumes that the system is monodisperse, i.e. that all micelles have approximately the same size and shape. However, Vass et al also suggest a modification for polydisperse systems:[105]

$$\frac{d\Sigma}{d\Omega} = n_{mic} \cdot \left(\overline{\Delta A^2(q)} + \overline{A(q)^2} \times \overline{S(q)}\right) = n_{mic} \cdot (\overline{\Delta P(q)} + \overline{P(q)} \times \overline{S(q)}$$

Equation 2-57

Where

$$\overline{A(q)} = \sum_i w_i \langle A_i(q)\rangle$$

Equation 2-58

$$\overline{A^2(q)} = \sum_i w_i \langle {A_i}^2(q)\rangle$$

Equation 2-59

$$\overline{\Delta A^2(q)} = \sum_i w_i \langle {A_i}^2(q)\rangle - \sum_i w_i \langle A_i(q)\rangle$$

Equation 2-60

The term *i* is the aggregation number of the micelle. $\langle A_i(q)\rangle$ and $\langle {A_i}^2(q)\rangle$ are the values of $\langle A(q)\rangle$ and $\langle A^2(q)\rangle$ for a micelle with aggregation number *i*, and w_i represents the probability of a micelle having an aggregation number *i*:

$$w_i = \frac{1}{\sqrt{2\pi}p}\exp\left[-\frac{(i-\bar{n})^2}{2p^2}\right]$$

Equation 2-61

Note that $\bar{n}$ is the mean aggregation number and p is a parameter for the polydispersity.

2.2.9. Interpreting scattering patterns

In SAXS experiments, data is obtained in the form of a scattering curve. This plots the intensity of scattering against scattering angle, 2θ. Using Equation 2-13, this can be converted into a graph of $I(q)$ against q.

Information about the system can be obtained in one of two ways; directly from the scattering pattern, or from its pair distribution function, $p(r)$. The latter is obtained using the Generalized Indirect Fourier Transform (GIFT) method.

2.2.9.1. Guinier approximation

The Guinier approximation can be used to approximate the radius of gyration of the particle directly from the scattering pattern $I(q)$ vs q.

The expression is derived from Equation 2-23;[98] the term $\frac{\sin qr}{qr}$ is replaced with its Maclaurin series:

$$f(x) = f(0) + x\frac{df}{dx}(0) + x^2\frac{d^2f}{dx^2}(0) + x^3\frac{d^3f}{dx^3}(0) + \cdots$$

Equation 2-62

$$\frac{\sin x}{x} = 1 - \frac{x^2}{3!} + \frac{x^4}{5!} - \cdots$$

Equation 2-63

This is substituted into Equation 2-23:

$$I(q) = 4\pi\int_0^\infty p(r)\cdot\left(1 - \frac{q^2r^2}{6} + \frac{q^4r^4}{120} - \cdots\right)dr$$

Equation 2-64

For low q, the q^4 and larger terms will be small enough to be negligible. Thus Equation 2-63 can be rearranged:

$$I(q) = 4\pi\left(\int_0^\infty p(r)dr - \frac{q^2}{6}\int_0^\infty r^2 p(r)dr + \cdots\right)$$

Equation 2-65

$$I(q) = 4\int_0^\infty p(r)dr\left(1 - \frac{q^2}{6}\frac{\int_0^\infty r^2 p(r)dr}{\int_0^\infty p(r)dr} + \cdots\right)$$

Equation 2-66

The term $4\int_0^\infty p(r)dr$ can be simplified by using the relation:

$$\lim_{\theta\to 0}\frac{\sin\theta}{\theta} = 1$$

Equation 2-67

This gives the relation:

$$4\int_0^\infty p(r)dr = 4\int_0^\infty p(r)\frac{\sin 0}{0}dr = I(0)$$

Equation 2-68

The term within the bracket can be simplified by applying a definition of the radius of gyration, R_g:

$$R_g^2 = \frac{1}{2}\frac{\int_0^\infty r^2 p(r)dr}{\int_0^\infty p(r)dr}$$

Equation 2-69

Therefore, Equation 2-66 can be simplified as:

$$I(q) = I(0)\left(1 - \frac{q^2 R_g^2}{3} + \cdots\right)$$

Equation 2-70

The term in the bracket can be approximated using the Taylor series for e^x:

$$e^x = 1 + x + \frac{x^2}{2!} + \frac{x^3}{3!} + \cdots$$

Equation 2-71

Applying this approximation gives Guinier's equation:

$$I(q) = I(0)\exp\left(\frac{-q^2R_g^2}{3}\right)$$

Equation 2-72

By taking the natural logarithm of both sides, the following equation is obtained:

$$\ln I(q) = \ln I(0) - \frac{R_g^2}{3}q^2$$

Equation 2-73

Therefore, by plotting a graph of ln $I(q)$ against q^2, the radius of gyration of the particle can be obtained.

While this method can be useful, it does have some limitations. It is only valid for the section of the scattering curve corresponding to low q values (i.e. high r values), due to the approximations used in the derivation of Guinier's equation (i.e. that q^4 and higher order terms are negligible); therefore, the accuracy of this method is determined by the limiting value of q.

2.2.9.2. Porod's law

For homogeneous particles, the surface area of the particles can be calculated from the scattering curve using Porod's law. According to this law, as q tends to infinity,[98]

$$I(q) \approx \frac{2\pi\rho^2 S}{q^4}$$

Equation 2-74

S is the particle surface and ρ is the density as before.

This is valid at large q only; this is because regions of large q correspond to very small distances within the solution. This means that clear contrasts can be seen between the particle and the solvent, allowing the particle-solvent interfaces to be studied.

2.2.9.3. Distance between particles

The distance between particles can be estimated using the position of the maximum peak, provided that this peak is due to the structure factor:[104]

$$q_{max} \sim \frac{2\pi}{d}$$

Equation 2-75

2.2.9.4. Concentration and micelle aggregation number

Equation 2-75 can be extended further; if the number of particles is directly proportional to the concentration (e.g. for micelles, if the aggregation number remains constant), then q_{max} will be proportional to the cube root of the concentration:[104]

$$q_{max} \propto \sqrt[3]{C}$$

Equation 2-76

It is possible to identify any change in micelle aggregation number with changing concentration by using this method.

2.2.9.5. Main cause of scattering – structure factor or form factor?

It is sometimes possible to determine whether a particular peak in the scattering pattern is due to $P(q)$ or $S(q)$ by altering the concentration. As the structure factor is strongly tied to concentration, reducing the concentration of the solution will cause any peaks due to $S(q)$ to have a reduced intensity relative to any peaks due to $P(q)$.

In addition, some conclusions may be drawn about the nature of $S(q)$ by examining the scattering pattern. For example, a charged surfactant micelle may have a sharper peak than a nonionic surfactant micelle due to repulsion effects; the micelles will be forced into a more ordered structure, particularly with increasing concentration, with the distances between the micelles more sharply set at the average interparticle distance.

2.2.10. Experimental setup

SAXS spectra were taken using a Bruker Nanostar SAXS machine. This machine uses an X-ray source operating at 40 kV and 35 mA to produce CuKα X-rays with a wavelength of 1.54 Å. These X-rays are then passed through cross-coupled Göbel mirrors and a series of pinholes to ensure that the beam is focused. This beam is then passed through a sample. This sample is either held as a powder or, if liquid, in a 2 mm capillary. X-ray scattering is then measured using a Hi-star 2D detector held 66 cm from the sample, with the gap between sample and detector held under vacuum. The detector will measure the radiation produced at each angle, and produce the final SAXS spectrum.[106]

2.2.11. Generalized Indirect Fourier Transformation (GIFT) analysis

2.2.11.1. Splines and B-splines

A spline is a function defined by a series of points, or 'knots', and the connecting curves between them. Let the knots be $\lambda_1, \lambda_2, \ldots \lambda_n$, where n is finite. Then the function $s(x)$ is a spline of order k if two conditions hold:[107]

1. $s(x) = f(x)$ for $\lambda_i \leq x \leq \lambda_{i+1}$, where $g(x)$ is a polynomial of degree ≤ k, and only depends on x.
2. $s(x)$ and all of its derivatives (up to and including $s^{(k-1)}(x)$) are continuous, i.e. the function is smooth everywhere.

They can be used to fit a curve based on a collection of points. Any spline of degree k can be calculated by a linear combination of basis splines, or B-splines, of degree k:[107]

$$s(x) = \sum_{i=-k}^{g} c_i N_{i,k+1}(x)$$

Equation 2-77

where c_i are constants, and $N_{i,k+1}(x)$ are B-splines.

2.2.11.2. Indirect Fourier Transformation (IFT) method

The Indirect Fourier Transform (IFT) method was developed by Otto Glatter in the 1970s. It allows the pair distribution function of the particle to be calculated, given only the maximum diameter of the particle. (However, this technique also requires that the data is extrapolated to "infinite dilution"; in other words, that $S(q)$=1 for all q.)[108]

Consider an approximation of $p(r)$ given by the following:

$$p(r) = \begin{cases} \sum_{\nu}^{N} c_\nu \varphi_\nu(r) & r < D \\ 0 & r \geq D \end{cases}$$

Equation 2-78

The terms c_ν are constants, and will be determined during the calculation. The functions φ_ν are cubic B-splines. (Note the similarity to Equation 2-77 above.)

To transform the B-splines from modelling $p(r)$ to modelling the scattering pattern, four transforms are used.[93] These are referred to as T_1, T_2, T_3 and T_4.

$$I(q) = \sum_{\nu}^{N} c_\nu T_4 T_3 T_2 T_1 \varphi_\nu$$

Equation 2-79

T_1 takes φ_ν from $p(r)$ to an idealized scattering function $I_1(q)$:

$$I_1(q) = \sum_{\nu}^{N} c_\nu \cdot 4\pi \int_0^\infty \varphi_\nu(r) \frac{\sin qr}{qr} dr = \sum_{\nu}^{N} c_\nu \psi_\nu$$

Equation 2-80

The remaining transformations compensate for the smearing effects caused by experimental conditions.

In practice, not all radiation produced will be of the same wavelength. This will cause a smearing effect and is compensated for in Transformation T_2:

$$I_2(m) = \int_0^\infty W(\lambda') I_1\left(\frac{m}{\lambda'}\right) d\lambda'$$

Equation 2-81

Here, $W(\lambda')$ is the wavelength distribution and m is a rescaled parameter equivalent to q;

$$m = \frac{\lambda a q}{2\pi}$$

Equation 2-82

The term a represents the distance between the sample and the detector.

Transformation T_3 (Equation 2-83) compensates for smearing caused by the slit length effect, while transformation T_4 (Equation 2-84) compensates for smearing caused by the slit width effect.

$$I_3 = 2\int_0^\infty P(t) I_2\left(\sqrt{m^2 + t^2}\right) dt$$

Equation 2-83

$$I_4(m) = \int_0^\infty Q(x) I_3(m - x) = Q * I_3$$

Equation 2-84

In both equations, *t* represents the displacement of the beam in the direction of the slit, and *x* represents the displacement of the beam perpendicular to the slit. *P*(*t*) therefore represents the intensity distribution in the direction of the slit, and *Q*(*x*) represents the intensity distribution perpendicular to the slit.

Once the transformations have been carried out, the B-splines should be representative of the raw scattering data. The parameters c_ν can be found using a linear least-squares method; at this point, these values of c_ν can be applied to Equation 2-78 to find an approximation of *p*(*r*).

2.2.11.3. Generalized Indirect Fourier Transformation (GIFT) method

The IFT method assumes that there is no contribution to scattering from interparticle effects, i.e. that *S*(*q*) = 1. However, in most solutions, this is not the case. Therefore, when calculating the intensity, a structure factor has to be considered.

The generalized indirect Fourier transformation (GIFT) method was published by Brunner-Popela and Glatter in 1996. Its key modification is to Equation 2-80:[109]

$$P(q) = \sum_{\nu}^{N} c_\nu \cdot 4\pi \int_0^\infty \varphi_\nu(r) \frac{\sin qr}{qr} dr = \sum_{\nu}^{N} c_\nu \psi_\nu(q)$$

Equation 2-85

$$I_1(q) = \sum_{\nu}^{N} [c_\nu \psi_\nu(q)] S(q,d) = \sum_{\nu}^{N} c_\nu \overline{\psi_\nu}(q,d)$$

Equation 2-86

S is now treated as a function of two variables: *q* (the scattering vector) and *d*. The vector *d* consists of 4 coefficients, d_1, d_2, d_3 and d_4 (known collectively as d_k), describing 4 parameters: ϕ (the volume fraction), *R* (the particle radius), μ (the polydispersity of the particles), and *z* (the particle charge).

To fit the scattering curve to *p*(*r*), the coefficients c_ν need to be found, and the coefficients d_k need to be improved. It is no longer possible to use a linear least-squares method to find c_ν.

First, the terms c_ν are found by solving the equation

$$\boldsymbol{c} = (\boldsymbol{B} + \lambda \boldsymbol{K})^{-1}\boldsymbol{b}$$

Equation 2-87

Here, ***b*** and ***c*** are vectors, and ***B*** and ***K*** are matrices. The terms in ***b***, ***B*** and ***K*** are given by the following:[109]

$$b_\mu = \sum_{i=1}^{m} \overline{\chi_\mu}(q_i, d) \frac{1}{\sigma^2(q_i)} I_{exp}(q_i)$$

Equation 2-88

$$B_{\mu\nu} = \sum_{i=1}^{m} \overline{\chi_\mu}(q_i, d) \frac{1}{\sigma^2(q_i)} \overline{\chi_\nu}(q_i, d)$$

Equation 2-89

$$K = \begin{pmatrix} 1 & -1 & & & \\ -1 & 2 & -1 & & \\ & & \ddots & & \\ & & -1 & 2 & -1 \\ & & & -1 & 1 \end{pmatrix}$$

Equation 2-90

where

$$\overline{\boldsymbol{\chi_\nu}}(\boldsymbol{q_i}, \boldsymbol{d}) = \boldsymbol{T_4 T_3 T_2} \overline{\boldsymbol{\psi_\nu}}(\boldsymbol{q}, \boldsymbol{d})$$

Equation 2-91

Values for *d* can then be refined using an iterative process.

2.2.12. DECON programme to determine approximate radial distribution functions

2.2.12.1. Convolution

The **convolution** of two functions *f* and *g*, written $f * g$, is defined as:[110]

$$(f * g)(x) = \int_0^x f(x - y) g(x) dy$$

Equation 2-92

Take as an example the functions:

$$f(x) = e^x \qquad g(x) = x^2$$

Equation 2-93

The convolution of $f(x)$ and $g(x)$, $(f * g)(x)$, is given by the integral

$$(f * g)(x) = \int_0^x e^{x-y} x^2 dy$$

Equation 2-94

$$(f * g)(x) = x^2 e^x \int_0^x e^{-y} dy = x^2 e^x (1 - e^{-x}) = x^2 (e^x - 1)$$

Equation 2-95

The convolution of two functions can be described as the effect of function g(x) on f(x) and vice versa.

A particularly useful result is given by the effect of Fourier transforms on convolutions. Let *F*(*x*) be the Fourier transform of *f*(*t*), and *G*(*x*) be the Fourier transform of *g*(*t*). If we find the convolution $h(t) = f * g(t)$, then take its Fourier transform, *H*(*x*), the following result is given:

$$H(x) = F(x)G(x)$$

Equation 2-96

In other words, the product of two Fourier transforms is itself the Fourier transform of the convolution of the initial two functions.

It was stated previously that the scattering intensity of the radiation, *I*(*q*), was derived by multiplying the Fourier transform of the electron density, $\rho(r)$, with its complex conjugate:

$$F(\boldsymbol{q}) = \iiint dV \cdot \rho(\boldsymbol{r}) e^{-i\boldsymbol{rq}}$$

Equation 2-97

$$I(\boldsymbol{q}) = F(\boldsymbol{q})F^*(\boldsymbol{q}) = \iiint \iiint dV_1 \cdot dV_2 \cdot \rho(\boldsymbol{r_1})\rho(\boldsymbol{r_2})\, e^{-i\boldsymbol{q}(\boldsymbol{r}_1 - \boldsymbol{r}_2)}$$

Equation 2-98

As *I*(*q*) is the product of two Fourier transforms, it can be seen that the reverse Fourier transform of *I*(*q*) – the pair distribution function, *p*(*r*) – would be given by the convolution of the electron density of the particle. Therefore, the electron density of the particle will be given by the deconvolution of the pair distribution function.

2.2.12.2. The DECON program

The DECON program allows the radial electron density to be determined from the experimental pair distribution for three types of symmetry: cylindrical, lamellar, and spherical.[111] This discussion will focus primarily on particles with spherical symmetry, as this best reflects that seen in micelles.

For a spherical system, the pair distribution function is given by:[111,112]

$$p(r) = r^2\tilde{\rho}^2(r)$$

Equation 2-99

The function $\tilde{\rho}^2(r)$ is the convolution square of the electron density and is given by

$$\tilde{\rho}^2(r) = \rho(x) * \rho(-x)$$

Equation 2-100

i.e. by the convolution of the electron densities.

In order to calculate the electron densities, the approximate electron density is modelled as a series of *N* step functions:

$$\bar{\rho}(r) = \sum_{i=1}^{N} c_i\varphi_i$$

Equation 2-101

The functions φ_i are the step functions of known width, and the functions c_i are the heights of the steps. In order to model the radial electron densities, the heights c_i must be found.

The average pair distribution function that would be generated by the above $\bar{\rho}(r)$ is given by

$$\bar{p}(r) = \sum_{i=1}^{N} V_{ii}(r)c_i^2 + 2\sum_{i>k} V_{ik}(r)c_ic_k$$

Equation 2-102

The functions c_i are the heights of the step functions as before, and the functions V_{ik} are the overlap integrals between steps *i* and *k*, for a shift of *r*. These functions can be calculated for each *ik* pair.

The purpose of the DECON program is thus to set the width of the step functions, calculate the overlap integrals of these step functions, and to use a least-squares method to calculate the values c_i that will most closely fit the known pair distribution function $p(r)$. From these values, the radial distribution function can then be approximated.

Glatter notes in his paper that "[DECON] can be used as a test for symmetry, as appreciable deviations from symmetry produce significant deviations in the approximation, whereas slight deviations from symmetry give good approximations and results"[111]. Therefore, where good results cannot be obtained from DECON, it is reasonable to assume that the particle lacks symmetry.

2.2.13. Modelled data

Whilst GIFT is useful in obtaining an accurate $p(r)$, it is useful to compare this $p(r)$ to one where a simple core-shell model is considered. To model the form factor of a core shell particle, Porod's equation for the form factor of a homogeneous sphere was used:[91]

$$P(q) = (\Delta\rho)^2 V^2 \left[3\frac{\sin qR - qR\cos qR}{(qR)^3}\right]^2$$

Equation 2-103

This formula assumes that the sphere, of radius R (and thus volume $V = \frac{4}{3}\pi R^3$), has constant electron density ρ. The difference in electron density of the solvent, ρ_{solv}, and that of the particle, ρ, is thus given by $\Delta\rho$.

This formula was adapted to a core-shell model, with inner core radius R_c and electron density ρ_c, and outer shell radius R_s and electron density ρ_s. The particle is modelled as a homogeneous sphere of radius R_s and electron density ρ_s, with a sphere subtracted of radius R_c and electron density ρ_s, and a sphere added of radius R_c and electron density ρ_c.

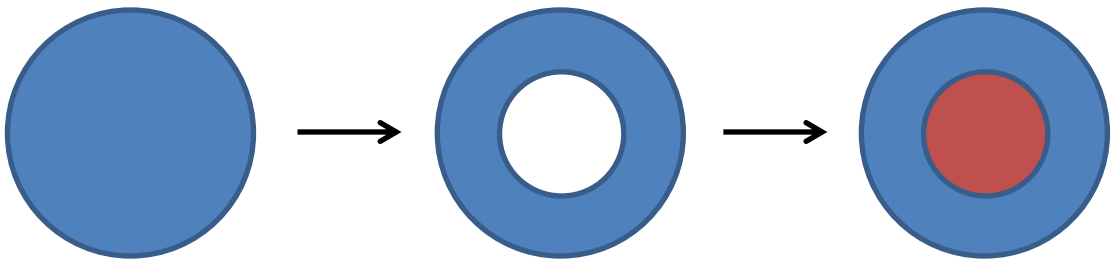

Figure 2-15: Creating the core-shell model

Therefore, the form function of the core-shell particle could be modelled using the equation:

$$P(q) = V_c^2(\rho_c - \rho_s)^2\Psi_c^2 + 2V_cV_s(\rho_c - \rho_s)(\rho_s - \rho_{solv})\Psi_c\Psi_s + V_s^2(\rho_s - \rho_{solv})^2\Psi_s^2$$

Equation 2-104

$$\Psi_x = 3\frac{\sin(qR_x) - qR_x\cos(qR_x)}{(qR_x)^3}$$

Equation 2-105

For the purposes of fitting experimental SAXS data, two further parameters were added, to alter the overall intensity of $P(q)$, and to change the background intensity;

$$P(q) = A[V_c^2(\rho_c - \rho_s)^2\Psi_c^2 + 2V_cV_s(\rho_c - \rho_s)(\rho_s - \rho_{solv})\Psi_c\Psi_s + V_s^2(\rho_s - \rho_{solv})^2\Psi_s^2] + B$$

Equation 2-106

This allows the scattering pattern to be broken down into seven parameters: electron density of solvent ρ_{solv}; electron density of inner core ρ_c; electron density of outer shell ρ_s; radius of inner core R_c; radius of outer shell R_s; overall intensity multiplier A; and background B.

A Microsoft Excel spreadsheet was set up, using this equation with user-entered values of the seven parameters named above to generate a simulated $P(q)$. The data generated was compared to experimentally-generated data and the set of parameters best modelling the experimental data was found.

2.3. Molecular Dynamics simulations - GROMACS

2.3.1. Background

GROMACS (Groningen Machine for Chemical Simulation) is an open-source software package originally developed at the University of Groningen[113–118]. The software is designed to run molecular dynamics simulations within a parallel computing system.

2.3.2. Process

To set up the data, the coordinate file (*.gro* – giving the coordinates and velocity of each atom in 3D space) and topology file (*.top* – giving the types of atoms and their molecular bonds) were created using an Amber forcefield.[119] This was either done using the program Scigress (for all molecules except hexane), or by using pre-generated files from the Automated Topology Builder and Repository,[120,121] (for hexane molecules).

Once the coordinate and topology files for each molecule were generated, the coordinate and topology file for the system to be modelled could be generated. For the topology file, this was done by combining the files to give atom types and bonds for all molecule types in the system, and specifying the number of each type of molecule. For the coordinate file, this was dependent on the situation being simulated.

2.3.2.1. Preformed micelles

For a preformed simulation (where the surfactants are arranged in a typical micelle structure, with the tail groups in the centre and the head groups exposed), one atom in the molecule (the first carbon atom in the tail group chain, with coordinates (s_x, s_y, s_z)) was assigned to be the start of the molecule. Another atom (the terminal non-hydrogen atom in the head group, with coordinates (e_x, e_y, e_z)) was defined to be the end of the molecule. The molecule can then be defined by a vector $\boldsymbol{m}$, where $\boldsymbol{m} = \begin{bmatrix} e_x - s_x \\ e_y - s_y \\ e_z - s_z \end{bmatrix}$. The remaining atoms in the molecule were also defined by their vector distance from the point (s_x, s_y, s_z). The point $(0, 0, 0)$ was defined to be the centre of the micelle. A random coordinate (x, y, z) was generated, and normalized to *R* (where *R* is a user-defined radius, being the smallest radius that could be used to generate a micelle) to give the coordinate (x_R, y_R, z_R) which was taken as the position of the start of the chain. It was then normalized by the length of the molecule, $\|\boldsymbol{m}\|$, to give $\boldsymbol{m_1} = \begin{bmatrix} x_m \\ y_m \\ z_m \end{bmatrix}$, which was taken to be the vector along which the molecule was oriented.

The molecule was rotated using Rodrigues' rotation formula:[122]

$$v' = v\cos\theta + (p \times v)\sin\theta + p(p \cdot v)(1 - \cos\theta)$$

Equation 2-107

Here, *v'* was the new position of the vector, *v* was the original position of the vector, θ was the angle of rotation and *p* was the unit vector about which the vector was rotated. (Although Rodrigues himself did not express this formula in these terms, he did produce a set of three equations from which they can be easily derived.)

Both θ and *p* could be calculated from the original vector of the molecule, $\boldsymbol{m}$, and the vector giving its new direction, $\boldsymbol{m_1}$.

$$\cos\theta = \frac{\boldsymbol{m}\cdot\boldsymbol{m_1}}{\|\boldsymbol{m}\|\|\boldsymbol{m_1}\|}$$

Equation 2-108

$$p = \frac{\boldsymbol{m}\times\boldsymbol{m_1}}{\|\boldsymbol{m}\times\boldsymbol{m_1}\|}$$

Equation 2-109

Rodrigues' formula was applied to all of the vectors defining the molecule to give their new coordinates relative to the start of the molecule. The vector $\begin{bmatrix} x_R \\ y_R \\ z_R \end{bmatrix}$ was then added, translating the molecule to start at (x_R, y_R, z_R).

This procedure was then repeated until the desired number of molecules had been added to the micelle. If the start of the new molecule was placed within a distance *D* of a previous molecule (where *D* is defined by the user), a new random coordinate was generated. If not, the positions of the atoms were written to the new coordinate file. They were also stored by the program to cross-reference against the future molecules added to the system.

This procedure left a sphere of radius *R* in the centre of the micelle. Hexane molecules, if required for molecular stability, were then added to this hole using a similar procedure. Two random vectors were generated, ***a*** and ***b***, such that $\|\boldsymbol{a}\|, \|\boldsymbol{b}\| < R$. The vector ***a*** was set as the position of the start of the molecule, and the vector (***b***-***a***) was set as the direction along which the hexane was positioned, and normalised accordingly. Rodrigues' rotation formula was then used to position the hexane molecule. If any of the atoms in the hexane atoms came within a too small distance *D* of any other atoms, new vectors ***a*** and ***b*** were found. If not, the molecule's position was added to the coordinate file.

2.3.2.2. Randomised systems

A similar algorithm was used to generate the randomised surfactant systems. A box was set up with sides of length 2*R*. For each molecule to be added to the system, two vectors were generated, $\boldsymbol{a} = \begin{pmatrix} a_x \\ a_y \\ a_z \end{pmatrix}$ and $= \begin{pmatrix} b_x \\ b_y \\ b_z \end{pmatrix}$, such that $-R < a_x, a_y, a_z, b_x, b_y, b_z < R$. The vector ***a*** was set as the start, and the vector ***b***-***a*** was normalized, and then used as the direction of the molecule. The procedure described previously was then followed.

2.3.2.3. The molecular dynamics simulation

Once all of the molecules in the system had been placed and recorded in the coordinate file, a solvent was added to the system using the *genbox* command within GROMACS. This took the coordinate file and filled the unoccupied space with a solvent molecule known to the program (in this system, *spc216*, a single-point charge model for water molecules). If required to neutralize the system, or to model the effects of calcium concentration, ions were then added using the *genion* command. This replaced the required number of solvent molecules with ions.

Energy minimization (EM) was then run on the system. In order to do this, *grompp* was run, to combine the topology file, the coordinate file, and the '.mdp' file (containing the parameters for the simulation). The output of this process was a '.tpr' file; *mdrun* was then run on this file to provide the simulation. Once the output of energy minimization had been produced (in the form of a '.gro' file), this was then used as the input coordinate file for the final molecular dynamics run. This was carried out using an appropriate '.mdp' file, the coordinate file generated by EM, and the topology file generated previously. The commands *grompp* and *mdrun* were used as before, but, as MD simulations are significantly more time-intensive than EM simulations, the simulation was spread over multiple nodes on Hamilton and run using the queuing system, rather than in the terminal.

2.3.2.3.1. Energy minimization – key parameters used

A steepest-descent algorithm was used to calculate the minimum energy. No additional constraints were added to the system. A maximum of 3,000,000 steps were used, with an initial step size of 0.01 nm. Energy minimization stopped when a force of less than 1000.0 kJ mol^{-1} nm^{-1} was reached.

2.3.2.3.2. Molecular dynamics – key parameters used

The integrator 'md' was used; this is the simplest molecular dynamics integrator provided by GROMACS. This was run with 10,000,000 steps and a time step of 0.001 ps. No additional constraints were used in the system. The simulation output 101 frames (i.e. one every 100 ps). A Nosé-Hoover temperature coupling method was used. The temperature for each component was set at 303.2 K.

2.3.2.4. *Output files*

There were three key outputs from the MD simulation: these were named by default 'confout.gro', 'traj.trr' and 'ener.edr'. The first, 'confout.gro', gave the final output configuration of the simulation, and could be used as input for further simulations. The second, 'traj.trr', gave the trajectory of the simulation in a series of 101 frames (the first being the initial configuration).The command *trjconv* was used to convert it into '.gro' file format, and to remove any molecules not needed in the calculations (such as water) from the frames. The final file format, 'ener.edr', gave the energies of the simulation.

2.3.3. Processing of data

A program was written by me in FORTRAN to extract quantitative data from my GROMACS outputs.

In the first step, the coordinates of each atom in a frame were read in (using code supplied by Dr Martin Walker[123]) and stored by the system. The program then cycled through each molecule in the system, and calculated the distance between each of its constituent atoms and the constituent atoms of every other atom in the system. If this interatomic distance was less than a given value (typically 0.25 nm), these molecules were assumed to be connected.

In graph theory, an adjacency matrix can be used to represent connections between objects ('nodes') in a graph. If a graph contains *w* nodes, the adjacency matrix *A* will be an $w \times w$ matrix such that:

$$A_{ij} = \begin{cases} 1; & nodes\ are\ connected \\ 0; & nodes\ are\ not\ connected \end{cases}$$

Equation 2-110

Consider the graph *G* shown in Figure 2-16 below. This consists of 5 nodes.

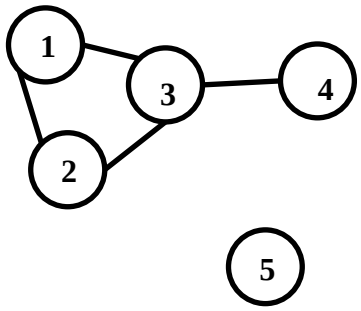

Figure 2-16: Graph *G* consisting of 5 nodes

The connections between the nodes in *G* can be represented using its adjacency matrix *A*:

$$A = \begin{bmatrix} 0 & 1 & 1 & 0 & 0 \\ 1 & 0 & 1 & 0 & 0 \\ 1 & 1 & 0 & 1 & 0 \\ 0 & 0 & 1 & 0 & 0 \\ 0 & 0 & 0 & 0 & 0 \end{bmatrix}$$

Equation 2-111

This theory was applied to the problem of surfactant aggregation. The adjacency matrix of the system was found by setting A_{ij} = 1 if the molecules were connected, and 0 otherwise. As no molecule was connected to itself, A_{ii} = 0 for all values of *i*.

The next part of the algorithm used a depth-first technique on the adjacency matrix to find the number of aggregates per sample, and the number of monomers per aggregate. For a sample containing *n* monomers, the values A_{ii} were read ($1 \le i \le n$). If A_{ii} = 1, then the program skipped to the next value of *i*; if A_{ii} = 0, then the values A_{ij} ($1 \le j \le n$) were copied to the array *B*. The molecule *i* was marked as 'visited' by changing A_{ii} from 0 to 1. The program counted the number of aggregates and the number of each type of molecule per aggregate; both counters were increased by one at this point.

$$A = \begin{bmatrix} 0 & 1 & 1 & 0 & 0 \\ 1 & 0 & 1 & 0 & 0 \\ 1 & 1 & 0 & 1 & 0 \\ 0 & 0 & 1 & 0 & 0 \\ 0 & 0 & 0 & 0 & 0 \end{bmatrix} \rightarrow A = \begin{bmatrix} \mathbf{1} & 1 & 1 & 0 & 0 \\ 1 & 0 & 1 & 0 & 0 \\ 1 & 1 & 0 & 1 & 0 \\ 0 & 0 & 1 & 0 & 0 \\ 0 & 0 & 0 & 0 & 0 \end{bmatrix}, B = \begin{bmatrix} 0 & 1 & 1 & 0 & 0 \end{bmatrix}$$

Equation 2-112

The coordinates of the 'marker atoms' of this molecule, as determined by the user, were looked up and placed in temporary storage in an array. For surfactants, these marker atoms were the first and last carbon atom of the hydrophobic tail, and the first and last non-hydrogen atom of the hydrophilic head; for Brightener 49 molecules they were the innermost carbon on the second and third conjugated rings, and the sulfur atoms. It should be noted that the technique of studying the distance of marker atoms from the centre of the micelle is one that is commonly used[124–128], although the algorithms and program used in this study were designed and built by myself as part of the project.

The program then cycled through the values of B_j. If B_j = 0, no action was taken. If B_j = 1, then the point A_{jj} in the adjacency matrix was visited. If A_{jj} = 1, then this molecule had already been visited, so B_j was set to 0 and no further action was taken. If A_{jj} = 0, then the

values A_{jk} were read. If A_{jk} = 1, then a 1 was placed in the array B at B_k and B_j was set to 0. The counter measuring the number of monomers in this aggregate was increased by one and A_{jj} was set to 1. The coordinates the marker atoms of molecule j were looked up and placed in temporary storage.

$$A = \begin{bmatrix} 1 & 1 & 1 & 0 & 0 \\ 1 & 0 & 1 & 0 & 0 \\ 1 & 1 & 0 & 1 & 0 \\ 0 & 0 & 1 & 0 & 0 \\ 0 & 0 & 0 & 0 & 0 \end{bmatrix}, B = [0 \quad \mathbf{1} \quad 1 \quad 0 \quad 0] \rightarrow A = \begin{bmatrix} 1 & 1 & 1 & 0 & 0 \\ 1 & \mathbf{1} & 1 & 0 & 0 \\ 1 & 1 & 0 & 1 & 0 \\ 0 & 0 & 1 & 0 & 0 \\ 0 & 0 & 0 & 0 & 0 \end{bmatrix},$$

$$B = [\mathbf{1} \quad \mathbf{0} \quad 1 \quad 0 \quad 0]$$

Equation 2-113

Once all values B_j had been cycled through, the sum of all values in B was calculated. If this value was greater than 0, the program cycled through the values of B_j again; if this value was equal to 0, then all values in the aggregate had been visited.

The approximate centre of the micelle was calculated (from the mean of the x,y, and z coordinates of the marker atoms). The mean distance of each marker atom type was then calculated and outputted. The program then continued cycling through the values of A_{ii} until all molecules in the system had been accounted for.

The mean distances of each marker atom, for each aggregate in the system, were output into text files. The program cycled through each frame output by the simulation, outputting the mean distances of the marker atoms each time. Once the program had been run, the text files were imported into Microsoft Excel to allow the overall average size of the micelles in the system to be calculated.

The program written was also used to determine the distances of the ions in the system from their nearest micelle centre. Each molecule type in the system was identified as either 'ion' or 'not an ion'. If the molecule was identified as not being an ion, it was used in the adjacency and micelle size calculations as before. If, however, it was identified as being an ion, it was not included in these calculations, and the related values of the adjacency matrix were set to 0.

Once the program had identified the centre of each micelle, it cycled through the positions of all ions in the system. For each micelle coordinate, the closest micelle centre

to it was calculated. The identifying number of the closest micelle, and the distance between the micelle centre and the ion, were recorded for each ion.

2.3.4. Finding aggregation number and size

Once the total number of micelles, the number of monomers per aggregate, and the mean distance of each type of marker atom from the centre of the micelle had been found, several measures were used to estimate the average aggregation number and micellar radii. One measure was to use the numerical mean:

$$Mean = \frac{\sum value\ of\ aggregate}{number\ of\ aggregates}$$

Equation 2-114

The 'value' of the aggregate could be its micelle radius, or its aggregation number, for example. While this was suitable for relatively homogeneous systems, it was not as useful in situations where one large aggregate dominates. The maximum aggregation number and micellar radius were also used; while these were useful for systems containing one large aggregate and few monomers, they only represented one micelle within the system.

Another measure was to use the mass-weighted average:

$$M.W.average = \frac{\sum number\ of\ monomers\ in\ aggregate\ \times value\ of\ aggregate}{number\ of\ monomers\ in\ system}$$

Equation 2-115

To see the relevance of this, consider a situation where 100 people are split into 3 groups of 90, 8, and 2 respectively. The mean tells us the average number of people per group (33), whereas the mass-weighted average tells us, on average, the number of people in the group of a randomly selected person (82).

Within this project, all three values for the average were calculated for the micellar radius and aggregation number. By comparing the three values, it was possible to determine the homogeneity of the system, and thus which value of the average was more appropriate to describe the system.

2.4. Materials used

Four surfactants found in detergents were studied in this project. These surfactants were supplied by P&G with concentrations as shown in Table 2-1 overleaf.

Table 2-1: Concentrations of P&G surfactants

Surfactant	Type	Concentration in water (mg/mL)
LAS	Anionic	450
AE1S	Anionic	700
AE7	Nonionic	1000
DEEDMAC	Cationic	n/a (supplied as solid)

In addition, four surfactants were used in Chapter 4 to crystallise the brighteners and $CaCO_3$. These surfactants, and their suppliers, are listed in Table 2-2. More information will be given in Section 4.1.1.5.

Table 2-2: Non-P&G surfactants used and their suppliers

Surfactant	Type	Supplier
AOT	Anionic	Sigma
Span 80	Nonionic	Fluka
Brij 30	Nonionic	Acros
CTAC	Cationic	Acros

Two optical brighteners were used in this project: Brightener 15 (also known as FWA-1, diamino stilbene, DASC-3 or disodium 2,2'-[(E)-1,2-ethenediyl]bis(5-[4-anilino-6-(4-morpholinyl)-1,3,5-triazin-2-yl]aminobenzenesulfonate)), and Brightener 49 (also known as FWA-5, DSPB-1, Tinopal CBS or benzenesulfonic acid,2,2'-([1,1'-biphenyl]-4,4'-diyldi-2,1-ethenediyl)bis-,sodium salt). Brightener 15 has the molecular formula $C_{40}H_{38}N_{12}Na_2O_8S_2$, and Brightener 49 has the molecular formula $C_{28}H_{20}Na_2O_6S_2$. Both compounds were used as supplied by P&G. These are shown in Figure 2-17 and Figure 2-18.

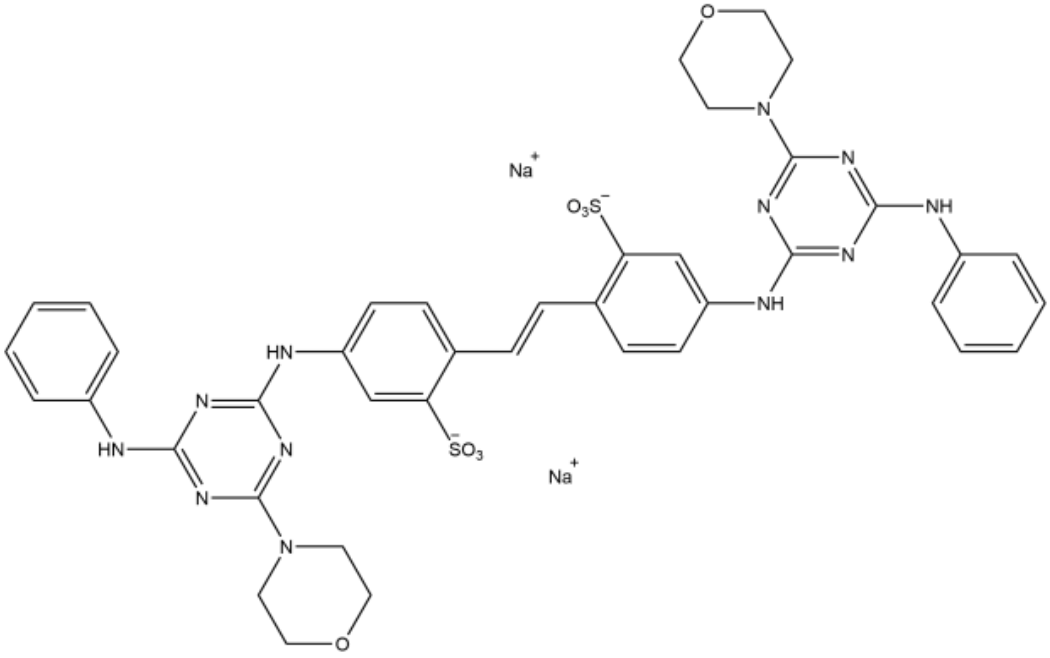

Figure 2-17: Brightener 15

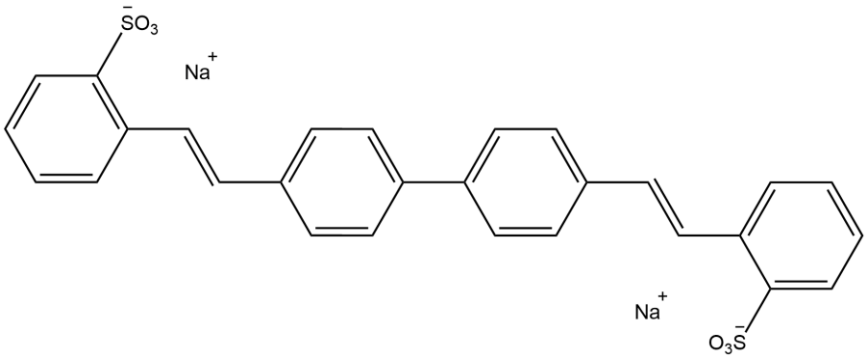

Figure 2-18: Brightener 49

Ultra-high purity water was obtained from a UHQ water unit.

$CaCl_2$ was obtained from Aldrich at 99+ % purity. Na_2CO_3 was obtained from Acros Organics.

3. Fluorescence work

3.1. Introduction

Within the detergent industry, improving brightener deposition is a key business goal. In this chapter, two methods of quantitatively testing brightener deposition were tested.

The first method, in which fabric samples were soaked in brightener solutions and then the fluorescence spectra of the fabric samples were taken, was comparable to many previous studies done on the brightener-detergent system, and was most directly comparable to the results seen by the consumer. For this method, three emission and three excitation spectra were taken for each fabric sample, and the mean peak height and the standard deviation in peak heights were found for each sample. The emission and excitation peak heights were used as a measure of brightener concentration, in common with previous studies[81,83]

The second method, in which fabric samples were soaked in brightener solutions, and then the fluorescence spectra of the solutions were taken, had the advantage of providing the spectrum of a homogeneous sample (the solution, in which free movement of brightener molecules is likely) rather than the spectrum of a fabric sample, in which the fabric is varied by nature and where brighteners are fixed in position. For this method, the area under the spectra, *A* was found. This quantity was known as the integrated fluorescence intensity, and can be used as a measure of fluorescence and thus concentration of brightener within the sample. This was used instead of the peak height because the change in brightener configuration with changing AE7 concentration caused the emission profile to change significantly, with an increase in peak height and decrease in width of the peak. This gave the emission spectra of the solutions containing both brightener and AE7 a greater peak height but comparable *A* to those without AE7.

This change in configuration with increasing AE7 concentration also had the effect of increasing both peak height and *A* of the excitation spectra for these samples; as the excitation spectra only showed the amount of fluorescent radiation with a given wavelength i.e. the wavelength of maximum emission, the solution with the greatest emission peak height at this wavelength will have the greatest peak height and *A* for the excitation spectrum of this wavelength.

Once a method of determining the brightener absorption onto the fabric was identified, the uptake of brightener by cotton and polycotton was determined, in solutions containing brightener with and without surfactant. This allowed the effect of surfactant addition on the deposition of the optical brighteners to be determined.

3.2. Experimental work

3.2.1. Deposition onto fabric samples

To prepare fabric samples, a 2 cm by 4 cm rectangle of unbrightened cotton (this is cotton without any brightener, supplied by P&G) was placed in 10 g of wash solution containing Brightener 49 and water only. The vial was covered with aluminium foil to prevent interactions with UV light. A magnetic stirrer bar was added and the solution placed over a magnetic stirrer for 30 minutes. The fabric was then removed; if a rinse step was to be used, the fabric was placed in UHQ water for several seconds and then immediately removed. The fabric was then placed on paper towels to dry and covered with aluminium foil.

The fabric samples were analysed using fluorescence emission spectroscopy and excitation spectroscopy. Three emission and three excitation spectra were taken using a Fluorolog® spectrometer, with the fabric sample moved between spectra to ensure that the spectrometer took a reading from different sections of the fabric each time. The maximum peak height was calculated for each emission and excitation spectrum. The mean and standard deviation of the peak height were found.

3.2.1.1. Initial test of deposition onto unbrightened cotton from brightener solution

Solutions were made up containing different concentrations of Brightener 49. This was deposited onto unbrightened cotton as described previously. The fabric was rinsed by mixing it with a magnetic stirrer bar in UHQ water for 2 minutes. The emission and excitation peak heights were found as described previously; these are shown in Figure 3-1 and Figure 3-2 respectively.

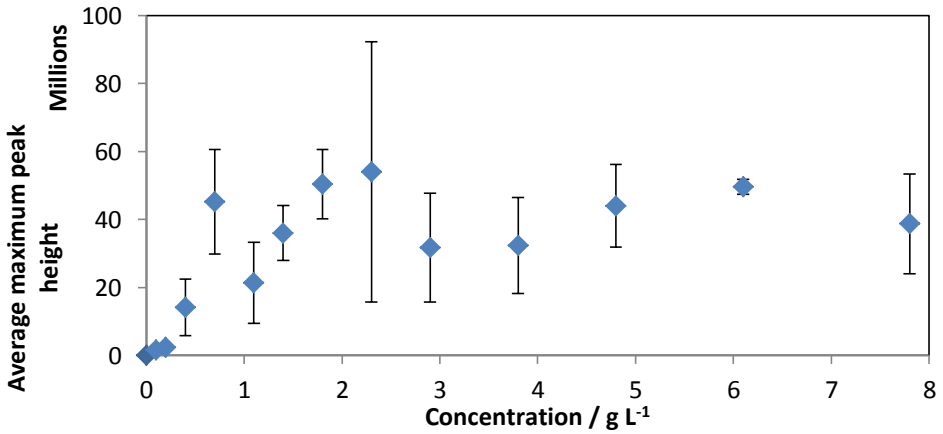

Figure 3-1: Emission peak height for fabric samples treated with varying concentrations of Brightener 49

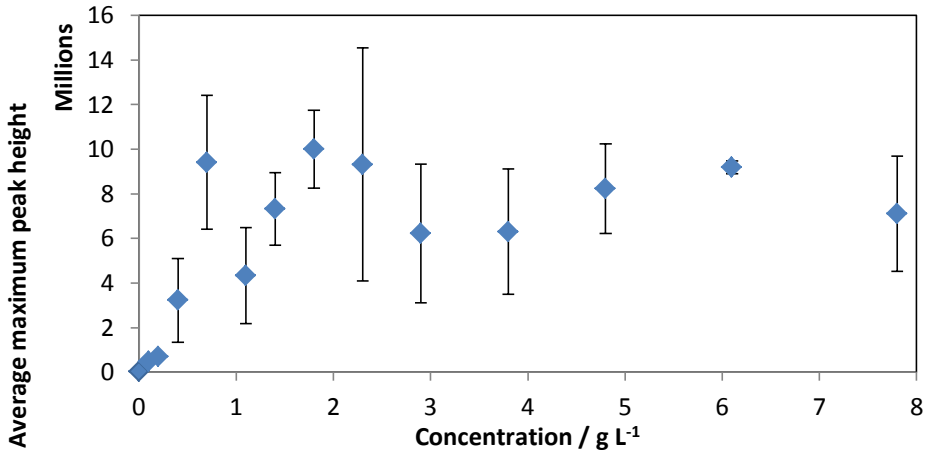

Figure 3-2: Excitation peak height for fabric samples treated with varying concentrations of Brightener 49

While this data shows a clear qualitative trend (increasing the brightener concentration increases the fluorescence of the fabric), the error on this data (given by the standard deviation of the data, and shown on the graph as the error bars) is too large to allow quantitative assessment.

3.2.1.2. Rinse step vs no rinse step

To test the effect of including a rinse step, solutions were made up containing different concentrations of Brightener 49 and deposited onto unbrightened cotton. Fabric samples were either rinsed by mixing with a magnetic stirrer bar in UHQ water for 2 minutes, or left unrinsed. The emission and excitation peak heights were found as described previously, and are shown in Figure 3-3 and Figure 3-4, respectively.

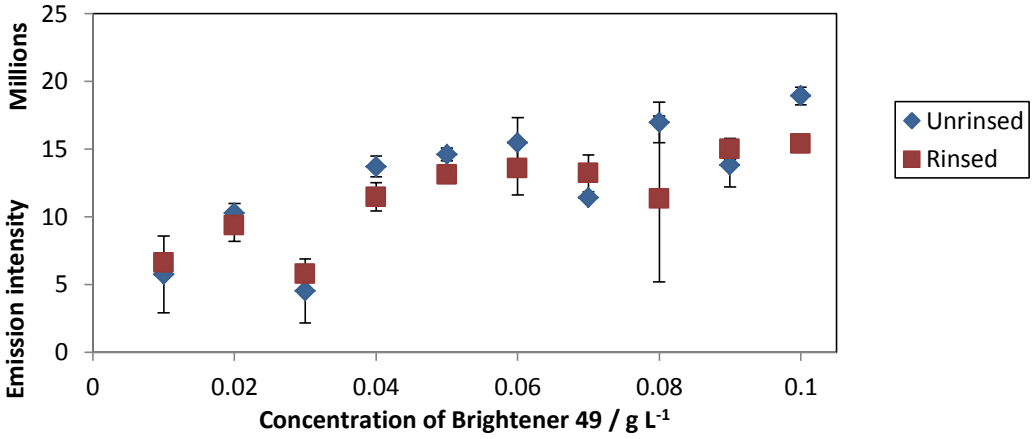

Figure 3-3: Emission peak height for varying concentrations of samples treated with Brightener 49, with and without a rinse step

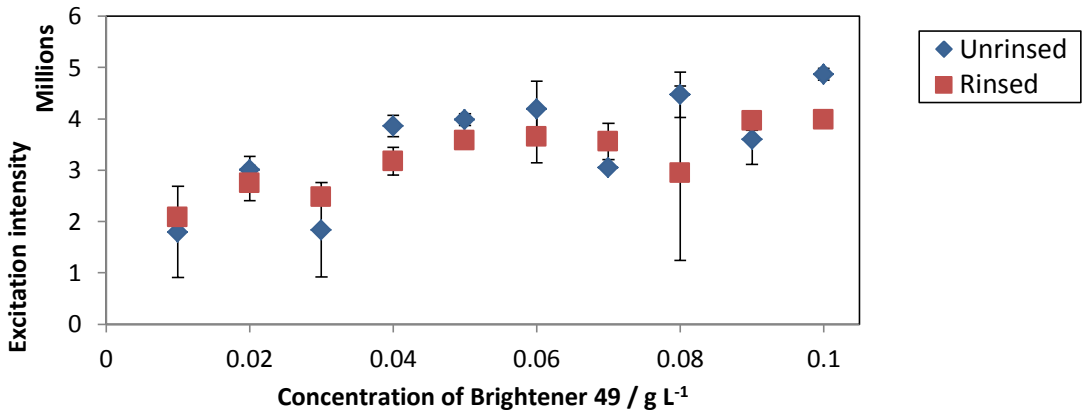

Figure 3-4: Excitation peak height for varying concentrations of samples treated with Brightener 49, with and without a rinse step

Again, although a clear qualitative trend is seen, the error on this data is too great to allow quantitative analysis.

3.2.1.3. Conclusions

Although the technique of deposition onto fabric initially showed promise, the error inherent in the technique was too great to continue using this method as the primary testing method. This may have been due to the natural inhomogeneity of the fabric; during the taking of the fluorescence spectra, a narrow beam was focused onto the fabric. As the natural weave of the fabric contained many areas where there were gaps between cotton fibres, and areas of greater thickness, the brightener deposition may not have been completely even on the lengthscales required for the experiment. For this reason, a new method was used to examine the deposition of brighter: the testing of solutions themselves, pre- and post- wash.

3.2.2. Fluorescence of brightener solutions

As experiments on the fluorescence of fabrics themselves proved prone to large errors, presumably due to the inhomogeneity of the fabric and thus uneven distribution of brightener on the lengthscales used, further fluorescence experiments were carried out on the solution state. Two types of experiments were carried out. Section 3.2.2.1 looks at the effect of the surfactant on the fluorescence of the brightener, while Section 3.2.2.3 looks at the effect of the wash process on the intensity of the fluorescence (and thus on the amount of brightener present in solution), allowing conclusions to be drawn about brightener deposition.

3.2.2.1. Effect of surfactant concentration on fluorescence

Solutions were made up containing 21.0 g L^{-1} AE1S, 25.6 g L^{-1} AE7, 0.0025 g L^{-1} Brightener 49, and 0.0025 g L^{-1} Brightener 49 with varying concentrations of AE1S and AE7. The absorbance, fluorescence emission, and fluorescence excitation spectra of these solutions were taken. These experiments were designed to determine the effect that the addition of surfactant has on the brightener fluorescence, and thus indicate whether an interaction exists between the brightener and the surfactant.

3.2.2.1.1. Absorbance results

The absorbance results for solutions of Brightener 49 containing AE1S and AE7 are shown in Figure 3-6 and Figure 3-7 respectively. The absorbance spectra of surfactant solutions without brightener are shown in Figure 3-5.

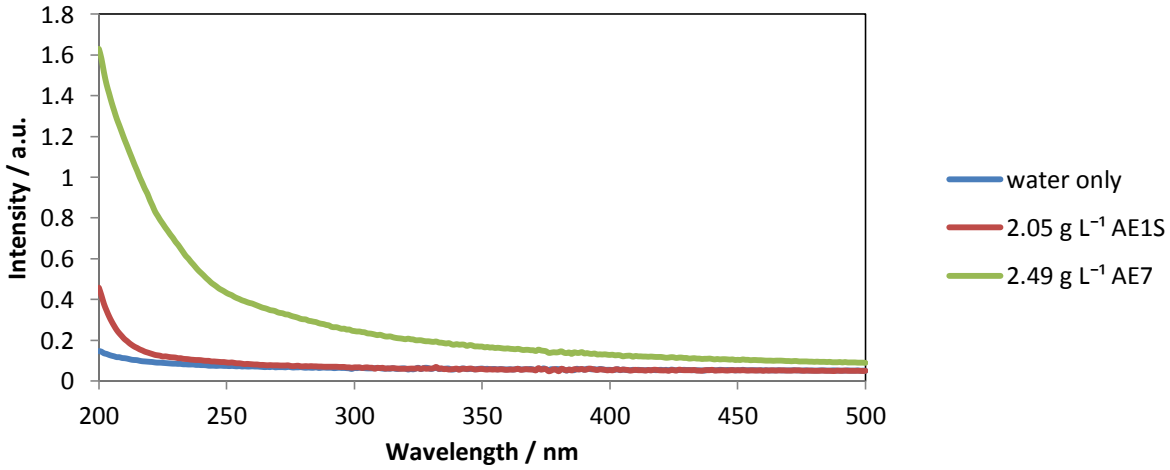

Figure 3-5: Absorbance spectra of surfactant solutions without brightener

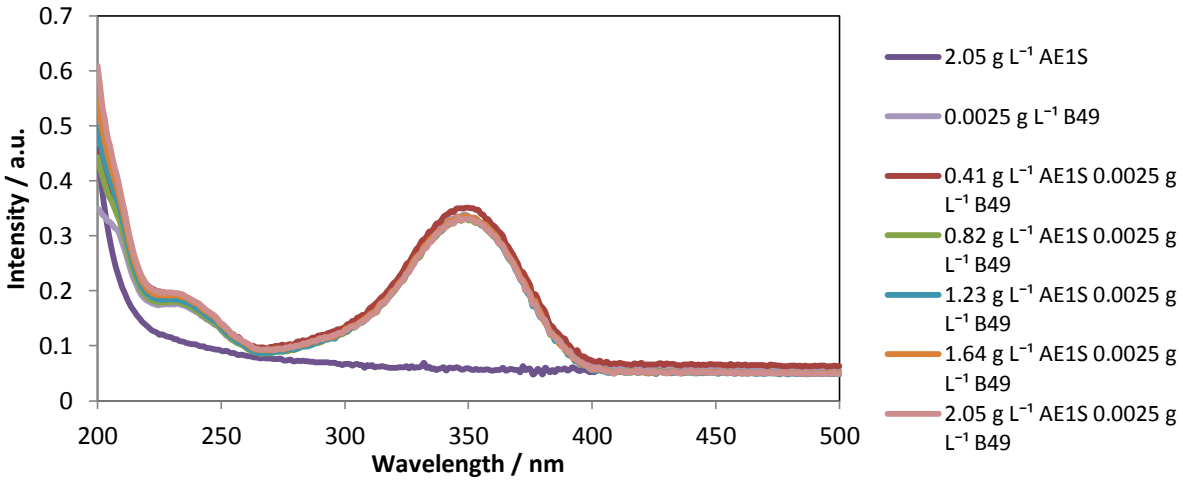

Figure 3-6: Absorbance spectra of 0.0025 g L^{-1} B49 solutions with varying concentrations of AE1S

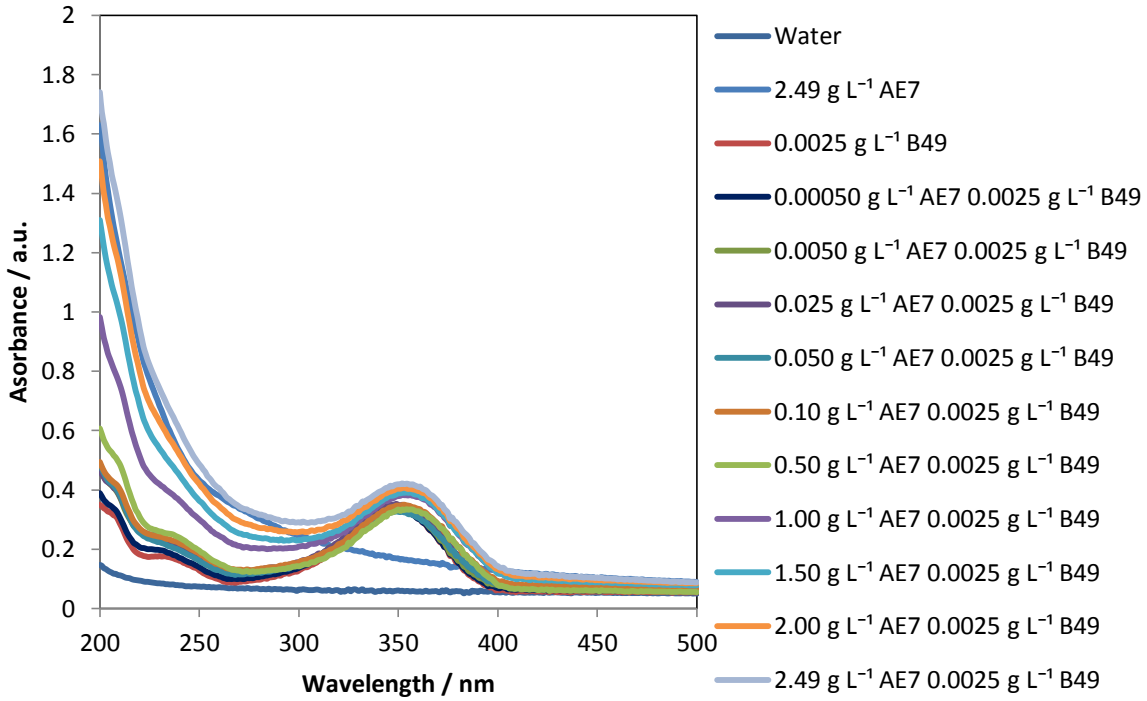

Figure 3-7: Absorbance spectra of 0.0025 g L^{-1} B49 solutions with varying concentrations of AE7

It can be seen from Figure 3-5 that the AE7 solution without brightener had a greater absorbance than the AE1S solution without brightener, particularly at low wavelengths. Figure 3-6 and Figure 3-7 show that the Brightener 49 has an absorbance peak at 350 nm. Figure 3-6 shows that the absorbance of brightener solutions was not affected by the AE1S concentration. Figure 3-7 also shows that, as the concentration of AE7 increased, the absorbance at low wavelengths (~ 200 nm) increased, but the absorbance at 350 nm (the absorbance peak of the brightener) remained relatively constant.

The relative increase in absorbance of the AE7 surfactant relative to the AE1S surfactant and water alone, and slight increase in absorbance of AE1S relative to water, were likely to be due to the presence of ether groups on the surfactant head groups. AE7 has approximately 7 $–OCH_2CH_2–$ groups, whereas AE1S will only have one (although for both surfactants, this is only an approximate degree of ethoxylation). These ether groups will absorb radiation at a wavelength of ~ 185 nm, due to the lone pair of electrons on the oxygen atom undergoing a $n \rightarrow \pi^*$ transition[129]. This is close to the peak seen in water alone of 190 nm.

The excitation spectra of Brightener 49 will confirm if the peak seen at 350 nm is due to the brightener; if there is a peak in the excitation spectrum at this wavelength, this will show that the fluorescence of the brightener is associated with incoming radiation at 350 nm, linking the absorbance of this radiation with the emission of radiation with a higher wavelength and lower energy.

3.2.2.1.2. Emission results

3.2.2.1.2.1. Solvatochromic effects and brightener position

The fluorescence emission spectra of 0.0025 g L^{-1} Brightener 49 solutions with AE1S and AE7 are shown in Figure 3-8 and Figure 3-9, respectively.

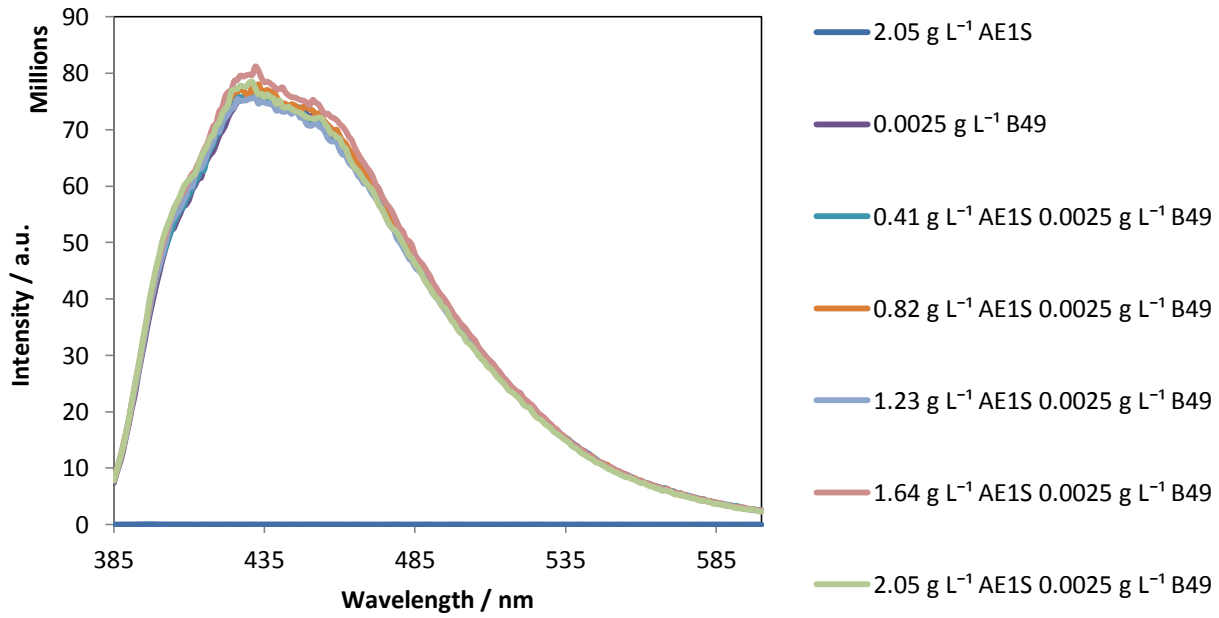

Figure 3-8: Fluorescence emission spectra of 0.0025 g L^{-1} B49 solutions with varying concentrations of AE1S

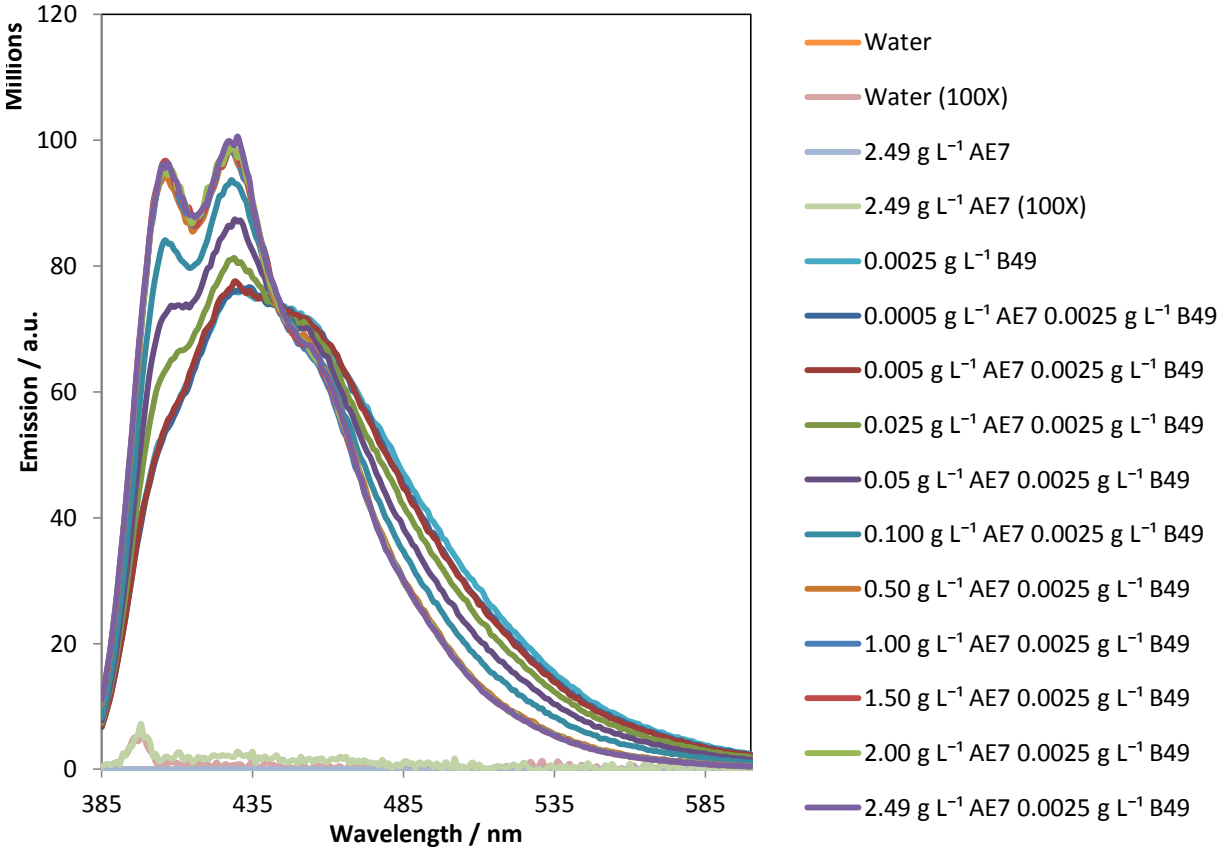

Figure 3-9: Fluorescence emission spectra of 0.0025 g L^{-1} B49 solutions with varying concentrations of AE7

It can be seen from Figure 3-8 and Figure 3-9 that the emission spectra of AE1S and AE7 without brightener present had very low intensities compared to those seen when brightener was present. When the brightener was present, a strong emission peak was seen at approximately 430 nm.

The most striking difference seen between the spectra of solutions containing brightener with AE1S, and with AE7, is that when AE1S was added to the brightener, no change was seen in the emission spectrum of the brightener, but when AE7 was added, a dramatic shift, and change in the peak structure, was seen, including a secondary peak appearing at 405 nm. This increase in structure can be explained by considering the environment in which the brightener existed.

If the fluorescence emission spectrum of the brightener alone was found, without any solvent, it would consist of a series of sharp peaks, corresponding to the excited state-ground state phase transitions causing fluorescence. However, when solvent is added to the system, interactions between the solvent and the brightener will affect the energy of the ground state, causing the peak to broaden. This peak broadening effect is strongest in solvents where a high degree of hydrogen bonding is present, such as water.

In this case, the peaks seen when the brightener was in water, and the peaks seen when the brightener was in AE1S solution, at a concentration significantly above its CMC, were virtually identical. This shows that the brightener was experiencing a similar degree of hydrogen bonding in each situation. Either the brightener was not interacting with the AE1S, and remained within the solution, or the brightener was interacting with the AE1S, but experienced a similar degree of hydrogen bonding to within the bulk solvent. In Chapter 6, data will be presented showing that the brightener was incorporated onto the surface of the micelle, but with a very high degree of water penetration, accounting for the high degree of hydrogen bonding seen.

When AE7 solution was used, at low concentrations no change in peak broadening was seen. However, as the concentration increased past the CMC, the degree of peak broadening decreased, giving a sharper series of peaks. This suggests that, as micelles were formed, the brightener entered an environment where it was less free to hydrogen bond. This could, for example, be the head group region of the AE7 micelle; although this region was polar, its $-(OCH_2CH_2)-$ groups would have been unable to form many hydrogen bonds with the $-SO_3^-$ groups, as counterions would be associated with the SO_3^- groups. This therefore suggests that the brighteners were being incorporated into the head group region of the AE7 micelle.

To further illustrate the effect of surfactants on the fluorescence emission spectrum, the change in the wavenumber of the absorbance peak, ν_a, and the wavenumber of the fluorescence emission, ν_e, were found. The point of maximum absorbance was used for the wavenumber of the absorbance peak, and the centroid of the emission spectrum was used as the wavenumber of the fluorescence emission, i.e.:

$$\nu_e = \frac{\sum_{i=1}^{N} E_i \nu_i}{\sum_{i=1}^{N} E_i}$$

Equation 3-1

Here, ν_i is the wavenumber of emitted radiation at point *i*, and E_i is the intensity of the emitted radiation.

From the change in $\nu_a - \nu_e$ with changing surfactant concentration, the solvatochromic shift of the systems could be determined. The change in $\nu_a - \nu_e$with changing surfactant

concentration is shown in Figure 3-10. The starting value from the Brightener 49 system, of 6927 cm^{-1} , is shown as a green line.

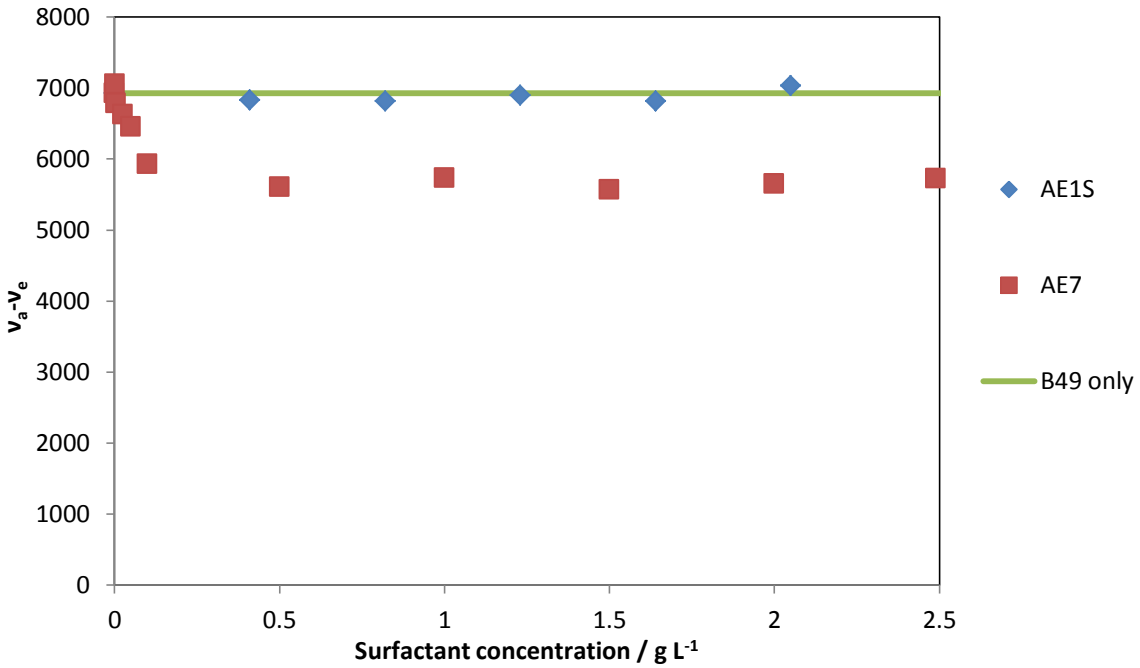

Figure 3-10: Change in ν_a-ν_e for B49 spectra with changing AE1S and AE7 concentrations

In the system containing AE1S and brightener, increasing the surfactant concentration did not have any effect on $\nu_a - \nu_e$, i.e. addition of the AE1S did not cause a solvatochromic shift.

However, as the concentration of AE7 is increased in the AE7 + Brightener 49 system, $\nu_a - \nu_e$ drops significantly until it stabilises at approximately 5600 cm^{-1}. This represents a hypsochromic ('blue') shift of 1300 cm^{-1} from the system containing brightener alone. This again provides clear evidence for the solvatochromic shift caused by the change in environment from water to the AE7 head group region.

3.2.2.1.2.2. Quantifying fluorescence

To estimate the amount of fluorescence emitted by each sample, the integrated fluorescence intensities were found by calculating the areas under the spectral lines, between 385 – 600 nm for emission spectra, and between 250 – 420 nm for excitation spectra. These are shown to three significant figures in Table 3-1 overleaf.

Table 3-1: Integrated fluorescence intensities for 0.0025 g L^{-1} B49 solutions with and without AE1S and AE7

Concentration of AE1S / g L^{-1}	Area under spectrum (AE1S system) / millions	Concentration of AE7 / g L^{-1}	Area under spectrum (AE7 system) / millions
0	7840	0	7840
0.41	7860	0.50	7660
0.82	7940	1.00	7630
1.23	7780	1.50	7660
1.64	8130	2.00	7680
2.05	7880	2.49	7700

It can be seen that the magnitudes seen were comparable for each system. In particular, while the values for AE7 were slightly lower, this still only represented a maximum difference of 6%. The consistency between these values suggested that the integrated fluorescence intensity was independent of surfactant concentration. Although the samples containing AE7 and Brightener 49 showed a greater peak height at 430 nm and 405 nm, this is compensated for by a narrowing of the spectrum and reduction in emission intensity at wavelengths over 440 nm.

The spectra for the solutions of AE7 and brightener not included in Table 3-1, i.e. 0.0005 g L^{-1} AE7 0.0025 g L^{-1} B49, 0.005 g L^{-1} AE7 0.0025 g L^{-1} B49, 0.025 g L^{-1} AE7 0.0025 g L^{-1} B49, 0.050 g L^{-1} AE7 0.0025 g L^{-1} B49, and 0.10 g L^{-1} AE7 0.0025 g L^{-1} B49, were taken two months after the other spectra. Therefore, due to changes in the lamp intensity in the experimental setup, these gave integrated fluorescence intensities that were consistent with each other, but not with the previous spectra. These spectra shown in Figure 3-9 were therefore normalised to the previous data. Their original integrated fluorescence intensities are shown in Table 3-2.

Table 3-2: Integrated fluorescence intensities for lower concentration AE7 samples prior to normalisation

AE7 concentration / g L^{-1}	Integrated fluorescence intensity / millions (3 s.f.)
0.0005	8410
0.005	8470
0.025	8480
0.050	8110
0.10	8560

The consistency seen between the integrated fluorescence intensities, and independence of these values from the surfactant concentration, suggested that the integrated fluorescence intensity was suitable to measure brightener concentration within the sample.

3.2.2.1.3. Excitation results

The excitation spectra obtained from the solutions are given in Figure 3-11 below and Figure 3-12 overleaf.

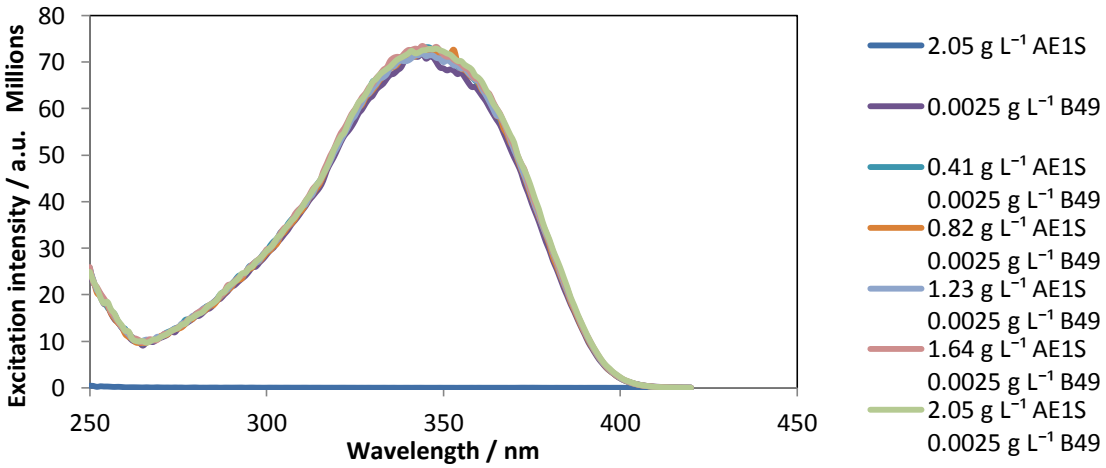

Figure 3-11: Fluorescence excitation spectra of 0.0025 g L^{-1} B49 solutions with varying concentrations of AE1S

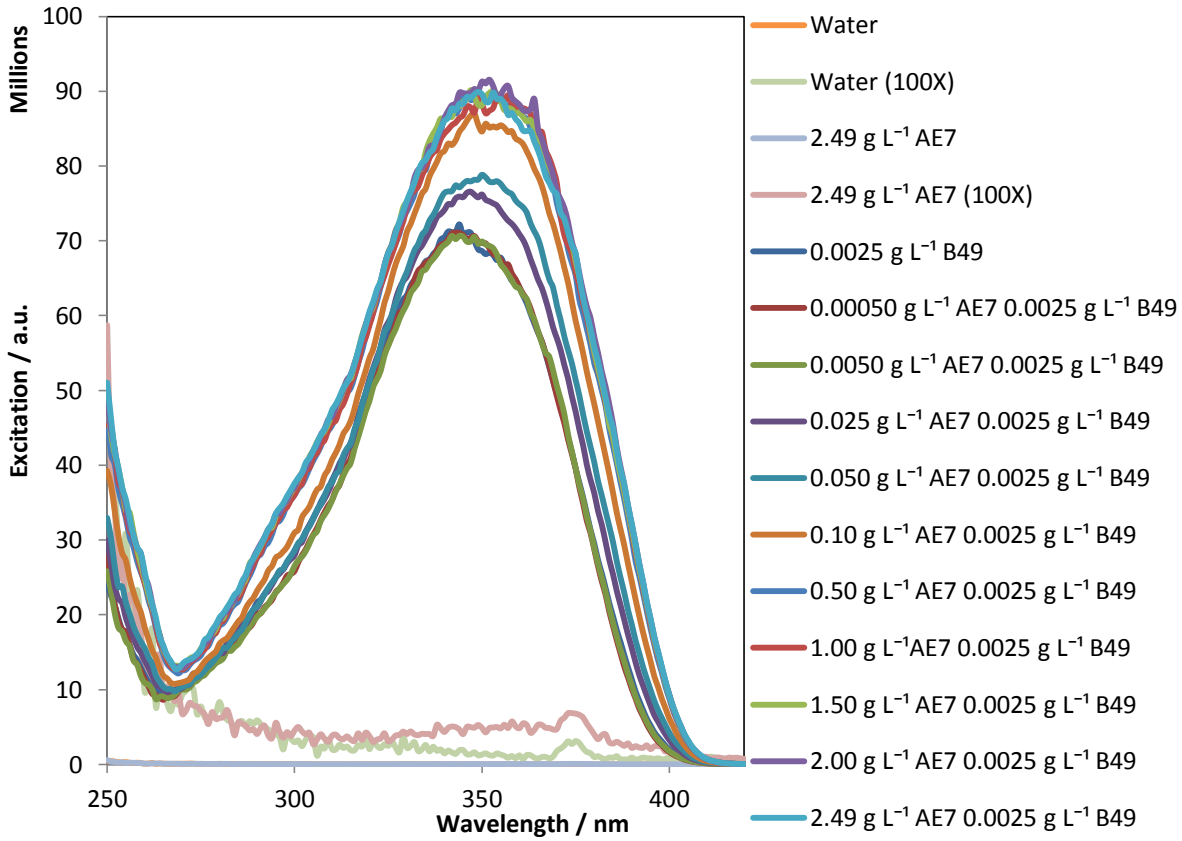

Figure 3-12: Fluorescence excitation spectra of 0.0025 g L^{-1} B49 solutions with varying concentrations of AE7

In all samples containing brightener, a single large peak was seen at approximately 350 nm. This matched the peak seen in the absorbance spectra shown in Figure 3-6 and Figure 3-7, confirming that the peak seen in the absorbance spectrum was due to the presence of Brightener 49.

To demonstrate this further, the absorbance and excitation spectra were normalised and compared. Examples of the absorbance and emission spectra given by brightener without surfactant, an AE1S/brightener system, and an AE7/brightener system can be seen in Figure 3-13, Figure 3-14, and Figure 3-15 respectively. For clarity, only one spectrum from each system is shown.

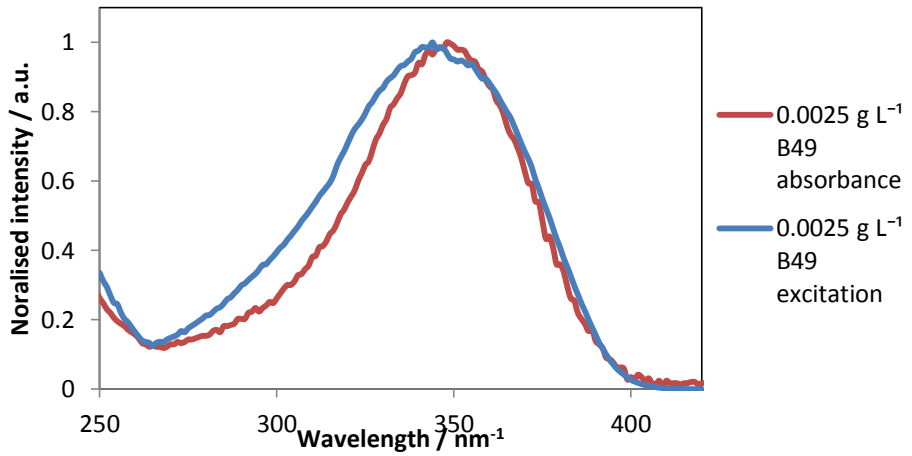

Figure 3-13: Comparison of the absorbance spectrum and fluorescence excitation spectrum of 0.0025 g L^{-1} Brightener 49 solution

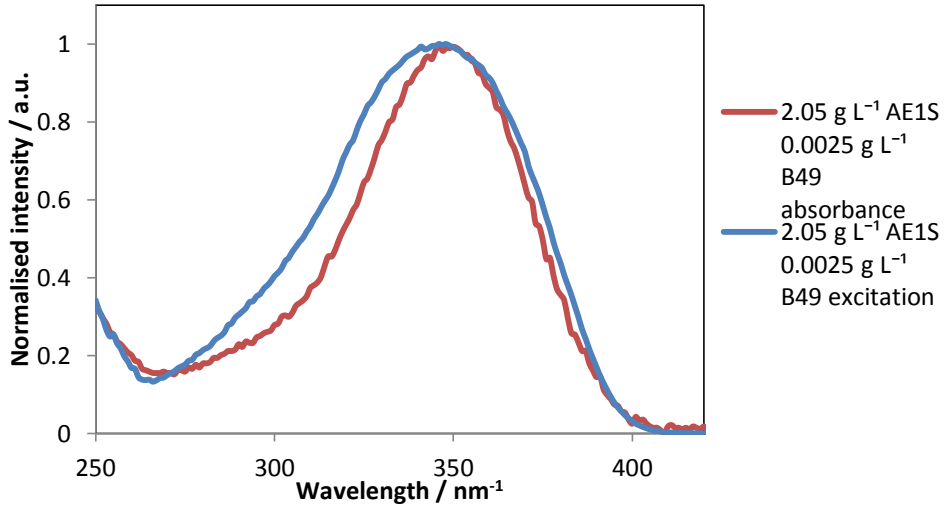

Figure 3-14: Comparison of the absorbance spectrum and fluorescence excitation spectrum of 2.05 g L^{-1} AE1S 0.0025 g L^{-1} Brightener 49 solution

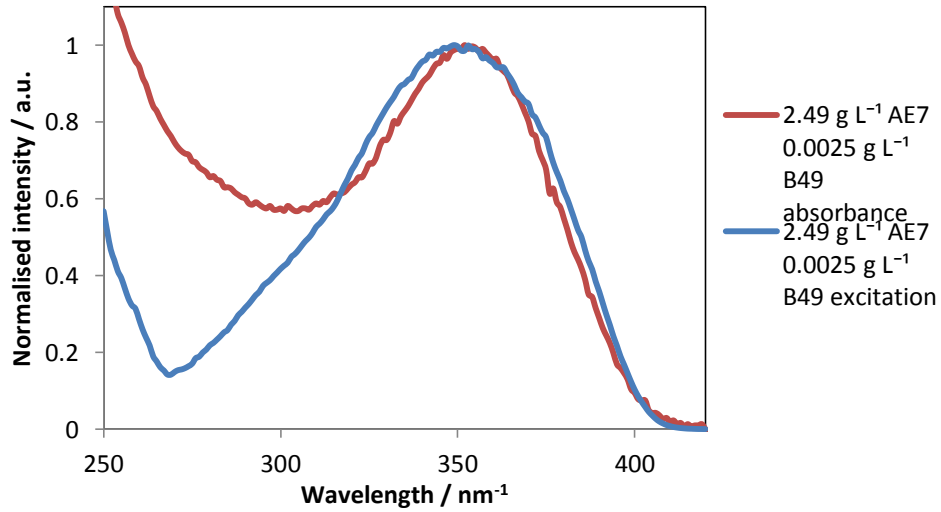

Figure 3-15: Comparison of the absorbance spectrum and fluorescence excitation spectrum of 2.49 g L^{-1} AE7 0.0025 g L^{-1} Brightener 49 solution

It can be seen that the absorbance and fluorescence excitation spectra peaks provided a good match. It can be seen that there were slight variances in peak intensity, particularly in the region of 250-350 nm; these were likely due to both the absorbance of the solvent and the surfactants, and to the fact that the emission of light by the brightener is not necessarily independent of the wavelength of exciting radiation[130].

The effect of the addition of surfactants on the fluorescence excitation spectra of the brightener can now be considered. It can be seen from Figure 3-11 and Figure 3-12 that the addition of AE1S had almost no effect on the excitation spectra of the brightener, but that the addition of AE7 caused a significant increase in the excitation, and an increase in intensity. This was due to the change in the emission peak structure seen with the addition of AE7; as the mixed AE7/brightener gave a greater peak height at 430 nm than the brightener only and AE1S/brightener systems, despite having a narrower peak and thus comparable integrated fluorescence intensity, it will have had a greater excitation peak at 430 nm for each excitation wavelength used, and thus a greater integrated fluorescence intensity for these spectra. The integrated fluorescence intensities are shown in Table 3-3 below.

Table 3-3: Integrated fluorescence excitation intensities for 0.0025 g L^{-1} B49 solution with and without varied concentrations of AE1S and AE7

Concentration of AE1S / g L^{-1}	Integrated fluorescence excitation intensity (AE1S system) / millions	Concentration of AE7 / g L^{-1}	Integrated fluorescence excitation intensity (AE7 system) / millions
0	5460	0	5460
0.41	5630	0.50	7470
0.82	5570	1.00	7510
1.23	5590	1.50	7620
1.64	5670	2.00	7680
2.05	5670	2.49	7630

Addition of AE7 caused a significant increase in the integrated fluorescence excitation intensity of the Brightener 49. However, addition of AE1S had little effect. This is again reflective of the increased peak heights at 430 nm when AE7 is present in the system.

Although the values seen in Table 3-3 are not consistent between systems, they are consistent within each system; comparable values were given for brightener samples at all AE7 concentrations. Similarly, the values given when AE1S was added were all comparable. Therefore, while these values cannot be used to give a direct comparison between systems, the percentage change in the integrated fluorescence intensity of a system can be used to show how the fluorescence of one particular system has changed with time and with addition of fabric. This percentage change should be comparable to that seen in the integrated fluorescence emission intensity.

As was the case for the emission spectra, the spectra for the solutions 0.0005 g L^{-1} AE7 0.0025 g L^{-1} B49, 0.005 g L^{-1} AE7 0.0025 g L^{-1} B49, 0.025 g L^{-1} AE7 0.0025 g L^{-1} B49, 0.050 g L^{-1} AE7 0.0025 g L^{-1} B49, and 0.10 g L^{-1} AE7 0.0025 g L^{-1} B49, as seen in Figure 3-12, were taken two months after the other excitation spectra. These were normalised using the same multipliers as for the emission spectra. These are given in Table 3-4 below.

Table 3-4: Raw and normalised integrated fluorescence intensities for brightener samples containing low concentrations of AE7

Concentration of AE7 / gL^{-1}	Raw integrated fluorescence excitation intensity / millions	Multiplier	Normalised integrated fluorescence intensity / millions
0.00050	5840	0.912	5330
0.0050	5870	0.905	5310
0.025	6510	0.903	5880
0.050	6480	0.946	6130
0.10	7630	0.895	6830

These normalised values are compared to the previous integrated fluorescence excitation intensities in Figure 3-16.

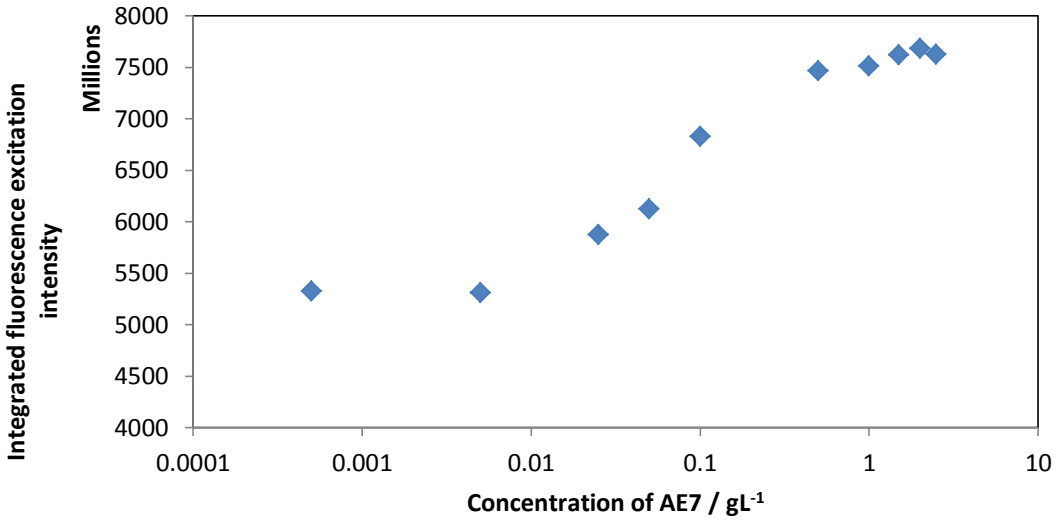

Figure 3-16: Effect of concentration of AE7 on the integrated fluorescence excitation intensity of Brightener 49 solution; note that a logarithmic scale is used for the x-axis.

A clear trend can be seen; as the concentration of AE7 increased, the integrated fluorescence intensity at first did not change as the concentration was below the CMC, and thus there were no micelles present to interact with the brightener; however, as the concentration of AE7 increased past the CMC, micelles started to form in the system, and some of the brightener molecules were incorporated into the micelles, causing the shifts in the emission seen previously and thus an increase in the integrated fluorescence excitation intensity. Once the maximum saturation of brightener into the micelles was achieved, i.e. almost all brightener was incorporated into micelles, no further shift in the emission spectrum was seen, and thus no further increase in the integrated fluorescence excitation intensity occurred with increasing AE7 concentration. This resulted in the plateau seen in Figure 3-16. The CMC of AE7 was expected at 0.1 g L^{-1}, which corresponds well to the transition seen.[30]

3.2.2.1.4. Conclusions

The Brightener 49 solutions were shown to give a peak in the absorbance spectra at 350 nm; this peak was not affected by the presence of surfactants. The nonionic surfactant AE7 was shown to absorb more low wavelength light (200 nm region) than the anionic surfactant AE1S, due to the large number of ethoxyl groups that made up its hydrophilic 'head' group, although the AE1S surfactant will absorb more light in the 200 nm region than water alone.

The primary fluorescence emission peak in the emission spectra of all Brightener 49 solutions was seen at approximately 430 nm. The integrated fluorescence intensity of the

emission spectra of Brightener 49 solutions was found to be consistent for all solutions, and not affected by the presence of surfactants. Thus it was determined that this would be a suitable measure of the change in brightener concentration in solution after washing with fabric.

The fluorescence emission spectra of the brightener was unaffected by the presence of AE1S, showing that the presence of this surfactant had little impact on its hydrogen bonding, or that the brightener was not interacting with the anionic surfactant. However, a dramatic solvatochromic shift and change in peak structure were seen in the solutions where AE7, the nonionic surfactant, was present in high concentrations. This change was correlated with the concentration of AE7, and was not seen at low concentrations below the CMC, showing that it was due to the brightener molecules interacting with the micelles, and the change in hydrogen bonding of the brightener molecule caused by this shift. This change reached a plateau at high concentrations of AE7, at the point when most brightener molecules are contained within the outer shell of the AE7 micelle and thus an increase in the number of micelles will not change the hydrogen bonding environment in which the brightener molecules exist.

All fluorescence excitation spectra of solutions containing Brightener 49 gave a single peak centred at 350 nm, mirroring the absorbance peak seen for these samples. The integrated fluorescence intensity of the excitation spectra was heavily influenced by the presence of the AE7 surfactant, as a result of the increase in emission peak height at 430 nm seen when high concentrations of AE7 were added to the brightener. For this reason, the excitation spectra could not be used alone to determine the change in brightener concentration between different surfactant solutions, but could be used to determine change in brightener concentration within a single system, in tandem with the emission spectra.

3.2.2.2. Effect of brightener concentration on fluorescence

Before using the fluorescence to quantitatively determine the proportion of brightener deposited in each system, it was necessary to confirm the effect of brightener concentration on the integrated fluorescence intensity of the emission and excitation spectra of brightener solutions. Solutions of 0.000625 g L^{-1} Brightener 49, 0.00125 g L^{-1} Brightener 49, 0.001875 g L^{-1} Brightener 49, and 0.0025 g L^{-1} Brightener 49 were made up. The fluorescence emission and excitation spectrum of each sample was taken. This will

allow the correlation between the fluorescence of the system and the concentration of the brightener to be determined. This correlation was required to be high to allow the fluorescence intensity to be used as a diagnostic test for concentration.

3.2.2.2.1. Emission results

The fluorescence emission spectra of brightener solutions of various concentrations are shown in Figure 3-17. Their corresponding integrated fluorescence intensities are shown in Figure 3-18.

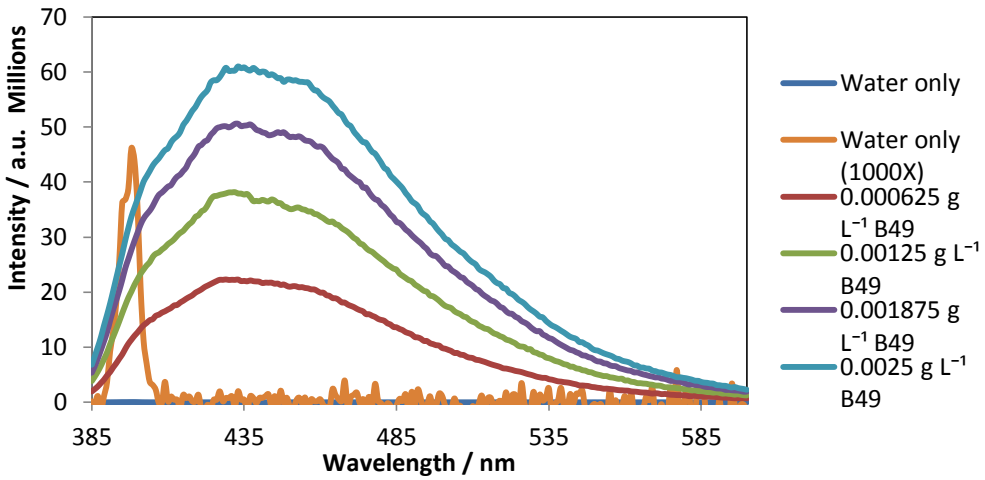

Figure 3-17: Fluorescence emission spectra for solutions of Brightener 49 at various concentrations

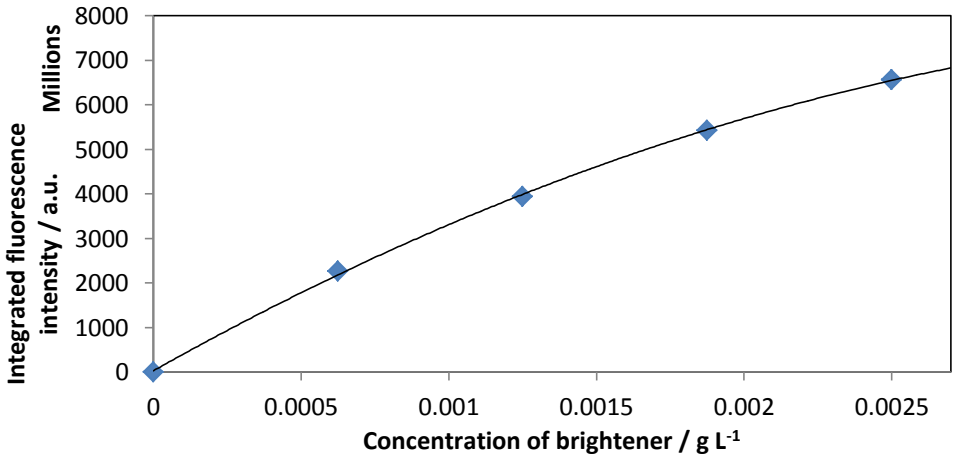

Figure 3-18: Effect of brightener concentration on the integrated fluorescence intensity of its fluorescence emission spectra

It can be seen that there was a very strong correlation between the concentration of brightener solution and the integrated fluorescence intensity. This showed that the

integrated fluorescence intensity was appropriate to use to measure the concentration of brightener in the solution.

The data in Figure 3-18 can be fit using the second-degree polynomial:

$$I.F.I = A(B \cdot [B49]^2 + C \cdot [B49] + D)$$

Equation 3-2

In this case, *I.F.I* is the integrated fluorescence intensity and [*B49*] is the concentration of brightener in the solution. This line is shown as a line of best fit in Figure 3-18; a good fit was seen. The parameters *B*, *C*, and *D* were calculated using the 'Regression' tool in Microsoft Excel, and are shown in Table 3-5 below. *A* was taken to be 1 in this instance, and was used in later sections to fit data taken at different lamp intensities to Equation 3-2.

Table 3-5: Parameters fitting Equation 3-2 to the data shown in Figure 3-18

Parameter (as given in Equation 3-2)	**Value**
B / g^{-2} L^2	-4.48 x 10^{14}
C / g^{-1} L	3.72 x 10^{12}
D / a.u.	3.11 x 10^{7}

These parameters were used in Section 3.2.2.3 to calculate the brightener concentrations remaining in each solution after addition of fabric. As the lamp intensity can vary, the parameter *A* can be found using a control sample; a solution containing 0.0025 g L^{-1} Brightener 49 was produced on the same day, in identical conditions to the samples with fabric added (without the addition of fabric), and its spectra found on the same day as the other samples. If its concentration, 0.0025 g L^{-1}, and integrated fluorescence intensity are known, then A can be found:

$$A = \frac{I.F.I}{(B \cdot [B49]^2 + C \cdot [B49] + D)}$$

Equation 3-3

Using the method of least squares, Equation 3-2 can now be solved for [*B49*]:

$$[B49] = -\frac{C}{2B} \pm \sqrt{\frac{4B(I.F.I - AD) + AC^2}{4AB^2}}$$

Equation 3-4

It was found that the negative root was applicable in this scenario; therefore, the concentration of each solution in Section 3.2.2.3 was given by:

$$[B49] = -\frac{C}{2B} - \sqrt{\frac{4B(I.F.I - AD) + AC^2}{4AB^2}}$$

Equation 3-5

3.2.2.2.2. Excitation results

The fluorescence excitation spectra of brightener solutions of various concentrations are shown in Figure 3-19. Their corresponding integrated fluorescence intensities are shown in Figure 3-20.

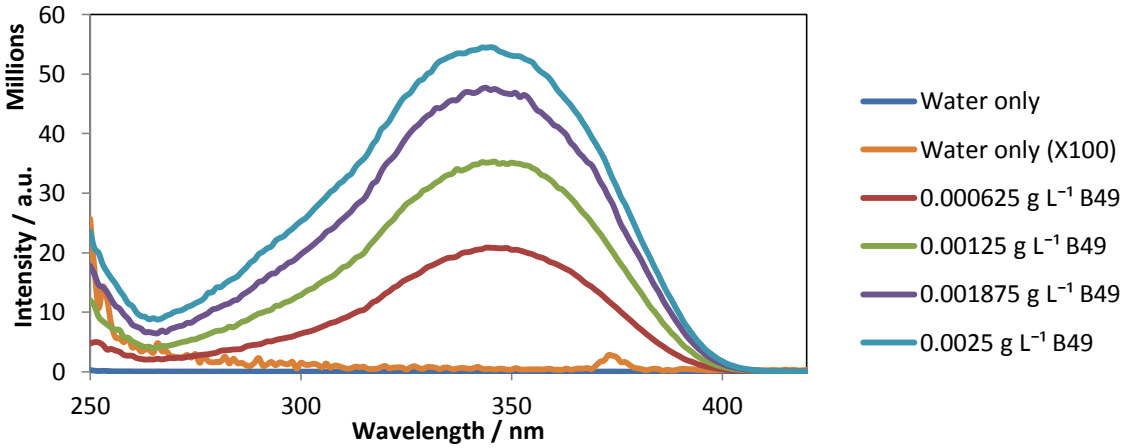

Figure 3-19: Fluorescence excitation spectra for solutions of Brightener 49 at various concentrations

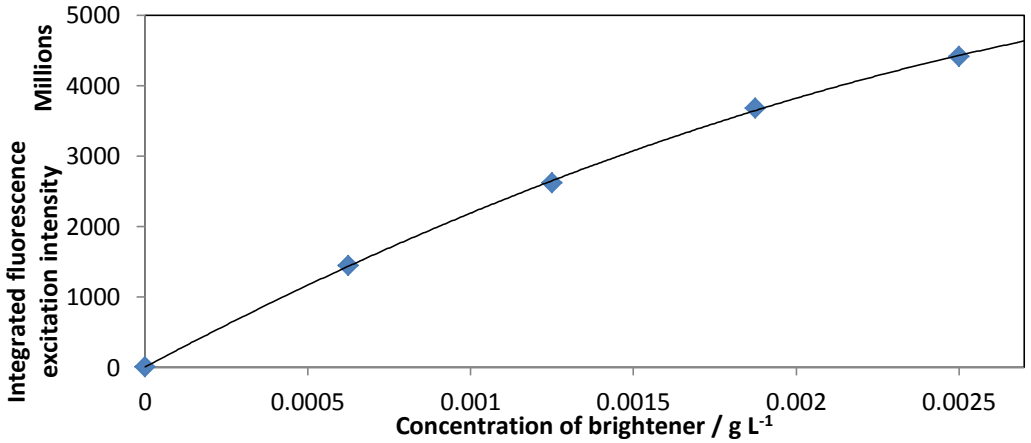

Figure 3-20: Effect of brightener concentration on the integrated fluorescence intensity of its excitation spectra

Again, the data could be fit well using the second-order polynomial given in Equation 3-2. This again showed the suitability of integrated fluorescence intensities to determine the amount of brightener remaining in solution after the addition of fabric. The parameters *B*, *C*, and *D* used to fit the data to Equation 3-2 are given in Table 3-6.

Table 3-6: Parameters fitting Equation 3-2 to the data shown in Figure 3-20

Parameter (as given in Equation 3-2)	Value
B/ g^{-2} L^2	-2.78×10^{14}
C / g^{-1} L	2.46×10^{12}
D / a.u.	8.18×10^{5}

These parameters were used to fit the data in Section 3.2.2.3 to the model, and thus determine the change in brightener concentration after the addition of fabric using the method described in Section 3.2.2.2.1 and Equation 3-5.

3.2.2.2.3. Conclusions

It was shown that there was a very strong correlation between the concentration of Brightener 49 in solution and the integrated fluorescence intensities of its emission and excitation spectra. This correlation was modelled using a second-order polynomial, and the parameters of this polynomial determined. This allowed future samples to be fit to this model, if the integrated fluorescence intensity of a solution of known brightener concentration was found.

3.2.2.3. Effect of addition of fabrics on fluorescence of Brightener 49 solutions

After a method of quantitatively determining the fluorescence of the brightener solution was determined, it was possible to use this to determine the amount of brightener deposited on fabric during the wash cycle.

For each solution to be tested, 5 identical test solutions were made up. To four of the vials, a fabric sample of a given mass (0.20 g) was added, for either 15, 30, 45 or 60 minutes. The fabric sample was then removed from the vial. One vial did not have fabric added and was labelled as '0 minutes'. This vial acted as a control, to give the initial integrated fluorescence intensity of the system; as the intensity of the fluorescence spectrum could fluctuate due to both conversion of the brightener from the trans- form

to the cis- form, and due to changes in the lamp intensity of the fluorimeter, it was important to use a control sample that was both made up on the same day as the other samples (to control for any decay in the fluorescence over time), and with a fluorescence spectrum that was taken on the same day as the other samples (to control for changes in the bulb intensity). All brightener solutions were covered in aluminium foil during storage to prevent the trans-cis conversion of the brightener.

To analyse the change in fluorescence of the solutions after the fabric was added, the fluorescence emission and excitation spectra were taken. The integrated fluorescence intensities of these spectra were found, and the percentage change from the control sample, i.e. 0 min, for that particular system was found. It was therefore possible to determine the effect of the addition of surfactants on the percentage decrease of the fluorescence, and thus on the deposition of the brightener in the solution; the greater the drop in percentage fluorescence, the more brightener has been removed from the solution, and thus deposited onto the fabric. The concentration of brightener remaining in the solution was also estimated using Equation 3-5.

The deposition was tested using two fabrics: cotton and polycotton. Both fabrics were samples of unbrightened fabric (i.e. with no brightener added during the manufacturing process), obtained from P&G. It is well established that stilbene brighteners have a strong affinity to the cellulose fibres in cotton, but little affinity to polyester fibres;[131] due to their ionic SO_3^- groups, these brighteners can form hydrogen bonds with the hydroxyl groups in cellulose, but not be absorbed by the highly hydrophobic polyester fibres.[132] As the polycotton fabric sample contained both types of fibre, some affinity should be seen between the brightener and the fabric, although the absorption of brightener onto this fabric was expected to be less than for the cotton sample.

3.2.2.3.1. Cotton

0.20 g of cotton was placed in a vial containing 10 mL of test solution, and allowed to soak for 15, 30, 45, or 60 minutes, then removed. The systems used were 2.05 g L^{-1} AE1S, 2.49 g L^{-1} AE7, 0.0025 g L^{-1} B49, 2.05 g L^{-1} AE1S 0.0025 g L^{-1} B49, and 2.49 g L^{-1} AE7 0.0025 g L^{-1} B49. Note that the surfactant only systems were used to generate control data for the surfactant + brightener systems. The fluorescence emission and excitation spectra of the solutions were then taken.

3.2.2.2.1.1. Emission results

The fluorescence emission spectra of the water, AE1S, AE7, Brightener 49, AE1S + Brightener 49, and AE7 + Brightener 49 solutions are shown in Figure 3-21, Figure 3-22, Figure 3-23, Figure 3-24, Figure 3-25, and Figure 3-26 respectively.

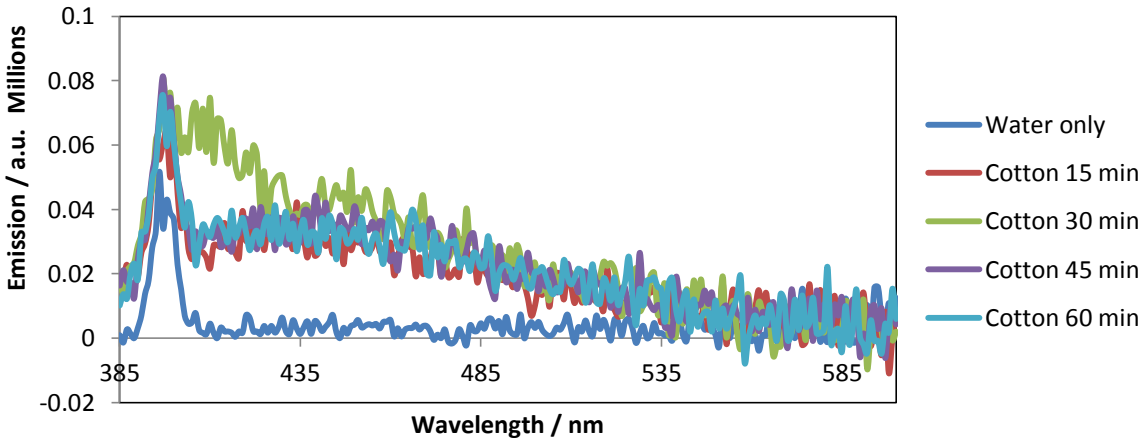

Figure 3-21: Fluorescence emission spectra of water at 0, 15, 30, 45, and 60 minutes after the addition of 0.2 g unbrightened cotton

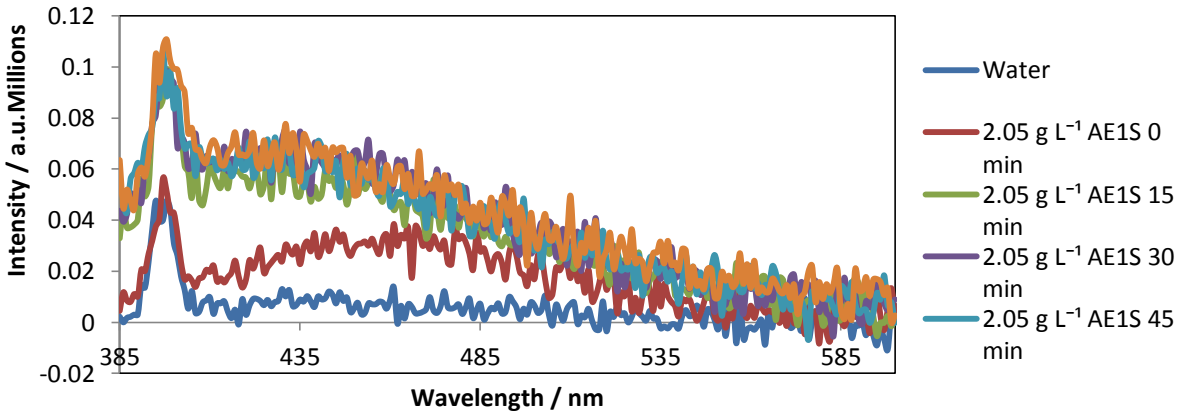

Figure 3-22: Fluorescence emission spectra of 2.05 g L^{-1} AE1S solution at 0, 15, 30, 45, and 60 minutes after addition of 0.2 g unbrightened cotton

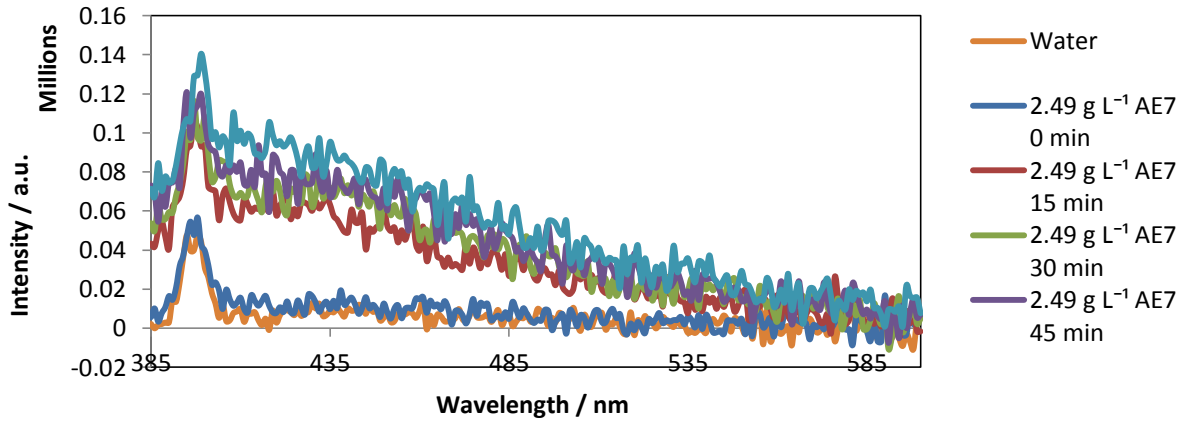

Figure 3-23: Fluorescence emission spectra of 2.49 g L^{-1} AE7 solution at 0, 15, 30, 45, and 60 minutes after the addition of 0.2 g unbrightened cotton

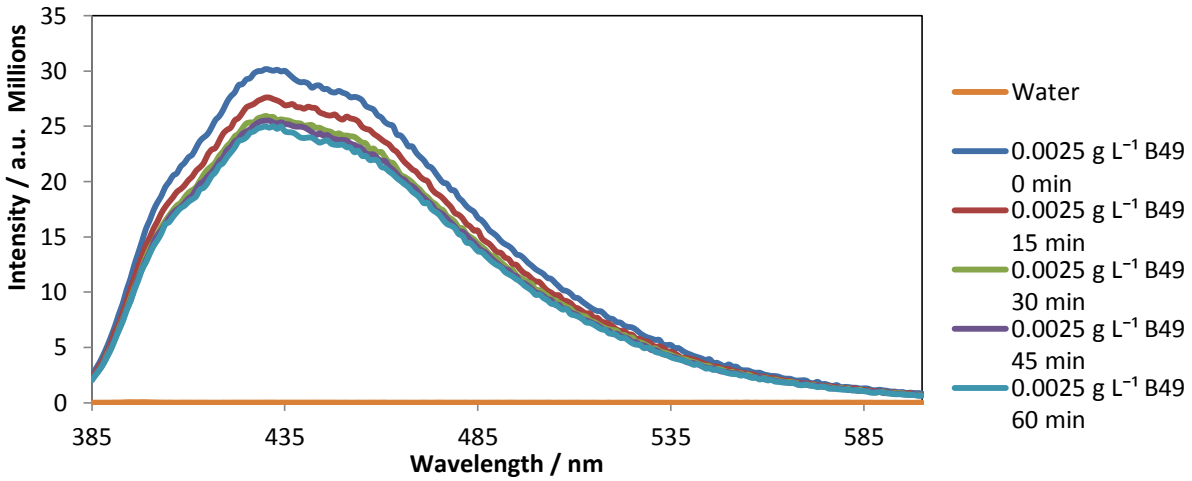

Figure 3-24: Fluorescence emission spectra of 0.0025 g L^{-1} Brightener 49 solution at 0, 15, 30, 45, and 60 minutes after the addition of 0.2 g unbrightened cotton

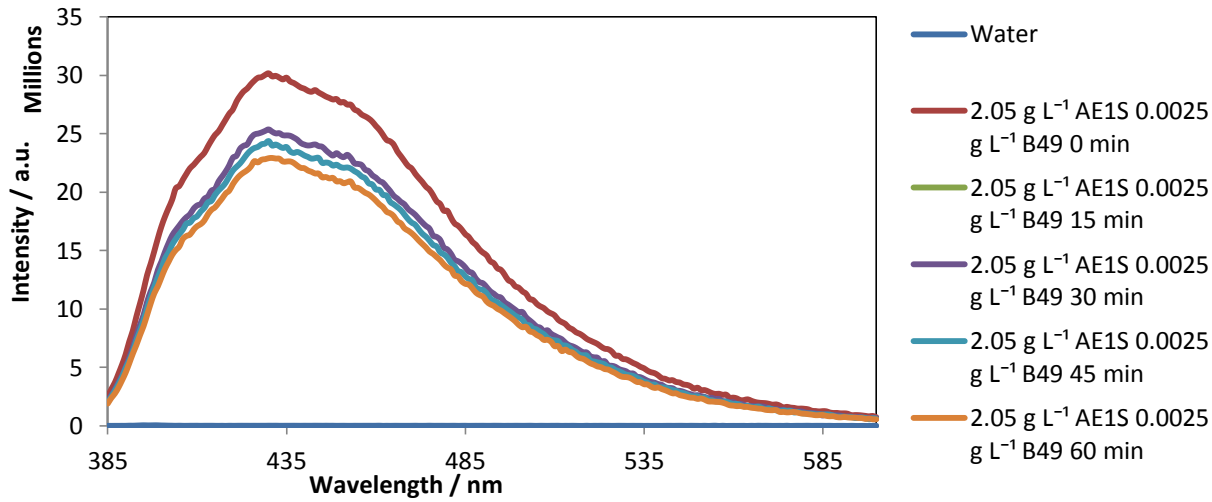

Figure 3-25: Fluorescence emission spectra of 2.05 g L^{-1} AE1S, 0.0025 g L^{-1} Brightener 49 solution at 0, 15, 30, 45, and 60 minutes after the addition of 0.2 g unbrightened cotton

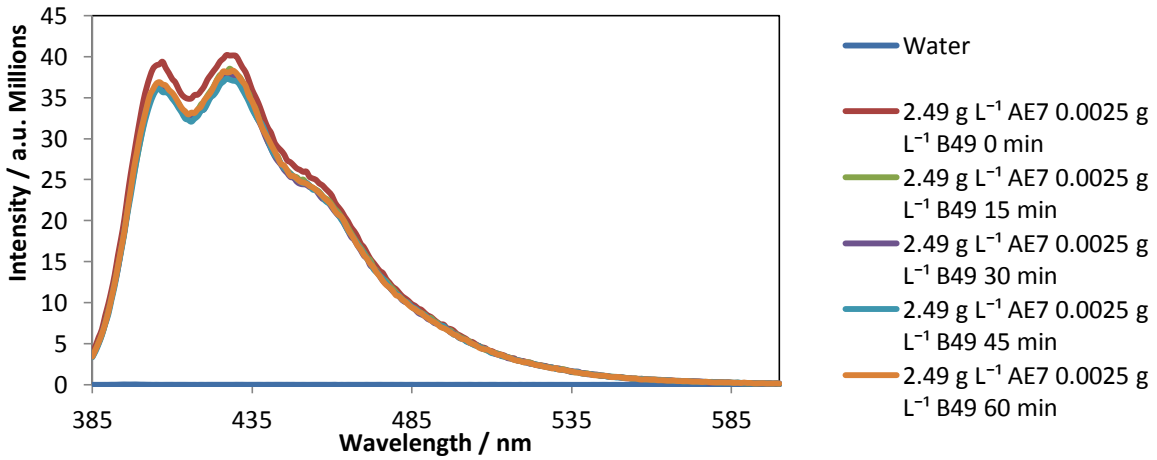

Figure 3-26: Fluorescence emission spectra of 2.49 g L^{-1} AE7, 0.0025 g L^{-1} Brightener 49 solution at 0, 15, 30, 45, and 60 minutes after the addition of 0.2 g unbrightened cotton

Figure 3-21, Figure 3-22 and Figure 3-23 show that a small amount of fluorescent material was deposited into the solution from the fabric sample (probably the cellulose fibres); however, it can be seen that the magnitude of this fluorescence was incredibly low when compared to the magnitude of the brightener fluorescence. In particular, the samples containing AE1S alone and AE7 alone showed an integrated fluorescence intensity of 9.04 x 10^6 and 1.14 x 10^7 respectively, 60 minutes after the addition of cotton fabric; the samples containing Brightener 49 alone, AE1S + B49, and AE7 + B49 gave integrated fluorescence intensities of 2.39 x 10^9, 2.17 x 10^9, and 2.77 x 10^9 respectively 60 minutes after the addition of cotton, values which are approximately 240 – 280 times greater than that for the surfactants alone; see Table 3-7. (These spectra were all taken on the same day, with the same lamp intensity, and thus can be directly compared.)

To estimate the reduction in the amount of fluorescent material, i.e. the brightener, in the solution during the wash process, the integrated fluorescence intensities of these spectra were calculated. These are shown in Figure 3-27 and Table 3-7 below. The sample containing water only was taken on a different occasion to the other data points, and thus may show a different starting magnitude; however, this system showed no significant change in intensity.

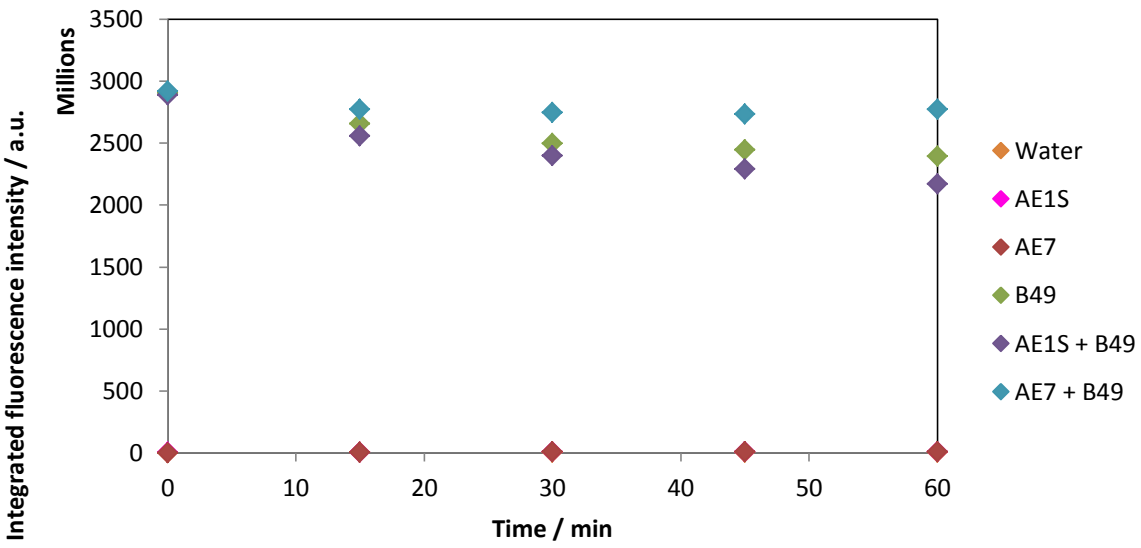

Figure 3-27: Effect of the length of wash on the integrated fluorescence intensity

Table 3-7: Effect of length of wash on the integrated fluorescence intensity

Time / min	Water / millions	AE1S / millions	AE7 / millions	B49 / millions	AE1S + B49 / millions	AE7 + B49 / millions
0	0.989	3.84	1.77	2900	2890	2920
15	4.19	7.42	7.25	2650	2560	2770
30	5.73	8.41	8.60	2500	2400	2740
45	4.74	8.24	9.63	2440	2290	2730
60	4.59	9.04	11.4	2390	2170	2770

3.2.2.2.1.2. Excitation results

The fluorescence excitation spectra of the AE1S, AE7, Brightener 49, AE1S + Brightener 49, and AE7 + Brightener 49 solutions are shown in Figure 3-29, Figure 3-30, Figure 3-31, Figure 3-32, and Figure 3-33 below and overleaf.

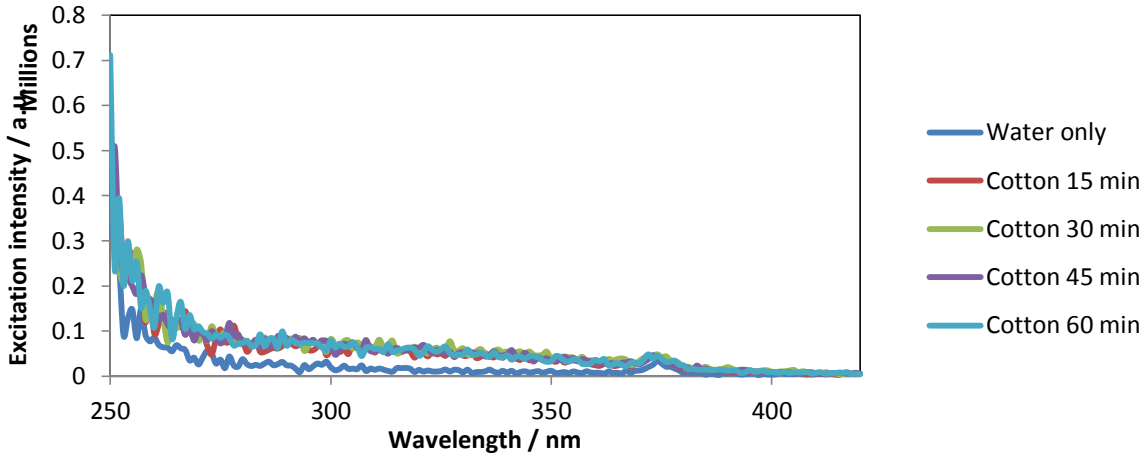

Figure 3-28: Fluorescence excitation spectra of water at 0, 15, 30, 45, and 60 minutes after the addition of 0.2 g unbrightened cotton

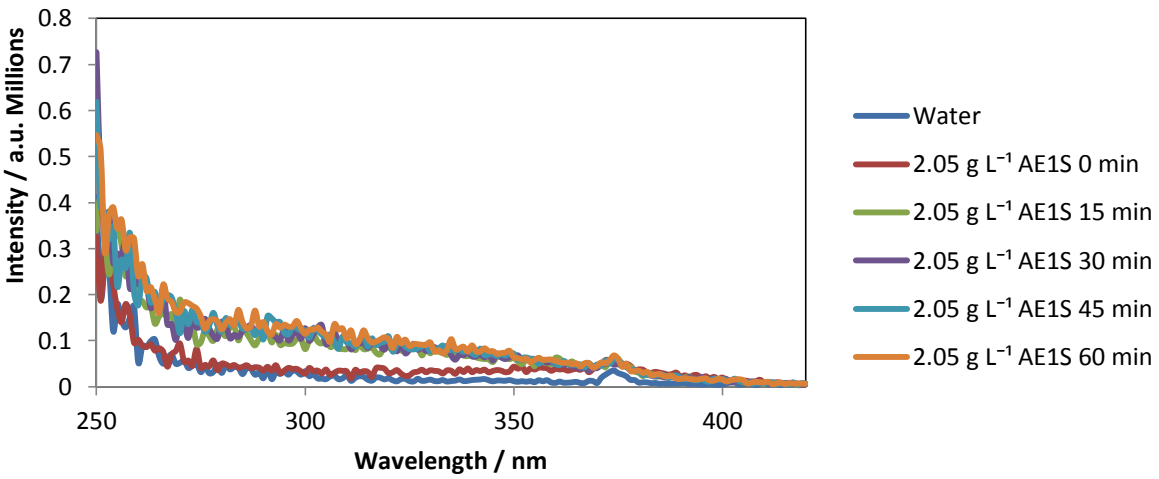

Figure 3-29: Fluorescence excitation spectra of 2.05 g L^{-1} AE1S samples at 0, 15, 30, 45, and 60 minutes after the addition of 0.2 g unbrightened cotton

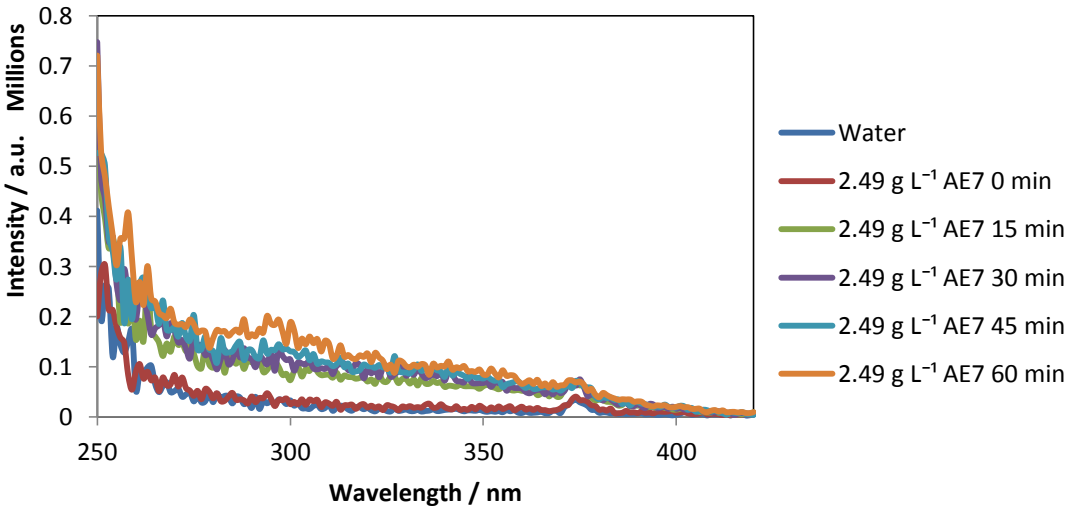

Figure 3-30: Fluorescence excitation spectra of 2.49 g L^{-1} AE7 samples at 0, 15, 30, 45, and 60 minutes after the addition of 0.2 g unbrightened cotton

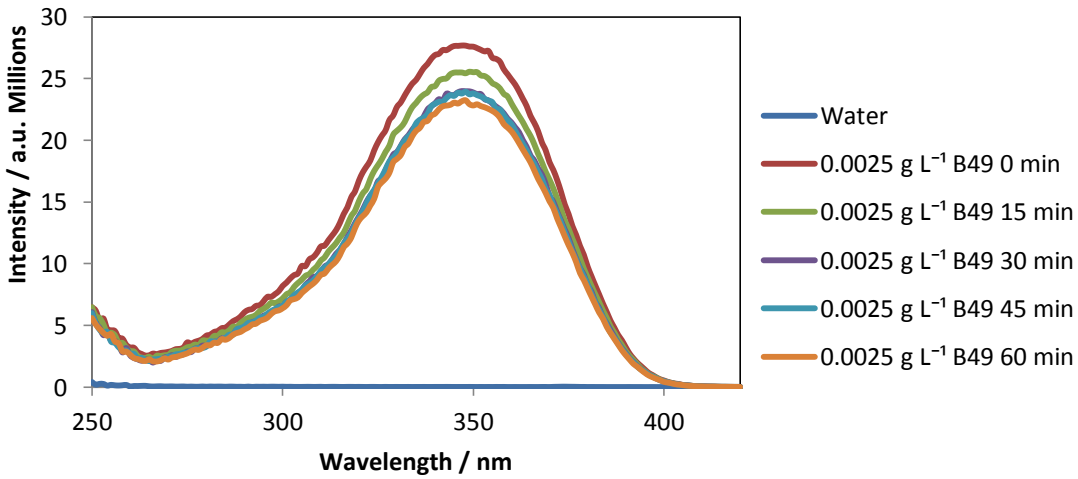

Figure 3-31: Fluorescence excitation spectra of 0.0025 g L^{-1} Brightener 49 samples at 0, 15, 30, 45, and 60 minutes after the addition of 0.2 g unbrightened cotton

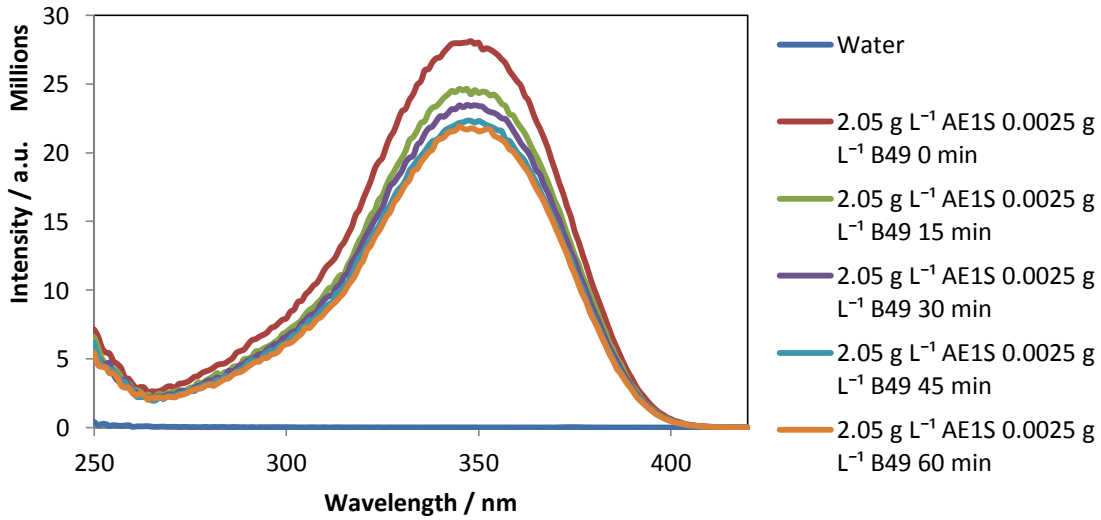

Figure 3-32: Fluorescence excitation spectra of 2.05 g L^{-1} AE1S, 0.0025 g L^{-1} Brightener 49 samples at 0, 15, 30, 45, and 60 minutes after the addition of 0.2 g unbrightened cotton

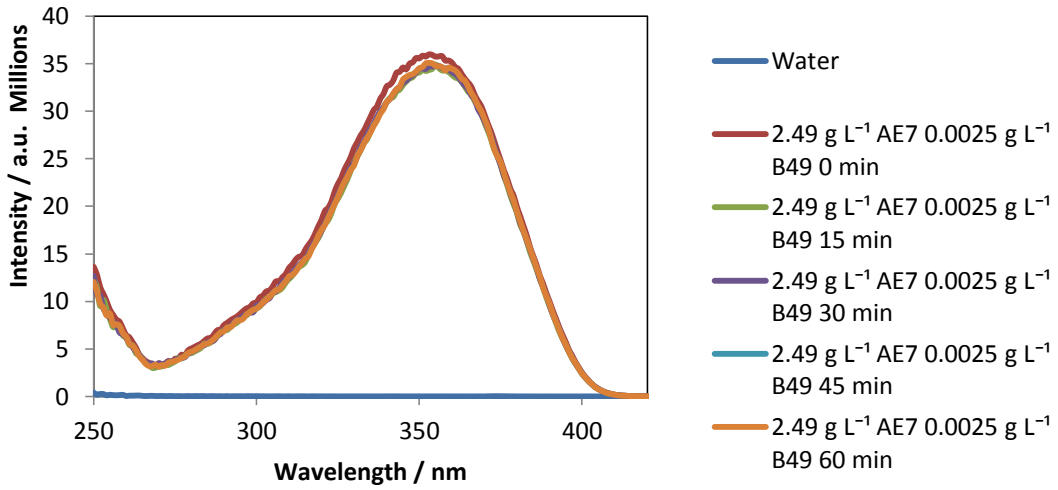

Figure 3-33: Fluorescence excitation spectra of 2.49 g L^{-1} AE7, 0.0025 g L^{-1} Brightener 49 samples at 0, 15, 30, 45, and 60 minutes after the addition of 0.2 g unbrightened cotton

The integrated fluorescence intensities are given in Table 3-8 and Figure 3-34 below.

Table 3-8: Effect of length of washing on integrated fluorescence excitation intensity

Time / min	Water / millions	AE1S / millions	AE7 / millions	B49 / millions	AE1S + B49 / millions	AE7 + B49 / millions
0	4.16	7.71	5.90	1890	1920	2610
15	9.59	13.9	14.1	1730	1670	2480
30	10.5	14.9	16.0	1600	1590	2500
45	10.1	15.6	17.5	1590	1500	2470
60	10.3	16.9	20.4	1550	1460	2500

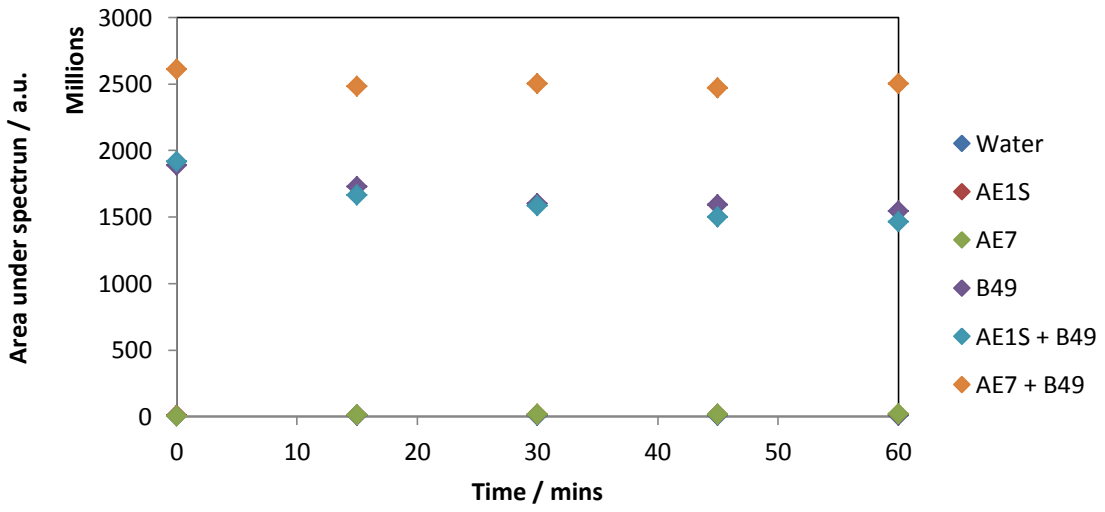

Figure 3-34: Effect of length of washing on integrated fluorescence excitation intensity

Again, the integrated fluorescence intensities given for the samples without brightener were several orders of magnitude lower than those containing brightener. However, this data differs from the emission data in that the initial values for the area given by each system differ. For this reason, the percentage change in the area under the curve was examined, rather than the absolute values.

3.2.2.2.1.3. Discussion and conclusions

The percentage changes in the integrated fluorescence intensity (IFI) for each brightener system are shown in Table 3-9 below.

Table 3-9: Effect of time of fabric addition on the integrated fluorescence intensity of the emission and excitation spectra of brightener solutions, with and without addition of surfactant. Values are given as a percentage of the starting value for each solution.

Time / min	B49 emission IFI / %	B49 excitation IFI / %	AE1S + B49 emission IFI / %	AE1S + B49 excitation IFI / %	AE7 + B49 emission IFI / %	AE7 + B49 excitation IFI / %
0	100	100	100	100	100	100
15	91.4	91.6	88.6	86.9	94.9	95.1
30	85.9	84.8	83.0	82.8	94.0	95.9
45	84.1	84.4	79.3	78.4	93.7	94.6
60	82.4	81.9	75.1	76.4	94.9	95.8

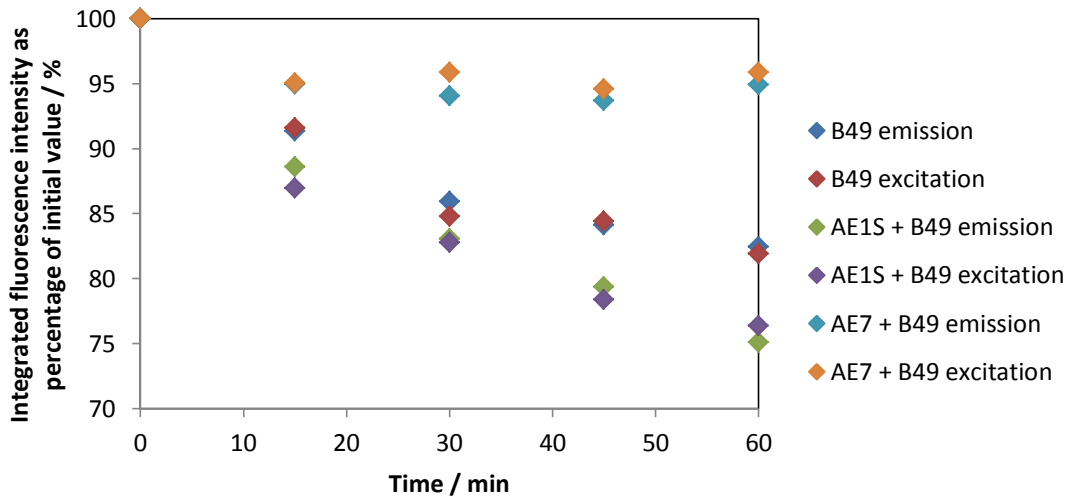

Figure 3-35: Effect of length of washing on the integrated fluorescence intensity of the emission and excitation spectra of the brightener solutions with and without surfactant. Values are given as a percentage of the starting value for each solution.

It can be seen that the percentage change obtained *via* the emission and excitation spectra for each system were very close.

For the B49, AE1S + B49, and AE7 + B49 solutions, the integrated fluorescence intensity of both the emission and excitation decreased as the length of wash increases, showing that brightener from solution had been absorbing onto the fabric. The lower this value, the more brightener had been removed from solution. The greatest decrease was seen in the solution containing AE1S + B49. As this decrease was greater than that seen in the brightener-only system, this suggests that the presence of AE1S was supporting brightener absorption onto the fabric. The least decrease was seen in the system containing AE7 + B49, suggesting that the nonionic surfactant inhibited the brightener uptake. These results will be given more physical meaning in Chapter 7, where they will be interpreted alongside the computational data seen in Chapter 6.

The concentrations of brightener in each system were found using the method described in Section 3.2.2.2 previously, using the sample of brightener which had not had fabric added as a control sample to calibrate the system. These concentrations are given in Table 3-10.

Table 3-10: Change in concentration of Brightener 49 after addition of cotton fabric

Time / minutes	**Concentration of Brightener 49 remaining in solution / g L^{-1}**		
	B49	**B49 + AE1S**	**B49 + AE7**
0	0.00250	0.00250	0.00250
15	0.00217	0.00204	0.00230
30	0.00196	0.00188	0.00230
45	0.00192	0.00176	0.00227
60	0.00186	0.00166	0.00231

The trends seen in the integrated fluorescence intensity translated to similar trends in the brightener concentration; the greatest drop in the brightener concentration was seen in the solutions containing the anionic surfactant AE1S, and the least drop was seen in the solutions containing the nonionic surfactant AE7. Interestingly, while the concentration of brightener in the B49 and B49 + AE1S solutions continued to decrease over the time period studied, the concentration of Brightener 49 in the B49 + AE7 solutions appeared to

plateau after 15 minutes, suggesting that no further deposition took place after this time point.

3.2.2.2.2. Polycotton

0.20 g of polycotton was placed in a vial containing 10 mL of test solution, and allowed to soak for 15, 30, 45, or 60 minutes. The systems used were 2.05 g L^{-1} AE1S, 2.49 g L^{-1} AE7, 0.0025 g L^{-1} B49, 2.05 g L^{-1} AE1S 0.0025 g L^{-1} B49, and 2.49 g L^{-1} AE7 0.0025 g L^{-1} B49. The surfactant only systems were used to generate control data for the surfactant/brightener systems. The fluorescence emission and excitation spectra of these samples were then taken.

3.2.2.2.2.1. Emission results

The fluorescence emission spectra of the AE1S, AE7, Brightener 49, AE1S + Brightener 49, and AE7 + Brightener 49 systems are shown in Figure 3-37, Figure 3-38, Figure 3-39, Figure 3-40, and Figure 3-41 below and overleaf.

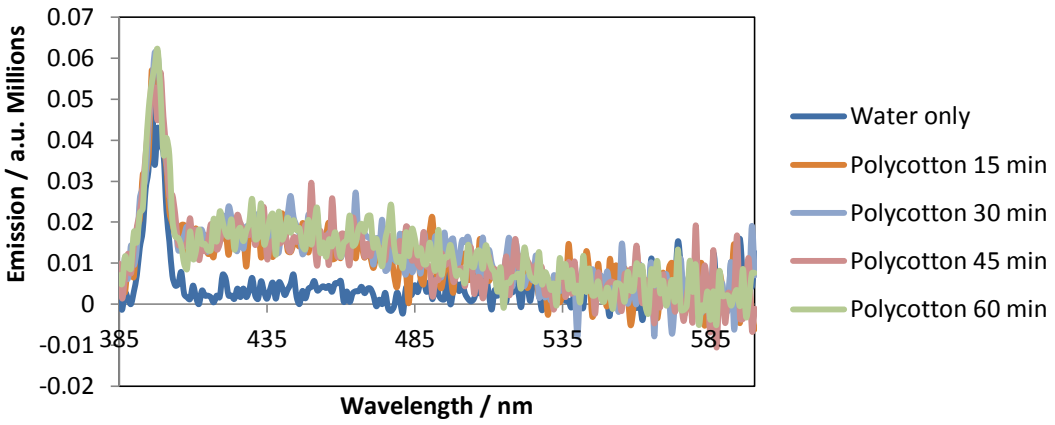

Figure 3-36: Fluorescence emission spectra of water at 0, 15, 30, 45, and 60 minutes after the addition of 0.2 g unbrightened polycotton

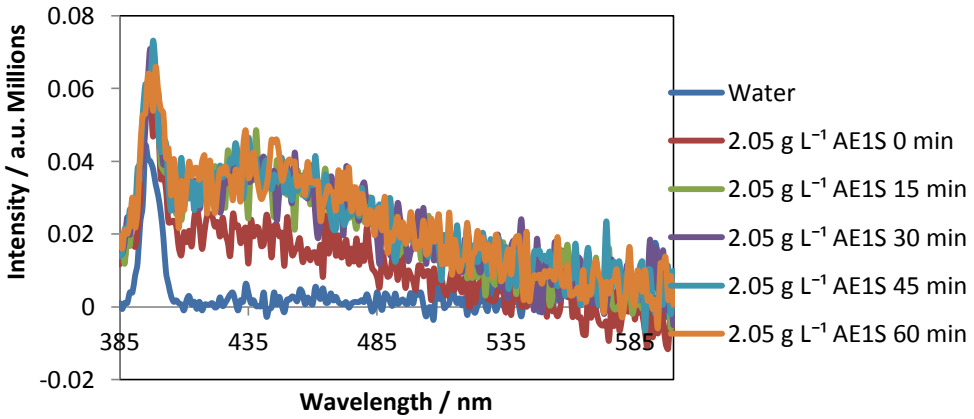

Figure 3-37: Fluorescence emission spectra of 2.05 g L^{-1} AE1S solution at 0, 15, 30, 45, and 60 minutes after the addition of 0.2 g unbrightened polycotton

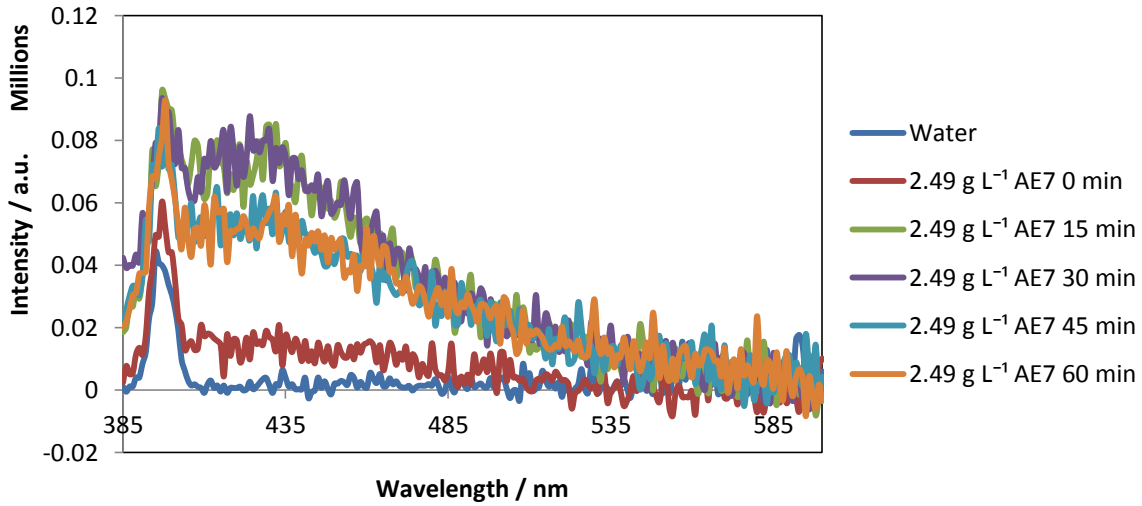

Figure 3-38: Fluorescence emission spectra of 2.49 g L^{-1} AE7 solution at 0, 15, 30, 45, and 60 minutes after the addition of 0.2 g unbrightened polycotton

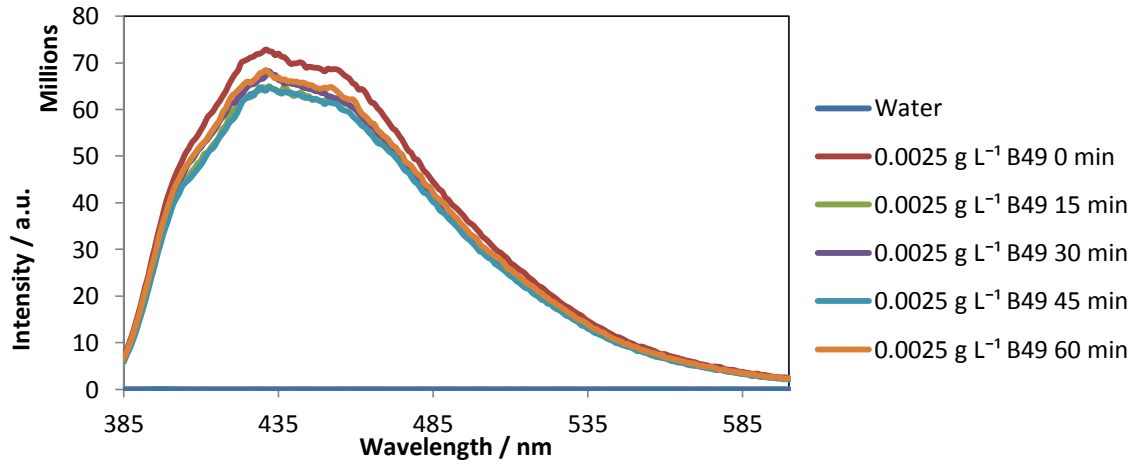

Figure 3-39: Fluorescence emission spectra of 0.0025 g L^{-1} B49 solution at 0, 15, 30, 45, and 60 minutes after the addition of 0.2 g unbrightened polycotton

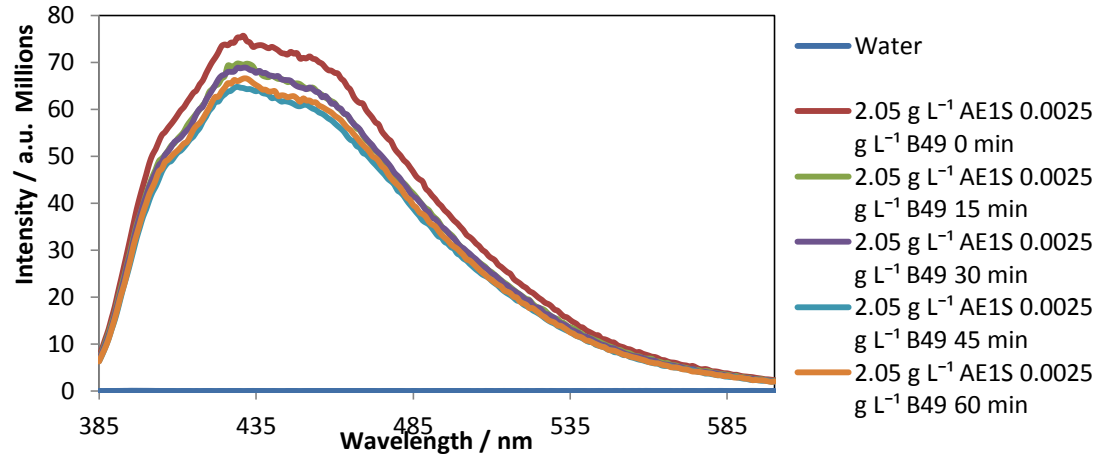

Figure 3-40: Fluorescence emission spectra of 2.05 g L^{-1} AE1S, 0.0025 g L^{-1} B49 solution at 0, 15, 30, 45, and 60 minutes after the addition of 0.2 g unbrightened polycotton

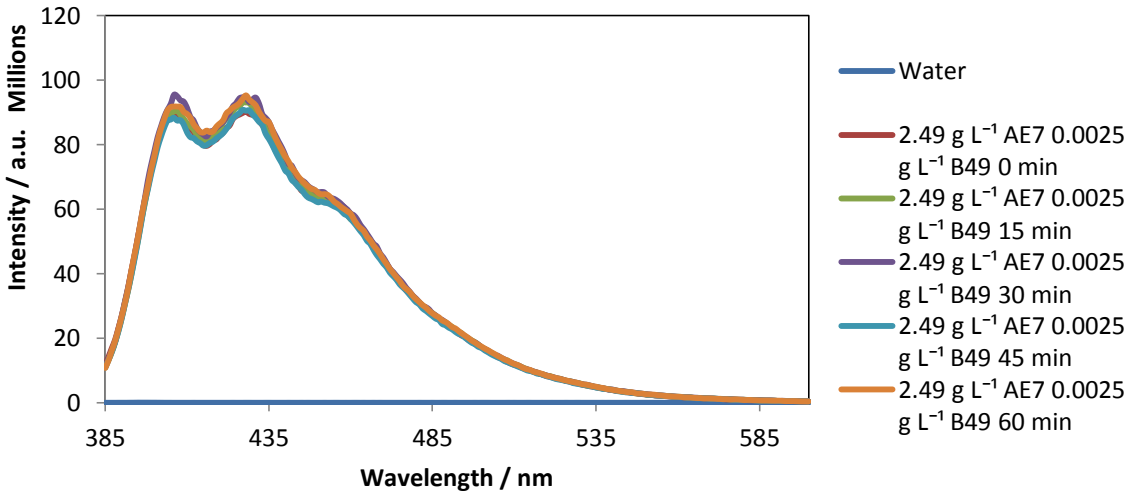

Figure 3-41: Fluorescence emission spectra of 2.49 g L^{-1} AE7, 0.0025 g L^{-1} B49 solution at 0, 15, 30, 45, and 60 minutes after the addition of 0.2 g unbrightened polycotton

The integrated fluorescence intensities (IFI) of these spectra were found. These are shown in Table 3-11 below.

Table 3-11: Effect of length of washing on integrated fluorescence emission intensity

Time / min	Water IFI / millions	AE1S IFI / millions	AE7 IFI/ millions	B49 IFI / millions	AE1S + B49 IFI / millions	AE7 + B49 IFI / millions
0	0.989	2.47	1.74	7490	7790	7110
15	2.32	4.49	7.25	6740	7080	7160
30	2.59	4.69	7.53	6920	7040	7330
45	2.45	4.90	6.03	6650	6590	7020
60	2.59	4.94	6.11	7030	6730	7290

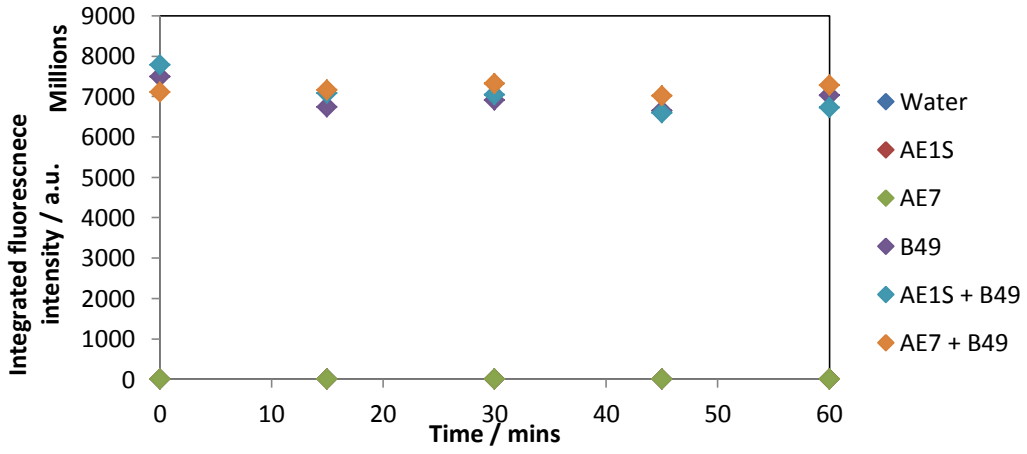

Figure 3-42: Effect of length of washing on integrated fluorescence emission intensity

3.2.2.2.2. Excitation results

The fluorescence excitation spectra of the AE1S, AE7, Brightener 49, AE1S + Brightener 49, and AE7 + Brightener 49 systems are shown in Figure 3-44, Figure 3-45, Figure 3-46, Figure 3-47, and Figure 3-48 below and overleaf.

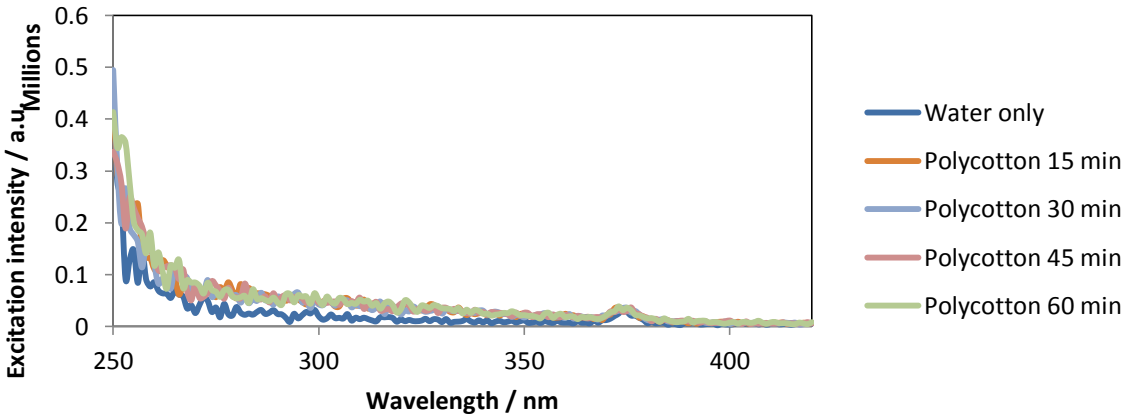

Figure 3-43: Fluorescence excitation spectra of water at 0, 15, 30, 45, and 60 minutes after the addition of 0.2 g unbrightened polycotton

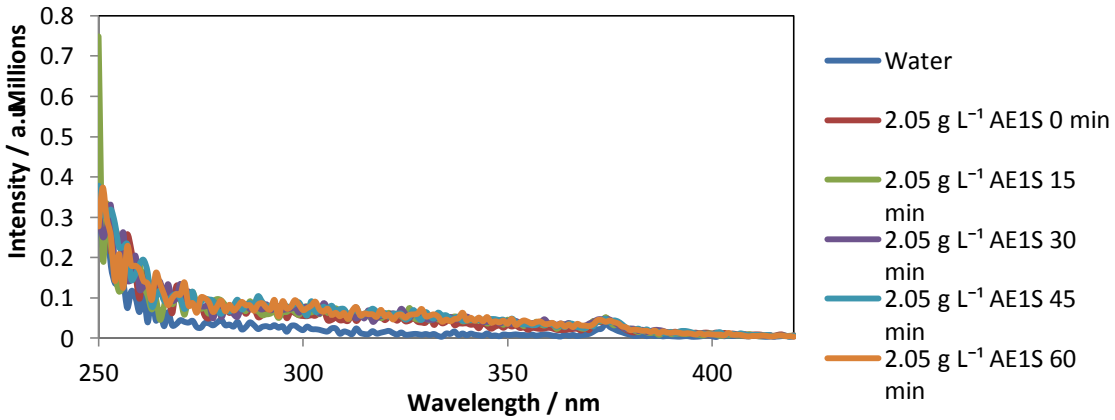

Figure 3-44: Fluorescence excitation spectra of 2.05 g L^{-1} AE1S solution at 0, 15, 30, 45, and 60 minutes after the addition of 0.2 g unbrightened polycotton

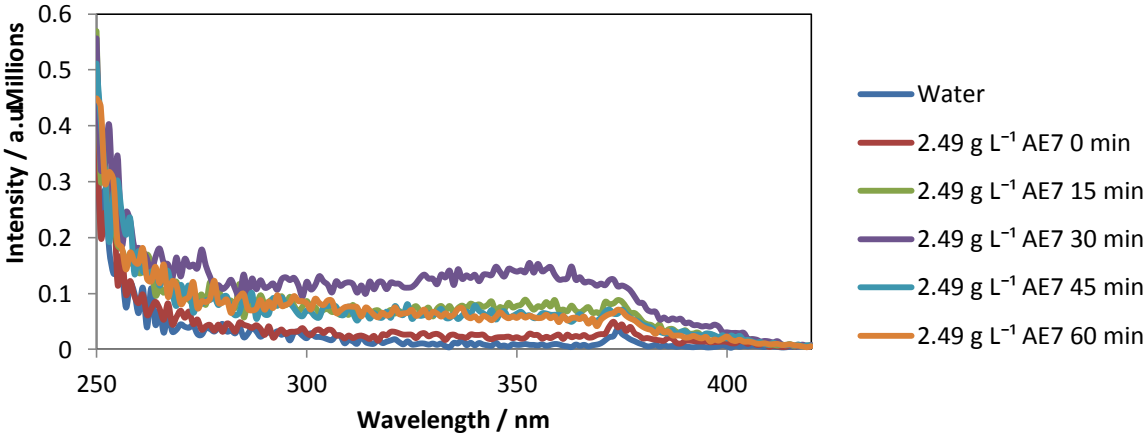

Figure 3-45: Fluorescence excitation spectra of 2.49 g L^{-1} AE7 solution at 0, 15, 30, 45, and 60 minutes after the addition of 0.2 g unbrightened polycotton

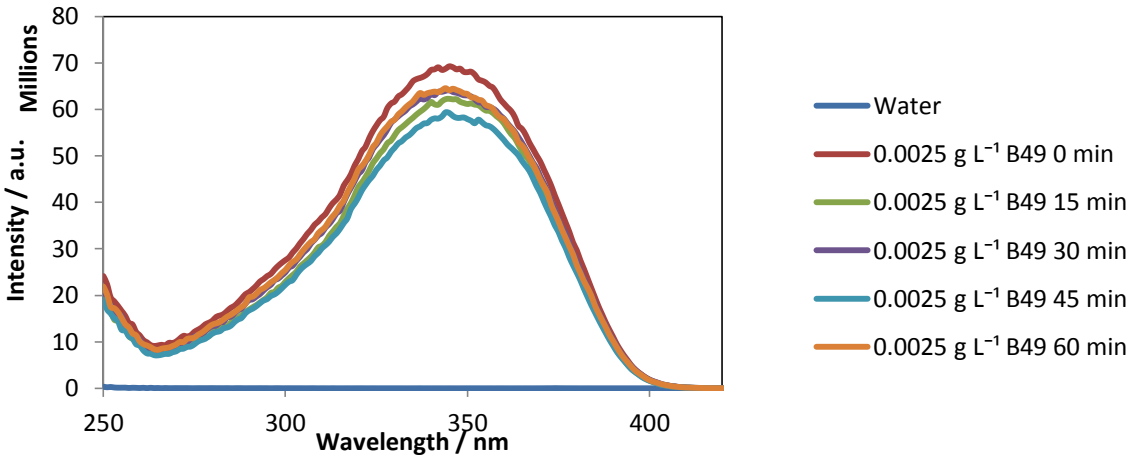

Figure 3-46: Fluorescence excitation solution of 0.0025 g L^{-1} Brightener 49 samples at 0, 15, 30, 45, and 60 minutes after the addition of 0.2 g unbrightened polycotton

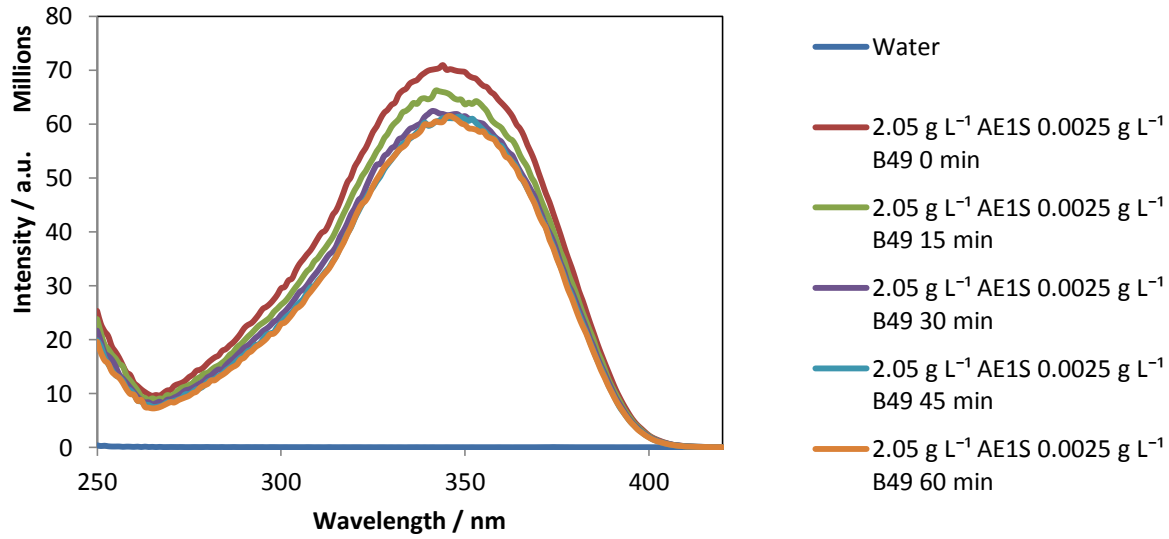

Figure 3-47: Fluorescence excitation solution of 2.05 g L^{-1} AE1S, 0.0025 g L^{-1} Brightener 49 samples at 0, 15, 30, 45, and 60 minutes after the addition of 0.2 g unbrightened polycotton

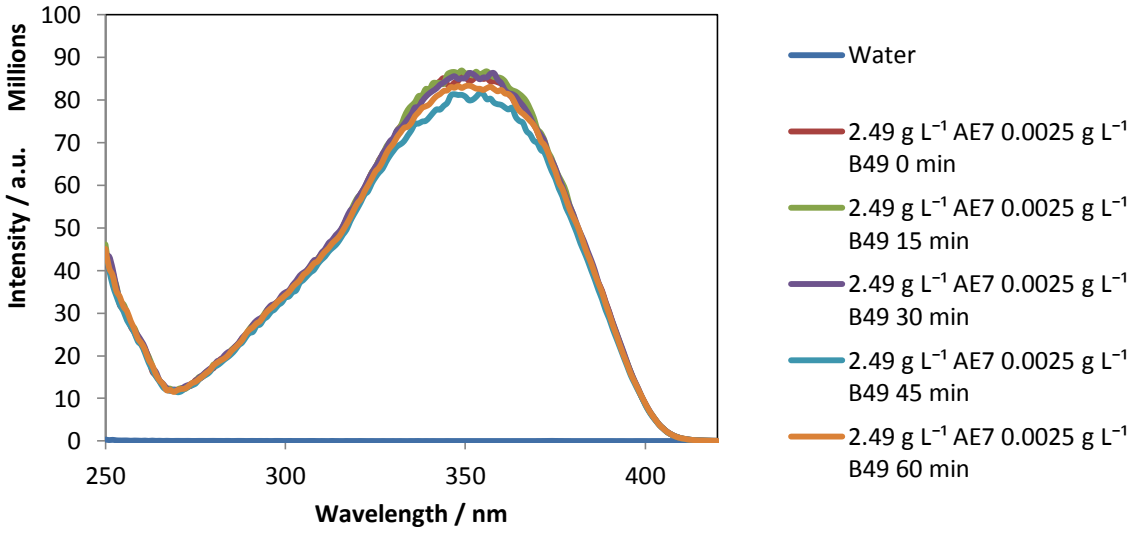

Figure 3-48: Fluorescence excitation solution of 2.49 g L^{-1} AE7, 0.0025 g L^{-1} Brightener 49 samples at 0, 15, 30, 45, and 60 minutes after the addition of 0.2 g unbrightened polycotton

The integrated fluorescence intensities (IFI) of these spectra are given in Table 3-12 below.

Table 3-12: Integrated fluorescence excitation intensities of spectra of solutions before and after addition of unbrightened polycotton

Time / min	Water IFI / millions	AE1S IFI / millions	AE7 IFI / millions	B49 IFI / millions	AE1S + B49 IFI / millions	AE7 + B49 IFI / millions
0	4.16	9.17	6.26	5320	5540	7160
15	7.69	9.54	12.8	4660	5120	7240
30	7.32	10.0	19.4	4920	4810	7220
45	7.76	10.6	12.2	4450	4640	6870
60	8.16	10.3	12.1	4940	4600	7080

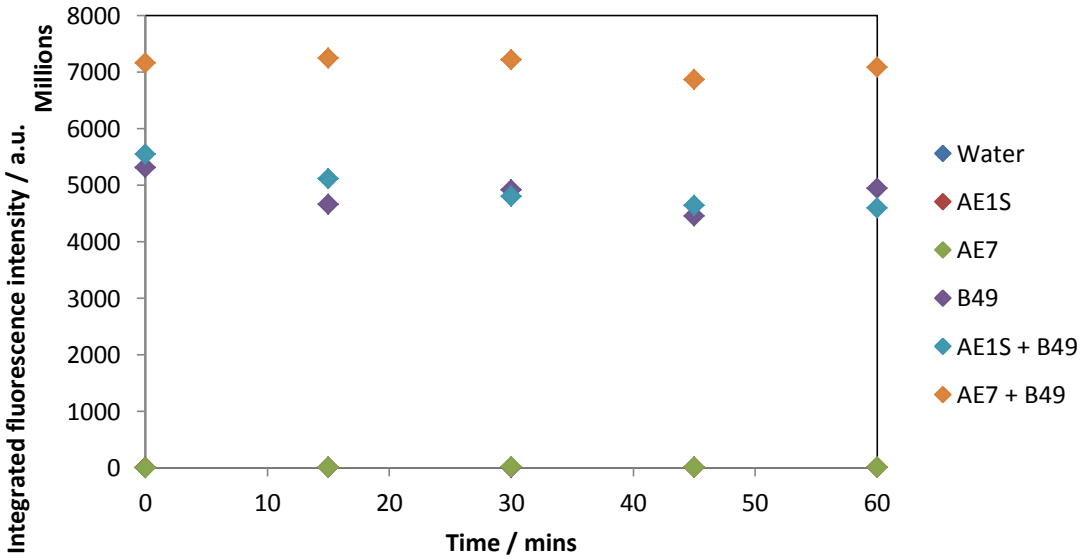

Figure 3-49: Integrated fluorescence excitation intensities of B49 solutions before and after addition of polycotton

3.2.2.2.2.3. Discussion and conclusions

The integrated fluorescence intensities at each time point are given in Table 3-13 as a percentage of the value at 0 minutes.

Table 3-13: Effect of length of washing on integrated fluorescence emission and excitation intensities for brightener solutions, with and without surfactants, before and after washing with polycotton fabric

Time / min	B49 emission IFI / %	B49 excitation IFI / %	AE1S + B49 emission IFI / %	AE1S + B49 excitation IFI / %	AE7 + B49 emission IFI / %	AE7 + B49 excitation IFI / %
0	100	100	100	100	100	100
15	90.0	87.7	90.8	92.3	101.8	101.2
30	92.3	92.5	90.4	86.7	103.1	100.8
45	88.8	83.7	84.6	83.7	98.7	95.9
60	93.9	93.0	86.4	82.9	102.5	98.9

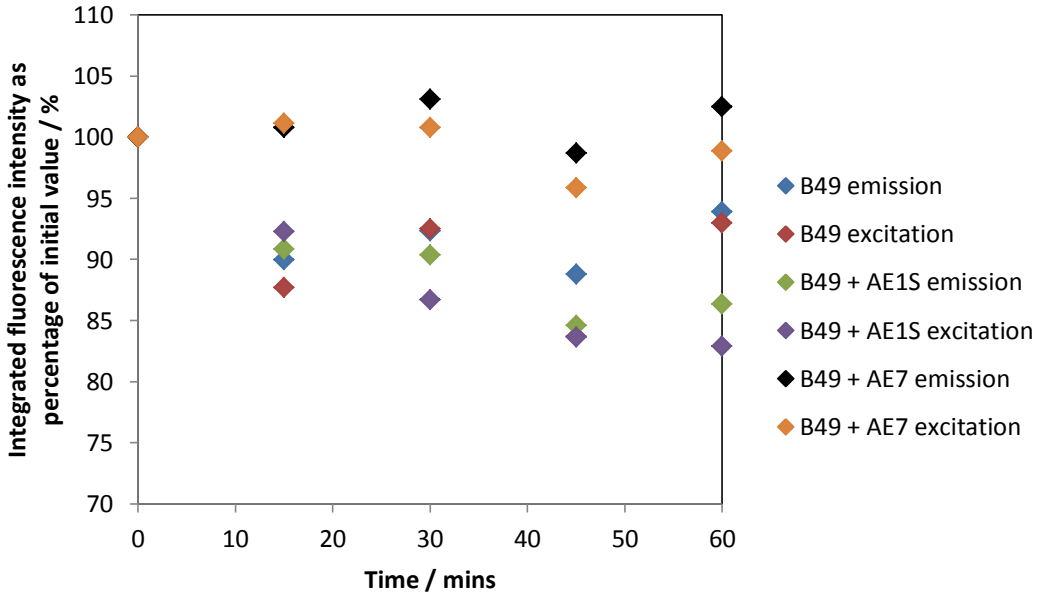

Figure 3-50: Effect of length of washing on integrated fluorescence emission and excitation intensities for brightener solutions, with and without surfactants, before and after addition of polycotton fabric

It can be seen that there was good agreement between the values obtained from the emission and the excitation spectra. However, there was a lot more scatter within these values than for the cotton samples, and the decrease in intensity was less severe.

The same trends seen in the cotton samples are seen here, however. The greatest change was seen in the samples containing Brightener 49 and AE1S, and little to no change was seen in the samples containing Brightener 49 and AE7.

The concentrations of brightener in each system were found using the method described in Section 3.2.2.2 previously, using the sample of brightener which had not had fabric

added as a control sample to calibrate the system. These concentrations are given in Table 3-14.

Table 3-14: Change in concentration of Brightener 49 after addition of polycotton fabric

Time / minutes	**Concentration of Brightener 49 remaining in solution / g L^{-1}**		
	B49	**B49 + AE1S**	**B49 + AE7**
0	0.00250	0.00250	0.00250
15	0.00208	0.00217	0.00254
30	0.00220	0.00207	0.00259
45	0.00199	0.00192	0.00239
60	0.00224	0.00194	0.00253

Again, the same trends were seen as for the integrated fluorescence intensities; the greatest decrease in concentration was seen in the B49 + AE1S solution, and no decrease was seen in the B49 + AE7 system. It is also notable that, unlike when cotton was used as the fabric, the Brightener 49 concentration of the brightener-only system plateaus after 15 minutes, and the concentration of brightener in the B49 + AE1S system plateaus after 45 minutes. It therefore appears that not only does the addition of AE1S increase the rate of deposition of the brightener, it also increases the amount of brightener that can be adsorbed onto the fabric.

3.2.2.2.3. Conclusions

There are two main findings of this section. Firstly, the brightener had a stronger affinity to the cotton fabric than to the polycotton fabric. This can be seen from the far more significant decreases in integrated fluorescence intensity over time for the solutions to which cotton had been added than for the solutions to which polycotton had been added; see Table 3-15. This is as expected, given the known affinity of stilbene-based brighteners for cotton fabrics and not for polyester and synthetic fibres.

Table 3-15: Percentage loss of integrated fluorescence intensity for each brightener system after 60 minutes

System	% loss of fluorescence intensity after 60 minutes washing cotton	% loss of fluorescence intensity after 60 minutes washing polycotton
B49	17.8	6.57
AE1S + B49	24.3	15.3
AE7 + B49	4.62	-0.703

The effect was most striking in the system containing Brightener 49 but no surfactant; the percentage of fluorescence lost after soaking cotton for 60 minutes was approximately 3 times that lost when polycotton is used. In the AE1S + B49 system, the change is less marked, with about 1.6 times more fluorescence lost when cotton was used than polycotton. However, the most surprising results are seen in the AE7 + B49 system, when using polycotton rather than cotton caused the fluorescence to increase slightly after 60 minutes. This particular effect is likely to be an effect of the fluctuation between samples as seen in Table 3-13, and not a significant, sustained change. It does not appear that any brightener was deposited from this solution.

Secondly, the addition of AE1S appeared to aid brightener deposition, whereas the addition of AE7 appeared to inhibit the deposition process. The decrease in integrated fluorescence intensity in AE1S + B49 solution was about 1.4 times that of B49 solution alone if cotton was added, and 2.3 times that of B49 solution if polycotton was added, whereas the decrease in integrated fluorescence intensity in AE7 + B49 solution was ¼ that seen in B49 solution if cotton was used, and no decrease was seen if polycotton was used, suggesting that the deposition process was entirely supressed.

This may be due to the physical interaction between the surfactant and the brightener; the closer to the surface of the micelle that the brightener was, the less easily it could detach and be deposited onto the fabric. As AE7 has a particularly long head group, this may have provided a larger area for the brightener to be held and thus strengthened the brightener-micelle interaction, reducing the probability that the brightener would detach. Further evidence for this theory will be given in Chapter 5 and Chapter 6, where the results seen via SAXS data and molecular dynamics simulations will be discussed.

It is also possible that the surfactant-fabric interactions may have had an effect on the deposition process; hydrogen bonding between the SO_3^- group on the AE1S micelle and the hydroxyl groups on the cellulose fibres may have carried any brightener-loaded AE1S micelles closer to the fabric surface, allowing the brightener to be deposited more easily. This is evidenced by the increase in brightener deposition with the addition of AE1S. For both the cotton and the polycotton fabric, the integrated fluorescence intensity of the AE1S + Brightener 49 solution was approximately 90% that of the Brightener 49 solution post-fabric soaking.

To determine whether the attraction of AE1S micelles to the cellulose fibres is a contributing factor in this system, future work could repeat this study at a large number of concentrations of AE1S, to determine the effect of AE1S concentration on the degree of deposition of the brightener. Repeating the study at a large number of AE7 concentrations would also determine the effect that these micelles are having; it would be seen whether the decrease in brightener deposition would plateau or continue with increasing AE7 concentration.

Future work could also repeat this experiment using a highly hydrophobic fabric such as polyester, AE1S micelles, and a brightener suitable for use with polyesters, i.e. a coumarin-based brightener rather than a stilbene-based brightener. In this case, the fibre-SO_3^- interaction would not be present, although the increased hydrophobicity of the coumarin brightener may affect its solubilisation in the micelle, causing it to be held further within the core of the micelle, and reducing its ability to detach from the micelle.

3.3. Conclusions

3.3.1. Effectiveness of methods to determine brightener deposition

Two methods of determining the deposition of the brightener were tested. The first method used the fluorescence spectra of the fabric with deposited brightener. Although a correlation was seen between the concentration of the sample used and the intensity of the fluorescence, the errors on the readings were large. This may have been due to the inhomogeneity of the deposition of the brightener across the fabric surface.

The second method used the integrated fluorescence intensities of brightener solutions. A strong correlation was seen between the concentration of Brightener 49 in the solution and the integrated fluorescence intensities of the emission and excitation spectra, allowing the effect of brightener concentration on the fluorescence intensity to be modelled using a second-order polynomial. The parameters of this polynomial were found for both the emission and excitation spectra. It was thus determined that this method was suitable for use to determine the amount of brightener deposited onto the fabric.

3.3.2. Effect of surfactant on fluorescence spectra of Brightener 49

When the anionic surfactant AE1S was added to the brightener, no change was seen in the fluorescence emission or excitation spectra. This shows that either the brightener is not being incorporated into the micelle, or that the brightener is incorporated into the micelle, but without any change in the hydrogen bonding on the brightener molecule, i.e. that the brightener molecule is still in contact with a large number of water molecules. This would correspond to the brightener being incorporated into the micelle/solvent boundary of the micelle.

When the nonionic surfactant AE7 was added to the brightener, a dramatic hypsochromic shift and increase in peak structure and height was seen in the fluorescence emission spectrum of the brightener. This shift occured in the region of the CMC of the AE7, showing that this was due to the incorporation of the brightener into the micelles, into a region where the brightener experienced less hydrogen bonding from the water molecules, i.e. the long-chain head groups of the surfactant micelle.

The integrated fluorescence intensity of the emission spectra did not change with changing surfactant concentration, showing that this was not dependent on surfactant concentration, but purely due to brightener concentration. The integrated fluorescence intensity of the excitation spectra did not change with changing AE1S concentration; however, it was affected by changing AE7 concentration, due to the increase in peak height at the wavelength studied. However, as this change was associated with the CMC of the surfactant, this change plateaued at a concentration of 0.50 g L^{-1} AE7; therefore, at significantly higher concentrations of AE7, the integrated fluorescence excitation intensity was dependent only on the brightener concentration.

3.3.3. Effect of fabric selection on brightener deposition

A far greater degree of brightener deposition was seen when cotton fabric was used, compared to the polycotton fabric, as given by the decrease in integrated fluorescence intensity. This was to be expected, given the affinity of the brightener with the cellulose in the cotton fibres, and its lack of affinity with the hydrophobic polyester fibres. This trend was still seen when surfactant was added; when AE7 was added, no significant change in the fluorescence of the solutions was seen after 60 minutes washing with polycotton samples, suggesting that the brightener deposition was virtually entirely inhibited.

3.3.4. Effect of surfactant on brightener deposition

It was seen that the addition of surfactants had a clear and visible effect on the deposition of the optical brightener. Addition of AE1S caused a significant increase in the amount of fluorescence lost, and thus the amount of brightener deposited, for both fabrics used. This was theorised to be due to hydrogen bonding interactions between the hydroxyl groups on the cellulose and the sulfate groups on the AE1S micelle drawing any micelle-brightener aggregate closer towards the fabric surface, increasing the efficiency of the brightener transfer onto the fabric.

The addition of AE7 surfactant caused little loss in fluorescence and hence little loss of brightener, in the brightener solution in which cotton fabric was added. In the system in which polycotton was added, brightener deposition was nearly entirely inhibited. This is potentially due to the position of the brightener within the AE7 micelle. The outer shell of the AE7 micelle consisted of long chains of ethoxylate groups. The evidence from Section 3.2.2.1.2.1 (emission spectra of brightener in surfactant solutions) showed that the brightener molecules were being held in an environment with less hydrogen bonding than the initial solvent, i.e. water. As the brightener is being held within this region, steric factors may have increased the energy required to release the brightener from the micelle. It will be seen in Chapter 5 that the outer shell region of the AE7 micelle is thicker than for the other surfactant micelles, and in Chapter 6 that the brightener is held deeply within this region. This will build up a picture of the brightener molecules being trapped within the outer shell of this micelle.

4. Crystallisation

4.1. Introduction

In this chapter, the crystallisation of both the brighteners themselves, and the calcium carbonate present in hard water, was examined. In the case of the brighteners, this was to characterise their crystal structures, which were not known, whereas in the case of the calcium carbonate, this was to determine the effects of the surfactants found in the detergent system on the rate of calcium carbonate crystallisation, and on the polymorph produced.

4.1.1. Theoretical background

4.1.1.1. Crystals and crystal structure

"[Cold] is responsible for creating rock-crystal, for this is hardened by excessively intense freezing. At any rate, it is found only in places where the winter snows freeze most thoroughly; and that it is a kind of ice is certain: the Greeks have named it accordingly."

Pliny the Elder, *The Natural History*, Book 37, chapter 9[133]

4.1.1.1.1. The unit cell and Miller indices

The term "crystal" comes from the Greek word *krustallos,* meaning *ice*. In the ancient world, this term was also used to refer to clear quartz, or rock crystal, SiO_2. As illustrated above, it was given this name not just due to its appearance, but due to the belief that this crystal was formed from ice itself. (Pliny notes in 77-79 AD that quartz crystal, as a form of ice, is highly susceptible to melting and thus can only be used "as a receptacle for cold drinks"[133]; as the melting point of quartz is approximately 1840 °C,[134] perhaps few ancient writers had tested this hypothesis.)

Crystals are solids made up of monomers, arranged in unit cells which are repeated throughout the solid. They can be distinguished by their cell parameters, and by their lattice planes.

Broadly speaking, crystals can be separated into 7 crystal systems depending on their cell parameters. These parameters are the length of the three axes *a*, *b*, and *c*, and their corresponding angles α, β, and γ. These crystal systems can then be further subdivided

into 230 space groups, depending on their specific symmetry. The 7 crystal systems are shown in Table 4-1 below.

Table 4-1: The seven crystal systems and their axial parameters

Crystal system	**Axial parameters**
Cubic	$a = b = c$, $\alpha, \beta, \gamma = 90°$
Tetragonal	$a = b \neq c$, $\alpha, \beta, \gamma = 90°$
Orthorhombic	$a \neq b \neq c$, $\alpha, \beta, \gamma = 90°$
Monoclinic	$a \neq b \neq c$, $\alpha, \gamma = 90°$, $\beta \neq 90°$
Triclinic	$a \neq b \neq c$, $\alpha, \beta, \gamma \neq 90°$
Trigonal	$a = b = c$, $\alpha, \beta, \gamma \neq 90°$
Hexagonal	$a = b \neq c$, $\alpha, \beta = 90°$, $\gamma = 120°$

Each unit cell will have a characteristic set of lattice planes associated with it. These lattice planes can be described using Miller indices, written (*hkl*). These give the distances and angle at which the lattice plane intersects the unit cell.

4.1.1.1.2. Polymorphism

Many compounds can exist in multiple crystal forms, known as polymorphs. Typically, one form will be the most stable, whereas the remaining polymorphs will be metastable. If an element has different crystal structures, these are known as allotropes. The most famous example of this phenomenon is carbon, which can exist as three main polymorphs: diamond, graphene or graphite, and buckminsterfullerene, C_{60}.

The Ritonavir case clearly illustrated the importance of understanding polymorphism. This drug, marketed as Norvir, was developed in 1996 to treat HIV infection. At the time of its discovery, only one crystalline form was known, with low bioavailability; as a result, the drug was dispensed as a solution in capsules. However, in 1998, batches of these capsules were found to contain a previously unknown, less soluble polymorph of the drug, which had crystallised out. The drug was removed from the market and reformulated, at huge cost to the manufacturer; three additional polymorphs were later discovered.[135] This case illustrates the importance of polymorph screening, and of determining the most stable polymorph of compounds.

4.1.1.2. Crystal formation & growth

4.1.1.2.1. Classical nucleation theory (CNT)

The Helmholtz free energy of formation of a crystal nucleus, ΔF, from a solution can be defined as shown in Equation 4-1:[136]

$$\Delta F = -n\Delta\mu + \gamma A$$

Equation 4-1

In this equation, n is the number of monomers in the growing nucleus, γ is the interfacial tension between the nucleus and the solution, A is the surface area of the nucleus, and $\Delta\mu$ is the supersaturation, which is the driving force for the crystallisation as it is the difference between the chemical potentials of the solute in the bulk solution and crystal phases.

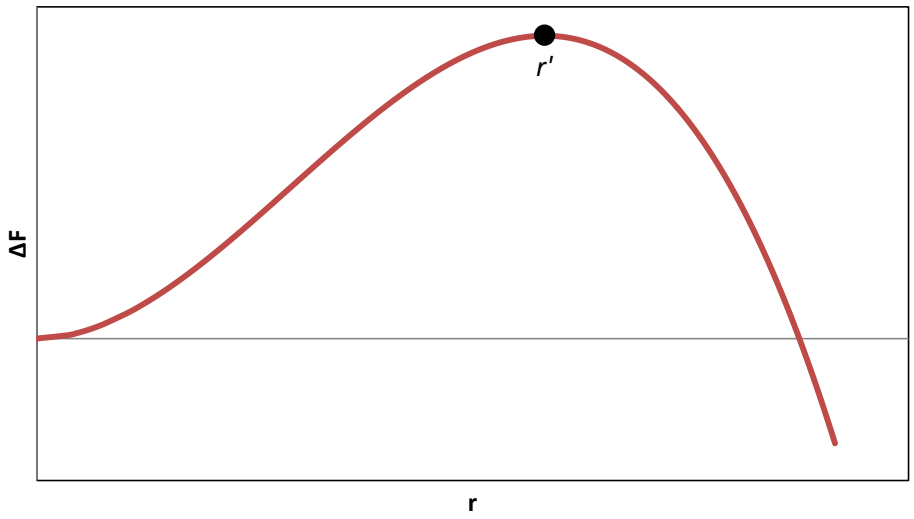

Figure 4-1: The effect of nuclear radius, *r* on *ΔF*, and the position of the critical nucleus, *r'*

Figure 4-1 shows the effect of the radius on ΔF. Initially, increasing the radius of the nucleus will increase ΔF, showing that this process is unfavourable. This is illustrated by finding the derivative of Equation 4-1 with respect to the radius r (after first substituting n and A for their equivalent in terms of r, assuming that each monomer has a volume of V_{mol}):

$$\Delta F = -\frac{4\pi r^3}{3V_{mol}}\Delta\mu + 4\pi r^2\gamma$$

Equation 4-2

$$\frac{\partial \Delta F}{\partial r} = -\frac{4\pi r^2 \Delta \mu}{V_{mol}} + 8\pi\gamma r$$

Equation 4-3

From Equation 4-3, the radius of the critical nucleus, *r'*, can be found:

$$r' = \frac{2\gamma V_{mol}}{\Delta \mu}$$

Equation 4-4

Once the nucleus has grown past the critical nucleus radius, an increase in radius will decrease *ΔF*, and thus further growth of the crystal will be thermodynamically favourable. The nucleus will therefore tend to grow more freely until the supersaturation is relieved.

4.1.1.2.2. Ostwald's rule of stages

Ostwald's rule of stages allows the polymorph produced when a compound is crystallised to be predicted. This rule states that, when a compound is crystallised, the least stable polymorph will be crystallised first. This will then form the most stable polymorph often through solvent-mediated phase transformations, where the metastable polymorph will gradually redissolve and its monomers instead join to a burgeoning nucleus of the stable polymorph. The rate of this polymorph transformation is system dependent and may be immeasurably slow so that the stable form never appears.

The cause of Ostwald's rule can be attributed to kinetic factors associated with the formation of critical nuclei; the metastable polymorphs will often form critical nuclei at lower radii than the stable nuclei, and will thus have to combat a lower energy barrier to form these nuclei. Therefore, the metastable nuclei will form more quickly, and it will be these that grow first.

Although Ostwald's rule of stages is commonly seen, it is not a universal law. It has been noted that the term Ostwald uses to refer to this rule, "*Satz*", can be used to describe statements of any degree of certainty, and thus need not be describing a rigid and universally applicable law.[137]

4.1.1.2.3. Thermodynamic control of crystal growth

Ostwald's rule of stages occurs because the nucleation process is under kinetic control, causing the least stable nuclei, which have the lowest energy barriers to their formation, to crystallise out directly. However, it is possible to bring the system under

thermodynamic control, causing the most stable nuclei to crystallise out in the first instance.[136] This can be achieved by placing the system into 3D-nanoconfinement, which can be done by carrying out the crystallisation within the droplets of a microemulsion.[136]

A microemulsion is a thermodynamically stable colloid, made up of droplets of one phase, aka the dispersed phase, stabilised by a surfactant, surrounded by a continuous phase. In this instance, the dispersed phase would consist of a monomer solution in a polar solvent, such as water, and the continuous phase of an oil such as hexane or heptane. Each droplet contains a finite number of monomers; therefore, as the crystal nucleus grows within the droplet, the supersaturation of the solution is rapidly depleted.

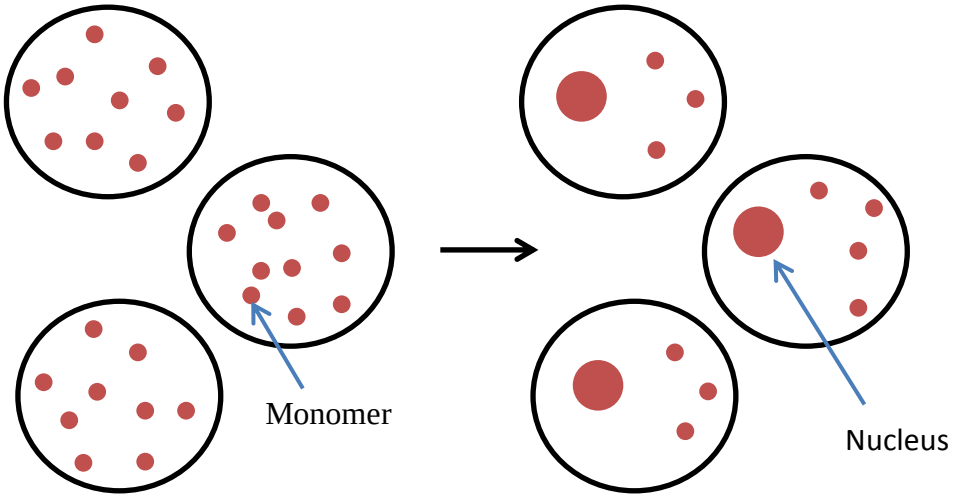

Figure 4-2: Depletion of supersaturation in a microemulsion

Equation 4-1 must therefore be adapted to correct for this decrease in the supersaturation of the solution; the adapted equation is given in Equation 4-5:[136]

$$\Delta F = -n\Delta\mu + \gamma A + NkT\left\{\ln\left(1 - \frac{v}{Vv_c c_0}\right) - \frac{1}{v_c c_0}\ln\left(1 - \frac{v}{V}\right)\right\}$$

Equation 4-5

In this equation, N is the initial number of monomers in the droplet prior to crystallisation, n is the number of monomers in the nucleus as previously, V is the volume of the droplet, v is the volume of the nucleus, and v_c is the volume of the monomer unit.

The supersaturation at the given nucleus size, $\Delta\mu$, is given by:

$$\Delta\mu = kT \ln\left(\frac{c}{c_{sat}}\right)$$

Equation 4-6

In Equation 4-6, *k* is the Boltzmann constant, *T* is the temperature of the solution, c_{sat} is the concentration of the solution at its saturation limit, and *c* is the concentration of the solution such that:

$$c = \frac{N-n}{V-v} = \frac{Vc_0}{V-v}\left(1 - \frac{v}{Vv_c c_0}\right)$$

Equation 4-7

Initially, nucleus formation proceeds as in the bulk solution, with the formation of a critical nucleus and subsequent growth. However, as the supersaturation is depleted, the rate of change in *ΔF*, the 'driving force' of the crystallisation process, is reduced. Eventually, *ΔF* reaches a minimum, r^*_{min}, termed the postcritical nuclear radius. The more stable a polymorph is, the less soluble it is, and thus the greater the supersaturation. Therefore, the postcritical nuclei of these more stable polymorphs will be formed at a larger radius and lower *ΔF*. This is shown in Figure 4-3 below.

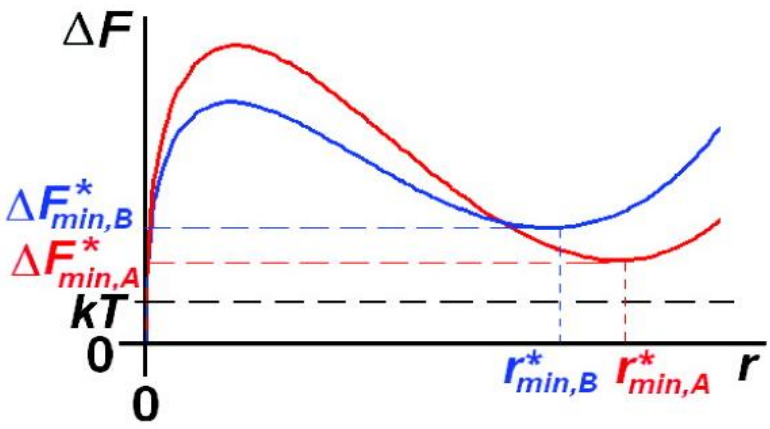

Figure 4-3: Effect of changing *r* on *ΔF* in conditions of 3D-nanoconfinement for a stable polymorph, *A* (shown in red) and a metastable polymorph, *B* (shown in blue). Adapted with permission from ([136]). Copyright 2011 American Chemical Society

If, at the postcritical nucleus minimum, *ΔF* < *kT*, then a significant number of these postcritical nuclei will be formed and persist, and thus these nuclei will grow into crystals. By tailoring the concentration of the solution in the droplets, and thus the supersaturation, it is possible to create a system where only the most stable polymorph has *ΔF*<*kT*, and thus only nuclei of the most stable polymorph will be formed in large

numbers. This occurs at the supersaturation at which the solute in the microemulsion droplets is just able to crystallise. This will result in the most stable polymorph being formed directly.

Once the postcritical nuclei have been formed, additional monomers can be transferred to the droplet through the formation of transient dimers when two droplets collide with sufficient energy. This will allow for further crystal growth until the radius of the crystal exceeds that of the droplet. In this case, the crystals are still likely to retain a layer of solution and surfactant, rather than be ejected into the continuous phase as bare crystals. This is because the bending of the surfactant to encase the larger crystals will most probably constitute a smaller energy penalty than the interfacial energy increase imposed by the crystal being in contact with the continuous phase. Note that further growth of the larger crystals can still occur by droplets impinging on the crystal and this will continue until the supersaturation is relieved. The crystals thus obtained are often of good quality due to their slow growth and can be used for single crystal X-ray crystallography to determine the polymorph obtained.

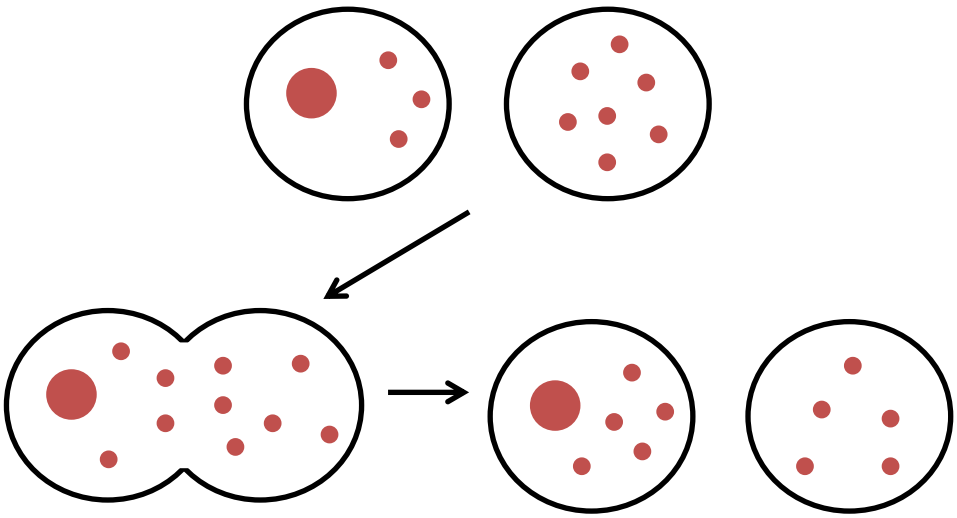

Figure 4-4: Formation of transient dimers and transfer of monomers

4.1.1.3. Techniques used to study crystals

4.1.1.3.1. Wide angle X-ray Scattering (WAXS)

In an X-ray scattering experiment, the crystal or material to be studied is placed in the path of an X-ray beam. When the X-rays hit the crystal, they will interact with its

electrons, causing scattering. This can be modelled as the X-rays being reflected by the lattice planes of the crystal, as shown in Figure 4-5.

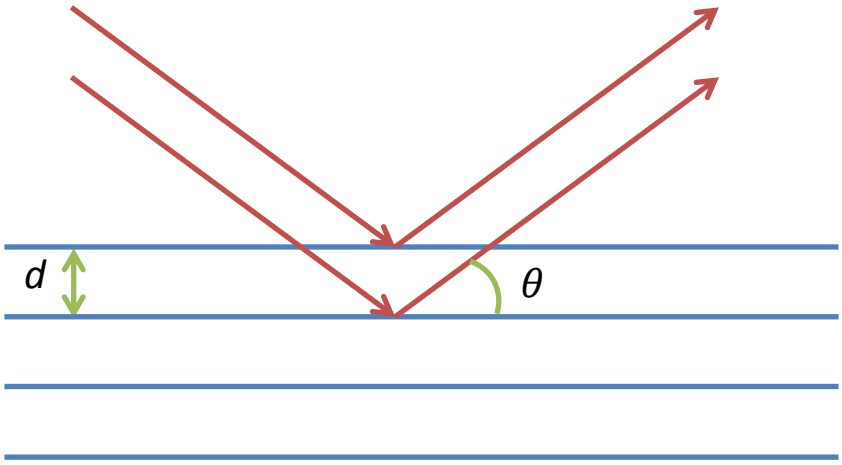

Figure 4-5: Scattering of X-rays by lattice planes in a crystal

In Figure 4-5, one photon strikes a lattice plane and is reflected, while another strikes a parallel lattice plane, at a distance *d* apart, and is reflected with the same angle, θ. The path length distance between the two beams will therefore be:

$$Path\ length\ difference = 2d \sin\theta$$

Equation 4-8

If the two photons are in phase, then constructive interference will occur; if they are out of phase, however, destructive interference will occur. Therefore, in order for a photon to be detected at an angle θ, the reflected photons must be in phase. Equation 4-8 can therefore be modified:

$$n\lambda = 2d \sin\theta$$

Equation 4-9

In this equation, *n* is an arbitrary integer (normally 1) and λ is the wavelength of the radiation.

In the WAXS experiment, the intensity of radiation at each scattering angle is detected. A series of peaks will be obtained; from the scattering angles of these peaks, the d-spacings, i.e. the distances between the lattice planes of the crystal, can be identified:

$$d = \frac{\lambda}{2 \sin \theta}$$

Equation 4-10

These d-spacings are characteristic to the crystal structure, and can be used to distinguish between polymorphs.

In this project, WAXS spectra were taken using a Bruker D8 WAXS machine. This uses an X-ray source operating at 40 kV and 35 mA, producing CuKα radiation with a wavelength of 1.54 Å.

4.1.1.3.2. Single-crystal X-ray crystallography

Single-crystal X-ray crystallography is used for cases when a large crystal (~0.1 mm) can be obtained. As for WAXS, the crystal is mounted and placed in the path of an X-ray beam and the scattering angles measured; however, much more structural information can be obtained from this method by varying the beam angle and detector angle. Note, though, that this technique is limited by its need for large, monocrystalline material.

In this project, single-crystal structures were provided by the departmental crystallography service.

4.1.1.3.3. Fourier-transform infrared spectroscopy (FTIR)

Infra-red (IR) spectroscopy, like fluorescence spectroscopy as described previously, relies on molecules absorbing photons. However, the mechanism by which this will happen is different.

The energy difference between the vibrational states of bonds in molecules corresponds to the energy of IR radiation. When an IR photon collides with the molecule, it may therefore be absorbed, causing the molecule to enter an excited vibrational state, increasing its bond vibration. Some vibrational modes for a linear molecule AX_2 are shown in Figure 4-6 overleaf.

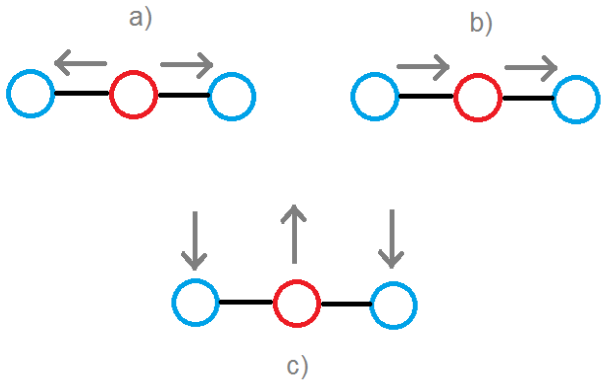

Figure 4-6: Some vibrational modes of a molecule AX_2

This figure shows two stretching modes – a symmetric stretch, a), and an antisymmetric stretch, b). The figure also shows a bending mode, c).

Vibrational modes are IR active, and can thus show peaks on an IR spectrum, if they change the dipole moment of the molecule. Assuming that atom X in Figure 4-6 is more electron-withdrawing than atom A (for example, in CO_2), then modes b) and c) will be IR-active (as the dipole of the molecule will shift), whereas modes a) and d) will be IR inactive (as there will be no overall change in the dipole of the molecule).

FTIR spectra were taken using a Nicolet Nexus FTIR spectrometer. This contains a mercury cadmium telluride (HgCdTe) IR detector, cooled using liquid nitrogen.

4.1.1.4. Calcium carbonate

Calcium carbonate is a common mineral, found in nature in a large number of rocks such as marble and limestone, and is a major component of the shells and eggshells of many species. It is known to commonly exist in four main forms: three crystalline polymorphs and one amorphous form, amorphous calcium carbonate (ACC). The three crystal forms are, in order of most stable to least stable, calcite, aragonite, and vaterite.

4.1.1.4.1. Characteristic data for $CaCO_3$ polymorphs

The crystal parameters of the three polymorphs of calcium carbonate are listed in Table 4-2 overleaf.

Table 4-2: Crystal data characteristic of the three crystal polymorphs of $CaCO_3$

Polymorph	**Crystal system**	**Space group**	***a* / Å**	***b* / Å**	***c* / Å**	**α / °**	**β / °**	**γ / °**
Calcite[138]	Trigonal	R-3c	4.9900	4.9900	17.0615	90	90	120
Aragonite[139]	Orthorhombic	Pmcn	4.9616	7.9705	5.7394	90	90	90
Vaterite[140]	Hexagonal	$P6_522$	7.2900	7.2900	25.3020	90	90	120

In this project, the polymorphs will be characterised using WAXS and FTIR. The characteristic peaks seen for these polymorphs using these techniques are given in Table 4-3 below and Table 4-4 overleaf.

Table 4-3: D-spacings and WAXS peaks seen for crystalline calcium carbonate polymorphs. As ACC is not crystalline, it will not show sharp scattering peaks when using WAXS.

Calcite[138]		Aragonite[139]		Vaterite[140]	
d-spacing / Å	**Intensity / % of maximum**	**d-spacing / Å**	**Intensity / % of maximum**	**d-spacing / Å**	**Intensity / % of maximum**
3.0357	100.00	3.3958	100.00	3.6450	56.83
2.4950	13.71	3.2735	56.97	3.3459	100.00
2.2848	20.16	2.7000	52.12	2.8245	11.03
2.0946	14.26	2.4841	28.68	2.7576	79.47
1.9125	19.67	2.4808	17.84	2.1044	61.25
1.8754	20.02	2.4110	15.29	1.8830	19.19
		2.3716	41.13	1.8251	49.98
		2.3422	28.75	1.6729	20.14
		2.3288	19.27	1.3096	11.26
		2.1896	13.75		
		2.1061	20.62		
		1.9772	71.44		
		1.8824	30.99		
		1.8767	18.95		
		1.8145	29.73		
		1.7419	31.05		
		1.7247	14.13		

Table 4-4: FTIR peaks seen for calcite polymorphs and ACC.[141]

Normal vibration	Calcite / cm^{-1}	Aragonite / cm^{-1}	Vaterite / cm^{-1}	ACC / cm^{-1}
ν_1	-	1083 - 1085	1089 - 1088	1067
ν_2	876 - 877	854	873 - 878	864
ν_{3a}	1420 – 1423	1488 – 1490	1487 – 1498	1490
ν_{3b}		1440 – 1442	1443 – 1445	1425
ν_{4a}	713	713 – 714	746 – 750	725
ν_{4b}		700	738 - 743	690

4.1.1.4.2. Calcium carbonate in nature

Bird eggshells consist almost entirely of calcite deposits, crystallising as the eggshell hardens. It has been shown that a large portion of this layer is reabsorbed by the growing bird embryo prior to hatching (approximately 5% for domestic chickens)[142]. In contrast, the shells of green sea turtles, *Chelonia mydas L.*, consist mainly of aragonite spherulites, with less than 5% calcite (although it appears that the calcite in these shells forms prior to the formation of aragonite spherulites)[143,144]. This appears to be due to the magnesium ions present acting as nuclei for aragonite crystal growth.[144] It has been shown that Mg^{2+} concentrations of less than 1% promoted growth of $CaCO_3$ crystals and supressed nucleation, but that concentrations above 1% inhibited crystal growth.[145]

Nacre, or mother-of-pearl, has a structure consisting of layers of 95% aragonite platelets, 5% natural polymers. This structure has a strength 3 times that of aragonite alone.[146] It is these layers that are deposited around a central impurity by oysters in order to form pearls.

In 2009, soil samples taken from the Mars Phoenix landing site were shown to contain approximately 3 – 5 % calcium carbonate by mass. It has been suggested that this was caused by either reactions between atmospheric CO_2 and either surface water or subsurface ice, which was later brought to the surface in the collision creating the Heimdall crater.[147] The polymorph of this calcium carbonate has not yet been identified.

4.1.1.4.3. Previous studies

Many studies have been carried out investigating the change in morphology of calcium carbonate crystals with the addition of surfactant. However, the majority of studies

carried out focus on the crystals produced after a certain period of aging, typically in the order of several hours, rather than examining the polymorph of the initial precipitate.

The most commonly used surfactant in these studies is sodium dodecyl sulfate (SDS). This surfactant has been found to adsorb onto the surface of growing $CaCO_3$ nuclei,[148] causing their growth rate to decrease (one study suggests by tenfold)[149]. Most studies agree that this favours the production of calcite in solution,[150–153] although some studies claim that vaterite[149] or a mixed aragonite/calcite material[154] was favoured instead. It has been suggested that this effect is due to the surfactant inhibiting vaterite production,[153] or by promoting the vaterite-calcite transition[152].

The effect of other surfactants on the polymorph produced has also been tested. LAS (for a configuration with an unbranched chain)[153,155] and the cationic surfactant dimethyl dioctadecyl ammonium bromide (DDAB)[156] were found to give vaterite, whereas the anionic surfactant sodium dodecylsulfonate (DDS)[155], cationic surfactant dodecyltrimethylammonium bromide (DTAB)[149] and anionic surfactant dioctyl sodium sulfosuccinate (Aerosol OT, or AOT)[150] have been found to give calcite.

While it is clear that the addition of surfactants can have an impact on the polymorph of calcium carbonate produced, it is not possible to predict which polymorph will be produced based solely on the charge carried on the surfactant. It has been suggested that the SO_3^- groups of SDS and DDS provide an enhanced surface for the nucleation of the (0 0 1) plane of calcite crystals, whereas LAS can improve the rate of vaterite production either due to its increased polarity, or the increased distance between its head groups increasing the spacing between the monomers in the calcium carbonate crystal.[153]

4.1.1.5. Surfactants used in this study

Due to the requirements for the formation of w/o microemulsions in order to try to crystallise the Brightener 49 and Brightener 15, the surfactants used elsewhere in the project could not be employed. Therefore, an alternative selection of surfactants was used for this application.

4.1.1.5.1. AOT

Dioctyl sodium sulfosuccinate, often referred to as Aerosol OT or AOT, is a branched anionic surfactant.

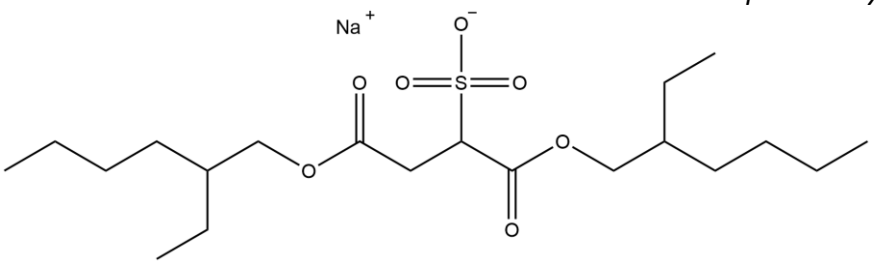

Figure 4-7: AOT

AOT has widespread use as a laxative, with the generic name Docusate and marketed under brand names such as DulcoEase and Peri-Colace. Although studies have been done to determine its efficacy in terminally-ill patients, where constipation is highly prevalent, results are inconclusive.[157]

4.1.1.5.2. Span 80

Span 80 is a nonionic surfactant with a highly polar head group, as shown in Figure 4-8. It can be used with Brij 30 as a cosurfactant.

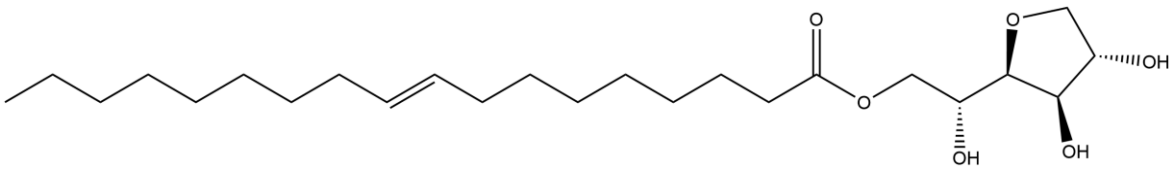

Figure 4-8: Span 80

4.1.1.5.3. Brij 30

Also known as Brij L4, Brij 30 is a nonionic surfactant used in this study as a cosurfactant for Span 80. Like AE7, it is an alcohol ethoxylate, although it only has 4 ethoxy groups per molecule, rather than 7 for the AE7. The structure of Brij 30 is shown in Figure 4-9 below.

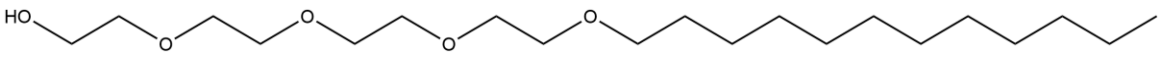

Figure 4-9: Brij 30

4.1.1.5.4. CTAC

Cetyl trimethyl ammonium chloride (CTAC) is a cationic surfactant. In this work, CTAC was used as an analogue for the cationic surfactant DEEDMAC used in fabric softening; as DEEDMAC is highly insoluble, solutions containing this surfactant are not optically clear, and thus the precipitation of $CaCO_3$ would be obscured, and the precipitate obtained would contain large amounts of DEEDMAC. The structure of CTAC is shown in Figure 4-10.

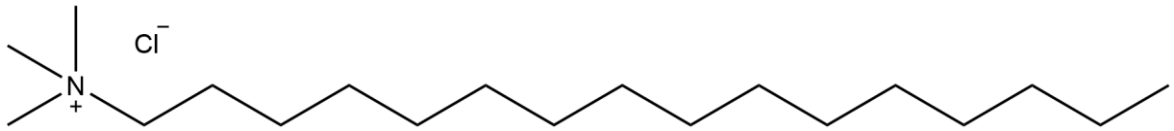

Figure 4-10: CTAC

4.1.2. Aims

This chapter had two aims. Firstly, to produce crystals of Brightener 49 and Brightener 15, and to characterise any crystals produced, and secondly, to identify the effect that the addition of surfactants had on the precipitation of $CaCO_3$, as this could occur in hard water systems during laundry washing.

4.2. Experimental

4.2.1. Crystallisation of brightener

In this section, the methods used to try to crystallise out the brightener, and the results of these experiments, will be detailed. Two methods were used: the vapour diffusion method, and the microemulsion method.

4.2.1.1. Experimental setup

4.2.1.1.1. Vapour diffusion experiments

In all methods of crystallisation used to grow single crystals, the aim is to control the supersaturation of the solution in order to slowly crystallise the product. The rate of crystallisation is kept low by using small supersaturations in order to ensure the addition of monomers to pre-existing nuclei, rather than forming new nuclei; the latter requires a larger energy barrier to be overcome and hence a larger supersaturation. Typical methods to increase the supersaturation include reducing the temperature of a saturated solution, and the slow addition of an antisolvent.

In the vapour diffusion method, the supersaturation of the solution is increased through the addition of an antisolvent. This is done by placing an open vial of a solution to be crystallised in a sealed vial of a miscible, volatile antisolvent, as shown in Figure 4-11.

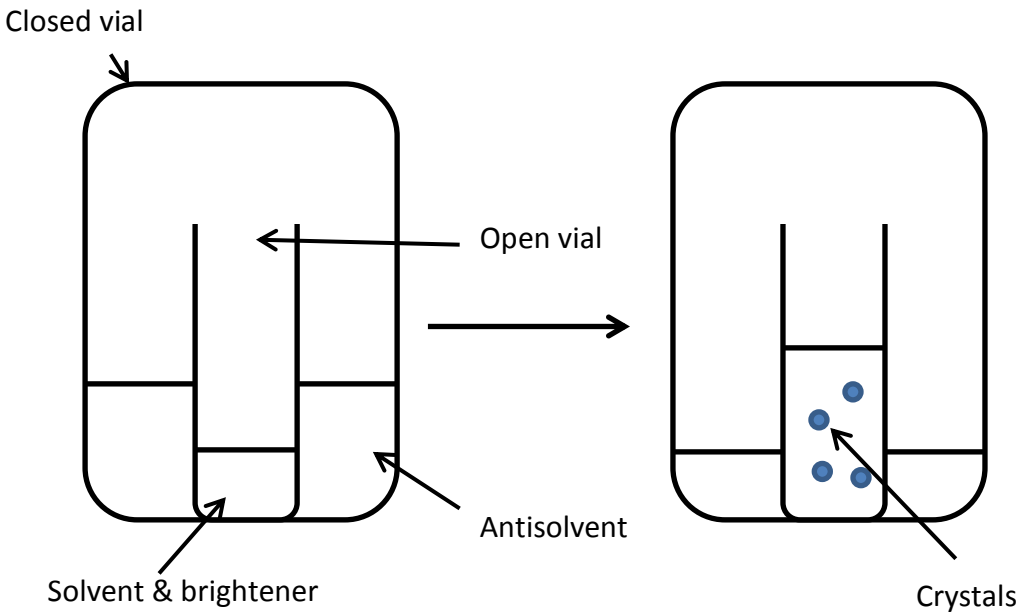

Figure 4-11: The process of vapour-diffusion crystallisation

The solvent and the antisolvent are kept separated by the glass walls of the open vial; however, the vapour of the antisolvent can still enter the inner vial, and vice versa. Depending on the relative volatility of the solvent and the antisolvent, either the solvent will evaporate from the inner vial and enter the antisolvent, or the antisolvent will enter the inner vial (as depicted in Figure 4-11.) In both scenarios, the supersaturation of the solution will be increased, causing the precipitation of the solute.

4.2.1.1.2. Crystallisation in microemulsions

For these experiments, microemulsions must be made. These consist of a non-polar continuous phase, typically a hydrocarbon such as hexane or heptane, containing droplets of a polar dispersed phase, consisting of either a solution of the monomer to be crystallised, or an antisolvent, stabilised by the addition of surfactant. These microemulsions are often referred to as water-in-oil or w/o microemulsions, although the polar solvent need not be water.

To produce the microemulsions used, a quantity of surfactant was weighed out and added to the continuous phase. This was agitated, either manually or through sonication as required, until all of the surfactant had dissolved. A known mass of this non-polar stock solution was then weighed out, into which a volume of the polar solution was added using a micropipette. This was then agitated, using a sonicator or a vortex mixer, until the

polar solvent had fully dispersed, at which point the microemulsion had formed and was optically clear.

To crystallise the brightener, two microemulsions were made up: one in which the dispersed phase was a solution of the brightener, and the other in which the dispersed phase was an antisolvent. These microemulsions were then mixed. This allowed the droplets to exchange material through the formation of transient dimers, increasing the supersaturation of the brightener solution and hopefully causing the brightener to crystallise.

4.3. Results

4.3.1. Vapour diffusion experiments

In order to set up the vapour diffusion experiments, suitable solvents and antisolvents needed to be found. Although both brightener molecules were soluble in water, this was unsuitable for use as a solvent in vapour diffusion experiments, as both brighteners were soluble in all solvents miscible with it.

Two solvents were used for the inner phase of the diffusion experiment: methanol and dimethyl sulfoxide (DMSO). These were used due to the solubility of both brighteners in these solvents, as given in Table 4-5. The solubilities of the solvents in water is also shown for comparison. Toluene was used as the antisolvent in both cases, as both brighteners were found to be insoluble in this solvent.

Table 4-5: Solubilities of brighteners in solvents used

Solvent	**Brightener**	**Solubility / g L^{-1}**
Water	Brightener 15 (literature)[158]	1.8
	Brightener 49 (literature)[159]	17.6
Methanol	Brightener 15	3.3
	Brightener 49	8.3
DMSO	Brightener 15	5

Table 4-6 gives the combinations of inner and outer phases tested, along with their results. All samples were refrigerated for 1 month.

Table 4-6: Combinations of inner and outer phases used for vapour diffusion experiments

Inner phase	Outer phase	Result
0.0101 g B49 1.30 mL MeOH	1 mL toluene	Thin, white 'needles' crystallised (1 month)
0.01 g B15 1 mL DMSO	1 mL toluene	No crystals (1 month) Outer vial empty
0.001g B15 300 µL MeOH	1mL toluene	No crystals Inner vial empty

The crystals obtained from the Brightener 49 experiments were submitted for X-ray crystallography. The results obtained are shown in Figure 4-12 to Figure 4-15 and Table 4-7. As no crystals could be obtained from the systems containing Brightener 15, no crystallographic data was obtained for these.

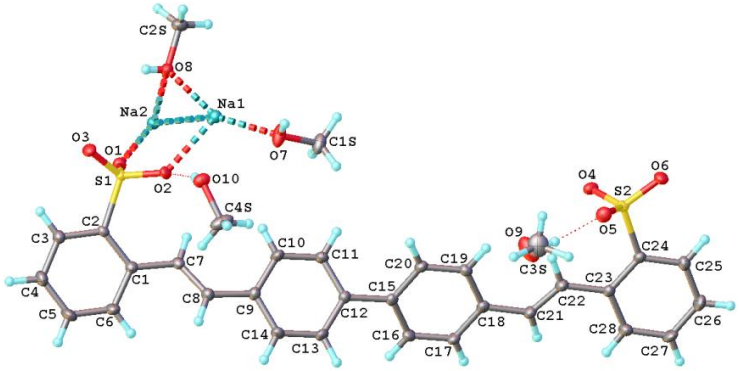

Figure 4-12: Crystal structure of Brightener 49 methanol solvate (single molecule). Carbon atoms are grey, hydrogen atoms are white, sulfur atoms are yellow, oxygen atoms are red, and sodium atoms are cyan.

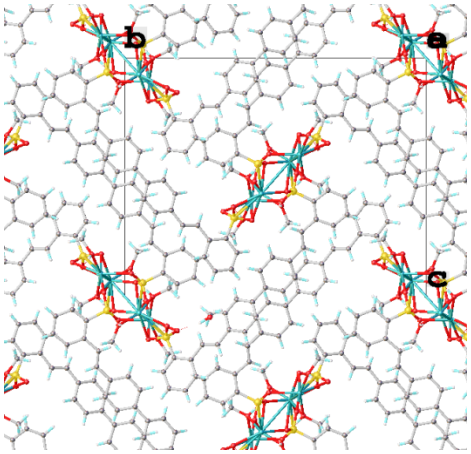

Figure 4-13: Crystal structure of Brightener 49 methanol solvate, showing (1 0 0) plane. The unit cell origin, *o* (top right corner), and vectors, *b* and *c,* are labelled. Carbon atoms are grey, hydrogen atoms are white, sulfur atoms are yellow, oxygen atoms are red, and sodium atoms are cyan.

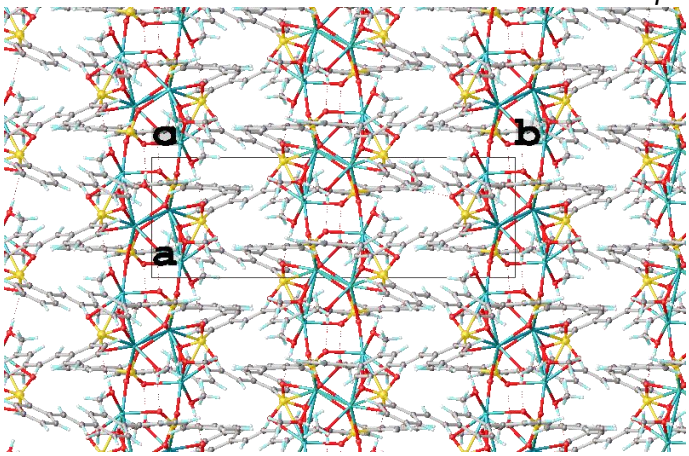

Figure 4-14: Crystal structure of Brightener 49 methanol solvate, showing (0 0 1) plane. The unit cell origin, *o* (top left corner), and vectors, *a* and *b*, are labelled. Carbon atoms are grey, hydrogen atoms are white, sulfur atoms are yellow, oxygen atoms are red, and sodium atoms are cyan.

Table 4-7: Crystal data for Brightener 49 methanol solvate

Empirical formula	$[C_{28}H_{20}O_6S_2]^{2-} \cdot 2Na^+ \cdot 4CH_3OH$
Formula weight	690.71
Temperature/K	120.0
Crystal system	monoclinic
Space group	$P2_1/n$
a/Å	7.7472(4)
b/Å	23.2491(13)
c/Å	18.6186(10)
α/°	90.00
β/°	98.5411(18)
γ/°	90.00

It can be seen in Table 4-7 that the empirical formula of this compound is $[C_{28}H_{20}O_6S_2]^{2-} \cdot 2Na^+ \cdot 4CH_3OH$; for each brightener molecule, four methanol molecules were incorporated (i.e. two per sulfate ion).

In this structure, the hydrocarbon backbones of the brightener have formed flat layers, and the polar groups (sulfate ions and methanol) have attached as ligands to the sodium ions to form columns running between the layers, connecting them. These columns are built up of subunits of Na^+ ions, with the sulfate ions and methanol acting as ligands. This can be seen in more detail in Figure 4-15.

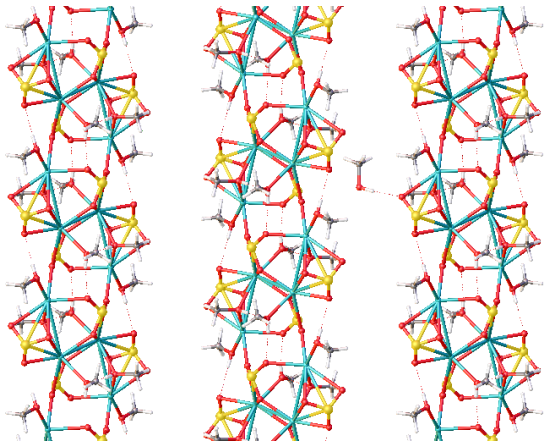

Figure 4-15: The columns from the Brightener 49 methanol solvate crystal. Carbon atoms are grey, hydrogen atoms are white, sulfur atoms are yellow, oxygen atoms are red, and sodium atoms are cyan. The hydrocarbon backbone of the brightener has been removed for clarity

The full data set generated from this crystal, including atom positions, bond lengths and angles, is included in Appendix 2.

One interesting aspect of the structure, as seen in Figure 4-12, is the configuration of the sulfate groups. In the structure seen, the molecule has rotated around its central C-C bond, to give the sulfate groups in the cis-position. In the MD simulation work shown in Chapter 6, the same trend was seen with the brightener molecules, with the hydrocarbon backbone interacting with the surfactant tail groups and the sulfate groups oriented outwards. This crystal data confirms that this is seen in experiments, as well as simulations.

The structures given show several sulfate-ion bonds per sulfate group, superimposed in the image given. This may show that there are occupancy factors of less than 1 for each sodium ion, methanol, sulfate group, or all three. This would show variation in the positions of these subunits throughout the crystal. This was not seen in the hydrocarbon backbone of the brightener, showing that these are held in more ordered positions.

This structure may be representative of the crystal structures generated during industrial production of Brightener 49. However, one limitation of these results is that methanol is not used as a solvent for domestic cleaning, and therefore this structure would not represent how Brightener 49 would crystallise on fabric in the wash. Ideally, a crystal without solvate, or a hydrate, would be obtained to demonstrate this. Due to the immiscibility of water with the available antisolvents, it was not possible to repeat the vapour diffusion experiment using water as the solvent. Evaporation and cooling methods

were used with solutions of Brightener 49 to obtain these crystals, but no crystals were produced.

4.3.2. Crystallisation in microemulsions

In order to obtain crystals suitable for WAXS studies or X-ray crystallography, microemulsions were used to try to obtain crystals of the brightener molecules. Studies were carried out on both brightener molecules. The process of crystallisation through microemulsions was used, as detailed previously.

4.3.2.1. Individual microemulsions

Samples of microemulsions containing supersaturated Brightener 49 as the dispersed phase were made up and left to precipitate. The supersaturated solution was made up by warming Brightener 49 solution to increase its solubility, and kept at a high temperature until it was added to the continuous phase and allowed to return to room temperature. This ensured that no precipitation would occur while the brightener was in the bulk solution. The samples made are shown in Table 4-8.

Table 4-8: Individual microemulsions

Continuous phase	**Dispersed phase**	**Volume of dispersed phase added / µL g^{-1}**
227 g L^{-1} Span 80, 227 g L^{-1} Brij 30, in heptane	100 g L^{-1} B49 in water	20, 40, 60, 80, 100
227 g L^{-1} Span 80, 227 g L^{-1} Brij 30, in heptane	33.3 g L^{-1} B49 in water	20, 40, 60, 80, 100
227 g L^{-1} Span 80, 227 g L^{-1} Brij 30, in heptane	16.7 g L^{-1} B49 in water	20, 40, 60, 80, 100

None of the samples tested produced any crystals; this may have been because the supersaturation of the brightener solution, while high enough to cause precipitation in the bulk, was too low to allow postcritical nuclei to form. For this reason, mixed microemulsions were created from one microemulsion containing droplets of brightener solution, and another containing droplets of an antisolvent. When mixed, the antisolvent should be transferred to the droplets of brightener solution through the formation of transient dimers, raising their supersaturation and allowing postcritical nuclei to form.

4.3.2.2. Mixed microemulsions

Mixed microemulsions were made up as described previously; the continuous and dispersed phases used are detailed in Table 4-9 below. These were then left in conditions of low light for several weeks to prevent the cis-trans interconversion of the brightener.

Table 4-9: Mixed microemulsion systems used.

System	Microemulsion 1		Microemulsion 2		Volume of dispersed phase added / µL g^{-1}
	Continuous phase	Dispersed phase	Continuous phase	Dispersed phase	
1A	1 g AOT stock	5 g L^{-1} B15 in DMSO	1 g AOT stock	Water	20, 30, 40, 50, 60, 70, [80 – did not settle]
1B	1 g AOT stock	3.75 g L^{-1} B15 in DMSO	1 g AOT stock	Water	20, 30, 40, 50, 60, 70
1C	1 g AOT stock	2.5 g L^{-1} B15 in DMSO	1 g AOT stock	Water	30, 40, 50, 60, 70, 80
1D	1 g AOT stock	1.25 g L^{-1} B15 in DMSO	1 g AOT stock	Water	20, 30, 40, 50, 60, 70
2	1g Span Brij stock	5 g L^{-1} B15 in DMSO	1g Span Brij stock	Water	40, 50, 60, 70, 80, 90 (All clouded on mixing)
3A	3g Span Brij stock	5 g L^{-1} B15 in DMSO	1g Span Brij stock	Water	10, 15, 20, 25, 30, 35
3B	3g Span Brij stock	3.75 g L^{-1} B15 in DMSO	1g Span Brij stock	Water	10, 15, 20, 25, 30, 35
3C	3g Span Brij stock	2.5 g L^{-1} B15 in DMSO	1g Span Brij stock	Water	10, 15, 20, 25, 30, 35
3D	3g Span Brij stock	1.25 g L^{-1} B15 in DMSO	1g Span Brij stock	Water	10, 15, 20, 25, 30, 35
4A	1g Span Brij stock	100 g L^{-1} B49 in water	1g Span Brij stock	MeOH	20, 40, 60, 80, 100
4B	1g Span Brij stock	33.3 g L^{-1} B49 in water	1g Span Brij stock	MeOH	20, 40, 60, 80, 100
4C	1g Span Brij stock	16.7 g L^{-1} B49 in water	1g Span Brij stock	MeOH	20, 40, 60, 80, 100

In Table 4-9, two stock solutions are referred to. "AOT stock" refers to 195 g L^{-1} AOT in cyclohexane. "Span Brij stock" refers to 227 g L^{-1} Span 80, 227 g L^{-1} Brij 30, in heptane.

Although none of these microemulsions produced material that was visible to the naked eye, 20 µL droplets were taken and examined under plane polarised light using an optical microscope. Although crystalline material could be seen in these samples, it was not possible to uniquely identify it as the brightener since the AOT surfactant can also crystallise, though this is less likely as precipitation of the surfactant would destabilise the microemulsion and lead to phase separation, which was not observed. Figure 4-16 shows some of this material produced by the AOT/cyclohexane system after 8 days; while no crystal habit can be identified, the material still allows plane polarized light through. This suggests that the material produced at this stage of the process could be crystalline.

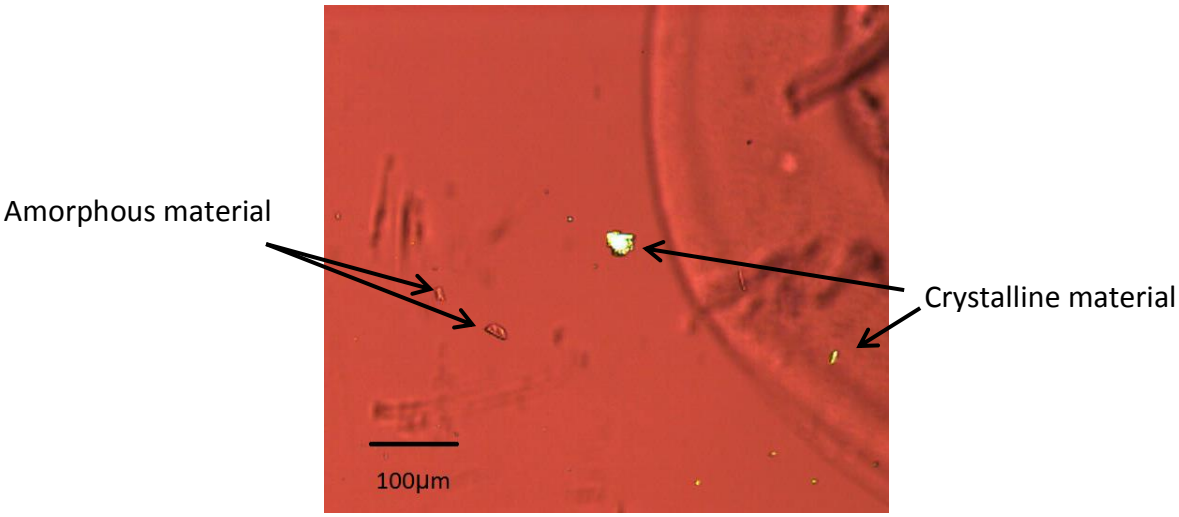

Figure 4-16: Material produced by AOT/cyclohexane system (allowed to grow for 8 days)

4.3.2.3. Seeding experiments

The crystalline material produced from the microemulsions was too small for single crystal X-ray crystallography, so instead the microemulsions produced in Section 4.3.2.2 were used to try to seed crystal growth. In this process, slightly supersaturated aqueous solutions of the brightener were made up, and a small amount of the microemulsion was added. As it is more thermodynamically favourable for crystal growth to occur on a pre-existing nucleus than for a new nucleus to form, any further crystal growth should grow the nuclei formed in the microemulsions.

To test the concentration of Brightener 15 to be used as the seeding solution, solutions of 2, 2.5, 3.3, 5, and 10 g L^{-1} Brightener 15 in water were made up. Although all samples

produced precipitate, the precipitate was produced slowly (in the order of hours, rather than minutes) in the samples of 2 and 2.5 g L^{-1} Brightener 15; therefore, these concentrations were used in the seeding experiments. The precipitate from these experiments in the bulk was a fine opaque precipitate; the material produced was thus too small and poorly crystalline to be used for single crystal X-ray crystallography.

To verify the visual effect of breaking the microemulsion, which might lead to clouding, and to distinguish this from precipitation, samples of microemulsions containing no brightener were added to water containing no brightener. This would show the effect of breaking the microemulsion on the visual appearance of the mixture. These microemulsions are shown in Table 4-10 below.

Table 4-10: Control 'blank microemulsions'

Microemulsion 1		**Microemulsion 2**		**Volume of dispersed phase added / µL g^{-1}**
Continuous phase	**Dispersed phase**	**Continuous phase**	**Dispersed phase**	
1 g 20% AOT in cyclohexane	DMSO	1 g 20% AOT in cyclohexane	Water	20, 30, 40, 50, 60, 70, 80

To make up the control “seeded solutions”, samples of 10, 20, and 40 µl/g of each of the above microemulsions were added to water.

The seeding experiments run are given in Table 4-11 overleaf.

Table 4-11: Seeded microemulsion systems

Bulk phase	**Systems used to seed**	**Volume added / µL g^{-1}**
2 g L^{-1} Brightener 15 in water	1A, 1B, 1C, 1D	40
2 g L^{-1} Brightener 15 in water	1A, 1B, 1C, 1D	20
2 g L^{-1} Brightener 15 in water	1A, 1B, 1C, 1D	10
2.5 g L^{-1} Brightener 15 in water	1A, 1B, 1C, 1D	20
2 g L^{-1} Brightener 15 in water	3A, 3B, 3C, 3D	20
2.5 g L^{-1} Brightener 15 in water	3A, 3B, 3C, 3D	20
10 g L^{-1} Brightener 49 in water	4A, 4B, 4C	100
20 g L^{-1} Brightener 49 in water	4A, 4B, 4C	100

Seeding experiments were carried out using all samples of each system; these systems are as listed in Table 4-9 in Section 4.3.2.2 previously.

The seeding experiments produced opaque milky-white material, as shown in Figure 4-17 below. A sample was removed and viewed under a microscope, using plane polarized light; this is shown in Figure 4-18. The microscope used was fitted with cross polarisers, which when used, only allow light through that has passed through a crystal lattice.

Figure 4-17: Typical material produced by seeding

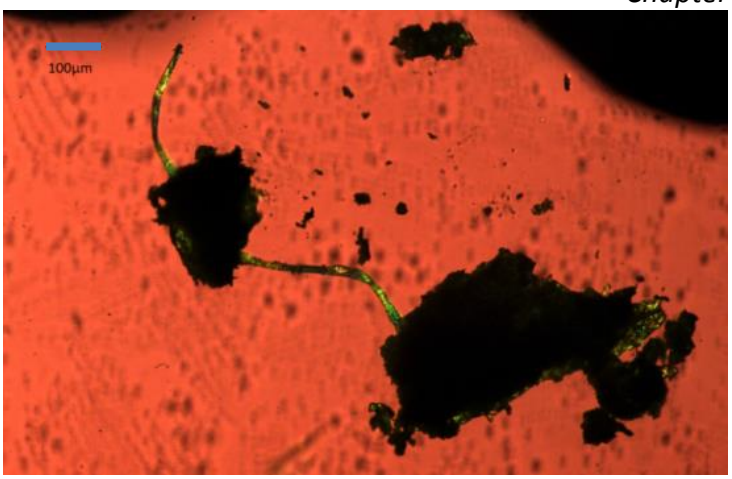

Figure 4-18: Typical material produced by seeding (under microscope). The scale bar in the top left-hand corner indicates 100 µm.

The material seen in Figure 4-18 does not allow plane polarized light through (suggesting that either the material is amorphous, or too thick to allow the light through), and does not appear to have a crystal habit. Although it may contain crystalline material, it is not a single crystal and cannot be used for crystallography. It may be that too many nuclei were formed in either the microemulsion crystallization or in the swelling process. Alternatively, this could be an illustration of Ostwald's rule of stages, in which an amorphous form nucleated around the small crystals present in the microemulsion because the precipitation was under kinetic control.

While material has clearly been produced, as a result of the addition of the microemulsions that contained small crystals, this material cannot be identified as crystalline.

4.4. Conclusions

Vapour diffusion crystallisation proved successful in the case of Brightener 49 in methanol. The resulting crystal gave an interesting multi-layered structure, with individual layers connected by interactions between the sulfate groups, methanol, and sodium ions, in a columnar structure. Within each brightener molecule, the sulfate groups were arranged in a cis-structure, rather than the trans-structure with two-fold rotational symmetry typically depicted. However, vapour diffusion crystallisation was unsuccessful in the case of Brightener 15, and attempts to produce a Brightener 49 hydrate also proved unsuccessful.

Attempts to produce Brightener 15 and Brightener 49 crystals *via* crystallisation from microemulsions also proved unsuccessful. Although viewing the microemulsions under plane-polarised light using an optical microscope identified some solid material, this did not grow into macroscopically-visible crystals, and when these microemulsions were used for seeding experiments, only amorphous or polycrystalline matter was produced.

The microemulsion process may show promise in the future for the production of crystalline brighteners. This could potentially be done through the use of a wider range of surfactant systems, solvents, and antisolvents, as the concentration of brightener and the amount of dispersed phase in this experiment were both low. In the case of the brightener concentration this was due to the low solubilities of the brighteners as shown in Table 4-5. The amount of crystalline matter could also be potentially increased by scaling up the system, allowing more material to be precipitated. In addition, the size of the crystals in the microemulsion could be increased by adding a brightener solution in which the solvent is miscible with water, but also slightly miscible with the continuous phase as well. This will lead to the brightener molecules partitioning into the droplets, along with only some of the solvent, the rest of which will partition into the much larger volume of the continuous phase. Hence, brightener molecules will be selectively added to the droplets, or to larger crystals with a layer of surrounding aqueous solution and surfactant, allowing the crystals there to grow to larger sizes. DMF would be an example of a suitable solvent, since this is miscible with water but also partially miscible with the heptane continuous phase.

4.5. Crystallisation of $CaCO_3$

In this section, the effect of the addition of surfactants on the precipitation of $CaCO_3$ was tested to determine if the surfactants in laundry detergent were affecting the crystallisation. Three surfactants were used: the anionic surfactant AE1S, the nonionic surfactant AE7, and the cationic surfactant cetyl trimethyl ammonium chloride (CTAC).

Solutions were made up containing 1 g L^{-1} of either $CaCl_2.2H_2O$ or Na_2CO_3, plus a given concentration of the surfactant. The two solutions were then mixed. The time taken until a precipitate formed was noted, and the precipitate was removed via centrifugation immediately to prevent interconversion of the $CaCO_3$ polymorphs. FTIR and WAXS data was then taken to determine the polymorph of $CaCO_3$ produced. Two sets of data were taken for each surfactant concentration in order to test for reproducibility.

Data was taken for the AE7, AE1S, and CTAC surfactants, and for AE1S/AE7 and AE7/CTAC mixes. An AE1S/CTAC surfactant mixture was created, but the surfactant precipitated out immediately, preventing further testing.

The control sample, containing 0.5 g L^{-1} $CaCl_2.2H_2O$ and 0.5 g L^{-1} Na_2CO_3 in water alone i.e. without surfactant, precipitated out in less than 4 minutes. SAXS and FTIR testing showed this to be producing vaterite crystals.

4.5.1. Results

Table 4-12 to Table 4-16 give the polymorphs produced from crystallisation experiments.

4.5.1.1. AE7

Table 4-12 shows the polymorphs of $CaCO_3$ obtained from solutions containing AE7, and the time taken for the precipitate to form.

Table 4-12: Data obtained from $CaCO_3$ crystallised in AE7

Conc. AE7 / g L^{-1}	**WAXS**	**FTIR**	**Time taken (minutes)**
2.49	Calcite	Calcite, possible aragonite/vaterite	8 – 13
4.98	Calcite	Calcite or vaterite	4 – 6
7.44	Calcite, possibly vaterite and aragonite	Inconclusive	3 – 5
9.90	Calcite	Calcite	10 – 47
12.3	Calcite, possible very weak aragonite, unidentified peaks	Calcite, unidentified peaks	>10 Sample 1: < 1 hour Sample 2: > 1 day

The most notable effect of the addition of AE7 is that calcite, the most stable polymorph of $CaCO_3$, is predominantly produced. It is not clear whether this is due to the calcium carbonate precipitating directly as the calcite polymorph, or because the AE7 increases the rate of the vaterite-calcite transition.

It can also be seen that the amount of AE7 added has affected the rate of precipitation. At low concentrations, increasing AE7 concentration decreased the time taken to precipitate $CaCO_3$; however, at higher concentrations ~ 10% by weight and above, increasing the concentration increases the time taken to precipitate.

4.5.1.2. AE1S

Table 4-13 shows the polymorphs of $CaCO_3$ obtained from solutions containing AE1S, and the time taken for the precipitate to form.

Table 4-13: Data obtained from $CaCO_3$ crystallised in AE1S

Conc. AE1S / g L^{-1}	**WAXS**	**FTIR**	**Time taken / mins**
2.05	Crystalline, but unidentifiable	Aragonite, possibly calcite and/or vaterite	2
4.09	Vaterite, possibly aragonite	Could be aragonite, possibly vaterite, some unidentified	15 – 16
6.12	Aragonite, vaterite, possibly calcite	One calcite/aragonite peak, one calcite/vaterite peak	Overnight – 3 days
8.14	Aragonite and vaterite	Calcite or vaterite	Overnight – 4 days

It can be seen that the AE1S has not had a significant effect on the polymorph produced; however, increasing the amount of AE1S in the solution dramatically increases the time taken for the calcium carbonate to precipitate. This would be consistent with the literature, where calcium carbonate nuclei are said to interact with anionic surfactants, either through individual surfactants being adsorbed onto the surface of the nucleus, or by the nucleus attaching to the outer shell of the micelle. It may be that the AE1S has adsorbed onto the crystal face of the aragonite and vaterite nuclei produced, inhibiting both further crystal growth and the vaterite-calcite transition.

4.5.1.3. CTAC

Table 4-14 shows the polymorphs of $CaCO_3$ obtained from solutions containing CTAC, and the time taken for the precipitate to form.

Table 4-14: Data obtained from $CaCO_3$ crystallised in CTAC

Conc. CTAC / g L^{-1}	WAXS	FTIR	Time taken
4	Calcite	Calcite	< 10 minutes
8	Calcite	Calcite	
12	Calcite, aragonite	Calcite	
16	Calcite, aragonite	Calcite	
20	Calcite, aragonite	Calcite	

Two main findings can be seen from this data. Firstly, when CTAC is used, calcite is the main polymorph produced (although at high concentrations some aragonite can be seen). Secondly, addition of CTAC has had no impact on the rate of precipitation.

4.5.1.4. AE7/AE1S mix

Table 4-15 shows the polymorphs of $CaCO_3$ obtained from solutions containing AE7 and AE1S, and the time taken for the precipitate to form.

Table 4-15: Data obtained from $CaCO_3$ crystallised in AE7/AE1S

Conc. AE7 / gL^{-1}	Conc. AE1S / gL^{-1}	WAXS	FTIR	Time taken
1.25	1.03	Calcite, aragonite and vaterite	Either calcite, or both aragonite and vaterite	8 – 14 mins
2.49	2.05	Aragonite and vaterite,, possibly calcite	Aragonite	1hr 28 min – 1 hr 37 mins
3.74	3.07	Crystalline but unidentified	Unidentifiable	5 hr 30 – Overnight
4.98	4.09	No peaks seen	Calcite/aragonite and aragonite/vaterite	1 – 2 days
6.21	5.11	Mostly amorphous but with peak at ~ 2.83 nm (vaterite?)	Unidentified, possible amorphous peak	1 – 3 days

Similar results are seen in this system to the AE1S-only system; while addition of the surfactant is not linked to production of a particular polymorph, it is linked with an increase in time taken to precipitate.

4.5.1.5. AE7/CTAC mix

Table 4-16 shows the polymorphs of $CaCO_3$ obtained from solutions containing AE7 and CTAC, and the time taken for the precipitate to form.

Table 4-16: Data obtained from $CaCO_3$ crystallised in AE7/CTAC

Conc. AE7 / g L^{-1}	Conc. CTAC / g L^{-1}	WAXS	FTIR	Time taken
1.25	2	Calcite, aragonite, and vaterite	Inconclusive	All showed precipitation in <10 mins
2.49	4	Calcite, aragonite	Calcite, possibly aragonite and/or vaterite	
3.74	6	Calcite	Calcite	
4.98	8	Calcite	Inconclusive	
6.21	10	Aragonite, vaterite	Inconclusive	

It can be seen that, while no one polymorph is consistently produced as in the CTAC-only system, the rate of $CaCO_3$ production is not affected by the inclusion of AE7.

4.6. Discussion

One main trend seen in all samples that didn't involve the cationic surfactant CTAC was that the amount of surfactant added to the system impacted the rate of $CaCO_3$ deposition, increasing the time taken for precipitation from approximately 4 minutes to up to 4 days. This suggests that, at high concentrations, the presence of the non-ionic and anionic surfactant is severely inhibiting the precipitation process. This is in line with the literature; multiple studies have found that SDS will inhibit $CaCO_3$ crystal growth, as detailed in Section 4.1.1.4.3.

This effect is most striking in the samples containing the anionic surfactant AE1S. This may be due to the anionic surfactant competing with the CO_3^{2-} ion and interacting with the Ca^{2+} ion, preventing the formation of precipitate. In literature studies with SDS, it has been hypothesised that, at SDS concentrations above the CMC, the calcium ions adsorb onto the micelle rather than multiple SDS molecules adsorping onto each face of the growing crystal.[153] In Chapter 5, SAXS data will be presented showing that adding calcium ions did not change the micellar size of AE1S micelles, and in Chapter 6, data from MD simulations will be presented showing that calcium ions in an AE1S system have a low

mean distance from the outer shell of the micelle, suggesting that Ca^{2+} ions do adsorb onto the micelles. The effect of the AE1S addition seen here is consistent with this view of Ca^{2+} interaction with the micelle.

In the AE7 system, high surfactant concentrations above ~10% by weight were also associated with a decreased rate of precipitation, although not to the same extent as for the AE1S system. The nonionic surfactant should not be interacting strongly with the ions, due to its lack of charge. Nevertheless, the interaction may be sufficiently strong to cause some adsorption of the surfactant onto the growing crystals when the surfactant is present in such large quantities, thereby impeding further crystal growth.

In the CTAC system, calcite was exclusively produced, with no change in rate seen with changing concentration. In 2007, Szcześ *et al* found that, firstly, a cationic surfactant interacted with negatively charged $CaCO_3$ nuclei, and secondly that the presence of cationic surfactant increased the rate of the vaterite-calcite transition.[149] These findings are therefore in line with the literature.

When mixed surfactant systems are used, attributes from one or both surfactant systems are seen. When AE1S and AE7 are used, the reduction in precipitation rate caused by the AE1S is seen, whilst it appears that the AE1S has control over the polymorph formed. When CTAC and AE7 are used, the rate of precipitation is not reduced, but the control over the polymorphs formed is lost: a mixture of polymorphs is seen. This suggests that, perhaps, the formation of mixed, less positively charged micelles occurs so that calcite is no longer nucleated predominantly when the more positively charged CTAC only micelles are not prevalent.

There were unidentifiable FTIR peaks in some of the AE1S and AE1S/AE7 systems, which could be due to surfactant-calcium precipitates. Further experiments would attempt to produce this material alone, and to obtain a crystal structure for it, allowing it to be identified in future samples.

4.7. Conclusions

The aim of the first section was to produce high quality single crystals of Brightener 49 and Brightener 15 using vapour diffusion and microemulsion crystallisation methods. Using the vapour diffusion method, Brightener 49 methanol solvate crystals were produced. On a molecular level, these showed a layered structure, with the sulfate ions in

a cis-position around the central bond, and with layers of brighteners connected *via* ligand-ion bonding between the sulfate ions, methanol, and sodium ions. No Brightener 15 crystals could be produced using vapour diffusion methods, and no crystals of sufficient size of either brightener were produced using microemulsion methods to allow single crystal analysis.

The effect of surfactants found in laundry detergent on the crystallisation of $CaCO_3$ was also tested. The results were largely in line with the literature, with the anionic surfactant supressing the vaterite-calcite transition and reducing the rate of precipitation, the cationic surfactant causing the precipitation of calcite but not affecting the rate of precipitation, and with the nonionic surfactant having a complex effect on the rate, but causing the precipitation of calcite.

5. SAXS

Small Angle X-ray Scattering (SAXS) of the surfactants with and without brightener and added $CaCl_2$ are detailed in this chapter.

5.1. Brightener and surfactant systems

In this section, SAXS data was taken for surfactant systems containing varying concentrations of Brightener 49. This was to determine, first, if there was any interaction between the brightener and the surfactant, and if an interaction between the brightener and the surfactant was occurring, into which part of the micelle the brightener was being incorporated. The changes in micelle radius with the addition of brightener were also determined. The SAXS data were analysed using two different methods to ensure consistency in the findings. First, the data was analysed using GIFT analysis (see Chapter 2 Section 2.2.3), which is model independent, except for the requirement of approximately spherical particles with a diameter less than a user-specified cut-off and the adoption of a hard sphere structure factor; the adoption of the latter typically has little effect on our findings because the concentration of scattering particles is low, so the structure factor is close to 1. Second, the SAXS data were analysed by assuming they arose solely from the form factor (i.e. the structure factor was set as 1) and then a modelled core shell particle form factor was adopted, since GIFT analysis showed that the scatterers were inhomogeneous (as would be expected for micelles containing hydrophobic cores and hydrophilic shells).

5.1.1. Nonionic surfactant AE7 + Brightener B49

5.1.1.1. Raw SAXS data

Aqueous solutions were made up containing 25.6 g L^{-1} AE7 and varying amounts of Brightener 49. SAXS data was taken (8 hours) for these samples at a detector distance of 66 cm. Literature values obtained by Li *et al* suggest that AE7 micelles have an aggregation number of approximately 300 and a CMC value of 0.1 g L^{-1}.[30] The area of the head groups in these micelles is therefore approximately 47 $Å^2$. These data are shown in Figure 5-1 overleaf.

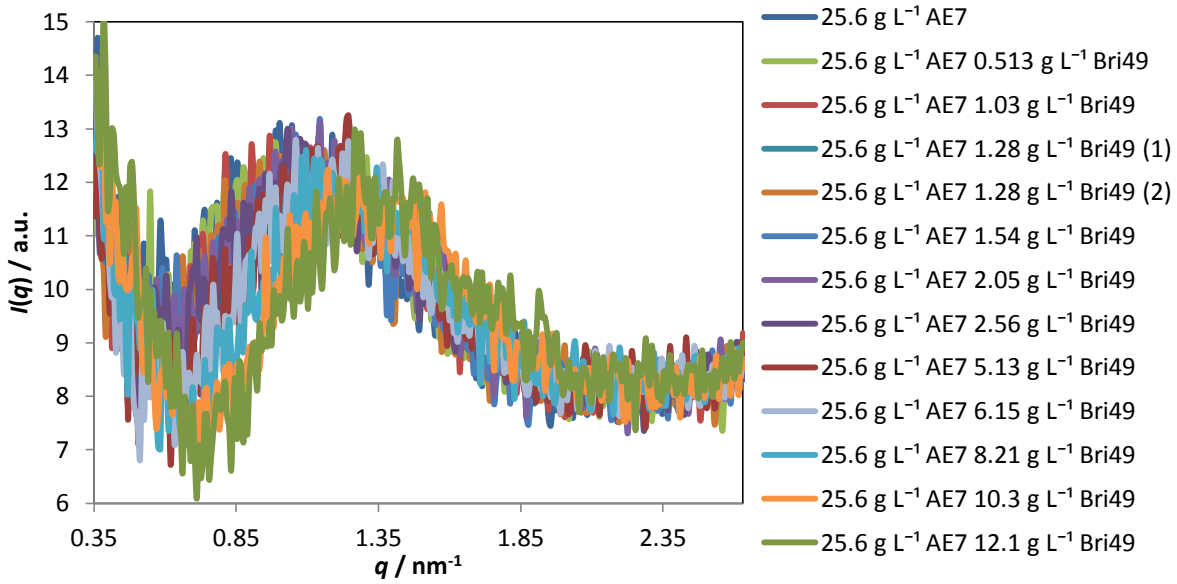

Figure 5-1: Raw SAXS data for solutions of 25.6 g L^{-1} AE7 with varying concentrations of Brightener 49

A clear peak shift to higher *q* is seen as the brightener concentration is increased.

More information can be obtained from this data by determining the pair distribution function, p(r). This quantity describes the probability of finding a vector of length r within the scattering particle, weighted by the electron density contrast between the particle (i.e. the micelle) and the surrounding solution at the vector's ends. Therefore, by determining p(r), information such as the particle size, structure and electron density contrast could be determined.

The pair distribution function is related to the form factor, $P(q)$, through the equation:[93]

$$P(q) = 4\pi \int_0^\infty p(r) \frac{\sin qr}{qr} dr$$

Equation 5-1

As the total scattering intensity, $I(q)$, is related to $P(q)$ through the equation

$$I(q) = nP(q)S(q),$$

Equation 5-2

(where n is the number of scattering particles in solution) then, if the effects of the structure factor, $S(q)$, on the scattering intensity I(q) can be calculated, P(q) can be determined, and p(q) found through a reverse Fourier transformation of this data. This was carried out using GIFT (Generalized Indirect Fourier Transformation) analysis, as discussed in Chapter 2.

The pair distribution functions, $p(r)$, for these samples are shown in Figure 5-2, Figure 5-3 and Figure 5-4 below and are indicative of core-shell scattering particles. The scattering functions $I(q)$ used to determine $p(q)$ were not obtained on an absolute scale, and hence to more readily compare the $p(q)$ functions, the data were normalised to the leftmost peak, i.e. a constant electron density for the core was assumed, in Figure 5-3, and to the rightmost peak in Figure 5-4, i.e. a constant electron density for the particles' shell was then assumed.

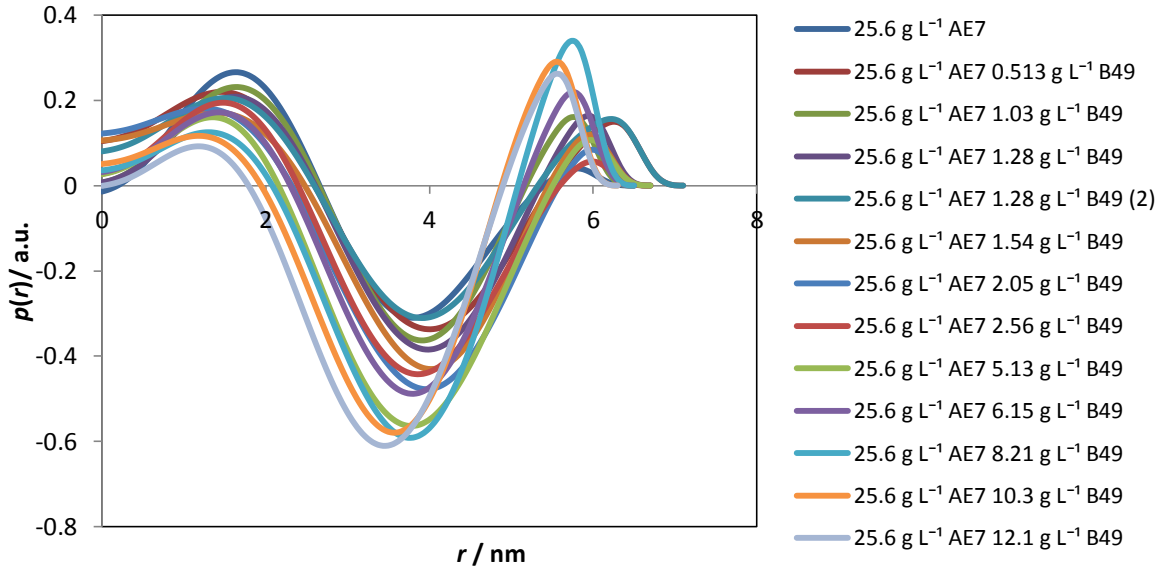

Figure 5-2: Pair distribution function $p(r)$ for AE7 and brightener in solution

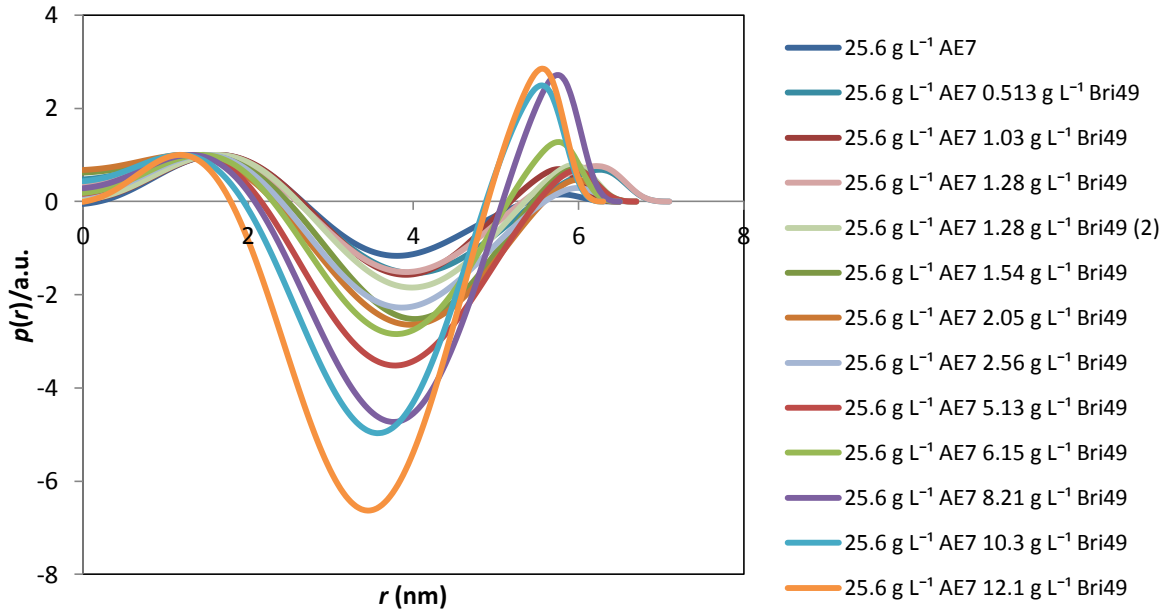

Figure 5-3: Pair distribution function $p(r)$ for AE7 and brightener in solution (normalized to first peak)

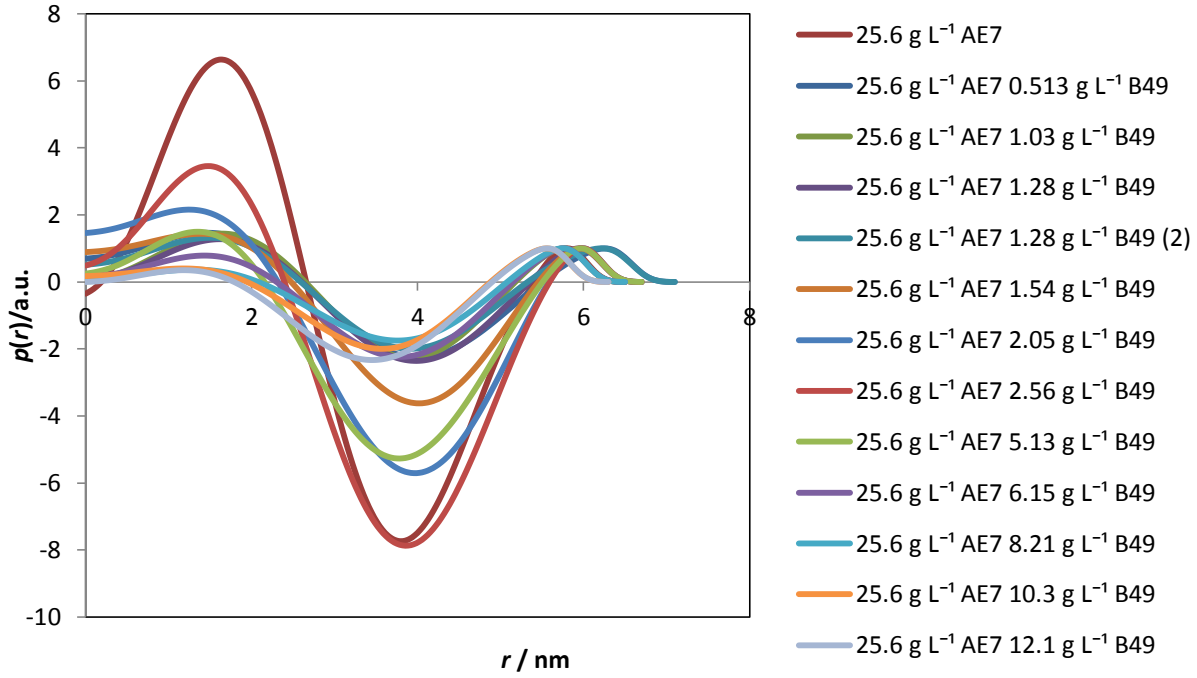

Figure 5-4: Pair distribution function *p*(*r*) for AE7 and brightener in solution (normalised to second peak)

Accordingly, Figure 5-3 shows the effect of brightener concentration on the electron density contrast of the outer shell, assuming that the electron density contrast of the inner core is constant. As the concentration of brightener increased, the magnitude of the rightmost peak was seen to increase. This would indicate that, if the electron density of the core was constant, then as the concentration of the brightener increased, the electron density contrast between the outer shell and the surrounding water increased.

In contrast, Figure 5-4 shows the effect of brightener concentration on the electron density contrast of the inner core, assuming that the electron density contrast of the outer shell remained constant. As the concentration of brightener increased, the magnitude of the leftmost peak decreased. This would indicate that, if the electron density of the outer shell was constant, then as the concentration of the brightener increased, the electron density contrast between the inner core and the water decreased.

The estimated electron densities of the core, shell, solvent and brightener are shown in Table 5-1.

Table 5-1: Electron densities of substances used

Substance	**Calculated electron density / e^{-} $Å^{-3}$**
AE7 (head group)	0.34
AE7 (tail group)	0.26
Water	0.33
Brightener 49	0.47

The electron density of Brightener 49 is much greater than that of the head or tail group of AE7. Therefore, if the brightener was incorporated into the head group region of the micelle, i.e. the shell, it would have increased the electron density of the region, increasing the electron density contrast between the outer shell and the solvent, as was indeed observed. Likewise, if the brightener was incorporated into the core, i.e. the tail group region of the micelle, it would have increased its overall electron density, reducing the electron density contrast between the core and the solvent; again, this was observed. Therefore, either scenario would have been plausible with the SAXS data.

The diameter of the micelles was given by the distance at which p(r) falls to 0. The inner core diameter was given approximately by the point of inflection between the minima and the second maxima; this was calculated from p(r) using the program Origin. These values are shown in Table 5-2.

Table 5-2: Radii calculated using GIFT for samples of brightener and AE7. All radii quoted to 2 s.f.

Concentration of brightener in sample / g L^{-1}	**Inner core radius / nm**	**Micellar radius / nm**
0	2.3	3.3
0.513	2.6	3.6
1.03	2.5	3.3
1.28	2.6	3.4
1.28 (2)	2.5	3.6
1.54	2.5	3.4
2.05	2.6	3.4
2.56	2.5	3.4
5.13	2.5	3.4
6.15	2.5	3.3
8.21	2.5	3.3
10.3	2.3	3.2
12.1	2.3	3.2

There was little variation in the radius of the inner core and outer shell with increasing brightener concentration. This could suggest that, instead of brightener molecules becoming incorporated into the micelle, and swelling it, the brightener molecules were replacing surfactant molecules within the micelle. This would have led to an increase in the number of micelles in solution, and thus a decrease in the mean distance between micelles, which might have led to increased interactions between the micelles that would have been apparent in the structure factor, $S(q)$.

Inspection of the generated hard sphere structure factors for AE7 with and without Brightener 49 show that there was a large amount of fluctuation in the structure factor peak and thus the mean separation between the micelles (corresponding to $q = \frac{2\pi}{d}$, where d is the mean separation between micelles and q is the position of the structure factor peak). These are shown in Figure 5-5 and Table 5-3 overleaf. This random scatter may indicate that the structure factor was not being modelled well by the GIFT program in this instance; however, it can be noted that the structure factor does not deviate far

from 1, so for $q > 0.5$ nm^{-1}, the structure factor would not have been contributing significantly to the final I(q).

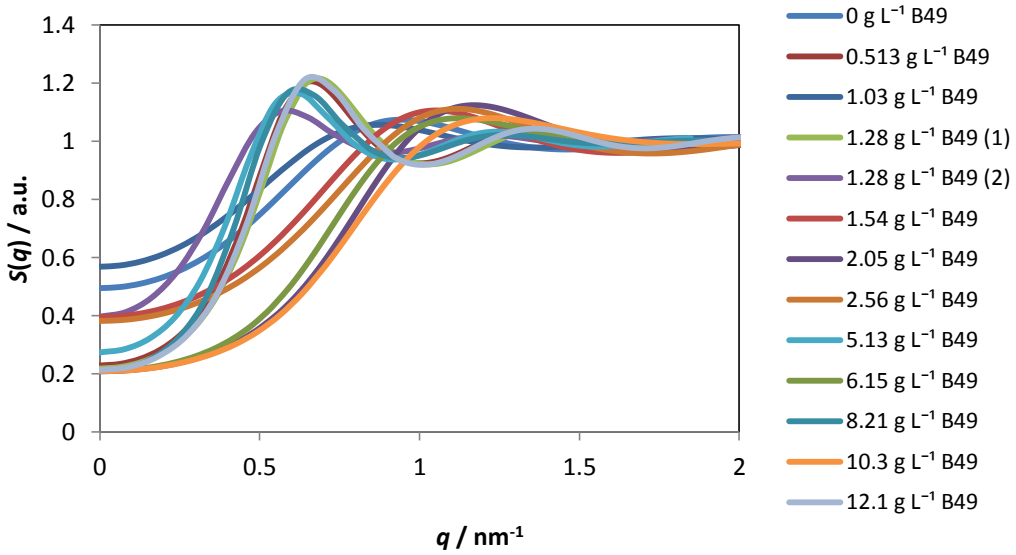

Figure 5-5: *S*(*q*) calculated during GIFT analysis for 25.6 g L^{-1} AE7 samples with varying concentrations of brightener

Table 5-3: Positions of *S*(*q*) peaks and corresponding intermicellar distances for the AE7/brightener system

Concentration of brightener / g L^{-1}	Position of *S(q)* peak / nm^{-1}	Distance between particles calculated from *S*(*q*) peak / nm
0	0.95	6.64
0.513	0.66	9.50
1.03	0.87	7.18
1.28 (1)	0.68	9.20
1.28 (2)	0.57	11.07
1.54	1.05	5.97
2.05	1.17	5.35
2.56	1.11	5.65
5.13	0.63	10.04
6.15	1.12	5.59
8.21	1.17	5.39
10.3	1.23	5.11
12.1	0.64	9.78

The intensities of the second maxima in the raw p(r) functions range from 0.012 – 0.25; the errors in these peak heights range from ±0.09 – 0.3. Therefore, the variation seen could have been due to the error inherent in GIFT analysis. Therefore, to confirm the trend, a simple model of the core-shell form factor was used to determine the effect of brightener concentration on the electron density of the inner core and outer shell.

5.1.1.2. Comparison to core-shell form factor modelled data

The SAXS data obtained for 25.6 g L^{-1} AE7 were compared to a simulated curve for the form factor, $P(q)$, of the micelle assuming a spherical core-shell structure where the core comprises the surfactant's hydrophobic tail groups and the shell the surfactant's hydrophilic head groups. The equation for this form factor was given in Chapter 2, Section 2.2.5. The structure factor, $S(q)$, was assumed to be 1 throughout, i.e. the micelles were at infinite separation. (Although this is never the case in an experimental system, at low concentrations the mean intermicellar distances are great enough that $S(q)$ deviates only slightly from 1 for $q > 0.5$ nm^{-1}.) The distance and electron density contrast parameters of the modelled system were adjusted in order to fit the simulated curve to the experimental data. The results are shown in Figure 5-6 below. Note the deviation between the experimental and simulated patterns at $q < 0.5$ nm^{-1} are likely to be due to primary beam scatter contributing to the experimental SAXS pattern; the surfactant systems are weak scatterers and so residual primary beam scatter is noticeable at low q.

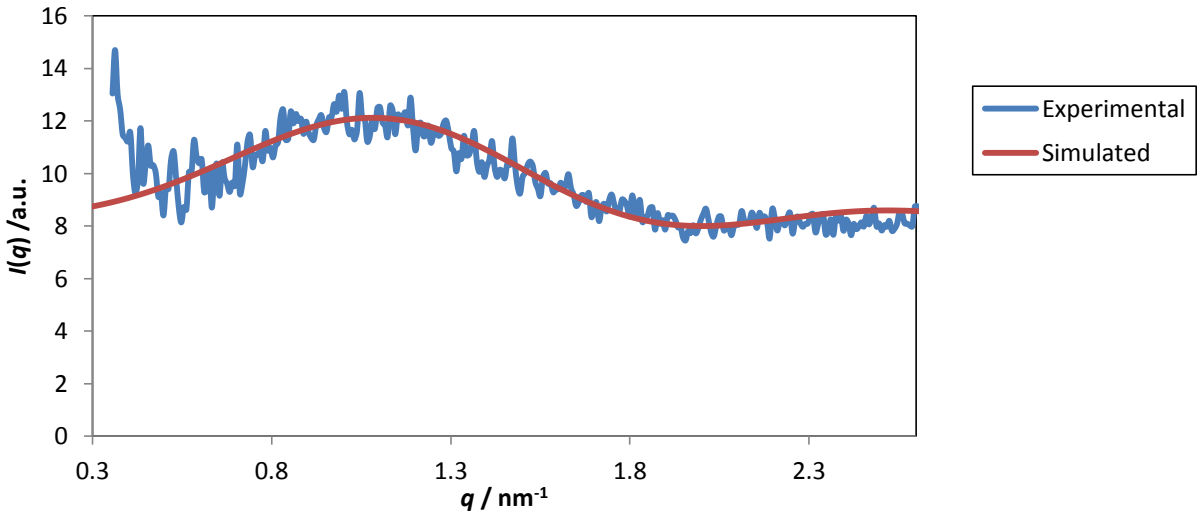

Figure 5-6: Comparison of experimental SAXS data and simulated $P(q)$ for 25.6 g L^{-1} AE7. The deviation from the experimental and simulated curves at low q occured because the experimental curve was dominated by scattering from the primary unscattered beam at these low q values.

The parameters required to fit this data are shown in Table 5-4 overleaf.

Table 5-4: Parameters required to fit simulated data to experimental data

Parameter	**Value**
Inner core radius / nm	2.54
Inner core electron density / $e^- Å^{-3}$	0.26
Outer shell radius / nm	3.25
Outer shell electron density / $e^- Å^{-3}$	0.385
Solvent electron density / $e^- Å^{-3}$	0.33
Background	8
Scale factor	10^{10}

The curves produced by adding brightener were fitted by first changing the electron density of the outer shell (and the scale factor), then by changing the electron density of the inner core (and scale factor). The effect of brightener concentration on electron density of the outer shell (assuming constant electron density for the inner core), and the effect of brightener concentration on electron density of inner core (assuming constant electron density for the outer shell), are shown in Figure 5-7 and Figure 5-8 respectively.

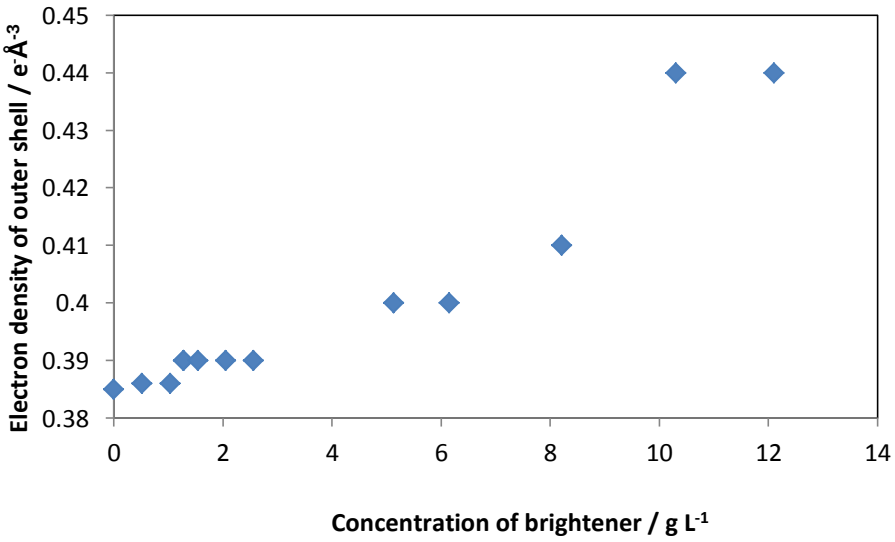

Figure 5-7: Effect of brightener concentration on electron density of the outer shell (assuming constant electron density for the inner core)

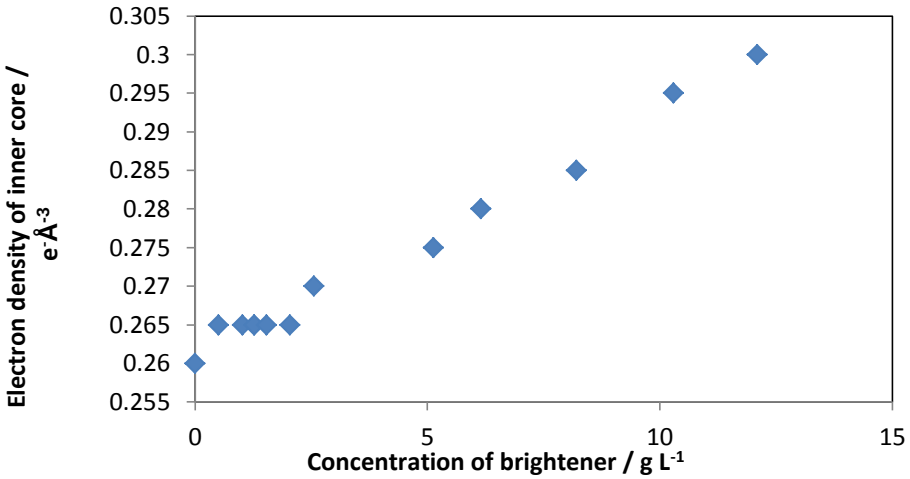

Figure 5-8: Effect of brightener concentration on electron density of inner core (assuming constant electron density for the outer shell)

It can be seen that, if the electron density of the outer shell was assumed to be constant, then the modelled electron density of the inner core increased with increasing brightener concentration. Likewise, if the electron density of the inner core was assumed to be constant, then the modelled electron density of the outer shell increased with increasing brightener concentration.

5.1.1.3. DECON results

To determine which model of brightener incorporation (into the core or shell) was the most plausible, the density profile of the AE7 micelles with and without brightener were determined using DECON. This program modelled the density profile from the GIFT output, assuming that the micelles were perfectly symmetrical and monodisperse. The results are shown in Figure 5-9 below.

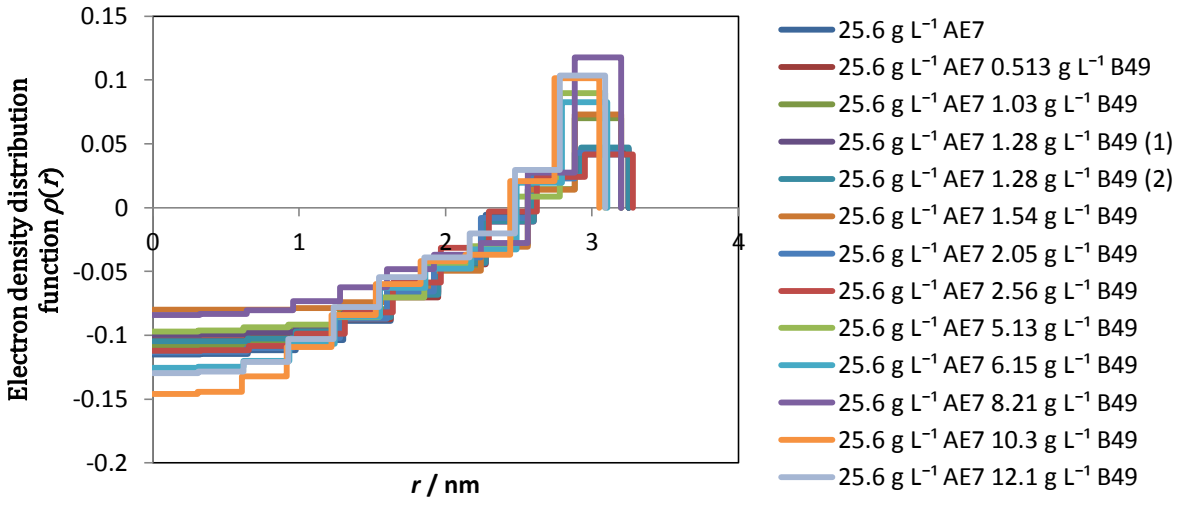

Figure 5-9: Density profile for AE7 micelles with and without brightener

At the centre of the micelle ($r = 0$), $\rho(r)$ was less affected by changes in brightener concentration, with the $p(0)$ value fluctuating with brightener concentration, giving values typically between 0.18 $e^- Å^{-3}$ and 0.25 $e^- Å^{-3}$. However, at larger r (corresponding to the outer shell of the micelle), $\rho(r)$ increased more systematically, increasing from 0.37 – 0.45 $e^- Å^{-3}$ with increasing brightener concentration. This corresponded to the brightener becoming incorporated mainly into the outer shell of the micelle.

The DECON results gave the electron density contrast between the micelle and the solvent. From these results, the electron densities of the inner core and outer shell were calculated. These were then compared to the electron densities used to fit the form factor model to the data in Section 1.1.2. This is shown in Figure 5-10 below. (It is assumed that the electron density of the inner core was constant, and the electron density of the outer shell increased.) These electron densities given with increasing brightener concentration are given in Table 5-5 overleaf.

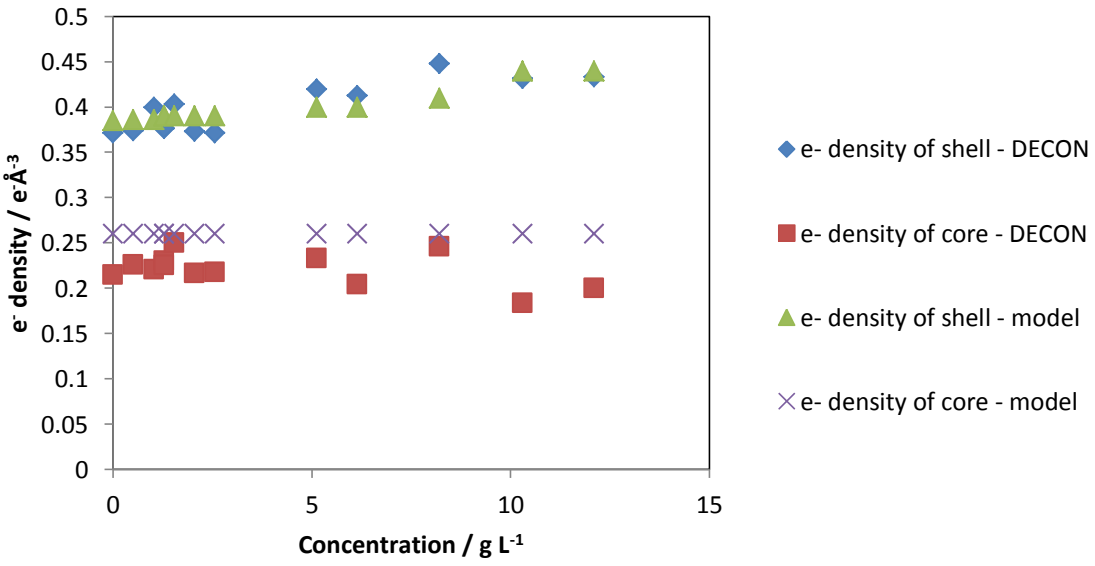

Figure 5-10: Comparison of electron densities calculated using DECON with modelled electron densities

Table 5-5: Calculated electron densities for AE7 + B49 micelles

Concentration / g L^{-1}	e^- density of shell (DECON) / $e^-Å^{-3}$	e^- density of core (DECON) / $e^-Å^{-3}$	e^- density of shell (model) / $e^-Å^{-3}$	e^- density of core (model) / $e^-Å^{-3}$
0	0.371	0.215	0.385	0.26
0.513	0.374	0.226	0.386	0.26
1.03	0.400	0.221	0.386	0.26
1.28	0.376	0.230	0.39	0.26
1.28 (2)	0.377	0.225	0.39	0.26
1.54	0.403	0.250	0.39	0.26
2.05	0.373	0.217	0.39	0.26
2.56	0.372	0.218	0.39	0.26
5.13	0.420	0.233	0.4	0.26
6.15	0.413	0.205	0.4	0.26
8.21	0.448	0.246	0.41	0.26
10.3	0.431	0.184	0.44	0.26
12.1	0.433	0.200	0.44	0.26

The modelled electron densities and the DECON electron densities for the outer shell matched well, suggesting that the model used was accurate. (Although there was an average difference of 0.036 $e^- Å^{-3}$ between the modelled electron densities and the electron densities from DECON for the inner shell, the same trend was seen in each.)

5.1.1.4. Components of micelles

By calculating the volumes of the outer shell and the number of electrons contributing to the electron density per surfactant, and using the electron densities calculated by DECON and verifying by modelling, the aggregation number of the micelles could be calculated. This was found to be 194 (compared to 300 in the literature)[30]. This would lead to a head group area of ~ 0.7 nm^2 (compared to 0.32 nm^2 in the literature)[160]. The error in calculating radii through GIFT analysis is typically 0.2 nm; this would lead to an error of approximately 6% in the radius calculated for this system, and thus of 18% in the volume, and thus the aggregation number. Thus the aggregation number for this system would be within the range 159 – 229.

The solubility of the brightener in water was given by Procter & Gamble as 17 g L^{-1};[161] it was determined experimentally that the brightener solubility in the AE7 concentration used was 31 g L^{-1}. Therefore, approximately 65% of the brightener in solution should have partitioned into the micelles. Assuming that each brightener molecule replaced one surfactant molecule in solution, the average components of micelles at each brightener concentration could be calculated. These are shown in Table 5-6 below.

Table 5-6: Components of micelles at changing brightener concentration

Conc. of Brightener 49 / g L^{-1}	**No. of brightener molecules per micelle**	**No. of surfactant molecules per micelle**
0.513	2	192
1.03	5	189
1.28	6	188
1.54	7	187
2.05	9	185
2.56	11	183
5.13	21	173
6.15	24	170
8.21	31	163
10.3	38	156
12.1	43	151

5.1.1.5. Structure factor peak

The scattering curves showed good agreement with the modelled form factors, suggesting that the *I*(*q*) peak seen was due to the core-shell micelle form factor. However, if a peak due to the structure factor had been present, it would have been be seen at:

$$q \approx \frac{2\pi}{d}$$

Equation 5-3

Here, q is as previously, and d is the average distance between micelles in solution.

Using the concentration and molecular weight of the surfactant, d was estimated to be 15 nm for the sample with no brightener present. Therefore, a structure factor peak would have been seen at ≈ 0.52 nm^{-1}. This does not correspond to the main peak seen, which for the pure surfactant occurs at between 1.0 nm^{-1} – 1.1 nm^{-1} (see Figure 5-1), showing that this peak is indeed mostly due to the form factor of the micelle.

As discussed previously, adding brightener to the solution would have displaced surfactant from the micelles, increasing the number of micelles in solution and decreasing the mean distance between micelles. This will have increased the q-value of the main structure factor peak; the more surfactant molecules displaced per brightener, the greater this shift will have been.

The calculated main structure factor peaks for the micelles containing brightener (using the same assumptions as in Section 5.1.1.4) are shown in Table 5-7.

Table 5-7: Estimated structure factor peaks for micelles containing brightener

Brightener concentration / g L^{-1}	**Estimated structure factor peak / nm^{-1}**
0.513	0.53
1.03	0.53
1.28	0.53
2.05	0.54
2.56	0.54
5.13	0.56
6.15	0.56
8.21	0.57
10.3	0.59
12.1	0.60

These structure factor peak values did not correspond to the experimental SAXS $I(q)$ peak values seen, which increased with brightener concentration from ≈1.1 to 1.4 nm^{-1} (see Figure 5-1), showing that these peaks were mostly due to the form factor of the brightener-incorporated micelles. The lack of significant micelle-micelle interactions, which would have caused the structure factor to deviate more from 1, is also apparent from the GIFT analysis. A typical hard sphere structure factor used in the GIFT analysis is shown below in Figure 5-11; its value deviated only slightly from 1 in the q-range studied (0.35 nm^{-1} to 2.6 nm^{-1}).

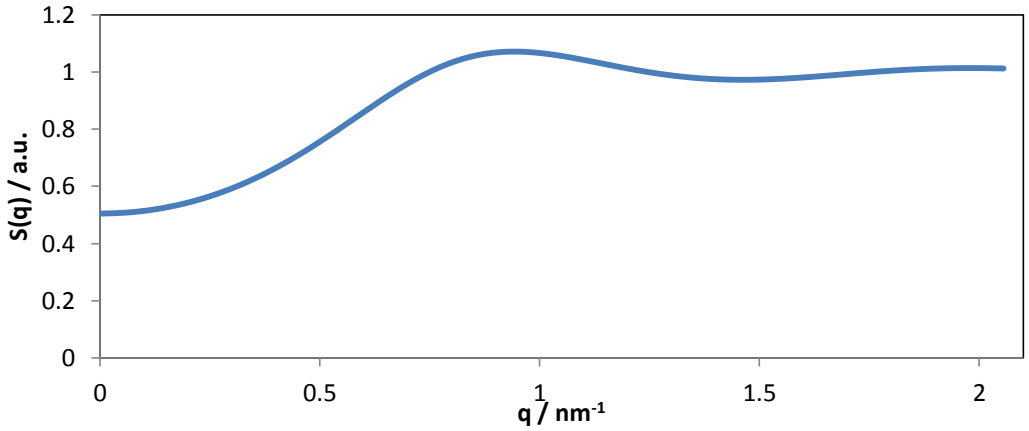

Figure 5-11: Simulated S(q) for 25.6 g L^{-1} AE7

In addition, the position of the minima in I(q) occurring after the main peak could be used to estimate the radius of the inner core, using the equation:

$$q_{min}R \sim 4.48$$

Equation 5-4

The estimated minima in $I(q)$ varied from 2.0 to 2.3 nm^{-1} in these samples (see Figure 5-12 overleaf).

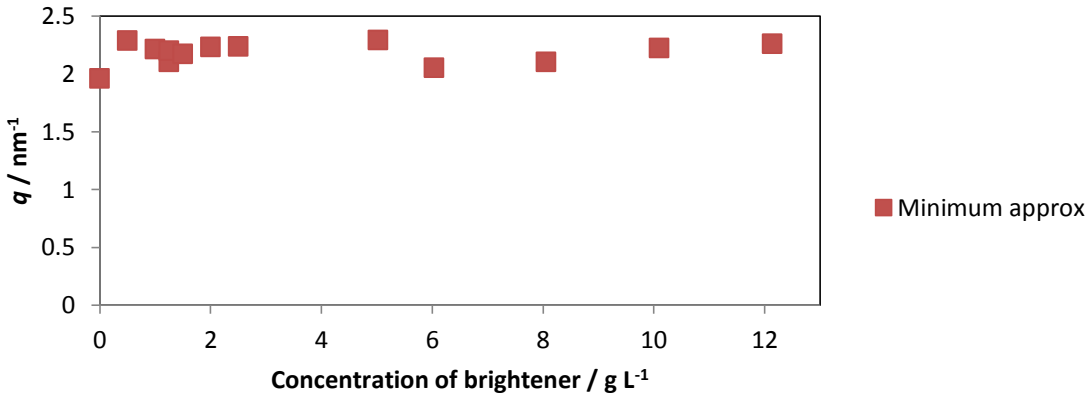

Figure 5-12: Effect of brightener concentration on position of minima in I(q)

These values corresponded to inner core radii of 2.0 – 2.3 nm, which compare well to the radii of 2.3 – 2.6 nm obtained through GIFT analysis.

5.1.1.6. Conclusions

The aggregation of AE7 in the presence of varying concentrations of Brightener 49 was investigated. It was found that, when no brightener was present, the AE7 formed micelles with an aggregation number of approximately 159 - 229. Adding brightener did not change the inner core or outer shell radius of the micelle, but did increase the electron

density of the outer shell, indicating that the brightener was being incorporated into this region. It was shown that the peaks in $I(q)$ were due to the form factor, rather than the structure factor.

In addition, the electron densities obtained via DECON provided a good fit for those obtained using a core-shell model, suggesting that this micelle could be modelled as spherical.

5.1.2. Anionic surfactant AE1S + Brightener 49

5.1.2.1. Raw data

SAXS data was collected for samples containing 21.0 g L^{-1} AE1S, with varied concentrations of Brightener 49 added. This data is shown in Figure 5-13 overleaf.

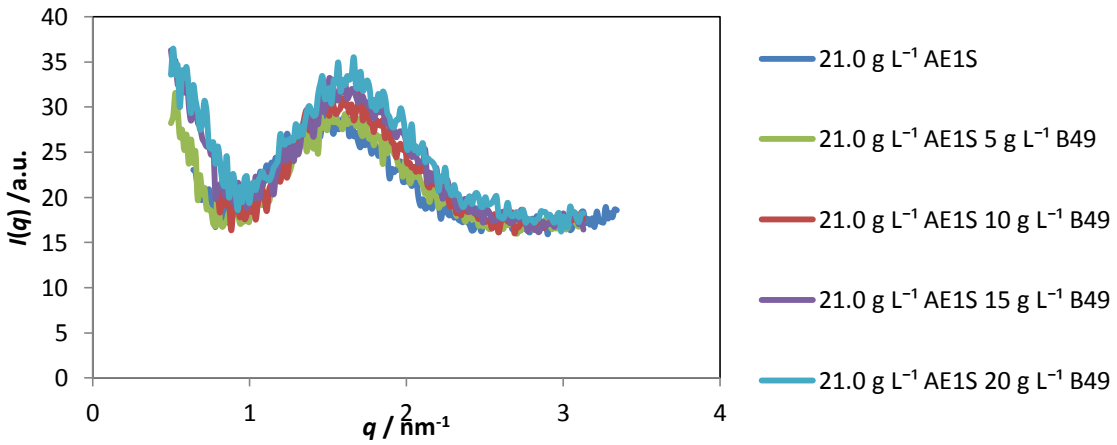

Figure 5-13: Raw SAXS data for AE1S systems containing B49

The increase in brightener concentration had two main effects on the $I(q)$ peak; firstly an increase in intensity, and secondly a marginal shift to higher q. To find the effect of the brightener concentration on the structure of the AE1S micelle, its pair distribution function was found.

5.1.2.2. GIFT analysis

The pair distribution functions of these samples were found through GIFT analysis. These are shown in Figure 5-14. These pair distribution functions were also normalised to the first peak, to show the relative heights of the second peaks; these are shown in Figure 5-15.

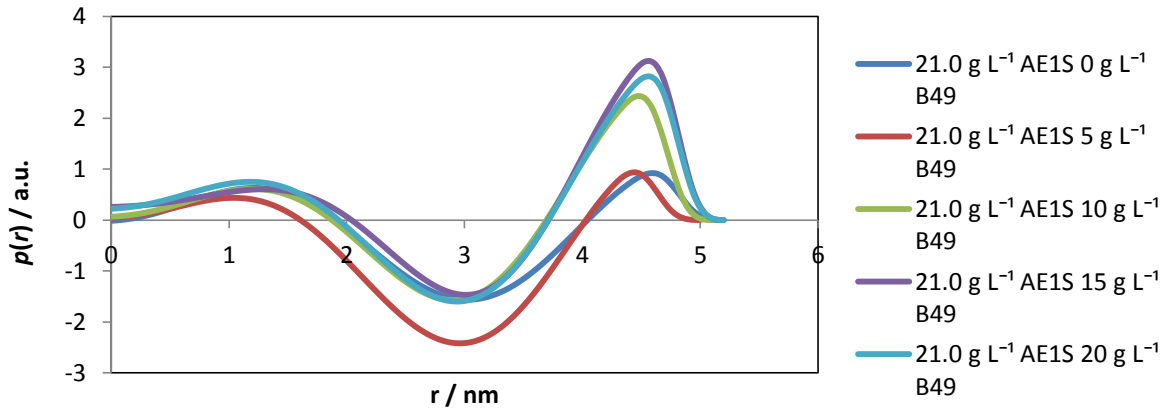

Figure 5-14: Pair distribution function for AE1S systems containing B49

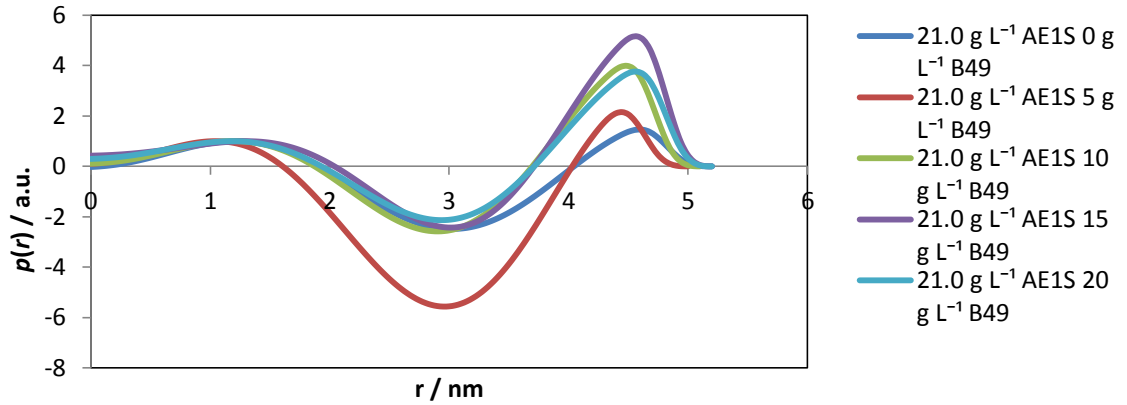

Figure 5-15: Pair distribution function for AE1S systems containing B49 (normalised to first peak)

Figure 5-15 shows that, as the brightener concentration increased, the height of the second maximum increased relative to the first. This is shown more clearly in Figure 5-16 below. This would suggest that the electron density contrast between the outer shell and the solvent increased as the concentration of brightener increased, and thus the overall electron density of the outer shell increased, and the brightener was being incorporated into the outer shell of the micelle.

If the same data was normalised to the second maximum, this would have shown the height of the first peak decreasing as the concentration of brightener was increased, suggesting that the electron density contrast between the inner core and the solvent was decreasing, and thus that the electron density of the inner core increased, suggesting brightener incorporation into the inner core. As the 'outer shell' model was proven correct in the previous case, this was the one that the remaining data was primarily compared to, although the electron densities generated were compared to both models to confirm that this model was correct.

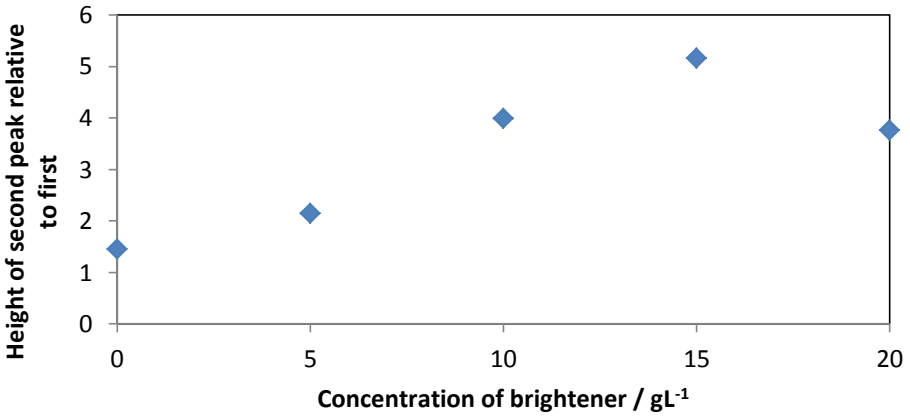

Figure 5-16: Height of second peak in p(r) relative to the first, for AE1S systems containing B49

The inner core and micellar radii of this system are given in Table 5-8 below.

Table 5-8: Inner core and micellar radii of AE1S systems with varying concentrations of brightener

Concentration of brightener / g L^{-1}	Inner core radius / nm	Micellar radius / nm
0	2.0	2.6
5	2.0	2.5
10	1.9	2.6
15	2.0	2.6
20	2.0	2.6

It can be seen that there was very little change in the inner core and micellar radii as the concentration of brightener was increased. This would suggest that the addition of brightener did not affect the overall size and shape of the micelle.

5.1.2.3. Core-shell form factor modelling results

The tail groups of the AE1S were estimated as having an electron density of 0.26 $e^{-}Å^{-3}$ assuming the inner core was similar to liquid hydrocarbon. This value was similar to the value of 0.21 $e^{-}Å^{-3}$ obtained from fitting the core-shell form factor to the $I(q)$ curve with the inner core and micelle radii values taken to be those determined from GIFT analysis (see Table 5-9).

Table 5-9: Parameters for form factor model for 21.0 g L^{-1} AE1S system

Parameter	Value
Inner core radius / nm	2.0
Outer shell radius / nm	2.6
Inner core electron density / $e^{-}Å^{-3}$	0.26
Outer shell electron density / $e^{-}Å^{-3}$	0.40
Background	17.5
Multiplier / $x10^{10}$	9.00

The inner core electron density value of 0.26 $e^{-}Å^{-3}$ could be used to estimate the number of tail groups in the micelle (i.e. the aggregation number) using:

$$No.\,of\,tail\ groups = \frac{\frac{4}{3}\pi r_{\text{inner}}^{3}\rho_{e^-}}{Electrons\ per\ tail}$$

Equation 5-5

This gave an aggregation number of 83, which compares well with literature values ranging from 43-80.[32,33] Note that estimating the aggregation number of the micelles by using Equation 5-5 but replacing the tail groups by head groups (i.e. $No.\,of\,head\ groups = \frac{\frac{4}{3}\pi r^{3}\rho_{e^-}}{Electrons\ per\ head}$) gave values that were too high and thus not realistic because there was likely to be a large amount of water penetrating into the head group region of the micelle, thus increasing the number of electrons within it without increasing the number of head groups. (In Chapter 6, this was shown to be the case with AE1S micelles; the small ionic head groups provided comparatively little coverage for the surface of the micelle, and thus large amounts of water were present within this region. This was not the case for the AE7 micelle, where the long polar head groups provided good coverage, and thus less water penetration would have occurred.) Again, by estimating the error in the radius to be ~ 0.2 nm as is typical, the percentage error in the aggregation number can be given as ~24 %. This gives the estimated range of the aggregation number as 63 – 103.

The raw SAXS data for AE1S with brightener added (as shown in Figure 5-13) was fit using the micelle radii from Table 5-9, but first with a constant outer shell electron density and

varied inner core electron density, and then with a constant inner core electron density and varied outer shell electron density. The results are shown in Table 5-10 below.

Table 5-10: Parameters used to fit AE1S systems to form factor model

Concentration of brightener / g L^{-1}	**Electron density of inner core (shell constant) / e^{-} $Å^{-3}$**	**Electron density of outer shell (core constant) / e^{-} $Å^{-3}$**
0	0.260	0.400
5	0.270	0.410
10	0.270	0.415
15	0.275	0.420
20	0.275	0.420

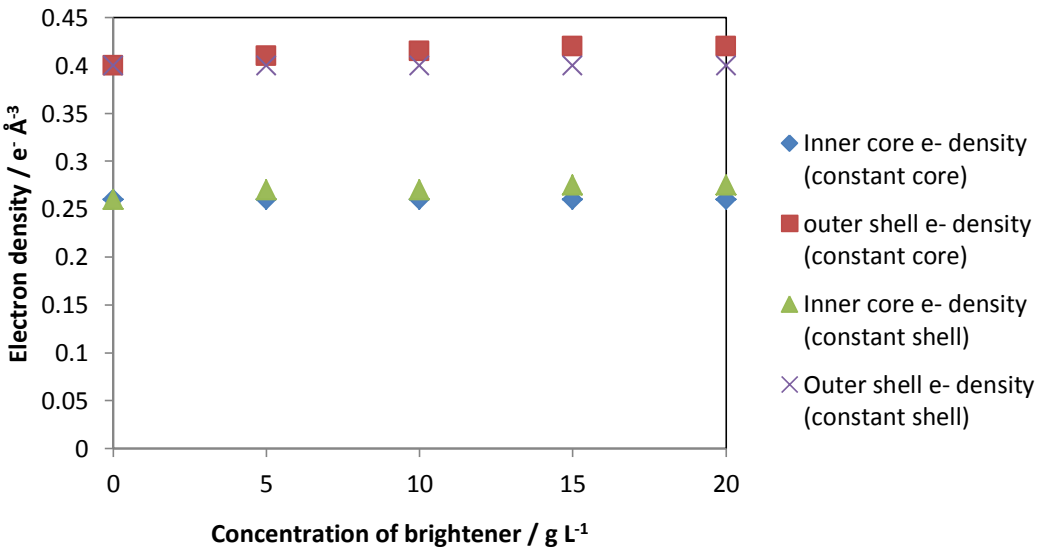

Figure 5-17: Change in modelled electron density given by both models (constant core and constant shell) for the AE1S system

Both models fit the data. However, it can be seen that the change in electron density was not particularly large. This would suggest that the effect of the brightener on the electron density of the AE1S micelle was not as significant as the effect of the brightener on the AE7 micelle. This may have corresponded to the brightener having a similar electron density to the AE1S micelle (which is plausible if the brightener was being incorporated into the outer shell, as the electron density of the head group of the AE1S surfactant can be estimated at 0.47 e^{-} $Å^{-3}$, assuming complete dissociation from sodium ions), or to the brightener not associating to the AE1S in such high numbers as in the AE7 system.

5.1.2.4. DECON results

The DECON results generated by analysis of the AE1S system, and their corresponding maxima and minima electron density contrast values, are shown in Figure 5-18 and Figure 5-19 respectively.

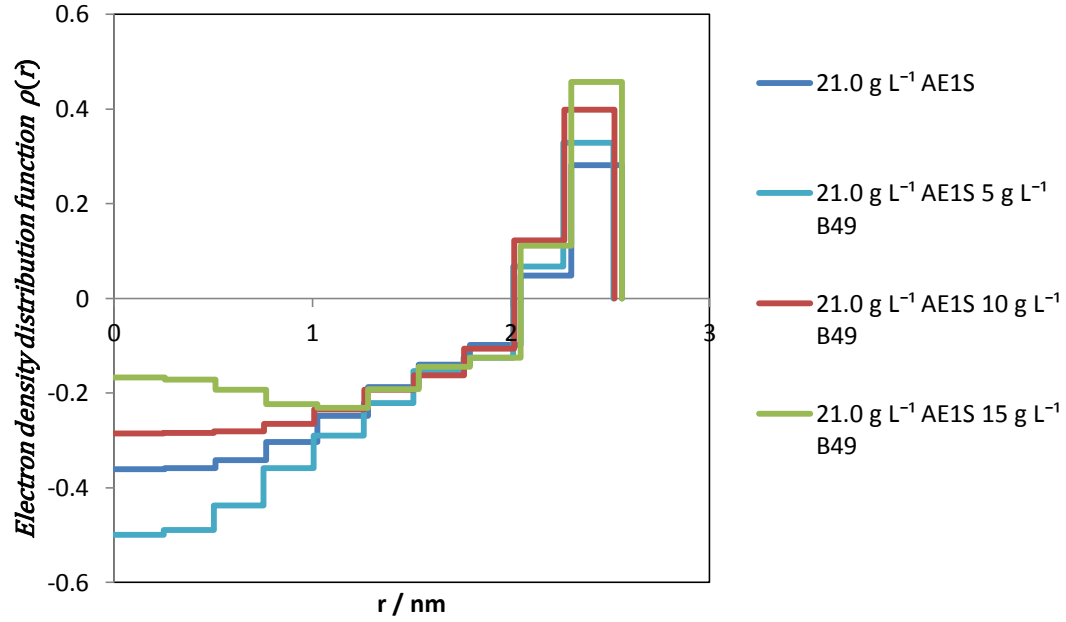

Figure 5-18: DECON results for AE1S systems containing B49

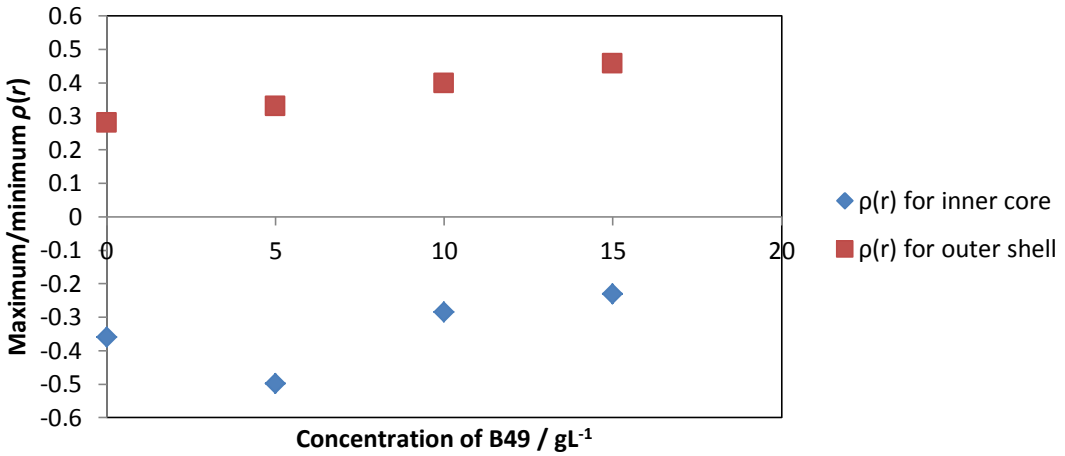

Figure 5-19: Maximum and minimum ρ(r) for AE1S systems containing brightener

The electron densities generated for this system are given in Table 5-11.

Table 5-11: Electron densities of AE1S micelles, with various concentrations of brightener, generated using DECON

Concentration of brightener / gL^{-1}	Electron density of core / $e^{-}Å^{-3}$	Electron density of shell / $e^{-}Å^{-3}$
0	-0.031	0.611
5	-0.169	0.659
10	0.045	0.728
15	0.099	0.787

The values generated using DECON were compared to those from the model in Figure 5-20.

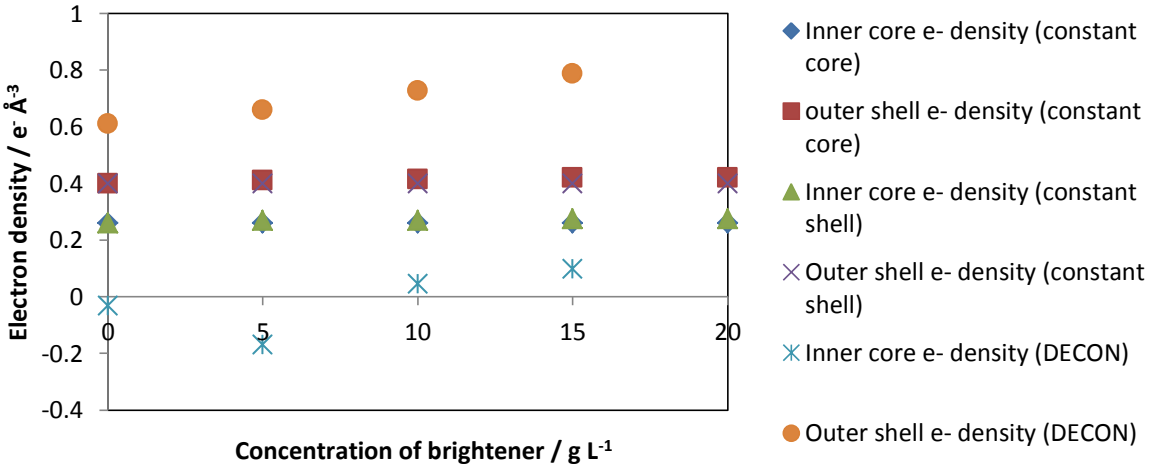

Figure 5-20: Electron density for AE1S micelles, calculated using DECON and *via* the modelled form factor

As can be seen here, the DECON values and the modelled values compared very poorly. In addition, the DECON values were not physically possible; for several concentrations, the electron density of the inner core was determined to be negative. This is likely due to the fact that the DECON program assumed perfect spherical symmetry. The disparity between the results generated by DECON and what was physically possible suggested that the AE1S micelles were not, in fact, spherical. (Further evidence for this will be provided in Chapter 6). As previously stated in Chapter 2, Section 2.2.4.2, the identification of non-spherical particles due to poor DECON outputs was highlighted as a potential application of the DECON program by Glatter in 1981.[111]

5.1.2.5. Conclusions

A number of features of the AE1S-brightener interactions were determined from this data. Firstly, their micellar radii were not greatly affected by the addition of Brightener 49. Their electron densities were slightly affected by the addition of brightener, but this

was not as significant an effect as that seen in a nonionic system. In addition, a few properties of the micelles themselves could be seen. In particular, it appeared that the outer shell was very diffuse, with the ionic groups not covering the entire surface of the micelle, allowing penetration of water into this region. It also could be seen that the micelle was not spherical. The physical meaning of these two facts will be examined in more detail in Chapter 6.

5.1.3. Anionic surfactant LAS + Brightener 49

5.1.3.1. Raw SAXS data

SAXS data was collected for samples of 15.8 g L^{-1} LAS containing various concentrations of Brightener 49. This raw data is shown in Figure 5-21 below.

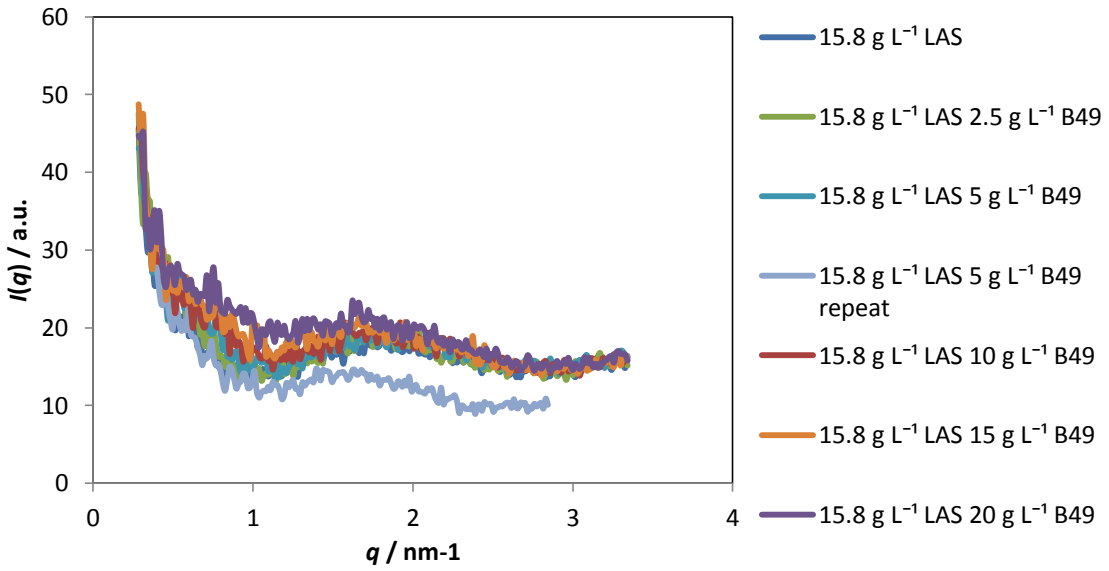

Figure 5-21: Raw SAXS data for varied concentrations of B49 with LAS

The most immediately striking feature of this data is its very low peak height. This may have been indicative of the LAS being a poorly scattering particle, perhaps due to low electron density contrast between its head and tail groups and the solvent. As the tail group was estimated to have an electron density of 0.26 e^{-} $Å^{-3}$, and the head group as 0.31 e^{-} $Å^{-3}$ (assuming total dissociation of Na^{+} ion; this would rise to 0.40 e^{-} $Å^{-3}$ if the ion does not dissociate), whereas the solvent will have an electron density of 0.33 e^{-} $Å^{-3}$, this is definitely plausible. This data also showed that the $I(q)$ peak did not shift significantly to higher or lower q as the concentration of brightener was increased. To examine this further, the pair distribution function of the micelles were found.

5.1.3.2. GIFT analysis

The pair distribution function of each sample was found from the SAXS scattering pattern through GIFT analysis. These are shown in Figure 5-22 overleaf.

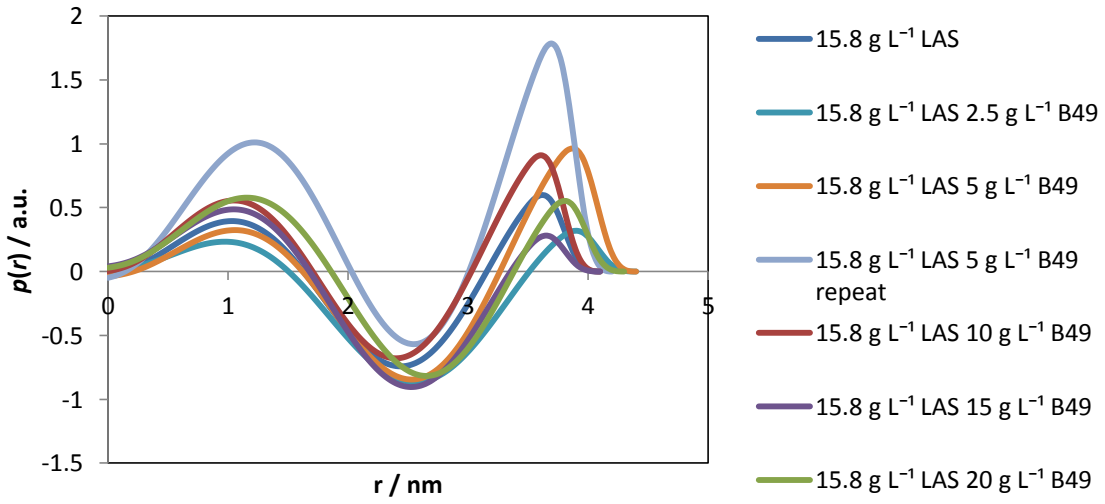

Figure 5-22: Pair distribution functions for varied concentrations of B49 with LAS

Figure 5-23 shows these pair distribution functions normalised to the first peak, while Figure 5-24 shows the height of the second peak relative to the first. It can be seen that there was no strong correlation between the height of the second peak relative to the first, and the concentration of brightener. However, if there was a slight negative correlation between the two, similar results to these would be obtained.

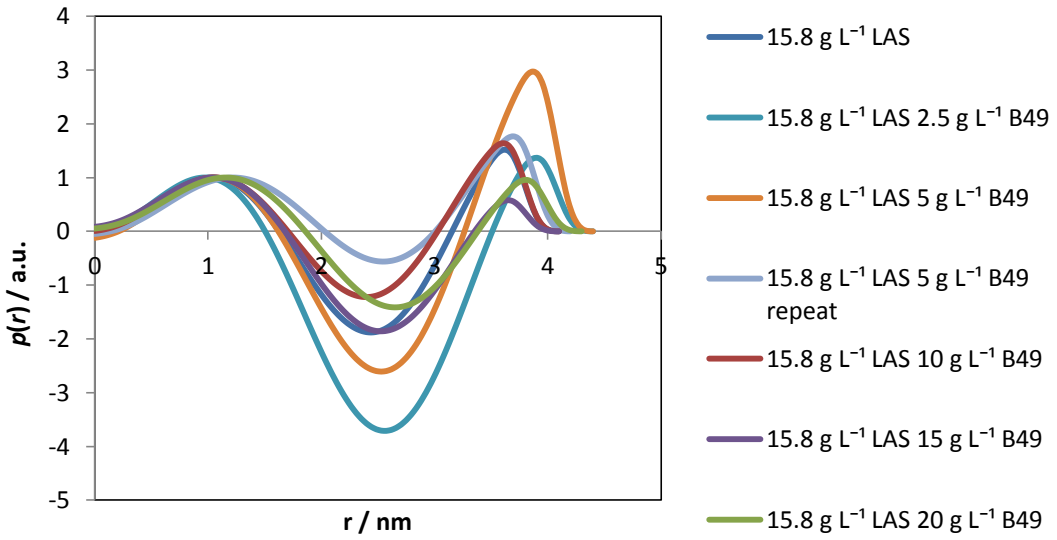

Figure 5-23: Pair distribution function *p*(*r*) for varied concentrations of B49 with LAS (normalised to first peak)

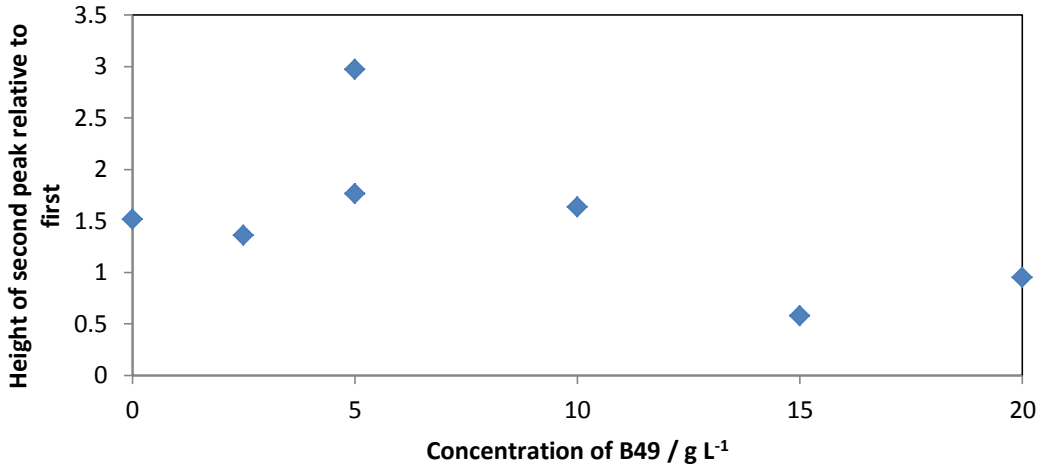

Figure 5-24: Variation in *p*(*r*) peak heights with varying B49 concentration in LAS

In this case, for the 'constant core' and 'constant shell' models, this would have indicated that either the electron density of the inner core was decreasing (and thus the electron density contrast between the inner core and outer shell was increasing), or that the electron density of the outer shell was decreasing (and thus the electron density contrast between the solvent and the shell was decreasing). The first situation would be implausible, as the brightener was presumed to be more electron dense than the solvent, whereas the hydrocarbon chains of the LAS were presumed to be less electron dense. The second scenario would be implausible if the brightener was taking up space that would be occupied by the water. However, if each brightener molecule was replacing an LAS molecule in the micelle, was less electron dense than the head group of the LAS, and was being incorporated into the head group of the micelle, then the given effect on the pair distribution would be seen.

Table 5-12 shows the effect of brightener concentration on the inner core and micellar radii of the LAS micelle.

Table 5-12: Inner core and micellar radii for 15.8 g L^{-1} LAS, with and without brightener

Concentration of brightener / g L^{-1}	Inner core radius / nm	Micellar radius / nm
0	1.6	2.0
2.5	1.7	2.2
5	1.7	2.2
5 (repeat)	1.7	2.1
10	1.6	2.0
15	1.6	2.0
20	1.7	2.2

It can be seen that, while there was some variance in the inner core and outer shell radius between samples, this was not correlated with brightener concentration and so was more likely to represent the uncertainty in our micelle size determinations.

5.1.3.3. DECON

The radial distribution functions were found from the pair distribution functions using DECON. These are shown in Figure 5-25 below. The resulting maxima and minima values of the radial electron density contrast between the particle and the solvent are shown in Figure 5-26 overleaf.

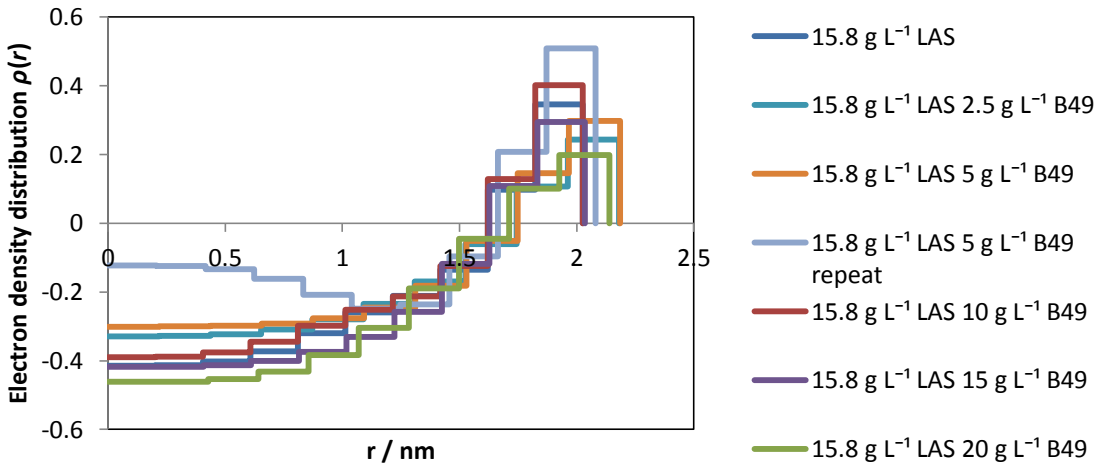

Figure 5-25: DECON results for varying concentration of B49 in LAS

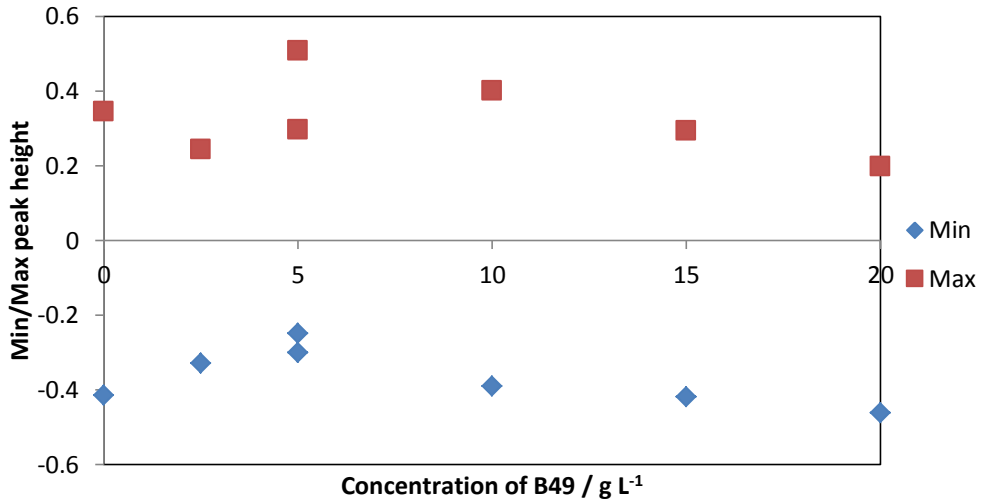

Figure 5-26: Variation in peak height given by DECON for B49 in LAS

The electron densities calculated from these maxima and minima are shown in Table 5-13 below.

Table 5-13: Electron densities for inner core and outer shell of LAS + B49 micelles (calculated using DECON)

Concentration of brightener / g L^{-1}	Electron density of inner core / $e^{-}Å^{-3}$	Electron density of outer shell / $e^{-}Å^{-3}$
0	-0.08	0.68
2.5	0.00	0.57
5	0.03	0.63
5 (repeat)	0.08	0.84
10	-0.06	0.73
15	-0.09	0.62
20	-0.13	0.53

It can be seen that not all of these values were physically realistic; in particular, many of the values given for the electron density of the inner core were negative, which is clearly physically impossible. This was likely to be due to the non-spherical nature of these aggregates, as for the AE1S system. One trend that was seen, however, is that there was a weak negative correlation between the electron density of both the inner core and the outer shell, and the concentration of brightener in the system. This would be consistent with the 'surfactant replacement' model described in Section 5.1.3.2.

5.1.3.4. Modelling I(q)with the core-shell form factor model

The simple core-shell form factor model was used fit to the SAXS *I*(*q*) data as before. When fitting the data to the initial curve, the electron density of the LAS head group and tail group were estimated at 0.41 $e^{-}Å^{-3}$ and 0.26 $e^{-}Å^{-3}$, respectively. The micelle radii obtained from the GIFT analysis were used.

Table 5-14 gives the parameters of the modelled curve for the sample containing only 15.8 g L^{-1} LAS (i.e. no brightener).

Table 5-14: Parameters used to fit modelled curve to that produced by 15.8 g L^{-1} LAS

Parameter	Value
Inner core radius / nm	1.6
Outer shell radius / nm	2.0
Inner core electron density / $e^{-}Å^{-3}$	0.26
Outer shell electron density / $e^{-}Å^{-3}$	0.40
Background	14
Multiplier / $x10^{11}$	1.5

The remaining curves were fit using the same inner core and outer shell radii, and either the same outer shell electron density and a varied inner core electron density (the 'constant shell' model), or the same inner core electron density and a varied outer shell electron density (the 'constant core' model). The electron densities generated in this way are shown in Table 5-15 below.

Table 5-15: Electron densities for LAS + brightener system

Concentration of brightener / g L^{-1}	Electron density of inner core (constant shell model) / $e^{-}Å^{-3}$	Electron density of outer shell (constant core model) / $e^{-}Å^{-3}$
0	0.260	0.400
2.5	0.260	0.400
5	0.263	0.405
10	0.255	0.395
15	0.248	0.390
20	0.245	0.388

It can be seen that, for both models, there was a slight decrease in the electron density as the concentration of brightener increases.

5.1.3.5. Conclusions

The peak heights from GIFT analysis, and the electron densities from the core-shell model and DECON, corresponded to those expected if the brightener was being incorporated into the outer shell. However, the correlation was not strong enough to definitively support a hypothesis.

5.1.4. Anionic surfactant AE1S + nonionic surfactant AE7 + Brightener 49

5.1.4.1. Raw data

SAXS data was collected for samples containing 10.5 g L^{-1} AE1S, 12.8 g L^{-1} AE7, and varying concentrations of brightener. This data is shown in Figure 5-27 below.

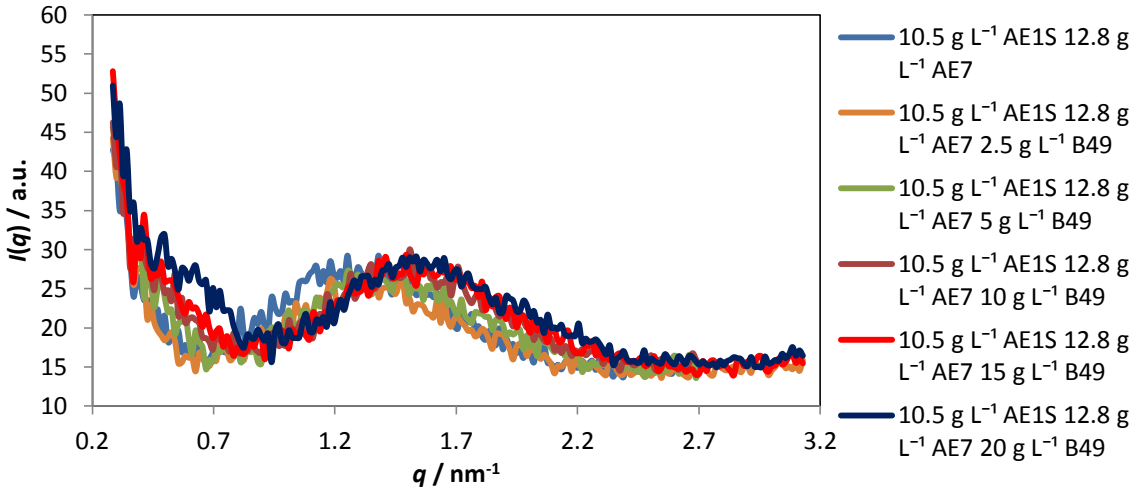

Figure 5-27: SAXS data for AE1S & AE7 solutions with and without brightener

It can be seen that, as the concentration of brightener was increased, the $I(q)$ peak shifted to higher q. This shows that the addition of brightener had an effect on the scattering of the micelles. To examine this effect in more detail, the pair distribution function of the micelles was found to determine any changes in micelle radius and electron density.

5.1.4.2. GIFT analysis

The pair distribution functions of the AE1S/AE7 system were found using GIFT analysis, and are shown in Figure 5-28.

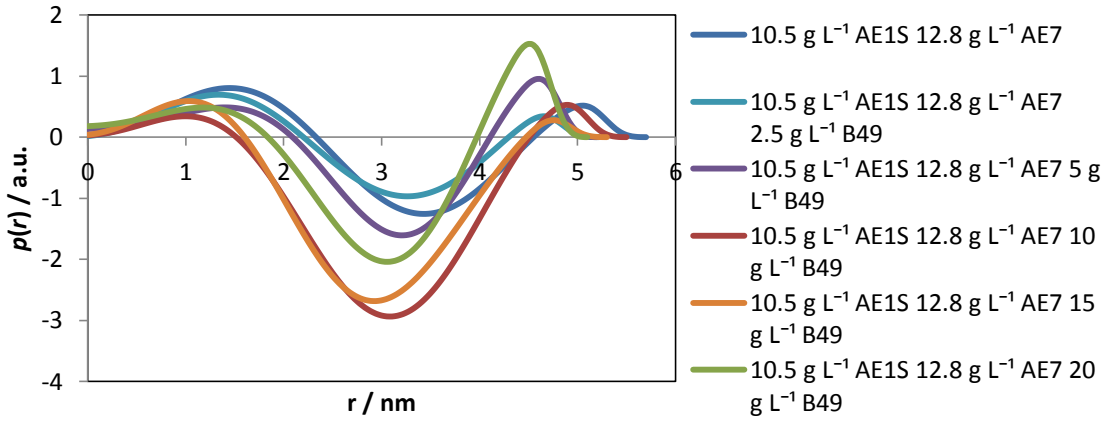

Figure 5-28: Pair distribution function *p*(*r*) for AE1S & AE7 systems with and without B49

The inner core and micellar radii determined from these pair distribution functions are shown in Table 5-16 below.

Table 5-16: Inner core and micellar radii for AE1S/AE7

Concentration of brightener / g L^{-1}	**Inner core radius / nm**	**Micellar radius / nm**
0	2.2	2.9
2.5	2.1	2.6
5	2.0	2.6
10	2.0	2.7
15	1.9	2.6
20	2.0	2.6

It can be shown that, although there was some slight fluctuation in the inner core and outer shell radii of the system, these were not large, and there was no correlation between the brightener concentration and either the inner core radius or the micellar radius. This shows that the addition of brightener did not affect the size of the micelle.

To determine the effect of the brightener on the electron density of the system, the pair distribution functions were normalised to the first peak. These normalised pair distribution functions are shown in Figure 5-29 overleaf, and the heights of the second peaks relative to the first are shown in Figure 5-30 overleaf.

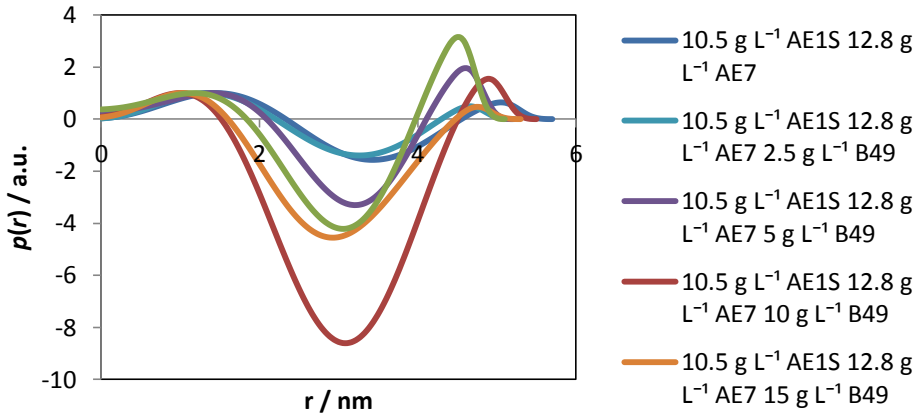

Figure 5-29: Pair distribution function *p*(*r*) for AE1S & AE7 systems (normalised to first peak)

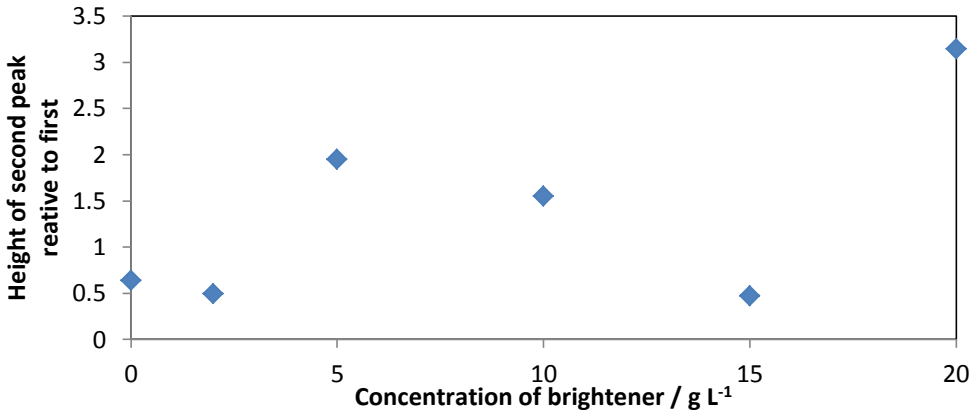

Figure 5-30: Change in height of second peak with change in brightener concentration in AE1S & AE7 systems

It can be seen that, although there was some scatter in the data (in particular, the sample containing 15 g L^{-1} brightener appeared at first to be an outlier), the height of the second peak increased relative to the first as the brightener concentration increased. It was not immediately clear whether this change is due to the error inherent in GIFT analysis or due to an actual change in the structure of the micelle with increasing brightener concentration; when repeated, the 15 g L^{-1} brightener sample gave a value of 0.53 for the height of the second peak relative to the first, suggesting that this value was not just an outlier, and that a large amount of the variation was due to error. If the change was due to a change in the electron density of the micelle, the increase in the height of the second peak seen indicated that either the electron density contrast between the outer shell and the solvent was increasing, and so the electron density of the outer shell was increasing, showing that the brightener was being incorporated into the outer shell (if the 'constant core' model holds), or that the electron density contrast between the inner core and the solvent was decreasing, and so the electron density of the inner core was increasing,

showing that the brightener was being incorporated into the inner core (if the 'constant shell' model holds). To distinguish between the models in this case, the radial electron density was found using DECON.

5.1.4.3. DECON

The radial electron density of each sample was found using DECON; the resulting functions are shown in Figure 5-31 below.

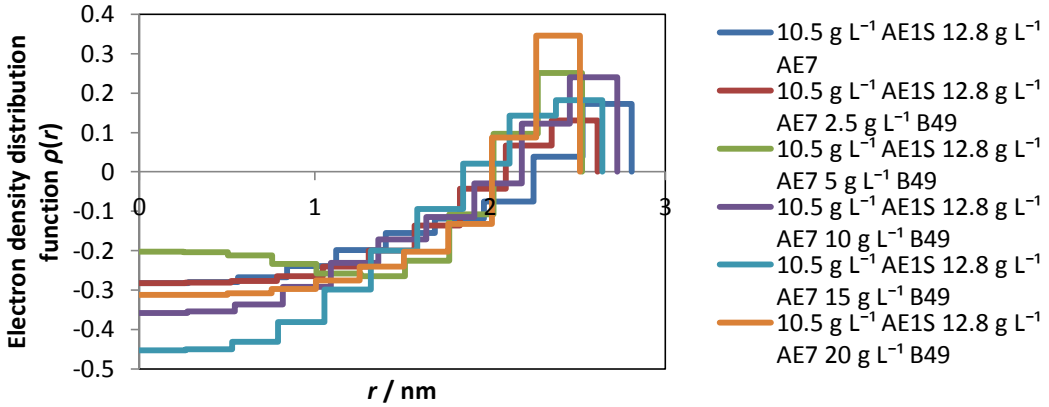

Figure 5-31: DECON results for AE1S & AE7 systems

The maxima and minima of these functions are shown in Figure 5-32. These were used to calculate the electron densities given in Table 5-18 in Section 3.1.4.4.

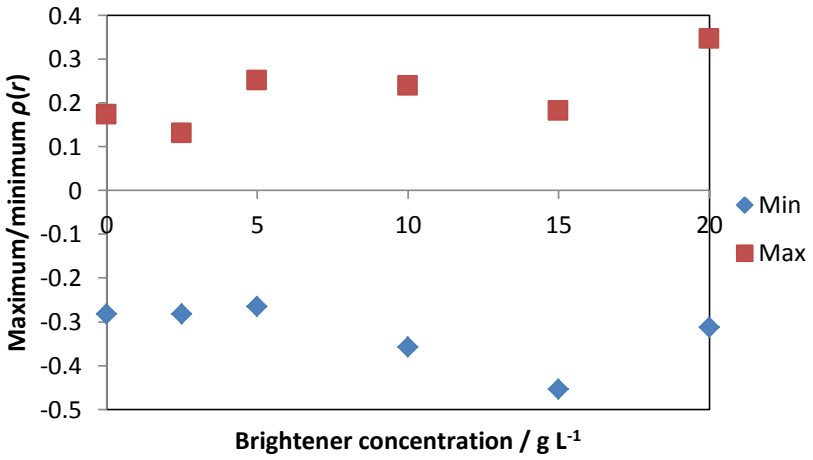

Figure 5-32: Minimum and maximum peak height for DECON systems (AE1S & AE7 systems)

The electron densities generated in this instance were compared to those found using the simple core shell form factor model, using both a 'constant core' and 'constant shell' model.

5.1.4.4. Modelled core-shell form factor

The sample containing no brightener was modelled first, to give a basis for comparison. The micelle radii obtained from GIFT analysis, and the inner core electron density of 0.26 $e^- Å^{-3}$ expected from a liquid hydrocarbon core, were used as the initial parameters. The final parameters are given in Table 5-17 below.

Table 5-17: Parameters used to fit 10.5 g L^{-1} AE1S 12.8 g L^{-1} AE7 sample

Parameter	Value
Inner core radius / nm	2.20
Micellar radius / nm	2.85
Inner core electron density / $e^- Å^{-3}$	0.26
Outer shell electron density / $e^- Å^{-3}$	0.387
Background	15
Multiplier / $x10^{10}$	6.4

As previously, the aggregation number for these micelles could be estimated; this was given as 81 – 131.

Table 5-18 gives the modelled electron densities for all concentrations of brightener. Each concentration was modelled twice: first keeping the electron density of the outer shell at 0.387 $e^- Å^{-3}$, and secondly keeping the electron density of the inner core constant at 0.26 $e^- Å^{-3}$. The inner core and micellar radii were kept constant, but the background and multiplier were changed as required. The values for the electron density generated in this way were compared to those calculated using DECON in Figure 5-33 overleaf.

Table 5-18: Parameters for changing B49 concentration. Modelled electron densities are given for inner core (with outer shell electron density constant at 0.387 $e^{-}Å^{-3}$), and outer shell (with inner core electron density constant at 0.26 $e^{-}Å^{-3}$)

Concentration of brightener / g L^{-1}	Electron density of inner core (shell kept constant) / $e^{-}Å^{-3}$	Electron density of outer shell (core kept constant) / $e^{-}Å^{-3}$	Electron density of inner core (DECON) / $e^{-}Å^{-3}$	Electron density of shell (DECON) / $e^{-}Å^{-3}$
0	0.260	0.387	0.05	0.50
2.5	0.267	0.390	0.05	0.46
5	0.275	0.400	0.06	0.58
10	0.290	0.430	-0.03	0.57
15	0.295	0.430	-0.12	0.51
20	0.295	0.450	0.02	0.68

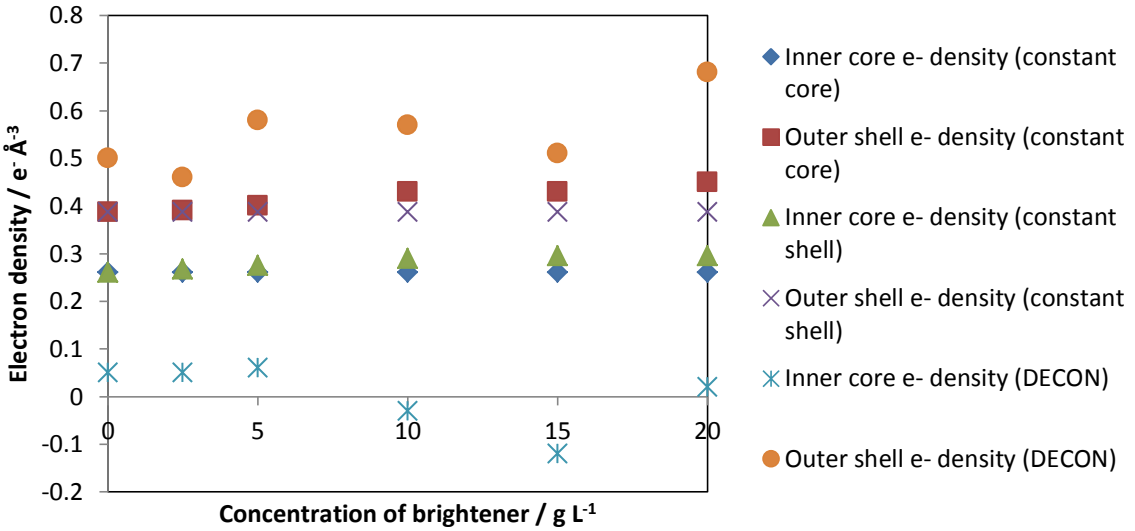

Figure 5-33: Effect of brightener concentration on electron density, as given by both models and by DECON

It can be seen that the electron densities obtained by the core-shell model did not correspond well to those obtained by DECON. This was not surprising as DECON failed to give physically realistic values for the electron densities, suggesting that the micelle was not spherical in this instance. However, the trend seen in the electron densities for the 'constant core' model was comparable to that seen in the DECON values; as the concentration of brightener increased, the electron density of the core remained constant (core shell model) or fluctuated randomly (DECON), while the electron density of the outer shell increased. This would suggest that the brightener was being incorporated into the outer shell of the micelle.

5.1.4.5. Conclusions

The data collected suggested that the brightener molecules were being incorporated into the outer shell of the mixed AE1S-AE7 micelles. However, DECON results suggest that these micelles could not fully be modelled using a spherical model.

5.1.5. Nonionic surfactant AE7 + cationic surfactant DEEDMAC + Brightener 49

SAXS data was taken for samples of 12.3 g L^{-1} AE7, 4.94 g L^{-1} DEEDMAC with varying concentrations of Brightener 49. These are shown in Figure 5-34 overleaf.

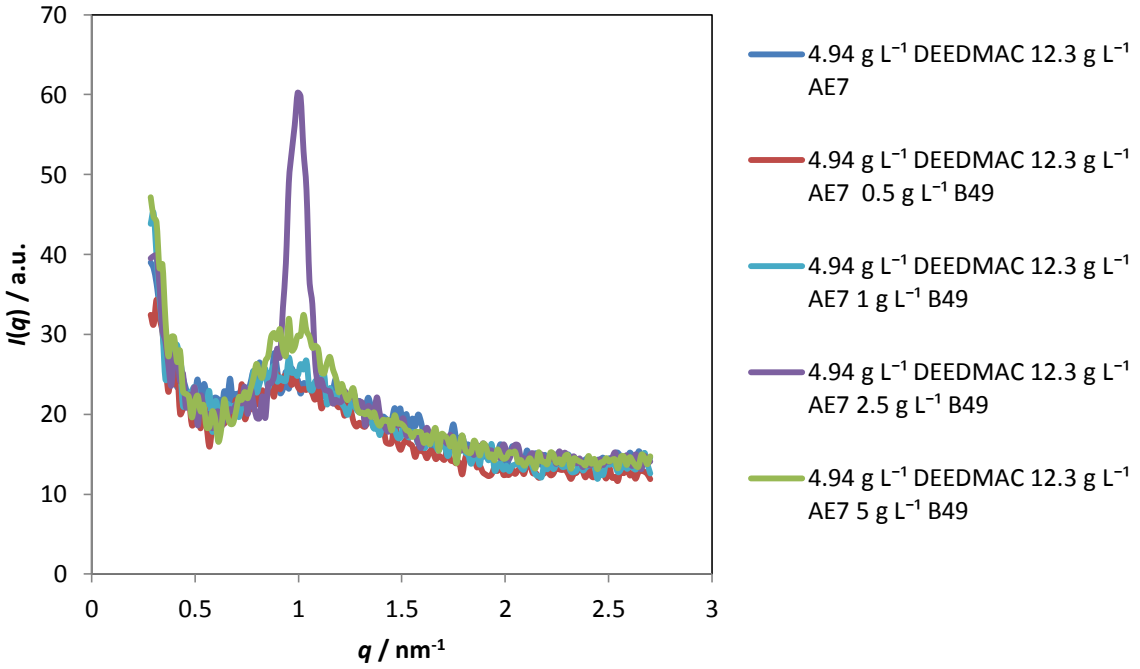

Figure 5-34: SAXS scattering for solutions of 4.94 g L^{-1} DEEDMAC, 12.3 g L^{-1} AE7, and varying concentrations of B49

The peak seen in $I(q)$ did not shift to higher or lower q as the concentration of brightener was changed. However, in all brightener-containing samples, a precipitate was formed, and in the sample containing 2.5 g L^{-1} B49, a sharp peak is seen in $I(q)$, indicating the presence of crystalline material. This precipitation effect was not unexpected; as the brightener and DEEDMAC have oppositely charged groups, it would be expected that they form a precipitate. As cationic surfactants are generally not used in large quantities in the wash solution, this is unlikely to have a great impact for standard wash conditions; however, future work in this area could look at the impact of the cationic surfactants found in fabric softener on brightener deposition and retention on the fabric. In addition, the solubility of DEEDMAC is known to be extremely low, and at the concentrations used

it is known to be dispersed rather than dissolved. Therefore, the peak in the initial sample is likely to be precipitated DEEDMAC.

As the peak seen in Figure 5-34 was due to the precipitation of crystalline material and not the micelle, further analysis was not carried out on this system.

5.2. Surfactant and calcium ions: hard water systems

In this section of work, calcium chloride was added to surfactant systems in order to mimic the effect of hard water. The concentrations used were chosen to be of the same order of magnitude as in hard water areas of the UK; while hard water is defined as that containing greater than 150 ppm, equivalent to 0.17 g L^{-1} $CaCl_2$, the hardest water areas of the UK can far exceed this. For example, the city of Brighton and Hove and its surrounding area has a water hardness of up to 300 ppm, equivalent to 0.33 g L^{-1} $CaCl_2$.[162]

5.2.1. Nonionic surfactant AE7 + $CaCl_2$

5.2.1.1. Raw data

SAXS data was collected for systems containing 25.6 g L^{-1} AE7 and varying concentrations of calcium chloride. This data is shown in Figure 5-35 below.

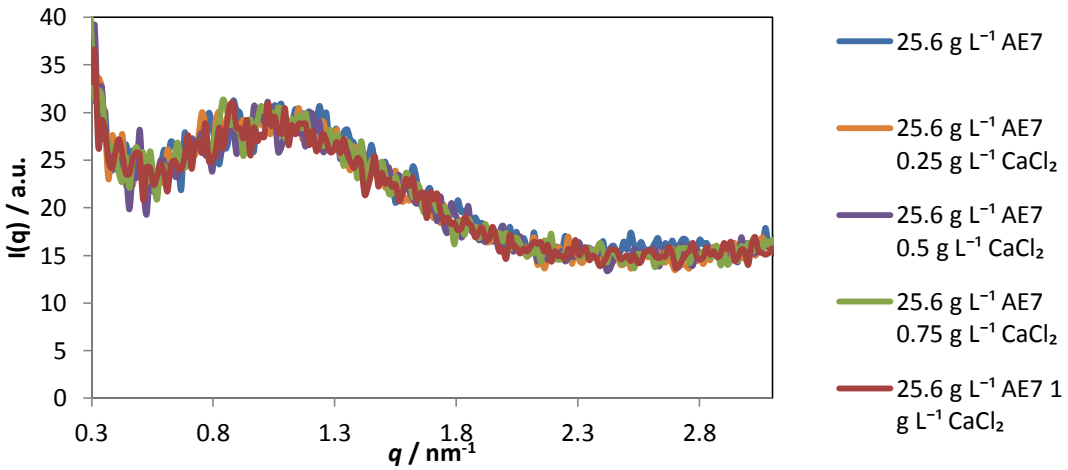

Figure 5-35: SAXS data for systems with AE7 & $CaCl_2$

It can be seen from this data that changing the concentration of $CaCl_2$ had little to no effect on the scattering curve of AE7; this would suggest that the Ca^{2+} ions were not interacting with the AE7 micelle. To confirm this effect, the pair distribution functions of these samples were found.

5.2.1.2. GIFT analysis

The pair distribution functions of the AE7 and $CaCl_2$ systems were found using GIFT analysis. These are shown in Figure 5-36 overleaf.

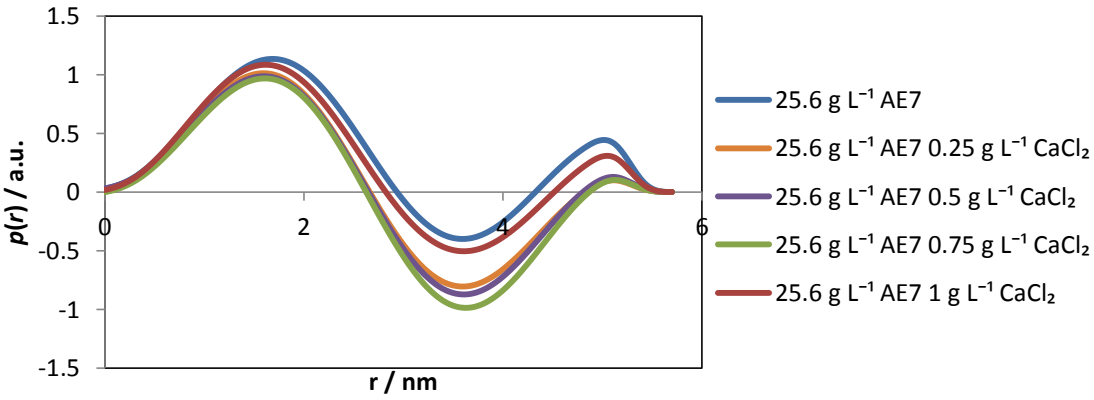

Figure 5-36: Pair distribution function $p(r)$ for AE7 & $CaCl_2$ systems

To see the effect more clearly, these curves were normalised to the height of the first peak. The resulting curves are seen in Figure 5-37 below. The heights of the second peaks relative to the first are seen in Figure 5-38.

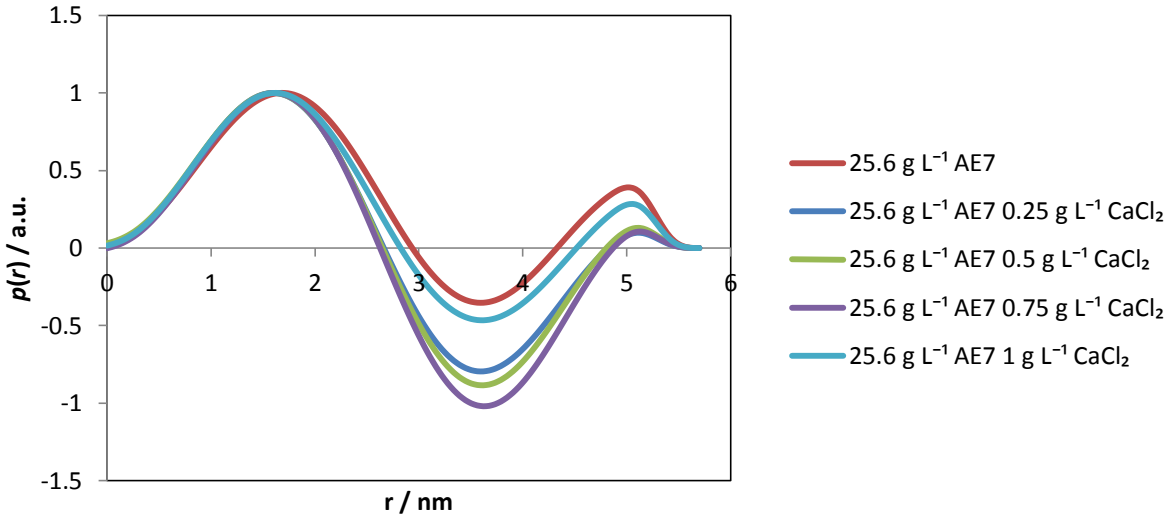

Figure 5-37: Pair distribution function $p(r)$ for AE7 & $CaCl_2$ systems (normalised to 1st peak)

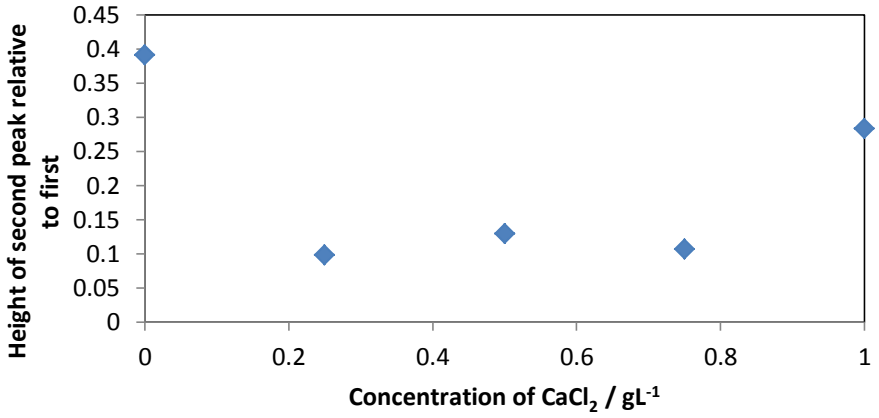

Figure 5-38: Heights of second peaks relative to first for the AE7 + $CaCl_2$ system

Although there was a lot of scatter in this data, there was no correlation between the concentration of $CaCl_2$ and the height of the second peak. This indicated that the calcium ions were having little to no impact on the electron density of the micelles formed.

The inner core and micellar radii obtained from this data are shown in Table 5-19 below.

Table 5-19: Inner core and micellar radii for AE7 micelles with varying concentrations of $CaCl_2$

Concentration of brightener / g L^{-1}	Inner core radius / nm	Micellar radius / nm
0	2.2	2.9
0.25	2.2	2.9
0.50	2.2	2.9
0.75	2.2	2.9
1.0	2.2	2.9

It can be seen that there was no change in the micellar radii as the concentration of $CaCl_2$ increased. This showed that the calcium chloride at these concentration levels was not affecting the structure of the micelle.

5.2.1.3. Modelled core-shell form factor

The SAXS $I(q)$ vs q data for the sample of 25.6 g L^{-1} AE7 was fit to a core shell form factor curve with the following parameters:

Table 5-20: Parameters to model 25.6 g L^{-1} AE7

Parameter	Value
Inner core radius / nm	2.2
Micellar radius / nm	2.9
Inner core electron density / $e^{-}Å^{-3}$	0.260
Outer shell electron density / $e^{-}Å^{-3}$	0.369
Background	15
Multiplier / $x10^{10}$	7.5

The inner core and micellar radii were taken from the pair distribution functions of this system, while the initial electron densities used were taken from the electron densities for the AE7 micelles found in Section 3.1.1.

The remaining samples were then modelled by changing either the electron density of the inner core, or the electron density of the outer shell. The results of this are shown in Table 5-21 below.

Table 5-21: Modelled electron densities for AE7 + $CaCl_2$

Concentration of $CaCl_2$ / g L^{-1}	Electron density of inner core (shell constant) / $e^{-}Å^{-3}$	Electron density of outer shell (core constant) / $e^{-}Å^{-3}$
0	0.260	0.369
0.25	0.255	0.366
0.50	0.258	0.368
0.75	0.257	0.366
1.0	0.256	0.366

When the 'constant shell' model was used, there was no change in the electron density of the inner core as the calcium chloride concentration is increased. When the 'constant core' model was used, there was a slight decrease in the electron density of the shell when calcium chloride was added, but this did not decrease further as more calcium chloride was added. This suggests, again, that the addition of calcium ions had little impact on the structure and electron density of the micelle. Physically, this probably means that the calcium ions were not interacting with the surface of the micelle. This is to

be expected, as the micelle had no ionic groups with which the ions may have strongly interaced. In addition, nonionic surfactants are known to be more stable in hard water than anionic surfactants, and thus would have been expected to interact less with them.

5.2.1.4. Conclusions

The addition of calcium chloride was not seen to have any strong effect on the electron densities of AE7 micelles. This suggested that the calcium ions were not interacting with the nonionic surfactant micelles.

5.2.2. Anionic surfactant AE1S + $CaCl_2$

5.2.2.1. Raw data

SAXS data was generated for a range of $CaCl_2$ concentrations of 0.25 g L^{-1} to 1 g L^{-1}, in 21.0 g L^{-1} AE1S solution. The results are shown in Figure 5-39 overleaf.

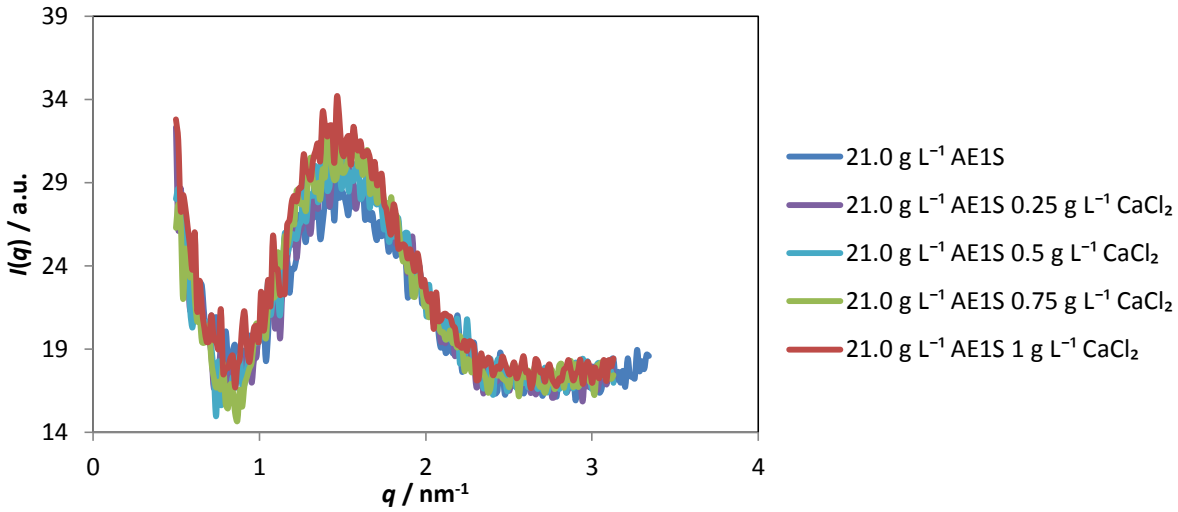

Figure 5-39: Raw SAXS data for AE1S + $CaCl_2$

It can be seen that there was little to no shift in the position of the peak in $I(q)$. This would suggest that there was little change in the size and structure of the scattering particles as the concentration of calcium ions was increased. While the precipitation of anionic surfactants in the presence of calcium and magnesium ions found in hard water is well documented[163], it should be noted that in this instance, the concentration of anionic surfactant used was far greater than that found in the typical wash solution, and thus the molarity of the surfactant will far outweigh that of the calcium ions: the highest concentration in terms of mol dm^{-3} of calcium ions used was only 15% that of the surfactant, at 0.0090 mol dm^{-3} $CaCl_2$, compared to 0.059 mol dm^{-3} AE1S. Therefore,

despite the increased valency of the calcium compared to the original sodium counterion, these results are not unexpected.

5.2.2.2. GIFT analysis

The pair distribution function of each system was calculated through GIFT analysis. The results of this are shown in Figure 5-40, and are shown normalised to the first peak in Figure 5-41.

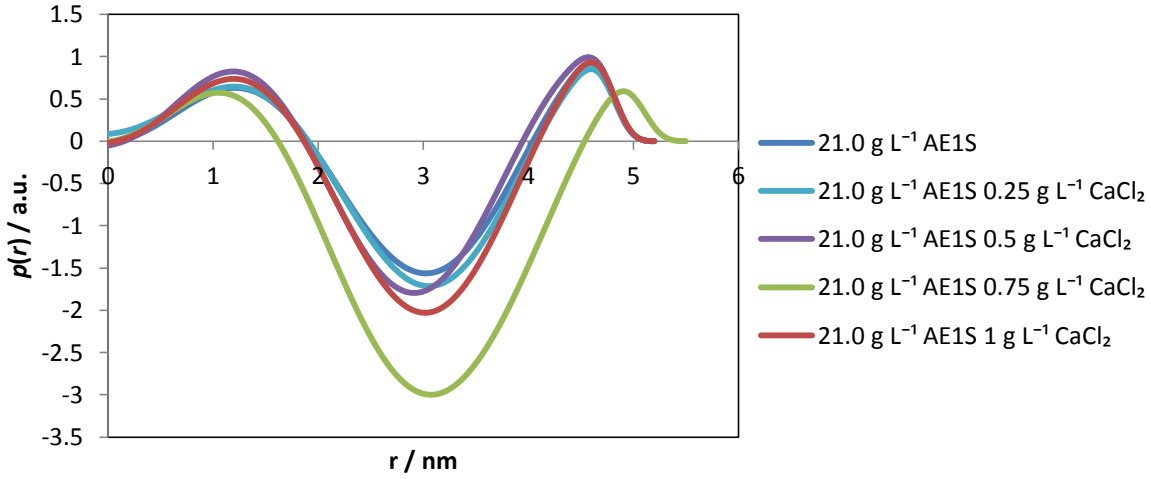

Figure 5-40: Pair distribution functions for AE1S + $CaCl_2$ systems

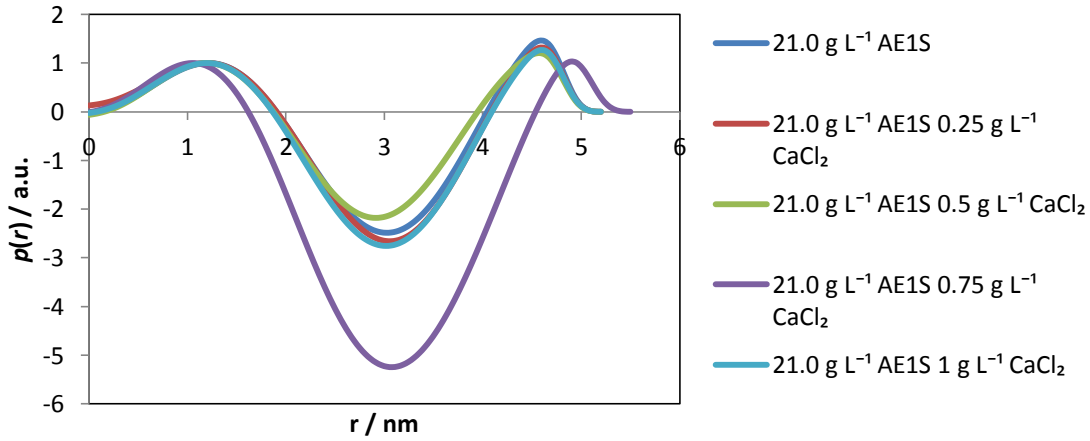

Figure 5-41: Pair distribution functions for AE1S + $CaCl_2$ systems (normalised to 1st peak)

The changes in the heights of the second peaks, relative to the first, are given in Figure 5-42.

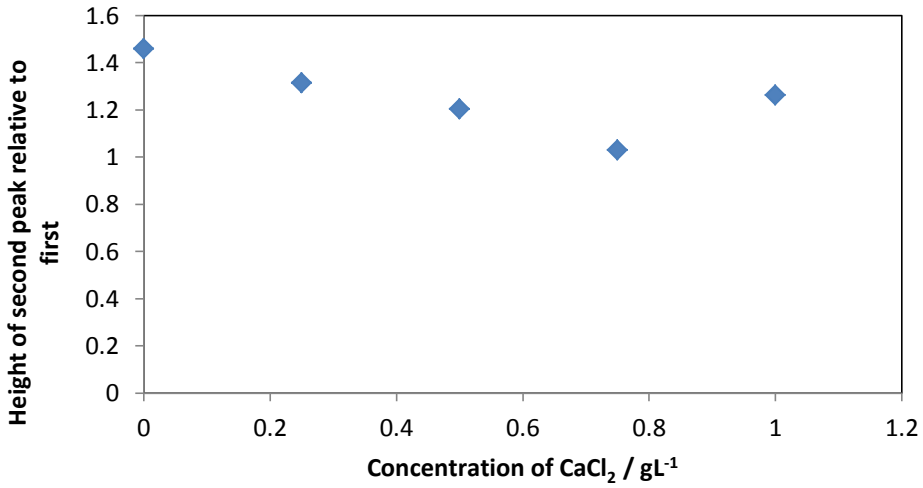

Figure 5-42: Change in height of second peak with change in $CaCl_2$ concentration

The inner core and micellar radii obtained through GIFT analysis are given in Table 5-22 below.

Table 5-22: Inner core and micellar radii for AE1S system with varying concentrations of $CaCl_2$

Concentration of $CaCl_2$ / g L^{-1}	Inner core radius / nm	Micellar radius / nm
0	2.0	2.6
0.25	2.0	2.6
0.5	1.9	2.6
0.75	2.1	2.8
1	2.0	2.6

It can be seen that there was very little change in the inner core and micellar radii of the micelles as the concentration of calcium chloride increased. This suggests that the structure of the micelles was not being strongly affected by the addition of the calcium ions at these concentration levels. There was also little change in the height of the second peak in relation to the first. This would indicate that the electron density was not being greatly affected.

5.2.2.3. Modelled core-shell form factor

The parameters from Table 5-9 above were again taken as those for 21.0 g L^{-1} AE1S. The electron densities of the inner core and outer shell were again varied (while keeping the other factor constant). The results obtained are shown in Table 5-23 below.

Table 5-23: Parameters to fit 21.0 g L^{-1} AE1S, with and without $CaCl_2$, for the constant shell and constant core models.

Concentration of $CaCl_2$ / gL^{-1}	Electron density of inner core (shell constant) / $e^{-}Å^{-3}$	Electron density of outer shell (core constant) / $e^{-}Å^{-3}$
0	0.26	0.40
0.25	0.26	0.40
0.5	0.25	0.40
0.75	0.26	0.40
1	0.25	0.39

It can be seen that the electron density was not greatly affected by an increase in calcium chloride concentration.

5.2.2.4. DECON

The radial electron density for each $CaCl_2$ concentration was generated using DECON. These are shown in Figure 5-43 below. The maxima and minima of these curves are shown in Figure 5-44.

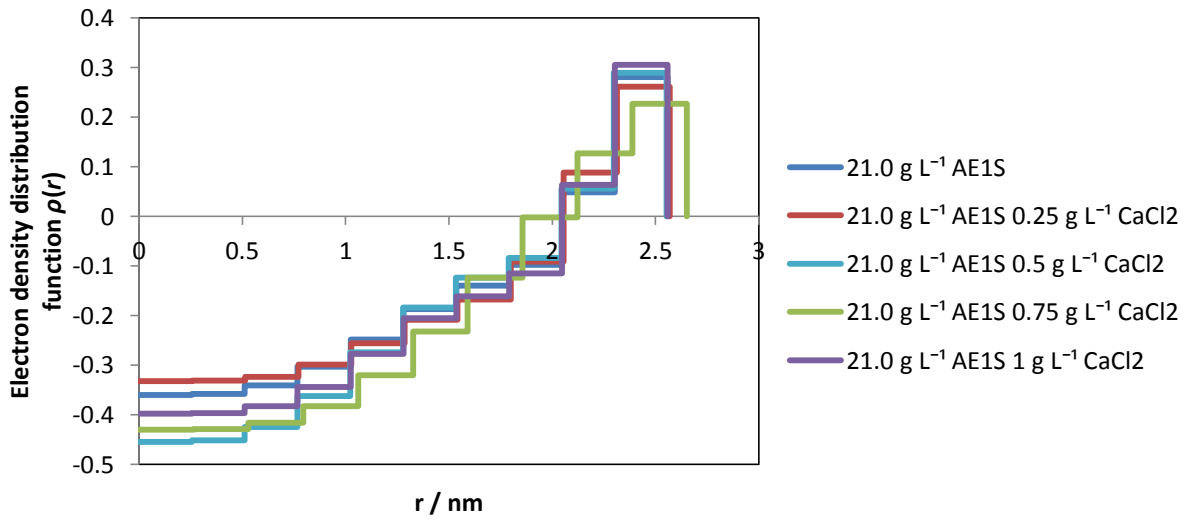

Figure 5-43: DECON results for AE1S + $CaCl_2$ systems

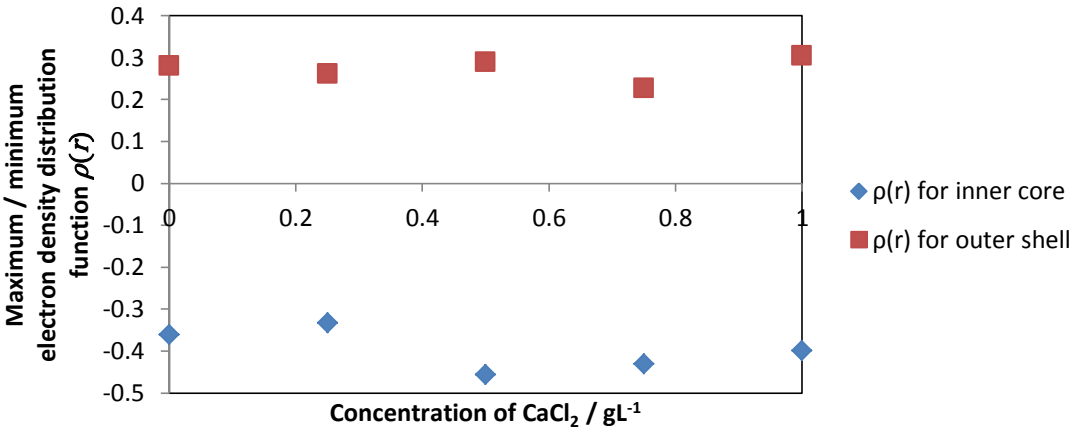

Figure 5-44: Maximum and minimum ρ(r) for AE1S + $CaCl_2$ systems

The electron densities generated using DECON are shown in Table 5-24 overleaf.

Table 5-24: Electron densities generated using DECON

Concentration of $CaCl_2$ / g L^{-1}	Electron density of core / $e^-Å^{-3}$	Electron density of shell/ e^- $Å^{-3}$
0	-0.03	0.61
0.25	0.00	0.59
0.5	-0.13	0.62
0.75	-0.10	0.56
1	-0.07	0.64

The electron densities generated using DECON are compared to those generated by the model in Figure 5-45 below.

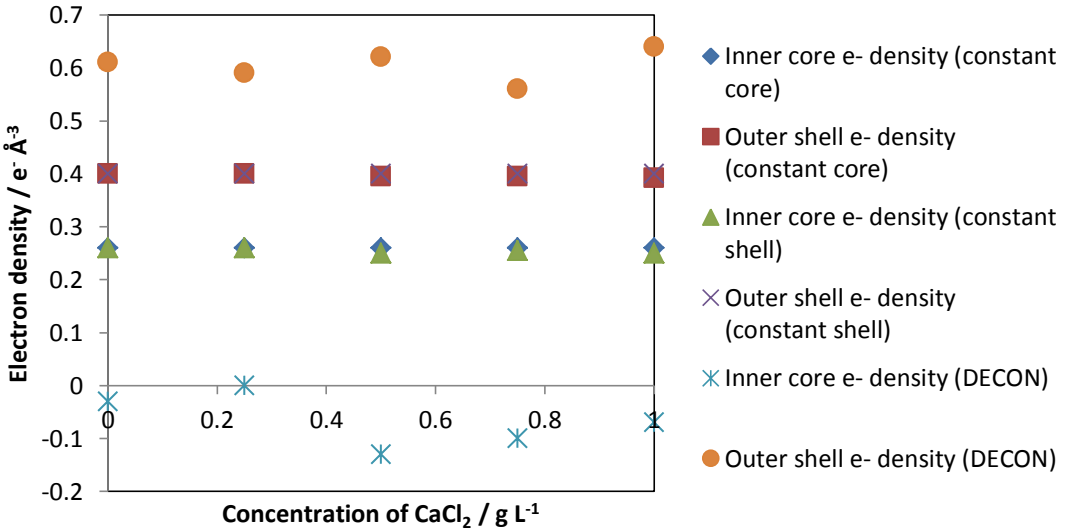

Figure 5-45: Electron densities given by DECON and by the models

As previously for AE1S systems, the electron densities given by DECON were not realistic. This was almost certainly for the same reason. The micelles were sufficiently non-spherical to prevent proper deconvolution of the pair distribution function. However, one trend was seen in both the DECON electron densities and the modelled electron densities; increasing the concentration of $CaCl_2$ was not correlated to a change in the electron density.

5.2.2.5. Conclusions

The addition of calcium chloride was seen to increase the intensity of the peak in the raw SAXS data. However, this did not translate into a change in the size or electron density of the AE1S micelle.

5.3. Conclusions

A number of conclusions can be drawn from the data presented in this chapter.

5.3.1. Shape and size of micelles

It can be seen that the largest micelles produced were the AE7 micelles, with an approximate radius of 3 nm; the smallest were the LAS micelles, with a radius of between 2.0 and 2.2 nm. The AE1S micelles had a radius of about 2.6 nm, which increased when the AE1S was mixed with AE7. This makes sense, as the AE7 had a similar hydrocarbon chain length to the AE1S, but a far longer head group. (The AE7 micelles had an inner core radius of 2.2 – 2.6 nm, whereas the AE1S micelles had an inner core radius of 1.9 – 2.0 nm. As the two surfactants do have a similar chain length, it would be reasonable to expect that they would have a similar inner core radius; the slight difference between them may be caused by the lower aggregation number of the AE1S micelle, being 63 – 103 for the AE1S micelle compared to 159 – 229 for the AE7 micelle, and the nonspherical configuration of the AE1S micelle, as indicated by the DECON results, and further shown in Chapter 6.)

In addition to their increased radius, the nonionic AE7 micelles appear to have been more spherical than their anionic counterparts. The DECON method used to calculate electron densities gave reasonable outputs for the AE7 system, but gave physically impossible results for the AE1S and LAS systems. This was a property of the aggregation which will be discussed in more detail in Chapter 6.

5.3.2. Surfactant-brightener interactions

Every surfactant system used showed some *I*(*q*) peak shift when brightener was included; this would suggest that the brightener was interacting with the surfactants in every system used. However, the change was far greater for the AE7 system than for the AE1S system, suggesting either that the brightener was interacting with the AE7 in greater numbers, or that the brightener was having a greater effect on the electron density of the head group. It can be noted that the AE1S is of similar length to the brightener molecule; the physical implication of the interaction will be discussed further in Chapter 6.

5.3.3. Surfactant-calcium ion interactions

There was no change in the scattering pattern of the AE7 system when calcium ions were added to the system at concentration levels up to 1 g L^{-1}. This shows that the calcium ions were having little impact on the system at these concentrations.

When the calcium ions were added to the AE1S system up to a concentration of 1 g L^{-1}, there was an increase in the intensity of the I(q) peak, but no shift in peak position, and no impact was seen on the micelle radius or electron density. This would suggest that, although the calcium ions were clearly interacting with these micelles, they were not significantly affecting their size, shape, or structure.

5.3.4. Final comments

During this chapter, I have shown through SAXS analysis the effect that the surfactant composition, the addition of brightener, and the addition of calcium ions have had on the shape, size, and electron density of the surfactant micelles. By characterising the micelles before and after the addition of brightener, it was possible to determine the position of the brightener within the surfactant micelle. This links the effect of the surfactant composition on the rate of brightener deposition seen in Chapter 3 to a physical configuration of the system; Chapter 6 will provide further evidence for this physical configuration.

Through SAXS analysis of the AE1S and AE7 systems with various concentrations of Ca^{2+}, it was shown that, although the Ca^{2+} interacted more strongly with the anionic surfactant than the nonionic surfactant, this was not linked to a change in the size or shape of the micelle. Further evidence for this will also be presented in Chapter 6.

6. Molecular dynamics simulations

6.1. Introduction

Molecular dynamics simulations were used to study the configuration of brightener molecules with surfactant micelles of varying composition. This was done to determine the position of the brightener within each surfactant micelle, in order to identify the cause of the effect that surfactant had on brightener deposition and the scattering intensity of mixed brightener/surfactant solutions. In Chapter 3, it was seen that the presence of AE1S promoted brightener deposition, and the presence of AE7 inhibited brightener deposition. The work presented in this chapter aimed to determine the physical differences between these micelle-brightener aggregates, and thus provide an explanation for the effect seen. The selection of surfactant systems used was also expanded, in order to visualise trends in micellar radius and aggregation number caused by their composition. Finally, data will be presented that connected the relative positions of calcium ions seen in hard water to the surfactant micelle, and determined the effect that this had on the system.

Two types of molecular dynamics simulations were run. The first type, using preformed micelles, took surfactant molecules and brighteners arranged in a micelle-type shape, as described in Chapter 2. The second type, using randomised micelles, used surfactant monomers and brightener molecules arranged randomly throughout the cube as defined by the boundary conditions, again as described in Chapter 2.

6.1.1. Previous studies on molecular dynamics simulation of micelles

A large amount of MD work carried out on surfactant systems relies on the micelle being preformed, as codified in the work of MacKerell Jr. In this system[124], and its successors[125,126,164], 60 SDS molecules were aligned along vectors given by C_{60} (buckminsterfullerene), with a small gap in the centre. The system was equilibrated in a vacuum to contract the micelle, then water and ions were added. After this, the molecular dynamics simulation was run. While this system allowed a micelle to be built as desired, by its nature it gave little indication as to the micelle shape formed through self-assembly. In addition, the method of assembly used only allowed for exactly 60 molecules to be used. While this method was acceptable for the study of SDS, the most commonly

used surfactant for such purposes, this method cannot be used for other micelle structures without adapting the method of placement.

The primary reason for the use of preformed micelles is the high computational cost involved in producing a self-assembled system.[165] One commonly used solution is coarse-graining[128,166]; in these systems, groups of 2-4 carbon atoms are represented by one particle, with the head group of the surfactant also represented by one particle. In this way, the entire surfactant molecule can be represented by a short chain of 'beads'. While the use of these models will reduce time and computational power required to run the simulation, some chemical detail will by necessity be lost.

There are several methods commonly used to obtain information from MD data. The radius of gyration is commonly calculated. Another method looks at the distribution of particular atoms within the system, to show the approximate final positions of these groups within the system. The symmetry of the micelle is also commonly studied, showing in many cases that the micelles thus produced have an ellipsoidal nature.[127]

6.1.2. Molecules used to model surfactants

The surfactants used in previous chapters are highly polydisperse. However, for this chapter, a monodisperse surfactant system was used for simplicity. Therefore, one representative molecule was used for each surfactant. The general molecular formulae of these surfactants, and the number of subunits for each example modelled, are given in Table 6-1 below.

Table 6-1: Modelled surfactants used in this chapter

Surfactant	General formula	m	n
AE1S	$CH_3(CH_2)_m(OCH_2CH_2)_nOSO_3^-$	12	1
AE7	$CH_3(CH_2)_m(OCH_2CH_2)_nOH$	14	7
DEEDMAC	$(CH_3)_2(CH_3(CH_2)_mCOOCH_2CH_2)_2N^+$	16	n/a

6.2. Experimental work

6.2.1. Preformed micelles

6.2.1.1. Surfactant systems and water only

To generate this data, preformed micelle systems were created containing surfactants, water, and counterions only in a cubic simulation box. The preformed micelles were spherical with a radius set to the minimum value that would ensure non-overlapping of the initially all-trans configuration tailgroups. The simulation was run for 10 000 ps. A typical initial and final configuration is shown in Figure 6-1 below.

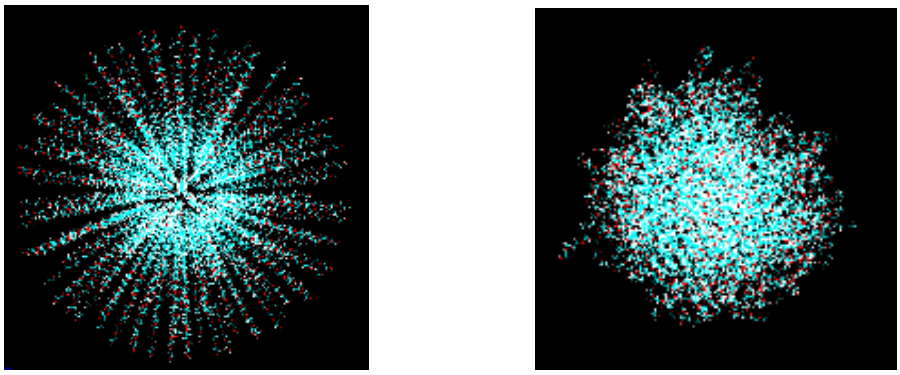

Figure 6-1: Configuration of a system containing 194 AE7 molecules at 303.2 K, before (L) and after (R) MD simulation. Water molecules omitted for clarity. Hydrogen atoms are coloured white, carbon atoms are coloured cyan, and oxygen atoms are coloured red.

The numbers of surfactant molecules used in the simulation were tailored to ensure micelle formation; for the AE7 systems, the number was set to the calculated aggregation number, whereas for the AE1S systems and AE1S/AE7 systems, an estimate for the appropriate number was based on the literature values of the aggregation number of AE1S[32,33] (although the lower end of the range was used to reduce computational load), with the box size taken to mirror the concentrations used. For the AE1S/DEEDMAC system, where an experimental system could not be created due to the precipitation of the surfactants, a 1:1 mix was used. The length of the cubic simulation box and the numbers of surfactant molecules used are shown in Table 6-2 overleaf.

Table 6-2: Composition of preformed micelles used

Surfactant system	Box length / nm	Number of each surfactant
AE7	12	194 AE7
AE1S	8	50 AE1S
AE1S AE7	12	70 AE1S, 50 AE7
AE7 DEEDMAC	12	118 AE7, 38 DEEDMAC
AE1S DEEDMAC	8	25 AE1S, 25 AE7

The mean distance of the start of the tail group, end of the tail group, start of the head group, and end of the head group from the centre of the micelle was then calculated. Hereafter, the atoms used for the tail and headgroups' start and end are referred to as 'marker atoms', as they mark the approximate boundaries of the head and tail group regions. An example of the mean distances found as the simulation proceeded is shown in Figure 6-2 below.

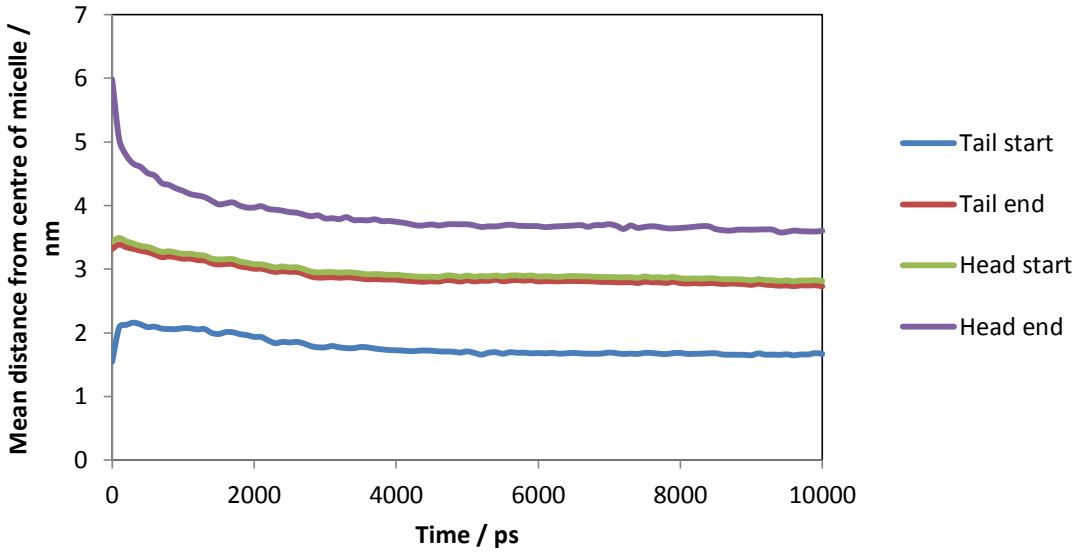

Figure 6-2: Distances of marker atoms from centre of micelle (AE7 system)

The approximate final inner core radius and the micellar radius produced in this way are given in Table 6-3 overleaf.

Table 6-3: Inner core and micellar radii for preformed micelles without brightener

System	Did micelle separate?	Inner core radius / nm	Micellar radius / nm
AE7	No	2.8	3.6
AE1S	No (one monomer separated)	1.6	2.0
AE1S/AE7	Yes	n/a	n/a
AE1S/DEEDMAC	Yes	n/a	n/a
AE7/DEEDMAC	No	2.0	2.3

There were two main issues relating to the centre of the micelle. First, as this centre was not occupied during the initial positioning of the micelle, the GROMACS tool *genbox* would fill this region with water molecules, which does not give an accurate representation of the micelle. The option of removing the water from this centre was not undertaken as this would have led to the micelle having a vacuum at its centre, which is clearly not realistic. Secondly, several of the systems separated into smaller aggregates. While this may be indicative of lower aggregation numbers in these systems, it could also be due to the initial physical distance between surfactant molecules being too great to ensure cohesion.

For this reason, the systems were repeated, placing an innermost core of hexane molecules to prevent a vacuum forming and the subsequent intrusion of water molecules. This also provided a more hydrophobic environment for the surfactant tail groups, and may have helped keep them 'locked in position'. While this may have been physically unrealistic in terms of the aggregation number, this kept the micelle stable and allowed the brightener-surfactant interaction to be modelled.

6.2.1.2. Surfactant and hexane systems

To combat the effect of the surfactant molecules separating, and to prevent water molecules entering the core of the surfactant molecule, a sphere of hexane molecules was added to the centre of the surfactant micelle. The hexane sphere was added in the space created after initially placing the surfactant molecules into a sphere. The hexane was assumed to fill this sphere entirely at its typical density of 0.654 g mL^{-1}. From this, the number of molecules needed to fill the space was calculated. The radius of this central

core, and the number of hexane molecules required to fill it, are shown in Table 6-4 below.

Table 6-4: Radii of hollow core and number of hexane molecules added

System	Radius of hollow core / nm	Number of hexane molecules added
AE7	1.3	42
AE1S	0.78	9
AE1S AE7	1.55	71
AE7 DEEDMAC	3.0	177
AE1S DEEDMAC	1.1	26

The simulation was then run as before. The mean radii of the marker atoms for these systems are shown in Table 6-5 below.

Table 6-5: Mean radii of marker atoms in preformed micelles containing hexane

Sample	Distance from centre of micelle / nm											
	AE1S				AE7				DEEDMAC			
	Tail start	Tail end	Head start	Head end	Tail start	Tail end	Head start	Head end	Tail start	Tail end	Head start	Head end
AE7					1.7	2.8	2.9	3.6				
AE1S	1.2	1.6	1.8	2.1								
AE1S + AE7	1.7	2.5	2.6	3.0	1.6	2.4	2.4	2.7				
AE1S + DEEDMAC	1.5	1.9	2.0	2.4					1.3	2.2	2.2	2.4
AE7 + DEEDMAC					2.1	3.0	3.1	3.6	2.0	3.3	3.4	3.6

The inner core and micelle radius values obtained from the tail and headgroup ends in Table 6-5 data are shown in Table 6-6, with mean values listed for the mixed surfactant systems.

Table 6-6: Inner core and micellar radii of micelles containing hexane

Sample	Inner core radius	Micellar radius
AE7	2.8	3.6
AE1S	1.7	2.1
AE1S + AE7	2.5	2.9
AE1S + DEEDMAC	2.1	2.4
AE7 + DEEDMAC	3.2	3.6

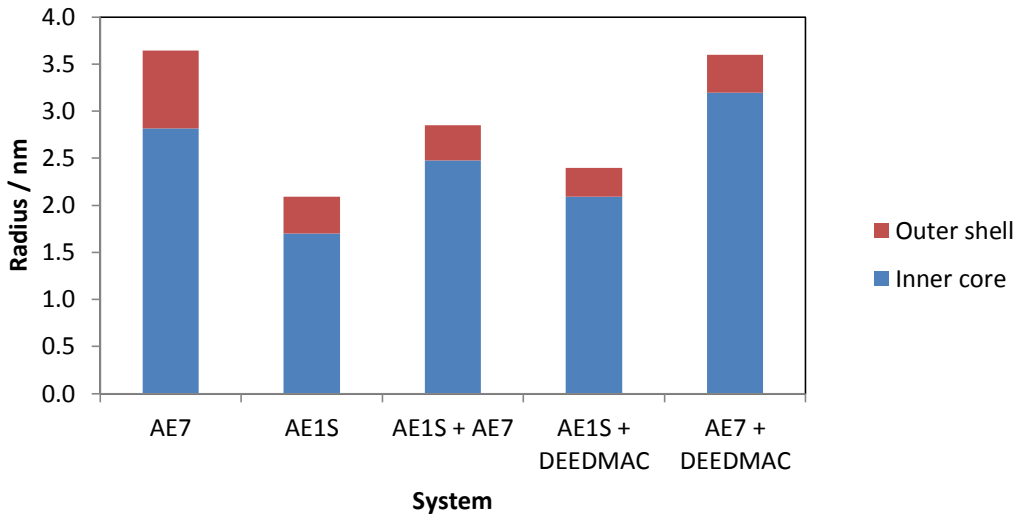

Figure 6-3: Micellar radii of preformed surfactants with hexane cores. Contributions from the inner core and outer shell are shown.

Caution must be taken when comparing these values to each other; as differing amounts of hexane were added to each micelle, this will have artificially swelled the micelles. However, the relative change in values when brightener is added can be compared, to show any effect that the addition of brightener has had on the micelle radius, and to identify how far into the micelle the brightener has penetrated.

6.2.1.3. Surfactant, hexane and brightener systems

For the runs containing brightener in preformed micelles, 5 surfactant molecules were each replaced by 1 brightener molecule. The new compositions of these micelles are given in Table 6-7 below. The brightener molecules were oriented towards the centre of the micelle, as shown in Figure 6-4 overleaf.

Table 6-7: Compositions of the surfactant/hexane/brightener micelles

System	Micelle composition
AE1S	45 AE1S, 5 B49
AE7	189 AE7, 5 B49
AE1S/AE7	67 AE1S, 48 AE7, 5 B49
AE1S/DEEDMAC	22 AE1S, 23 DEEDMAC, 5 B49
AE7/DEEDMAC	115 AE7, 37 DEEDMAC, 5 B49

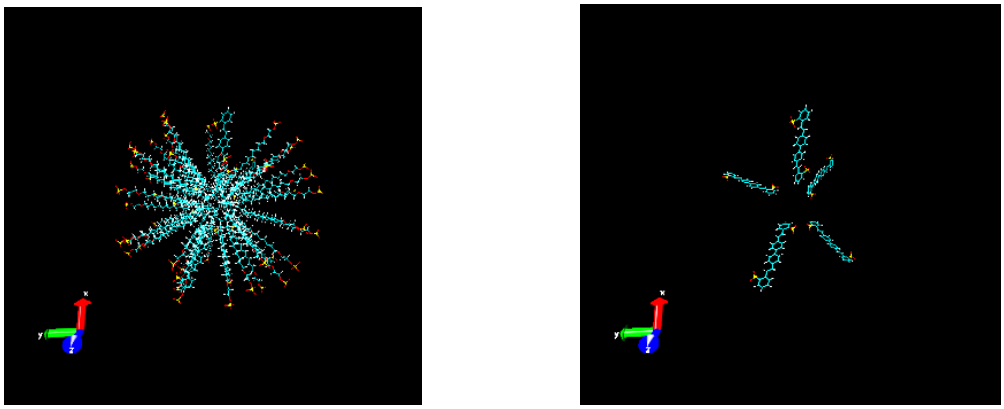

Figure 6-4: Starting configurations for AE1S, hexane and Brightener 49 sample, showing full micelle (L) and brightener only (R). Water molecules omitted for clarity. Hydrogen atoms are coloured white, carbon atoms are coloured cyan, oxygen atoms are coloured red, and sulfur atoms are coloured yellow.

AE1S and DEEDMAC molecules were both comparable in length to Brightener 49, and thus for the AE1S and AE1S/DEEDMAC micelles, the brightener was simply added by substituting it for a surfactant molecule in the micelle. However, the AE7 molecule was significantly longer than the other surfactants and the brightener, and thus when the brightener was added to the AE7, AE1S/AE7, and AE7/DEEDMAC micelles, it could be added into one of three regions; the head group region (brightener had the same micellar radius as the surfactant), the tail group region (one end of the brightener was aligned with the start of the surfactant tail), or an intermediate region. These starting configurations are illustrated in Figure 6-5 below.

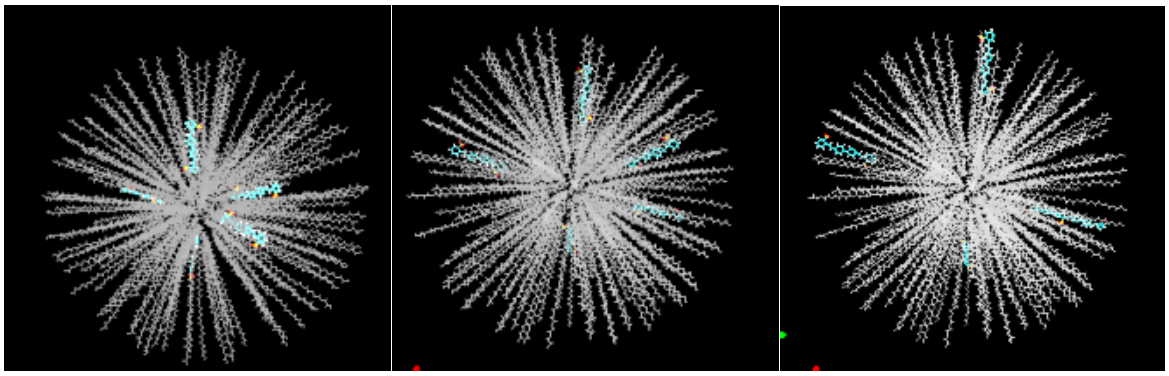

Figure 6-5: AE7 micelle, with hexane, including brightener in the tail group region (L), an intermediate region (C), and head group region (R). Water molecules omitted for clarity. Hydrogen atoms are coloured white, carbon atoms are coloured cyan, oxygen atoms are coloured red, and sulfur atoms are coloured yellow. AE7 molecule has been greyed out.

Figure 6-6, Figure 6-7, and Figure 6-8 show the inner core radii and micellar radii generated in this way, and the positions of the centres of each brightener molecule added to the simulation (labelled as B1 – B5). The centres of the brighteners were calculated by identifying four 'marker atoms' on the brightener: the two sulfur atoms, and the two

carbon atoms closest to the centre of rotational symmetry. The mean position of these four atoms was taken as the centre of the brightener molecule. These simulations were carried out twice; data for both runs are shown. The data is also given numerically in Appendix 1.

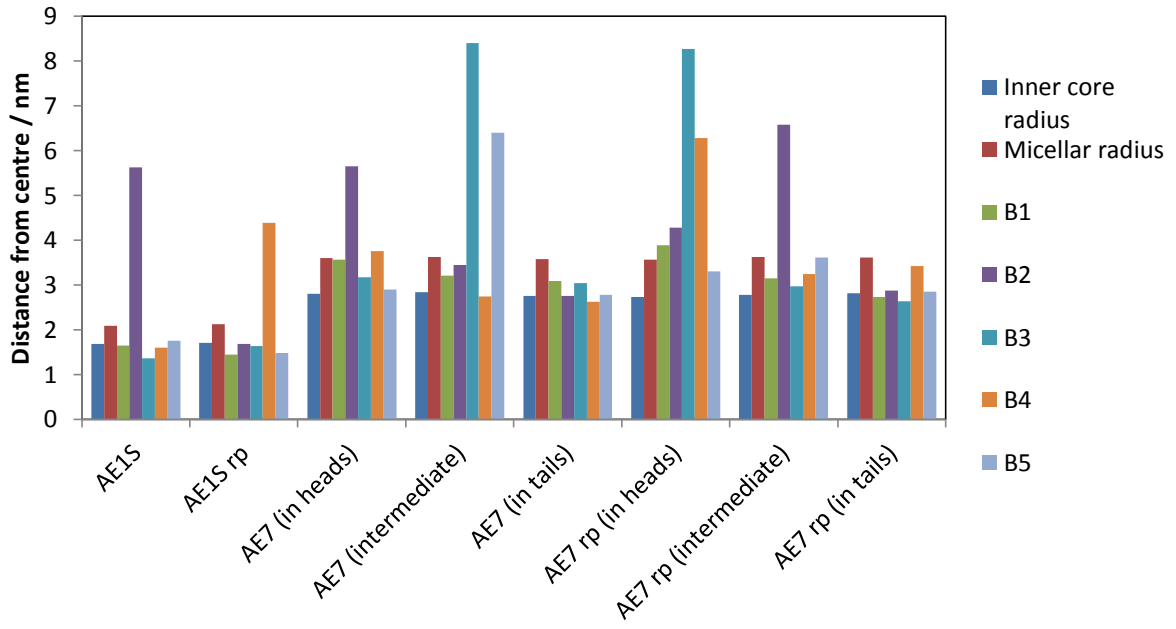

Figure 6-6: Inner core radii, micellar radii, and brightener positions for AE1S and AE7 systems

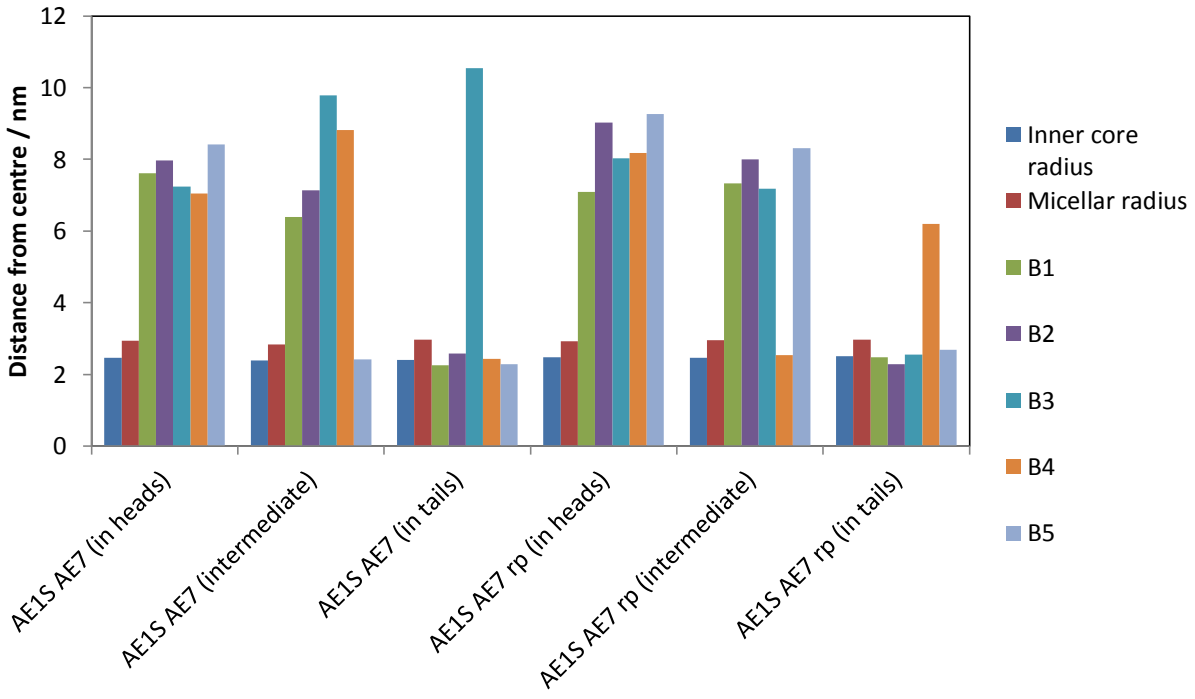

Figure 6-7: Inner core radii, micellar radii, and brightener positions for mixed AE1S/AE7 system

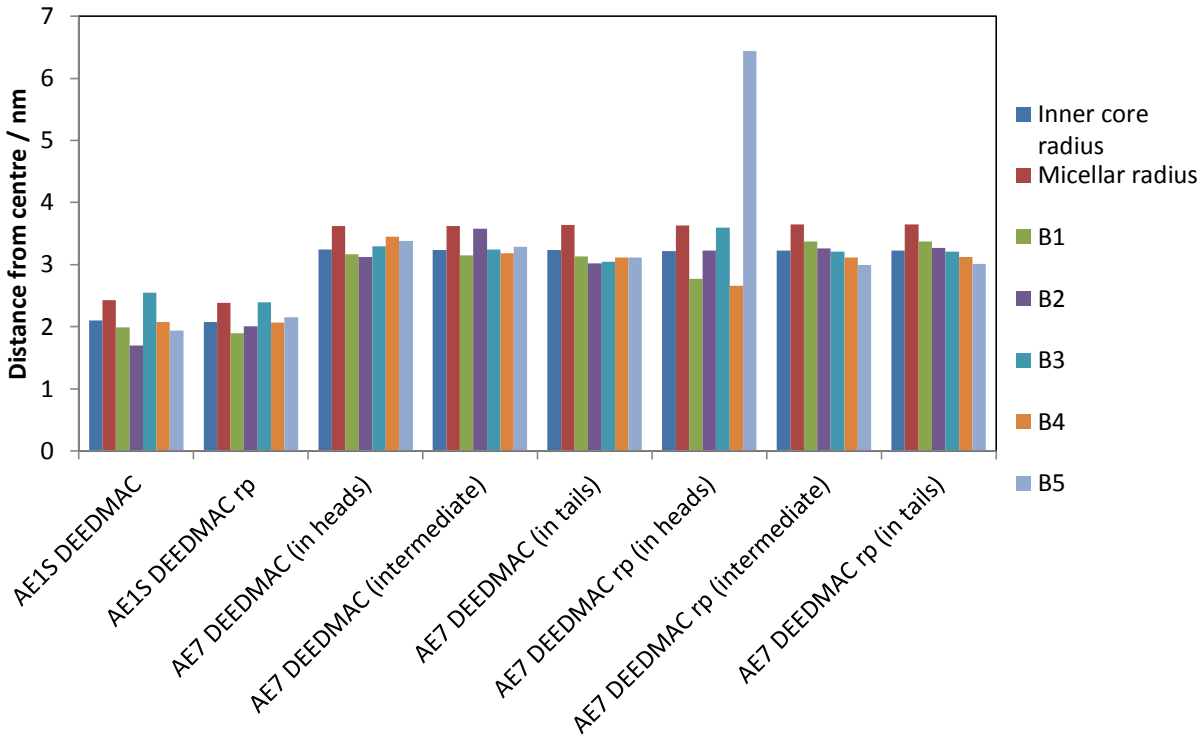

Figure 6-8: Inner core radii, micellar radii, and brightener positions for mixed AE1S/DEEDMAC and AE7/DEEDMAC systems

By looking at the position of each brightener in comparison to the inner core and micellar radii, it was possible to identify in which part of the micelle it had settled. If the distance from the brightener to the centre was significantly less than the inner core radius of the micelle, the brightener was in the inner core, while if its distance was significantly less than the micellar radius but greater than the inner core, it was in the outer shell region. If it was close to the radius of the inner core (i.e. between the lowest and highest value used to calculate the inner core radius), then it was assumed to be between the inner core and outer shell, whereas if it was close to the micellar radius then it was assumed to be on the interface between the outer shell and the solution. If it was significantly greater than the micellar radius then it was assumed to be within the solvent and no longer associated with the micelle.

These positions are shown in Table 6-8 and Figure 6-9 overleaf. Figure 6-6, Figure 6-7 and Figure 6-8 show that there was little deviation between the original set of experiments and the repeated experiments, with far more deviation happening between samples of different types. Therefore, the positions of repeat experiments have been combined with the corresponding original experiments.

Table 6-8: Positions of brighteners in preformed micelles

System	% in tails	% in head/tail boundary	% in heads	% in head/solvent boundary	% in solvent
AE1S	30	50	0	0	20
AE7 (in heads)	0	10	20	30	40
AE7 (intermediate)	0	10	50	10	30
AE7 (in tails)	10	60	30	0	0
AE1S AE7 (in heads)	0	0	0	0	100
AE1S AE7 (intermediate)	0	20	0	0	80
AE1S AE7 (in tails)	0	80	0	0	20
AE1S DEEDMAC	20	60	0	20	0
AE7 DEEDMAC (in heads)	20	60	10	0	10
AE7 DEEDMAC (intermediate)	0	90	10	0	0
AE7 DEEDMAC (in tails)	0	100	0	0	0

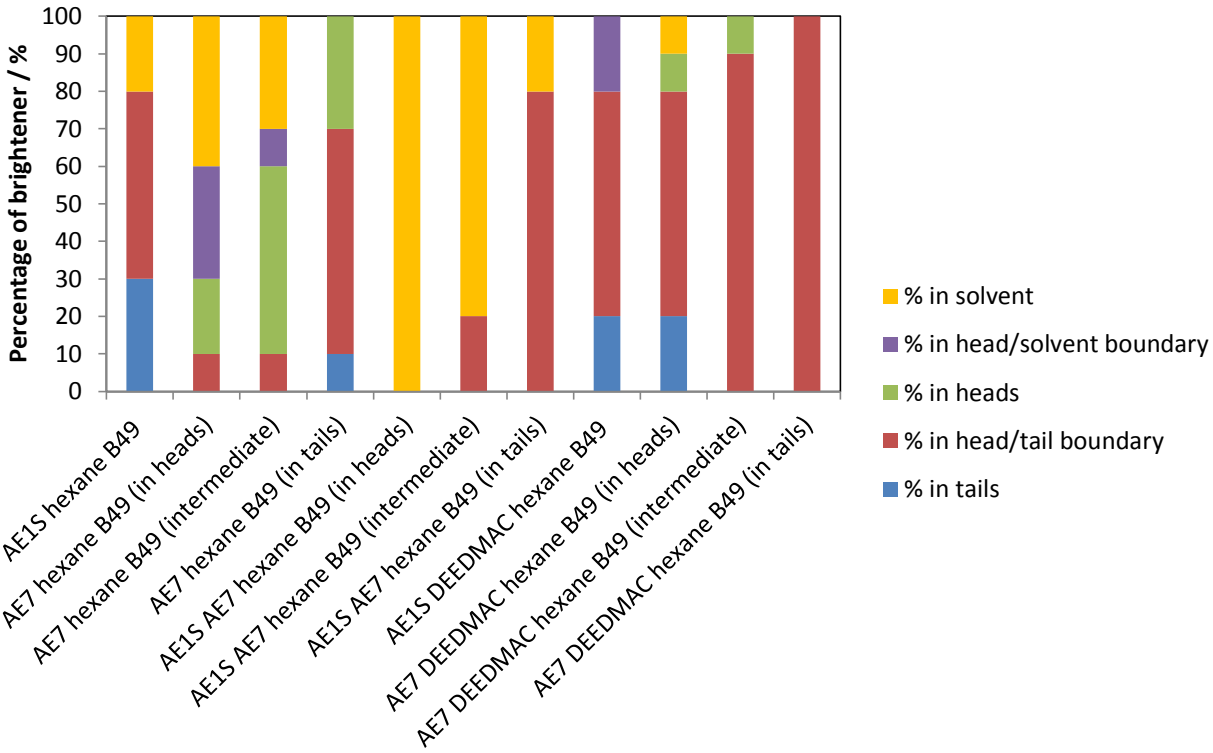

Figure 6-9: Proportion of brightener molecules in each position for each surfactant system

6.2.1.3.1. Single surfactant systems

It can be seen that, for systems where the brightener could initially be placed in multiple positions i.e. AE7, AE1S/AE7, and AE7/DEEDMAC, the initial brightener placement was the most important factor affecting the final brightener position within the micelle. Within the systems containing AE7 (i.e. AE7, AE1S/AE7, and AE7/DEEDMAC), placing the brightener within the head group initially resulted in far more brighteners ending the simulation in the solvent and at the head/solvent boundary than those simulations where the brightener was initially placed within the tail group region or an intermediate position. Similarly, placing the brightener initially within the tail group region resulted in far more brightener molecules ending the simulation within the tail group or at the head/tail boundary than if the brightener was initially placed in the head group or intermediate positions.

If the system was reaching a true thermodynamic equilibrium, then the final brightener position would not be affected by initial placement. Therefore, we can conclude that these systems were not reaching a true thermodynamic equilibrium, just a local equilibrium.

Within the AE1S only system, all of the brightener was found either in the inner core or core/shell boundary by the end of the simulation. This may be for several reasons; the anionic head group carries the same charge as the brightener, so repulsion of like charges may prevent the brightener settling in the outer shell. In addition, the AE1S has a far thinner outer shell than the AE7 (0.4 nm for the AE1S system, compared to 0.8 nm for the AE7 system). As a consequence of the short head groups of the AE1S, all of the brightener was initially placed in the inner core of the micelle, increasing the probability that it would remain in that position.

6.2.1.3.2. Mixed surfactant systems

When the brightener was added to the mixed anionic/non-ionic surfactant system i.e. AE1S/AE7, an interesting result occurred. Every brightener molecule added to the AE1S/AE7 micelles either ended the simulation in the core or core/shell interface, or escaped into the solvent. None was found within the outer shell or shell/solvent interface by the end of the simulation run. This contrasted with the results seen for the pure AE7 surfactant, where 30 – 60 % of the brightener molecules ended the simulation in this region, depending on the initial placement. This suggests that either the repulsion of like charges from the anionic head groups forced the brightener away from the outer shell, the thinner outer shell (0.4 nm for the mixed AE1S/AE7 surfactant system compared to 0.8 nm for the AE7 micelles alone) provided insufficient room for the brightener to be held, or the reduced number of nonionic head groups provided insufficient interactions between the nonionic head groups and the brightener. If each surfactant and brightener molecule in the micelle was assumed to occupy the same area on the surface of the micelle, then for the AE7 system with brightener, the AE7 represented 97.4% of the surface, whereas in the AE1S/AE7 system the AE7 only represented 40.0% of the surface.

The samples containing DEEDMAC (AE7/DEEDMAC and AE1S/DEEDMAC) had a high proportion of brighteners ending the simulation in the core/shell interface; in particular, the AE7/DEEDMAC had an incredibly high proportion end in this position, with 25 out of the 30 brightener molecules in this position by the end of the simulation. It must be noted that the AE7/DEEDMAC micelles had a particularly large region which could be described as the head/tail interface, typically extending from a radius of 3.0 nm to up to 3.5 nm, and a short distance between the end of this region and the end of the head group at ~ 3.6

nm. The distance from the micelle centre at which these regions occur are shown in Table 6-9 and Figure 6-10 below.

Table 6-9: Ranges of radii seen for the head/tail interface region of micelles

System	Core/shell interface radius / nm
AE1S	1.6 – 1.8
AE7	2.7 – 2.9
AE1S AE7	2.3 – 2.7
AE1S DEEDMAC	1.9 – 2.2
AE7 DEEDMAC	3.0 – 3.5

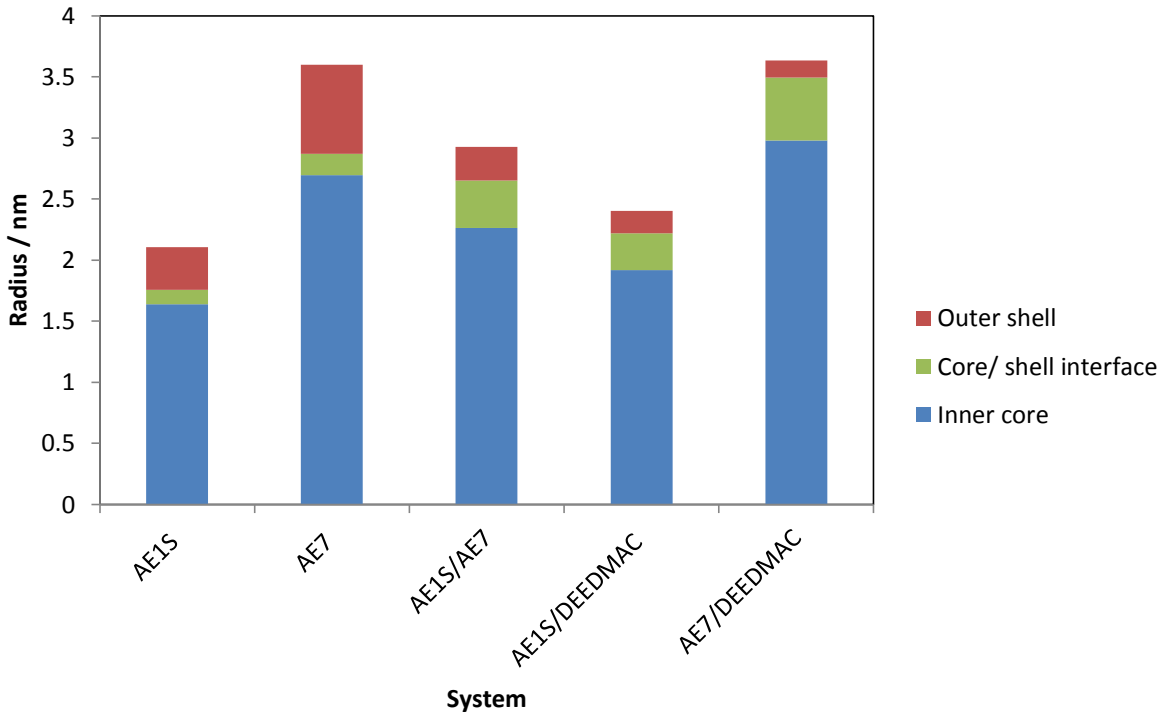

Figure 6-10: Radii of the inner core, core/shell interface, and outer shell regions relative to the micellar radii

The mixed micelle systems generally had a far larger core/shell interface region than the single surfactant systems. If there was a large disparity between the sizes of the surfactants, this was seen as a large core/shell interface, where the head groups of one surfactant occupied the same space as the tail groups of another. This disparity appeared

to be largest in the AE7/DEEDMAC system, likely due to the unusually long length and high aggregation number of the AE7.

6.2.1.4. Conclusions

In conclusion, while it was possible to see some change in brightener interaction between surfactant systems, the data generated in this way was highly dependent on the initial placement of brightener molecules, and on the addition of hexane. This data does provide some information on the relative strength of the interactions between brightener and the surfactant head groups, namely that these interactions were strongest in the AE7 micelles. However, it was imperative to obtain data from micelles generated in a more physically realistic manner (in other words, so that they do not contain hexane cores) to be confident about interactions between the brightener and surfactant molecules. This process is detailed in the following section.

6.2.2. Randomised micelles

6.2.2.1. Surfactant-only systems

To generate this data, randomised systems were created containing surfactants, water, and counterions only in cubic simulation boxes with a length 12 nm. The simulation was run for 40 000 ps. A typical starting and final configuration is shown in Figure 6-11 below.

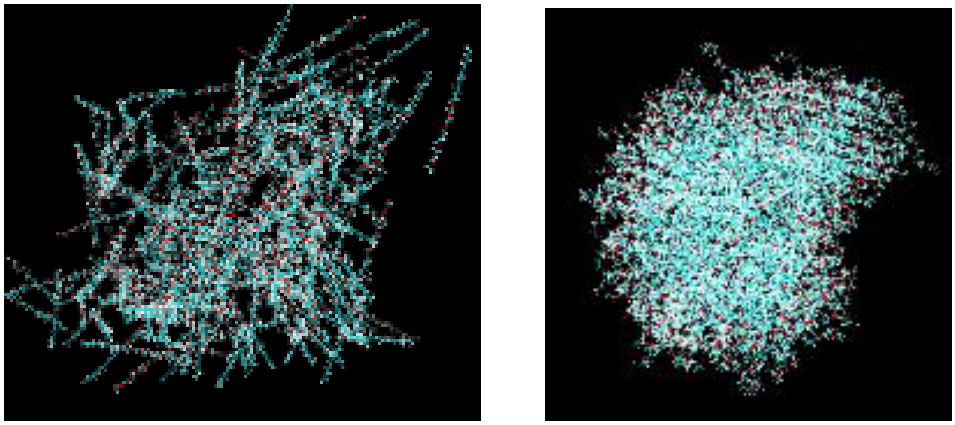

Figure 6-11: Starting and final configuration for randomised AE7. Water molecules omitted for clarity. Hydrogen atoms are coloured white, carbon atoms are coloured cyan, and oxygen atoms are coloured red.

Once the trajectory file was generated, the program described in Chapter 2 was run to generate aggregation numbers and micelle radii for these systems.

6.2.2.1.1. Numerical data: aggregation numbers and micellar radii

The compositions of the micelles are listed in Table 6-10 below.

Table 6-10: Compositions of randomised surfactant systems

System	No. of AE1S molecules	No. of AE7 molecules	No. of DEEDMAC molecules	Total no. of molecules
AE1S	200	0	0	200
AE7	0	200	0	200
AE1S/AE7	100	40	0	140
AE1S/DEEDMAC	100	0	20	120
AE7/DEEDMAC	0	100	50	150
AE1S/AE7/DEEDMAC	100	40	20	160

The number of micelles formed in each system, and the aggregation number calculated using each method, are listed in Table 6-11 and shown in Figure 6-12 and Figure 6-13.

Table 6-11: Number of micelles and aggregation number for each surfactant system

Surfactant system	No. of micelles	No. of monomers	Mean agg. no.	Maximum agg. no.	Monomer-averaged agg. no.
AE7	1	0	200	200	200
AE1S	13	1	15	35	20
AE1S/AE7	8	0	18	33	20
AE1S/ DEEDMAC	7	4	17	27	20
AE7/ DEEDMAC	4	0	38	86	59
AE1S/AE7/ DEEDMAC	7	0	23	33	26

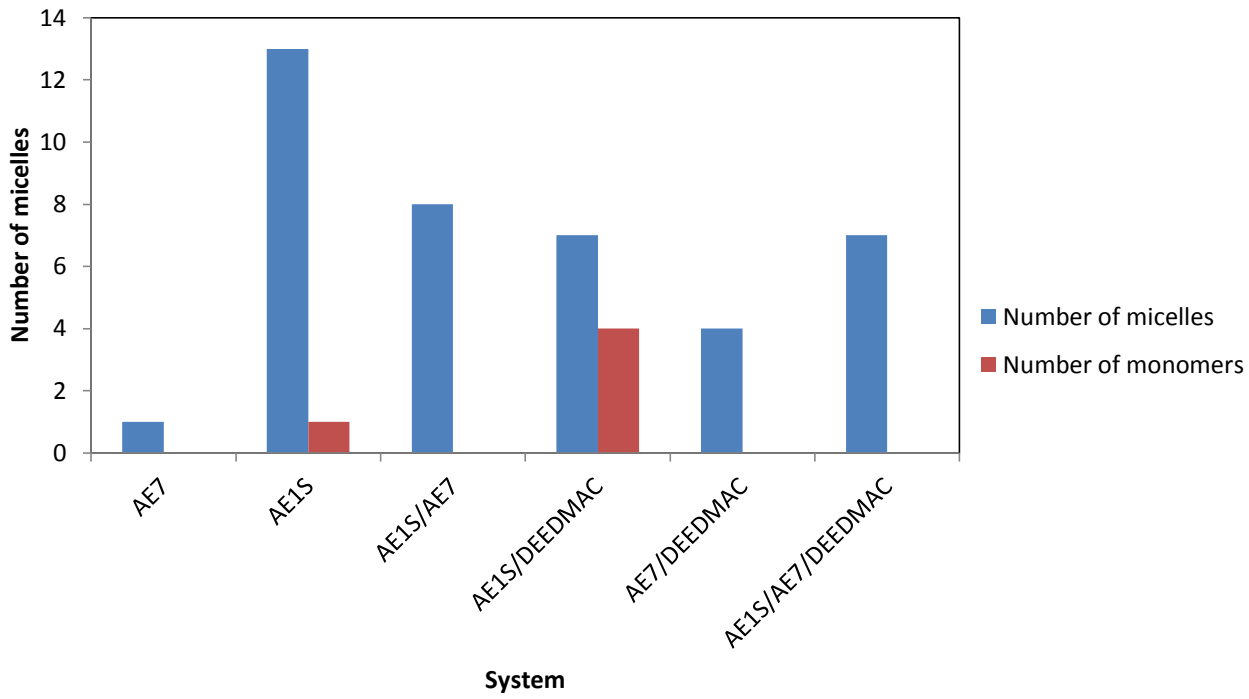

Figure 6-12: Number of micelles produced and number of monomers per surfactant system

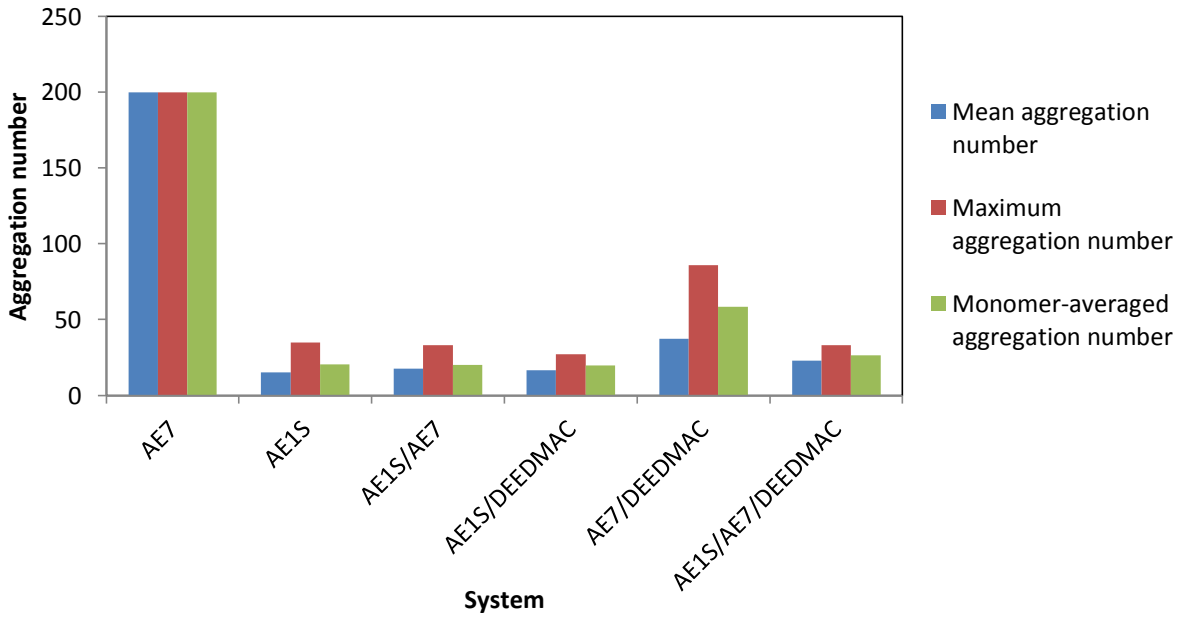

Figure 6-13: Mean, maximum, and monomer-averaged aggregation number for surfactant systems

A clear effect can be seen with AE7-dominant systems (i.e. those where AE7 is the most common surfactant such as the AE7 system and the AE7/DEEDMAC system): these systems tended to form micelles with large aggregation numbers. As the proportion of AE7 in these systems decreased, the aggregation number decreased and the number of micelles increased (i.e. the pure AE7 system formed a micelle with a very high

aggregation number, whereas the AE7/DEEDMAC micelle formed 4 micelles with a lower aggregation number, but still of a greater value than for the AE1S-dominant systems.)

AE1S-dominant systems showed the opposite effect; these had significantly lower aggregation numbers than the AE7-dominant systems, and addition of AE7 and DEEDMAC increased the mean aggregation number of these systems. Simultaneously, as the proportion of AE7 and DEEDMAC increased, the difference between the maximum and mean aggregation numbers of these systems decreases, suggesting that the micelles became more homogeneous. This can be seen most clearly by comparing the mean and maximum aggregation number of the AE1S system and the AE1S/AE7/DEEDMAC system; the AE1S system had a mean aggregation number of 15 and a maximum aggregation number of 35,giving a difference of 20, i.e. 133% of the mean value, whereas the AE1S/AE7/DEEDMAC system has a mean aggregation number of 23 and a maximum aggregation number of 33, giving a difference of 10, i.e. 43.5% of the mean value. The question was therefore raised as to whether AE1S would have this effect on an AE7-dominant system; this was addressed in simulations as detailed in Section 6.2.2.5.

The mean, maximum, and monomer-averaged inner-core and outer-shell radii of each system are shown in Table 6-12 below.

Table 6-12: Inner core and micellar radii for each surfactant system

System	Mean		Maximum		Monomer-averaged	
	Inner core radius / nm	Micellar radius / nm	Inner core radius / nm	Micellar radius / nm	Inner core radius / nm	Micellar radius / nm
AE1S	1.0	1.4	1.5	1.9	1.2	1.5
AE7	2.7	3.5	2.7	3.5	2.7	3.5
AE1S/AE7	1.1	1.6	1.5	1.9	1.2	1.6
AE1S/DEEDMAC	1.2	1.5	1.4	1.7	1.3	1.6
AE7/DEEDMAC	1.6	2.1	2.3	2.7	1.9	2.3
AE1S/AE7/DEEDMAC	1.2	1.6	1.6	1.9	1.4	1.7

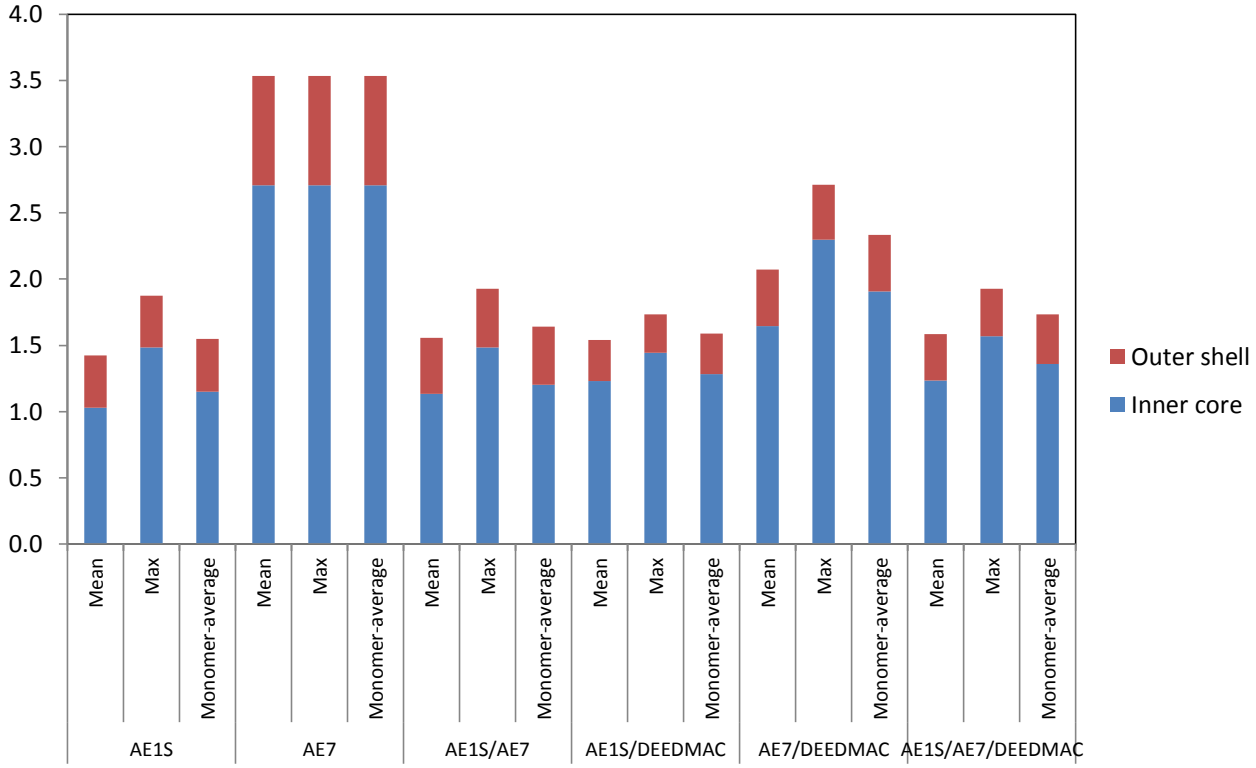

Figure 6-14: Inner core and micellar radii for each surfactant system

The same trends governing the aggregation number were seen in the radii of the micelles formed: an increase in the proportion of AE7 increased the inner core and micellar radius of the micelle, whereas increasing the proportion of AE1S decreased the radius.

These micelle radii were compared to the micelle radii once the brightener was added to the system. This showed the effect of brightener addition on the micelle radii and aggregation number; see Section 6.2.2.2.

6.2.2.1.2. Comparison of randomised simulations to SAXS data

The data obtained from these randomised simulations is compared to that obtained *via* SAXS in Table 6-13.

Table 6-13: Comparison of randomised simulation data to SAXS data

System	Mean aggregation number	Mean inner core radius / nm	Mean micellar radius / nm
AE1S (simulation)	15	1.0	1.4
AE1S (SAXS)	63 – 103	2.0	2.6
AE7 (simulation)	200	2.7	3.5
AE7 (SAXS)	159 – 229	2.3	3.3
AE1S + AE7 (simulation)	18	1.1	1.6
AE1S + AE7 (SAXS)	81 – 131	2.2	2.9

In the AE7 system, the randomised simulation showed good agreement with the SAXS data, in both their aggregation number and their micellar and inner core radii. However, the randomised AE1S data provided far lower aggregation numbers and radii than that given by SAXS for the AE1S system. This trend was also seen in the mixed AE1S/AE7 system; the randomised surfactant system gave a lower aggregation number, inner core radius, and micellar radius than the SAXS data.

This may be for one of two reasons. Firstly, GROMACS may not be modelling the ionic interactions sufficiently well for this purpose, perhaps overestimating the strength of the anionic repulsion, leading to less accurate results for those systems containing anionic surfactants. Alternatively, this difference between the results could be due to the timescales used. While it appears that the system has reached equilibrium after 40 000 ps, it may be that the micelles formed in this timescale would aggregate, if the molecular dynamics simulation was run for a significantly longer period of time. Future work could examine the effect of simulation time on the aggregation number and radii of these micelles.

6.2.2.1.3. Physical properties of micelles

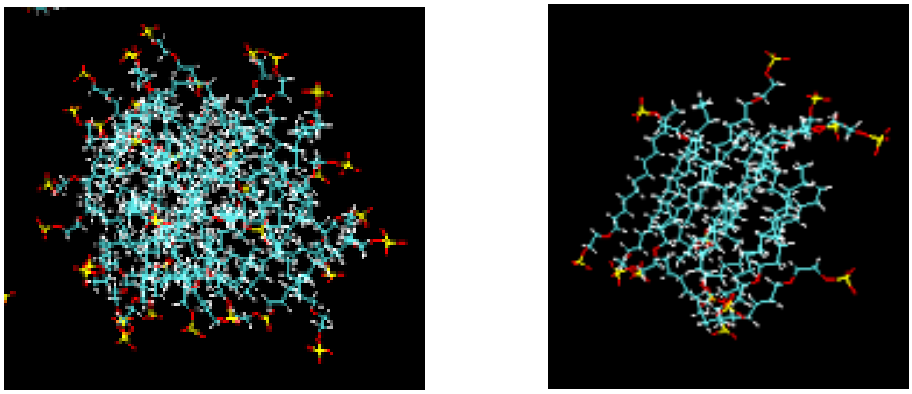

Figure 6-15: Two types of AE1S micelle seen: globular (L) and stacked (R). Water molecules omitted for clarity. Hydrogen atoms are coloured white, carbon atoms are coloured cyan, oxygen atoms are coloured red, and sulfur atoms are coloured yellow.

There were two types of AE1S micelles seen in the system; micelles with large aggregation numbers formed disordered, approximately globular aggregates, whereas micelles with low aggregation numbers tended to form 'stacked', roughly cylindrical aggregates, where the micelle chains were aligned parallel to each other, with the anionic head groups positioned at the faces of the cylinder. Both types of micelle appeared to have a very low density of the anionic head groups covering their surface. It should be noted that there is precedent for elliptical systems to be formed in MD simulations of micelles[127,128,166], in particular for systems where the surfactants self-assemble rather than being pre-formed into micelles[128]. In addition, literature studies showed that many systems that were initially formed into spheres formed ellipsoidal particles after several nanometres.[127] Therefore, a lack of spherical symmetry would not be unexpected, particularly for the AE1S system, where the DECON results from Chapter 5 indicated that the particles formed could not be modelled as spheres.

The sodium ions in the AE1S system were on average 0.8 nm from the surface of their nearest micelle, with a standard deviation of 0.7 nm. From this data, it can be seen that the ionic head groups of the surfactants and the sodium counterions did not form strong ion-ion pairs. This corresponded with the trends seen in the literature, where counterions generally were not strongly bound to ionic head groups.[124,126] The position of counterions in the system will be discussed in more detail in Section 6.2.2.6, where the positions of sodium and chloride counterions were compared to the position of calcium ions found in hard water.

The AE7 micelles differed from the AE1S micelles formed in that the AE7 had a very long polar head group; therefore, this surfactant micelle was expected to have a thicker outer shell. This can be seen in Table 6-12; the outer shell of the AE1S micelle had a thickness of approximately 0.4 nm, whereas the AE7 micelle had an outer shell thickness of approximately 0.8 nm. It can be noted that the head group length of AE7 was much greater than twice the length of the head group of the AE1S surfactant, and therefore the head group must have been folding. This meant that the head group of the AE7 was providing far better coverage for the surface of the micelle; see Figure 6-16.

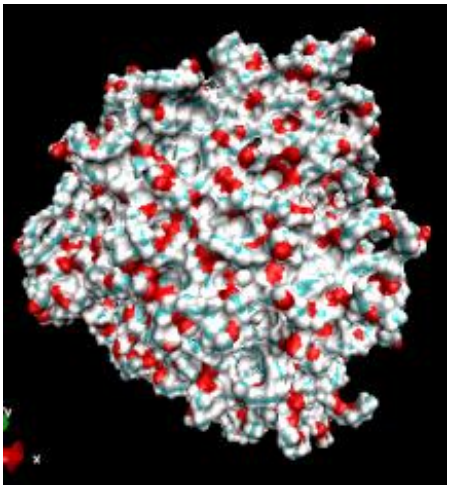

Figure 6-16: AE7 micelle generated from randomly-positioned surfactants and MD simulation. Oxygen atoms are shown in red, carbon atoms in blue, and hydrogen atoms in white.

It can be noted that none of the surfactant systems used formed a system where the tails all pointed inwards towards the centre. It is a well-recognised phenomenon in molecular dynamic simulations of surfactants that the surfactant tails form a close-packed system that does not point inwards, and that the terminal $–CH_3$ groups tend to orient themselves towards the surface of the micelle[124,126,164,166]. This could be seen in the data given by both the preformed and randomised solutions; the average distance from the centre of the micelle to the terminal carbon atom was at least 0.9 nm for each randomised system studied, and at least 1.1 nm for every preformed system studied.

6.2.2.1.4. Percentage coverage of micelle surface by head groups

6.2.2.1.4.1. AE1S

To estimate the percentage coverage of the head groups in the AE1S-only system, the area covered by each head group was estimated as 64 $Å^2$, as given in the literature[167]. Using the inner core radii and aggregation numbers calculated for this system via both

randomised and preformed micelle molecular dynamics simulations, and from the SAXS data collected in Chapter 5, the percentage coverage of head and tail groups in each system can be estimated. These are shown in Table 6-14.

Table 6-14: Estimated values for percentage coverage of head and tail groups in AE1S. All radii are shown to 1 d.p.

Method of calculation	**Inner core radius / nm**	**% coverage from heads**	**Predicted inner core radius / nm**	**Predicted % coverage from heads**
Randomised MD simulations (mean, aggregation number = 15)	1.0	72	1.1	60
Randomised MD simulations (maximum, aggregation number = 35)	1.5	81	1.5	79
Randomised MD simulations (monomer-average, aggregation number = 20)	1.2	77	1.2	66
Preformed MD simulation, aggregation number = 49	1.6	94	1.7	88
Preformed MD simulation, aggregation number = 80	2.0	106	2.0	104
SAXS data, aggregation number = 63 – 103	2.0	106	2.0	105

For each aggregation number, the inner core radius was predicted from the aggregation number itself and the volume of the surfactant tail (modelled using the density of tridecane, 0.756 g mL^{-1}, to give a volume per molecule of 4.05 x 10^{-28} m^3). The core was

assumed to be a sphere of liquid hydrocarbon at its normal density, and the inner core radius was thus:

$$r = \sqrt[3]{\frac{3N_{agg}V_{tail}}{4\pi}}$$

Equation 6-1

N_{agg} is the aggregation number and V_{tail} is the volume of the tail group.

For the radii calculated through MD simulations or SAXS, and through Equation 6-1, the percentage covering of the head groups was then calculated:

$$Percentage\ covering\ of\ head\ groups = \frac{100A_{head}N_{agg}}{4\pi r^2}$$

Equation 6-2

The terms of Equation 6-2 are the same as in Equation 6-1, with the addition of the term for the area per head group, A_{head}.

It can be seen that the radii given by Equation 6-1 corresponded well to those determined through SAXS or through MD simulations; where different values were obtained for the percentage coverage of the head groups for the same radius, these were due to rounding errors from the number of significant figures shown in Table 6-14.

Table 6-14 shows that the AE1S micelles generated from the MD simulation had an approximate head group coverage of 72-81 %. However, it can be seen that these head groups were not distributed evenly or packed tightly, with large patches of exposed hydrocarbon chains being seen on the surface of the micelle: see Figure 6-17.

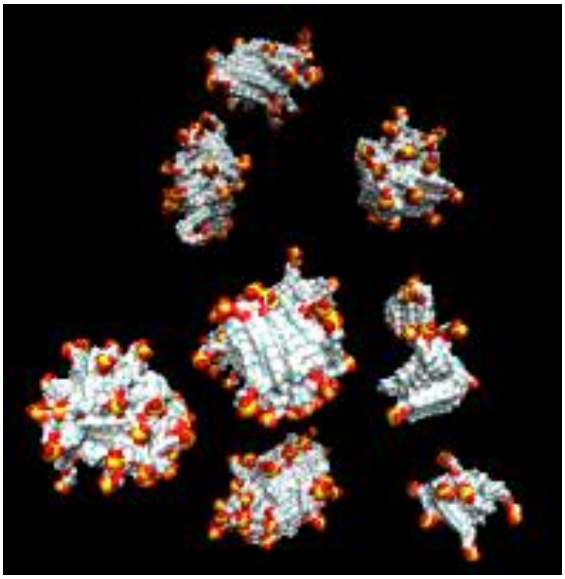

Figure 6-17: AE1S micelles produced through a randomly distributed MD simulation. Carbon atoms are shown in blue, hydrogen atoms in white, oxygen atoms in red, and sulfur atoms in yellow.

The relatively low density of the head groups at this aggregation number raised the question of how the head groups were arranged at high aggregation numbers. The AE1S was expected to have an aggregation number of 43-80,[32,33] giving a calculated head group coverage of 85-104 %.

In order to show the effect of the aggregation number on the percentage coverage of the head groups, and to show what this theoretical coverage would look like visually, a MD simulation was run using a preformed micelle containing 80 AE1S monomers. Figure 6-18 shows the micelle containing 49 monomers generated in Section 6.2.1.1, with a calculated head group coverage of 94 %, whereas Figure 6-19 shows the micelle containing 80 monomers, with a calculated head group coverage of 106 %.

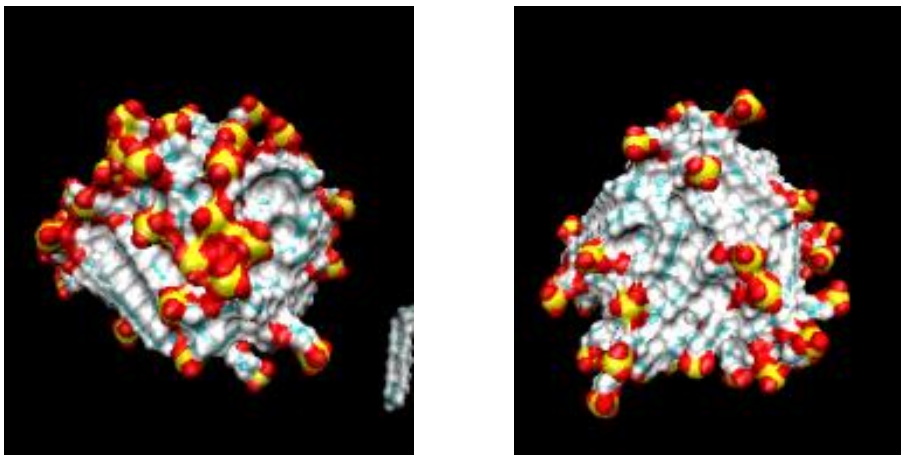

Figure 6-18: Preformed micelle containing of 49 monomers after molecular dynamics simulation. Carbon atoms are shown in blue, hydrogen atoms in white, oxygen atoms in red, and sulfur atoms in yellow.

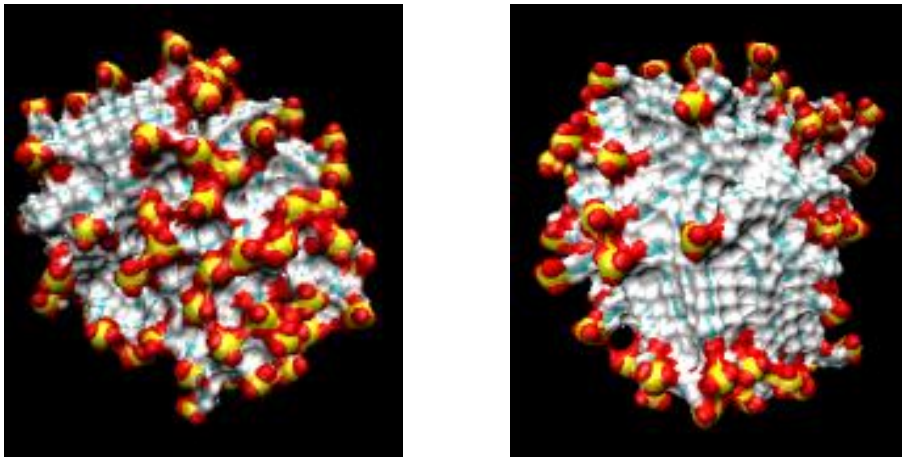

Figure 6-19: Preformed AE1S micelle containing 80 monomers after molecular dynamics simulation. Carbon atoms are shown in blue, hydrogen atoms in white, oxygen atoms in red, and sulfur atoms in yellow.

In both of these systems, there were regions of high head group density on the surface, leading to the overall high percentage coverage of the head groups. However, it can be seen that both the 49-monomer system and the 80-monomer system contained regions of low head group density, where the surface of the micelle consisted of hydrocarbon chains lying parallel to the surface.

While consideration of the hydrophobic effect may make this model seem unrealistic, given that some hydrocarbon chains remain in contact with the water, it can also be seen that the proportion of the hydrocarbon tails in contact with water was far lower in this configuration than for the monomers. In addition, the hydrocarbon tails in this configuration were free to form van der Waals forces with each other. Therefore, the formation of this micelle would be entropically favourable from the perspective of the surfactant.

The 80-monomer micelle was compared to the AE1S system measured through SAXS; the data obtained is shown in Table 6-15. It can be seen that the data obtained from this particular MD simulation was a good match for that determined through SAXS.

Table 6-15: Comparison between SAXS data and MD data for aggregation numbers ~ 80

System	Inner core radius / nm	Micellar radius / nm	Aggregation number
MD simulation – preformed micelle	2.0	2.4	80
SAXS	2.0	2.6	63 – 103

The findings shown here are well aligned with those seen previously in the literature; in 2015, Chun *et al* estimated that 58% of the surface of a simulated SDS micelle was occupied by hydrocarbon chain groups.[164] The same effect was seen by Wymore *et al* in 1999, where the authors described simulated dodecylphosphocholine surfactants lying across the surface of the micelle such that their entire chains were exposed to the solvent.[125] The same paper also described aggregates with low aggregation numbers as being packed in a monolayer-type structure with all chains aligned, similar to the 'stacked' aggregates seen in the AE1S system. These were said to form larger, more spherical micelles over time; further experiments on the AE1S system over longer timescales would indicate whether the same would happen in this AE1S system.

6.2.2.1.4.2. AE7

The percentage coverage of the head groups was calculated as before, using the literature value of 32 $Å^2$ per molecule;[160] this gave an approximate value of 73-93% head group coverage from the SAXS data, and 70% from the MD simulation. However, in this instance, this value is likely to be underestimating the percentage coverage. The literature value for the area of the head group was calculated using a Gibbs adsorption isotherm, examining the packing of the surfactants on the surface of the water. Under these conditions, the $–(OCH_2CH_2)–$ chains will be in the trans- form to maximise packing. When micelles are formed, however, these chains will be free to flex and will thus cover a greater area. Consequently, since this 73 – 93% range is likely to be an underestimate, it can be seen that in the AE7 micelles, the hydrocarbon tails experience minimal interaction with the water.

6.2.2.2. *Surfactant-brightener systems*

A similar set of systems were created, including surfactants as before, with the addition of 10 brightener molecules per system. The simulations were run as before.

Figure 6-20 shows the number of micelles, and Figure 6-21 shows the aggregation numbers for the surfactant-brightener systems. These were broken down into micelles containing brightener, and micelles that did not contain brightener molecules. This data is presented numerically in Appendix 1.

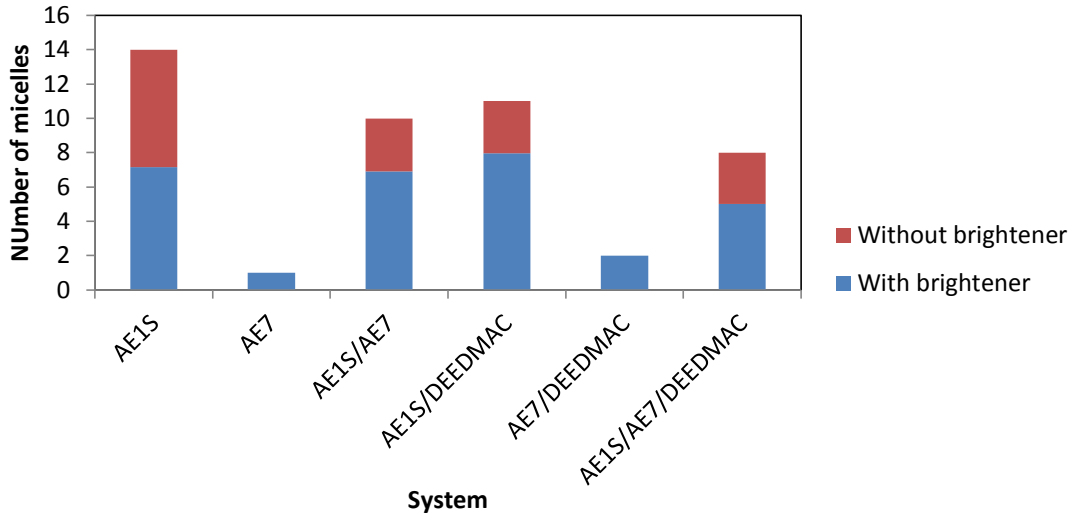

Figure 6-20: Number of micelles per system overall, containing brightener, and not containing brightener

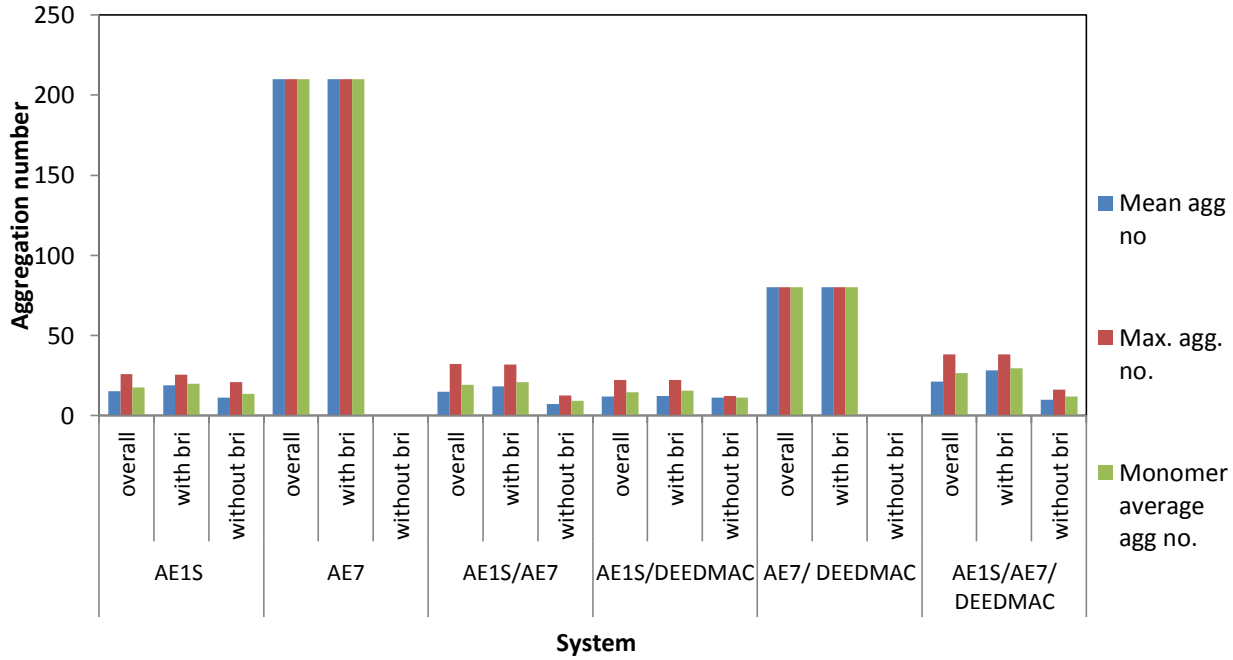

Figure 6-21: Mean, maximum, and monomer-averaged aggregation number for surfactant systems containing brightener. Data is listed for the system overall, for micelles containing brightener, and for micelles not containing brightener.

The mean, maximum, and monomer-averaged inner core radii, micellar radii, and brightener positions are shown in Figure 6-22 to Figure 6-27 overleaf. 5 values were given for each system; the relevance of these values are listed in Table 6-16 below. The data is given numerically in Appendix 1.

Table 6-16: Micelle categories used in figures below

Value	Significance
Before brightener	Gives the micellar radii for the surfactant system without any brightener present, as given in Section 4.2.1
After brightener: Overall	Gives the micellar radii for the surfactant system with brightener added, including both micelles which contained a brightener molecule and those which did not
After brightener: With bri	Gives the micellar radii for the surfactant system with brightener added, including only those micelles which contained at least one brightener molecule
After brightener: Without bri	Gives the micellar radii for the surfactant system with brightener added, including only those micelles which did not contain any brightener molecules
After brightener: Brightener	Gives the positions of the central carbon atoms and sulfur atoms of the brightener molecule itself

The micellar radii for the AE1S system are shown in Figure 6-22 below:

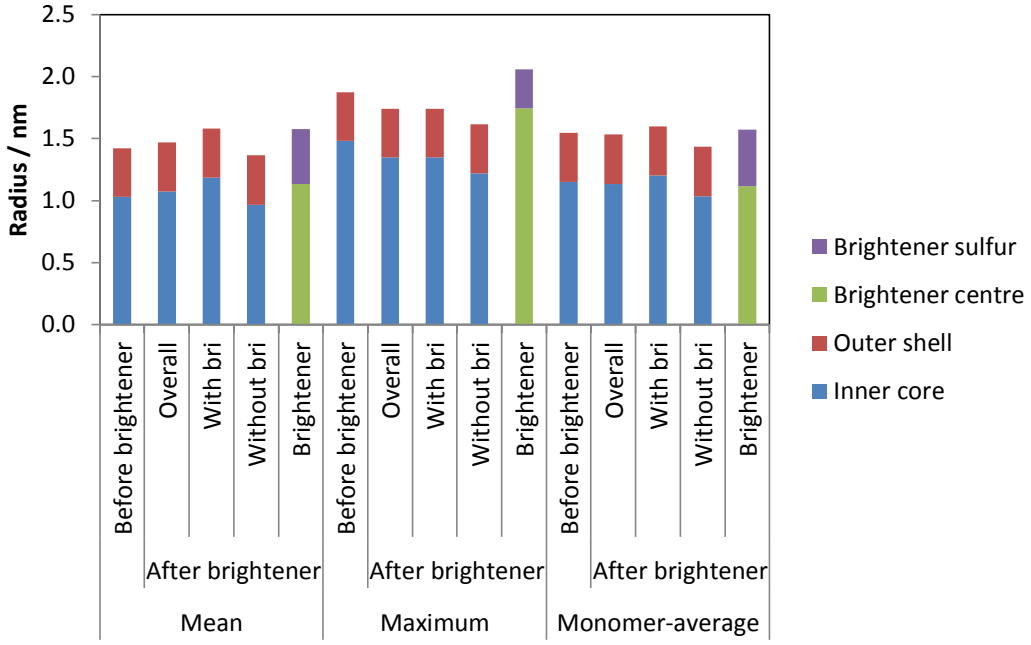

Figure 6-22: Micellar radii and positions of brighteners for randomised AE1S systems. Micellar radius was broken down into contributions from the inner core and outer shell. Brightener position was broken into positions of the centre-most carbon atoms and the positions of the sulfur atoms.

The micellar radii for the AE7 system are shown in Figure 6-23 below:

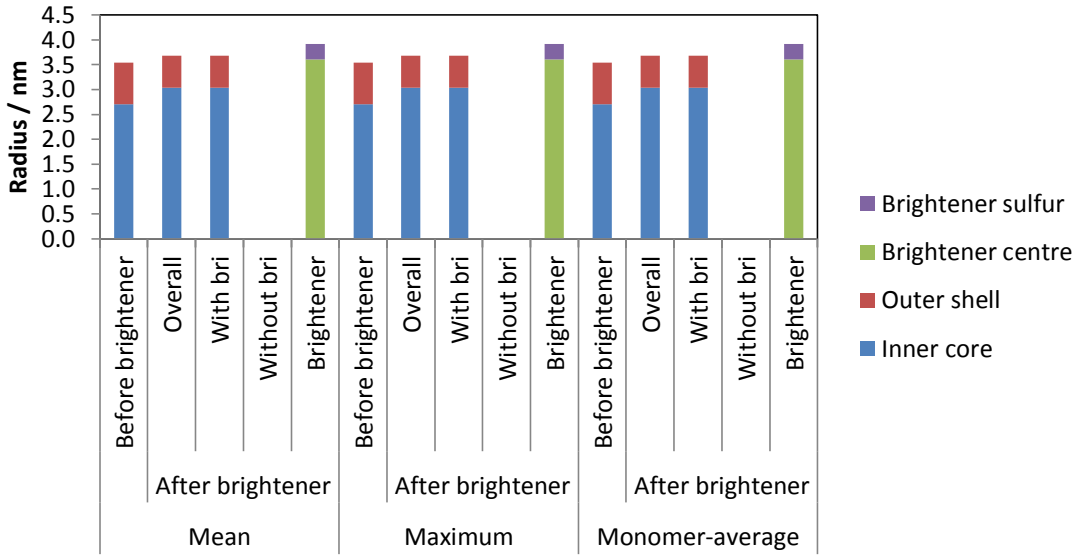

Figure 6-23: Micellar radii and positions of brighteners for randomised AE7 systems. Micellar radius was broken down into contributions from the inner core and outer shell. Brightener position was broken into positions of the centre-most carbon atoms and the positions of the sulfur atoms.

The micellar radii for the AE1S/AE7 system are shown in Figure 6-24:

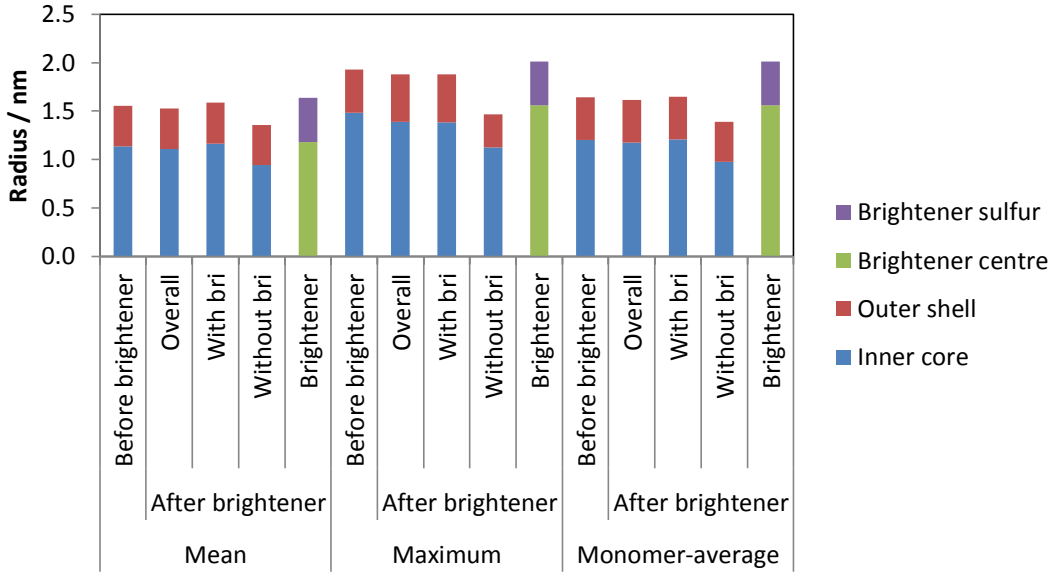

Figure 6-24: Micellar radii and positions of brighteners for randomised AE1S/AE7 systems. Micellar radius was broken down into contributions from the inner core and outer shell. Brightener position was broken into positions of the centre-most carbon atoms and the positions of the sulfur atoms.

The micellar radii for the AE1S/DEEDMAC system are shown in Figure 6-25:

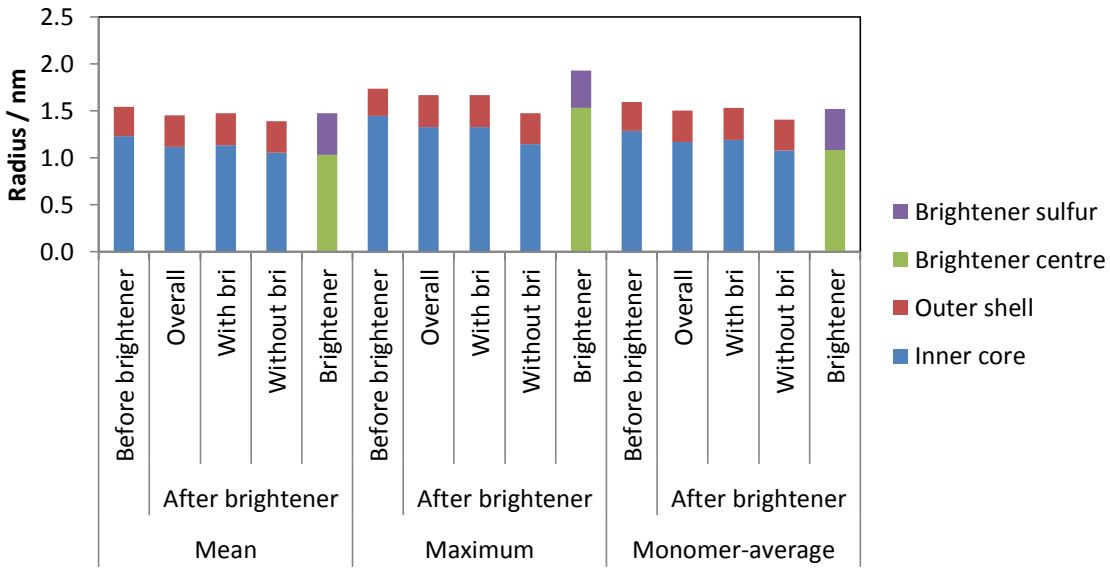

Figure 6-25: Micellar radii and positions of brighteners for randomised AE1S/DEEDMAC systems. Micellar radius was broken down into contributions from the inner core and outer shell. Brightener position was broken into positions of the centre-most carbon atoms and the positions of the sulfur atoms.

The micellar radii for the AE7/DEEDMAC system are shown in Figure 6-26:

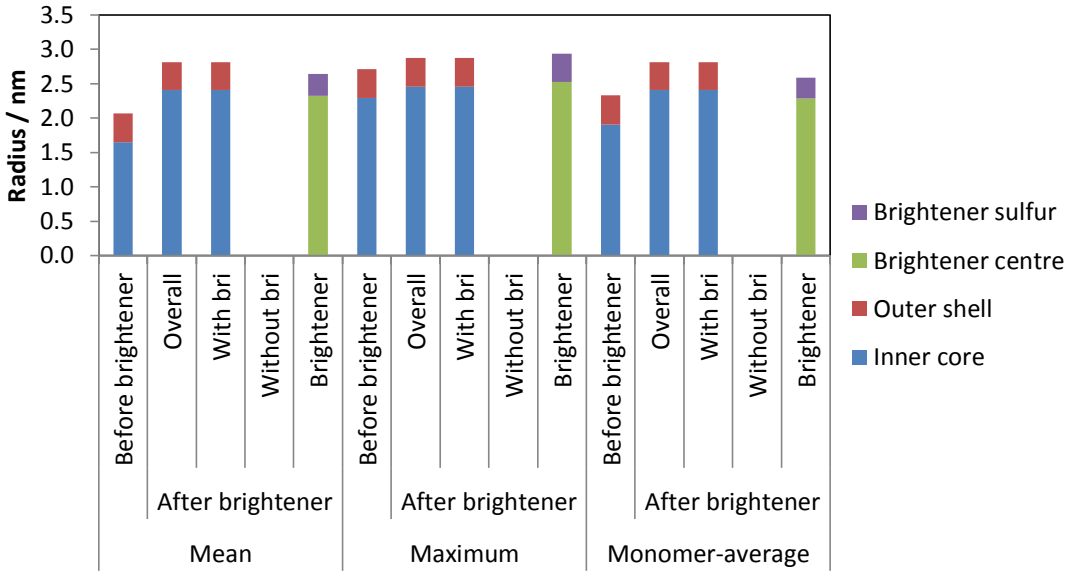

Figure 6-26: Micellar radii and positions of brighteners for randomised AE7/DEEDMAC systems. Micellar radius was broken down into contributions from the inner core and outer shell. Brightener position was broken into positions of the centre-most carbon atoms and the positions of the sulfur atoms.

The micellar radii for the AE1S/AE7/DEEDMAC system are shown in Figure 6-27:

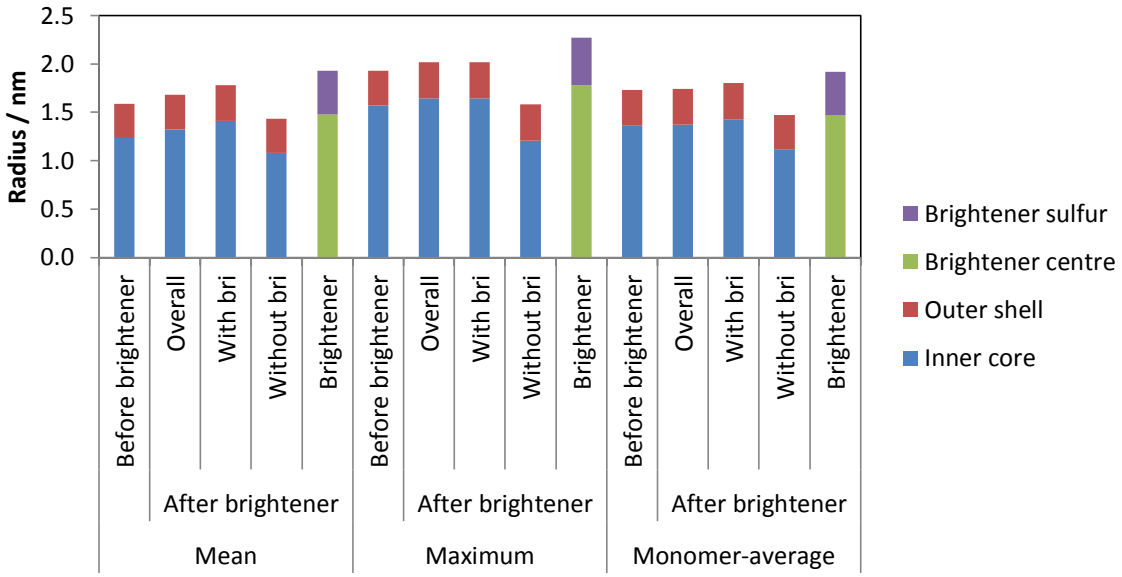

Figure 6-27: Micellar radii and positions of brighteners for randomised AE1S/AE7/DEEDMAC systems. Micellar radius was broken down into contributions from the inner core and outer shell. Brightener position was broken into positions of the centre-most carbon atoms and the positions of the sulfur atoms.

The effects seen in Figure 6-22 to Figure 6-27 will be discussed in Section 6.2.2.2.1 to Section 6.2.2.2.4.

6.2.2.2.1. General trend: position and orientation of the brightener molecule

Two trends seen in all brightener-surfactant simulations are that: firstly, the brightener molecules interact with the micelle surface, and are not located in the micellar core. Secondly, although all brightener molecules were set up with their sulfate ions in a trans- configuration, most underwent bond rotation of the centremost C-C bond during the simulation to position their ions away from the micelle, in a cis- configuration. As this is not the bond rotation responsible for fluorescence, this will not be seen directly in fluorescence work; however, the degree of rigidity in which the stilbene group is held may have an effect on the fluorescence emission spectrum, causing the spectrum seen to have an additional peak.[168]

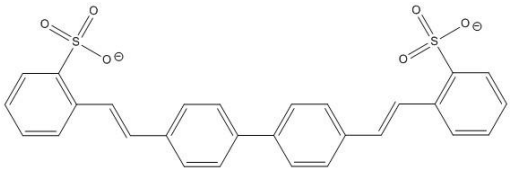

Figure 6-28: Typical final configuration of Brightener 49

6.2.2.2.2. AE1S/brightener

When the mean and monomer-averaged micelle radii were calculated, along with the radii of the brightener positions, the brightener appeared to be positioned with its centre at the inner core/ outer shell interface and its sulfur atoms at the outer shell/solvent interface. This could be understood more clearly when the micelles were studied visually, as shown in Figure 6-29 below.

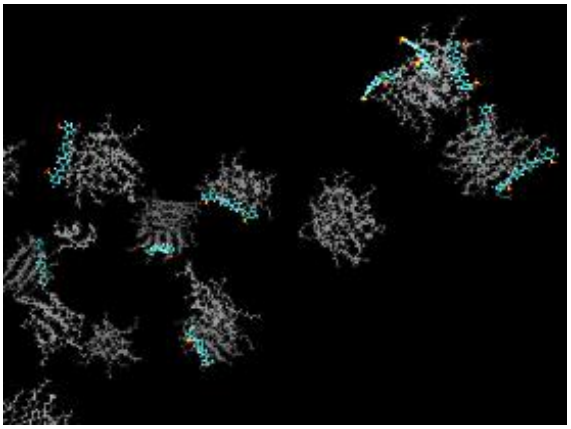

Figure 6-29: Brightener molecules associated to the surface of the AE1S micelle. Water molecules have been omitted and AE1S molecules have been shaded grey for clarity. Hydrogen atoms are coloured white, carbon atoms are coloured cyan, oxygen atoms are coloured red, and sulfur atoms are coloured yellow.

When the brightener molecules were added to the system, they were incorporated on the surface of the micelle, between the head groups. Generally, they lay with their hydrocarbon chains parallel with the AE1S tail group and their sulfate ions oriented outwards. In this way, it could be said that they acted like anionic surfactants with two head groups.

6.2.2.2.3. AE7/brightener

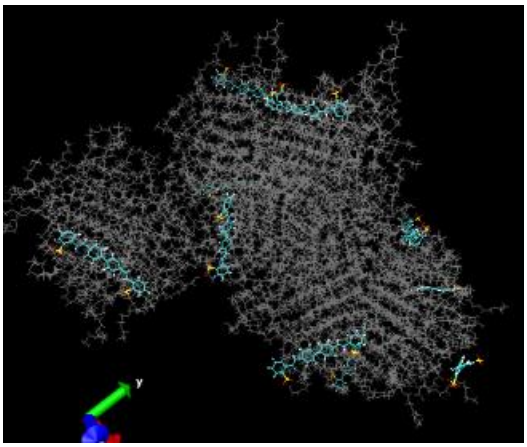

Figure 6-30: Position of brightener molecules within AE7 surfactant micelles. Water molecules omitted for clarity. Hydrogen atoms are coloured white, carbon atoms are coloured cyan, oxygen atoms are coloured red, and sulfur atoms are coloured yellow.

When brightener was added to the AE7 surfactant micelle, the inner core/outer shell boundary of the micelle was at approximately 3.0 nm from the centre, and the outer shell/solvent boundary was at approximately 3.7 nm. The centre of the brightener was approximately 3.6 nm from the centre, and its sulfur atoms groups were approximately 3.9 nm from the centre. This suggests that, on average, the brighteners were being incorporated into the head group region, roughly at a tangent to the surface of the inner core, with their sulfate ions extending outwards, perpendicular to the surface of the micelle.

There are a number of caveats to this result; firstly, the micelle produced in the simulation was not a perfect sphere (see Figure 6-30 above). Secondly, it can be seen that the chains of the micelle did not extend inwards to a point at the centre, but rather pack together. However, it is also evident that the brightener molecules were indeed incorporated onto the surface of the micelle, generally just within the head group region.

6.2.2.2.4. Mixed surfactant systems: AE1S/AE7, AE1S/DEEDMAC, AE7/DEEDMAC, and AE1S/AE7/DEEDMAC

The same trend was seen throughout all samples; the centre of the brightener was given at approximately the same radius as the inner core, with the sulfate ion positions giving the same radius as the outer shell. This corresponded to the brightener aromatic ring chains interacting with the surfactant hydrophobic chain groups, and the sulfate ions extending outwards to form part of the outer shell of the micelle.

6.2.2.2.5. Conclusions

In each system studied, the brightener was associated with the surface of the surfactant micelle. In AE1S-dominant systems, this generally meant that the brightener backbone was associated with the hydrocarbon chains of the surfactant, while in AE7-dominant systems this meant that the brightener was incorporated into the head group region of the surfactant.

It appears that the brighteners may have been associating with the surfactants in a similar way to another surfactant. The brightener had a hydrophobic backbone of connected aromatic rings, and hydrophilic ionic groups, so this is feasible. This raised two questions; would the brightener self-aggregate, and how did the brightener affect the micelle aggregation number? To answer the first question, a simulation was run containing a large number of brightener molecules. To answer the second, a series of simulations were run for three surfactant systems (AE1S only, AE7 only, and AE1S/AE7/DEEDMAC) using different concentrations of brightener.

6.2.2.3. Brightener-only aggregation

A system containing 200 brightener molecules and their counterions only was set up. This was run in the same manner as the surfactant-containing systems.

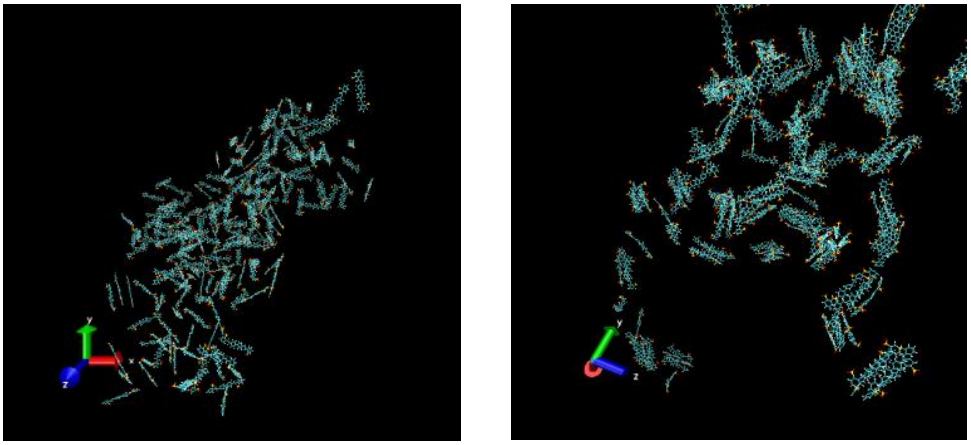

Figure 6-31: Brightener-only MD run before (L) and after (R). Water molecules omitted for clarity. Hydrogen atoms are coloured white, carbon atoms are coloured cyan, oxygen atoms are coloured red, and sulfur atoms are coloured yellow.

It must be noted that the concentration used was over 10 times the solubility limit for the brightener in solution (for a box of this size, this would be about 18 molecules); this was done in order to show the most direct comparison to the surfactant.

The system produced had an average of 50 monomers and 41 aggregates per frame; however, this was prone to a very large degree of fluctuation (compared to the formation of micelles in solution) as shown in Figure 6-32 and Figure 6-33 below. This instability of the aggregates formed suggests that these were not micelles, but rather an amorphous precipitate being formed (likely given the concentration was 10 times the solubility limit), with exchange of material between them via the dissolution of material back into the solvent.

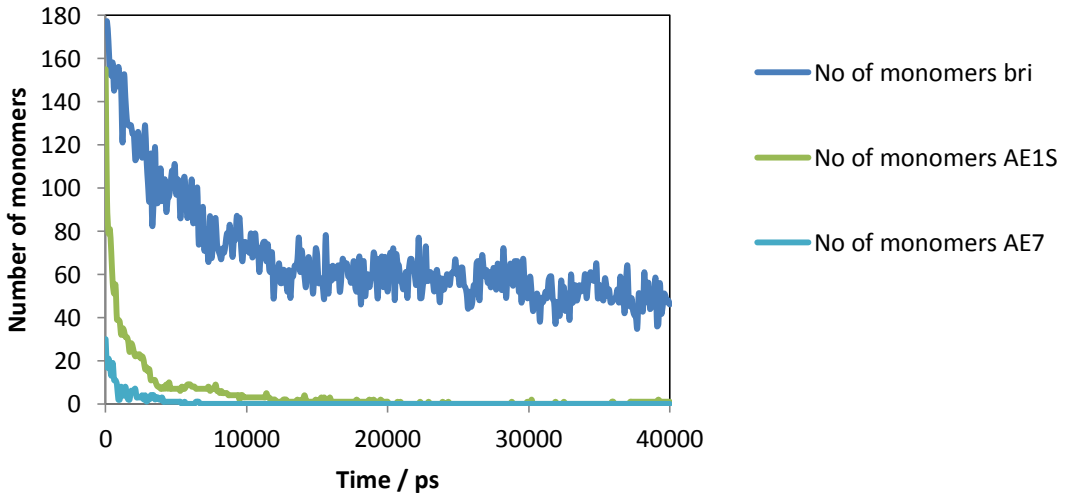

Figure 6-32: Change in the number of monomers in the brightener, AE1S, and AE7 solutions over time

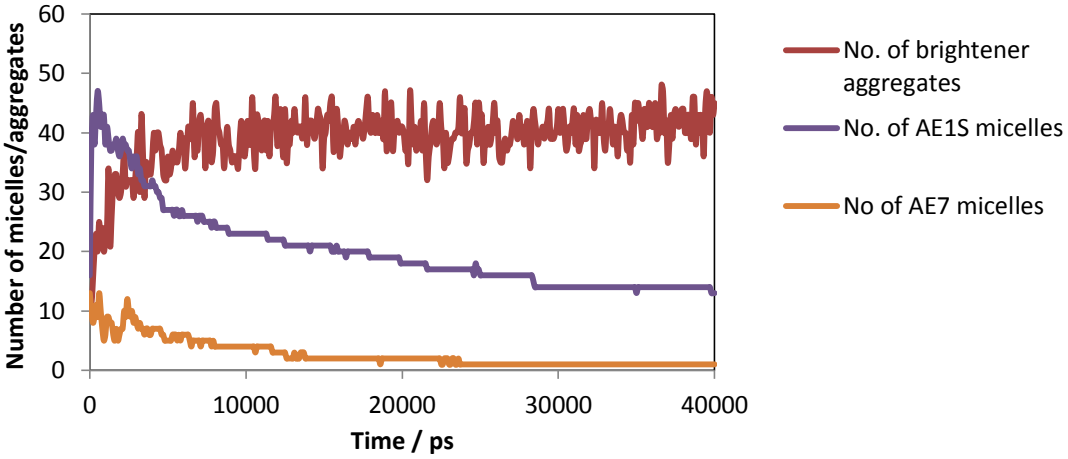

Figure 6-33: Change in the number of aggregates in brightener, AE1S, and AE7 solutions over time

The aggregation number of the precipitated brightener was also very low, being calculated to the nearest integer at 4 (mean), 10 (maximum), and 4 (monomer-averaged). These figures do not include the large number of monomers in solution.

In conclusion, while the brightener did show some aggregation behaviour, it was completely unlike that seen in surfactant systems, and was likely due to precipitation effects rather than micellar aggregation.

6.2.2.4. Varying concentration of brightener

For three surfactant systems previously studied (AE1S, AE7, and AE1S/AE7/DEEDMAC), the number of brightener molecules added to the system was varied from 5 to 20. This was designed to show how the brightener concentration affected the size of the micelle. The number of surfactant molecules used was kept constant. The data collected in Sections 6.2.2.1 and 6.2.2.2 were used to provide data points for 0 and 10 brightener molecules, respectively.

6.2.2.4.1. AE1S/brightener systems

Simulations were run with 200 AE1S molecules as before. The effect of the number of brightener molecules on the aggregation number, and inner core and micellar radii, are shown in Figure 6-34 and Figure 6-35 overleaf. Note that the data given was for the system as a whole, including individual micelles which did not contain a brightener molecule, but excluding monomers. This was to show how the brightener affected the micellar system as a whole, not just the individual micelles with which it interacted.

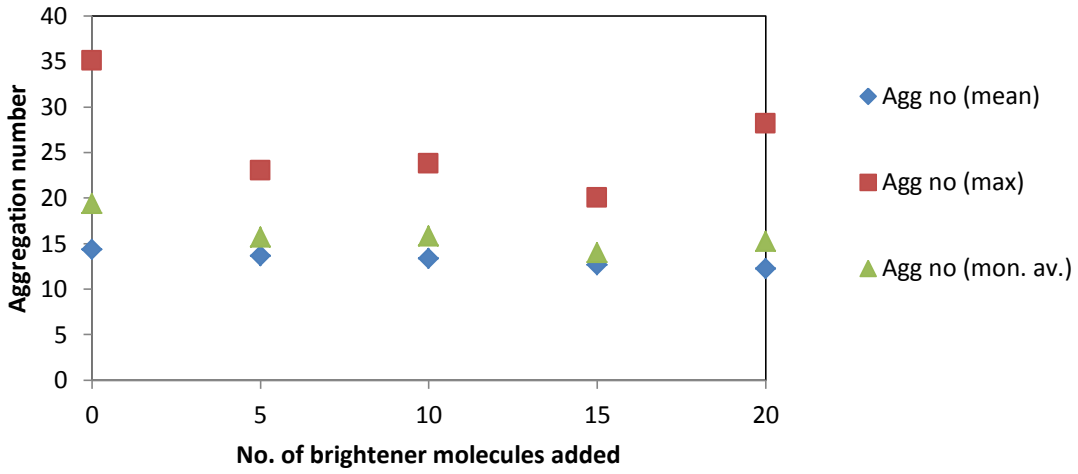

Figure 6-34: Effect of brightener concentration on the aggregation number of AE1S. Values are given using the mean, maximum (max) and monomer-averaged (mon. av.)

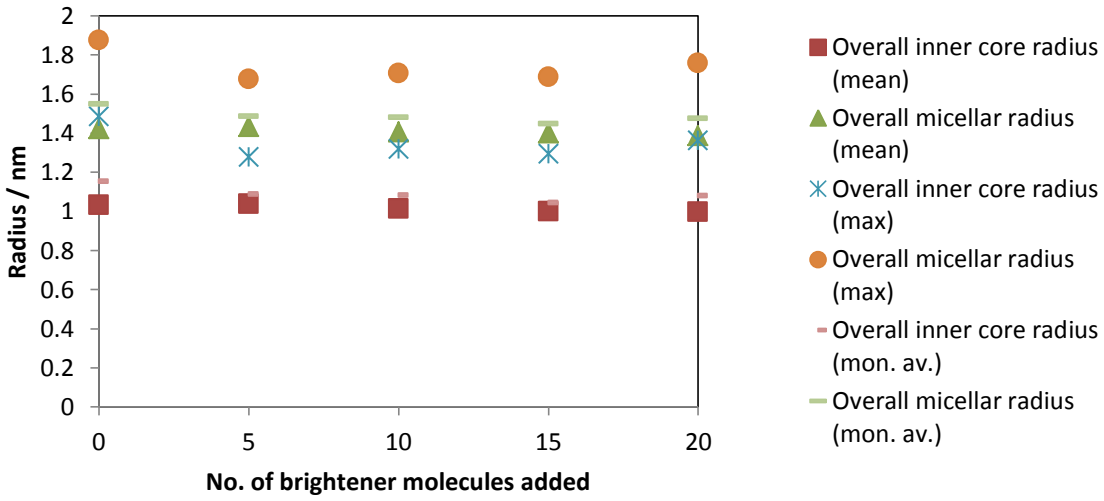

Figure 6-35: Effect of brightener concentration on the inner core and micellar radii of AE1S. Values are given using the mean, maximum (max) and monomer-averaged (mon. av.)

It can be seen that the aggregation number of AE1S was not greatly affected by the increasing concentration of brightener, although there was a very slight negative correlation between brightener concentration and aggregation number. The same trend was seen in the inner core and micellar radii: the micelle size was largely unaffected by changes in the brightener concentration. This is in agreement with the SAXS findings, where no significant change in micelle radius was seen with increasing brightener concentration.

6.2.2.4.2. AE7/brightener systems

The simulation was run using 200 AE7 molecules as before. Figure 6-36 and Figure 6-37 show the effect of brightener concentration on aggregation number, and inner core and micellar radii, respectively.

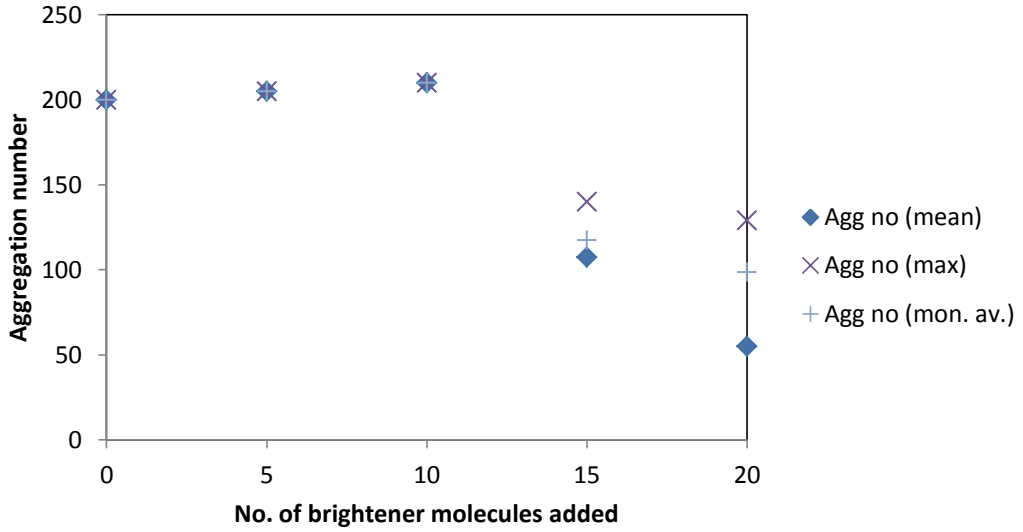

Figure 6-36: Effect of brightener concentration on aggregation number of AE7 micelles. Values are given using the mean, maximum (max) and monomer-averaged (mon. av.)

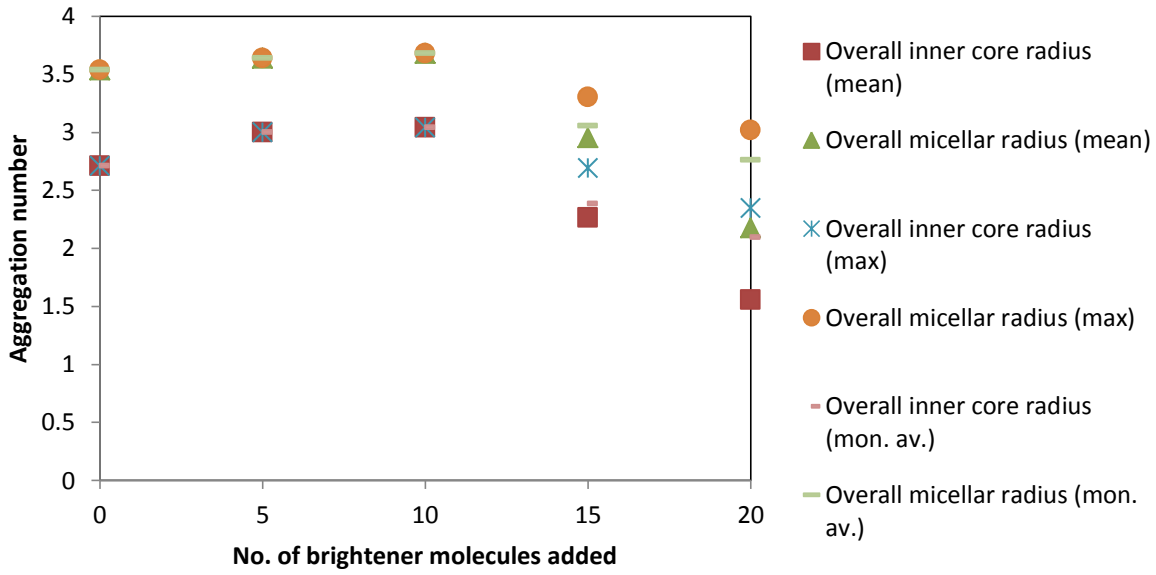

Figure 6-37: Effect of brightener concentration on AE7 inner core and micellar radii. Values are given using the mean, maximum (max) and monomer-averaged (mon. av.)

In this system, the addition of brightener had a drastic effect, but only after a certain concentration threshold had been passed. While the system had an initial aggregation number of 200 without brightener addition, when 5-10 brightener molecules were added, these additional molecules joined the main aggregate, causing the aggregation number to

increase. Once the number of brightener molecules added had reached 15, the micelle split to form micelles with an average aggregation number of 108 – 140, depending on average method used. Addition of a further 5 brightener molecules reduced the aggregation number further to an average of 55-129.

This effect appears to be analogous to the effect that the proportion of AE1S had on the aggregation numbers of randomised surfactant systems as discussed in Sections 6.2.2.1 and 6.2.2.2, where an increase in the proportion of AE1S in the system decreased the aggregation number and increased the number of micelles in solution, (and thus decreased the micelle radii).

The fact that the brightener had no effect on the AE1S aggregation number, but decreased the AE7 aggregation number so drastically, suggested that it was analogous to AE1S in such systems. This raised the question of whether the AE1S can be shown to have a similar effect on AE7 aggregation; this will be discussed in Section 6.2.2.5.

This data does not agree well with the SAXS data, which showed no significant change in micellar radius with increasing concentration of brightener, up to a concentration of 43 brightener molecules per micelle. It may be that the effects of increased brightener concentration in the simulation were caused by an overestimation of ionic repulsion between ionic molecules, as in Section 6.2.2.1.2; further experiments at longer timescales would clarify if this was the case.

6.2.2.4.3. AE1S/AE7/DEEDMAC/brightener systems

The system was run with 100 AE1S molecules, 40 AE7 molecules, and 20 DEEDMAC molecules as before. Figure 6-38 and Figure 6-39 show the effect of brightener concentration on aggregation number, and inner core and micellar radii, respectively.

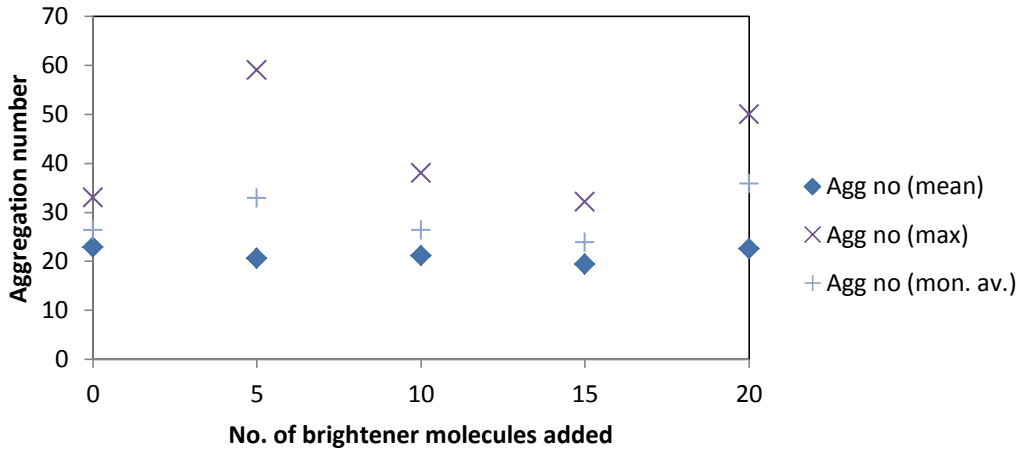

Figure 6-38: Effect of brightener concentration on aggregation number of AE1S/AE7/DEEDMAC system. Values are given using the mean, maximum (max) and monomer-averaged (mon. av.)

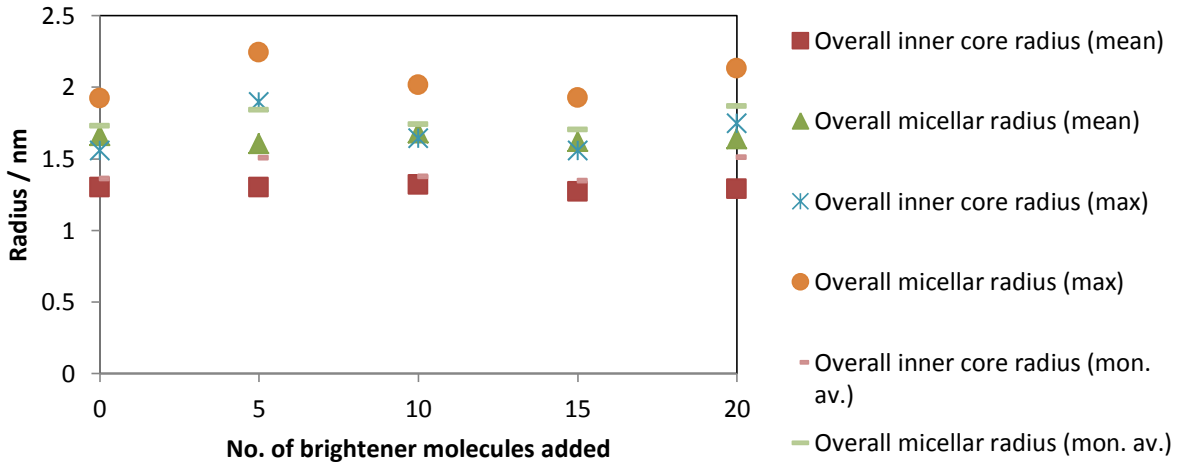

Figure 6-39: Effect of brightener concentration on inner core and micellar radii of AE1S/AE7/DEEDMAC system. Values are given using the mean, maximum (max) and monomer-averaged (mon. av.)

As in the AE1S system, the micellar aggregation number and radii seemed fairly stable, with little correlation between both the aggregation number and the radii, and the brightener concentration. Again, as this was an AE1S-dominant system, this supported the idea that the brightener was interacting in a similar manner to an AE1S surfactant molecule.

6.2.2.5. Variation of AE1S concentration in AE7-dominant micelles

Simulations were run as before containing 200 AE7 molecules, and 10, 15, 20, and 25 AE1S molecules. The results of these are shown in Figure 6-40 and Figure 6-41 below.

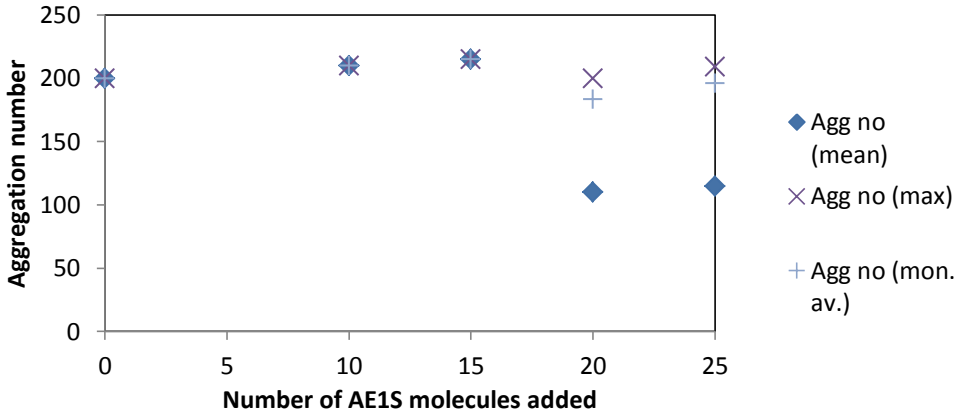

Figure 6-40: Effect of AE1S concentration on aggregation number. Values are given using the mean, maximum (max) and monomer-averaged (mon. av.)

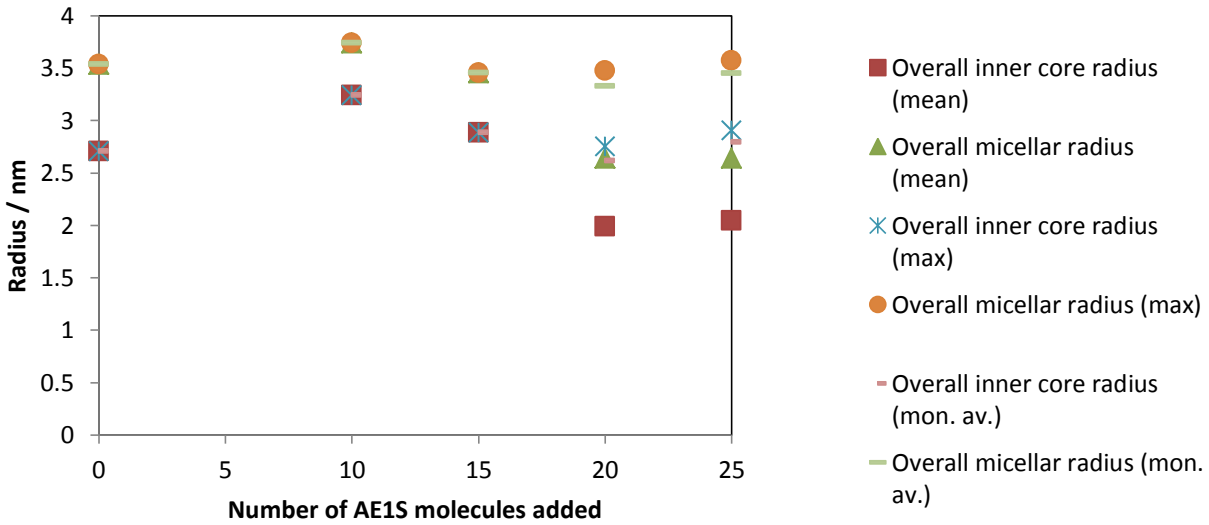

Figure 6-41: Effect of AE1S concentration on inner core and micellar radii. Values are given using the mean, maximum (max) and monomer-averaged (mon. av.)

By looking at the maximum aggregation number, the physical effect of the addition became clear; at low AE1S concentrations (0-15 molecules), the AE1S was incorporated into the micelle. At higher concentrations however, the maximum aggregation number remained relatively stable at approximately 200 – 210 molecules, with the remaining surfactant forming a smaller aggregate containing both AE1S and AE7 molecules.

Correspondingly, the inner core and micellar radius remained relatively stable once this threshold had been passed. This suggests that the effect of AE1S on aggregation number

and micelle size of AE7-dominant micelles was not seen at such low concentrations of AE1S. This shows that, while the brightener was similar to the AE1S in terms of its aggregation (as shown in the AE1S-only system), its effects on the system were stronger, perhaps due to the increase in charge (given its two sulfate groups), and its aromatic rings.

6.2.2.6. Addition of calcium ions to surfactant micelles

The aim of this work was to model the interaction between surfactant systems in detergent and the calcium ions found in hard water, as studied experimentally in Chapter 5. Surfactant systems were made as in Table 6-10, with the addition of 20 calcium ions, and sodium or chlorine ions as required to neutralise the system. These were run for 40 000 ps as before.

The number of micelles in each system, the number of monomers, and the average aggregation numbers are shown in Figure 6-42 and Figure 6-43.

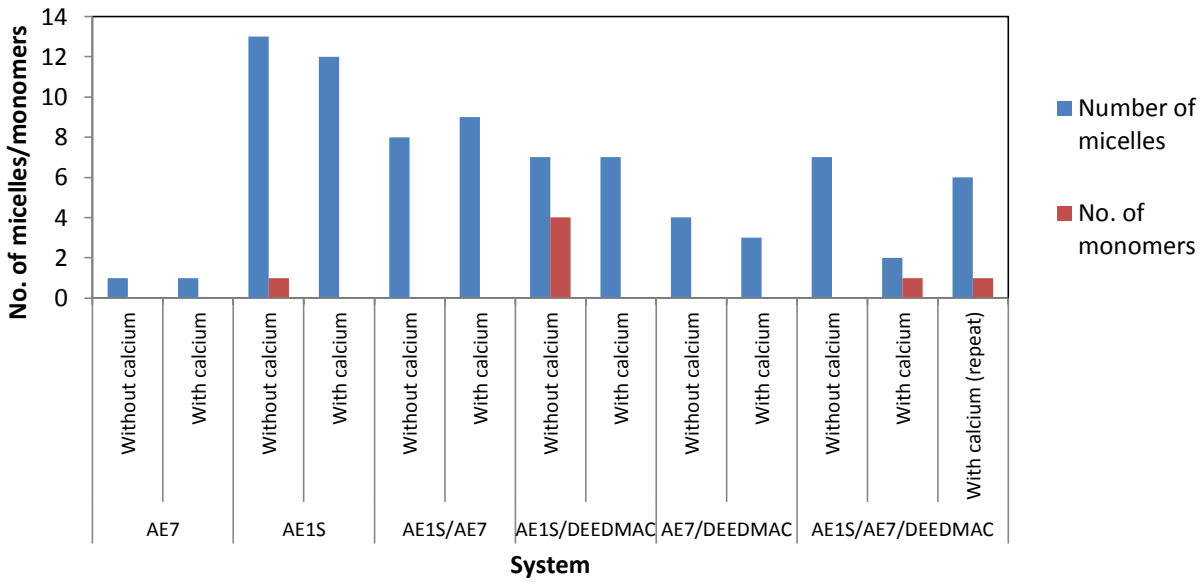

Figure 6-42: Numbers of micelles and numbers of monomers for surfactant systems with and without calcium ions

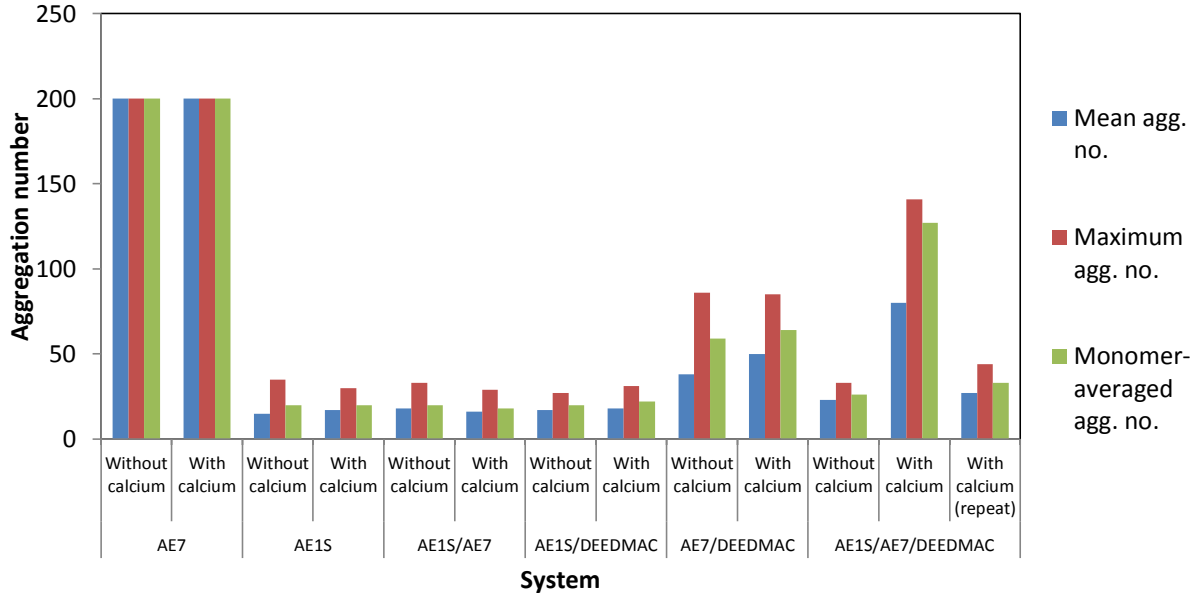

Figure 6-43: Mean, maximum, and monomer-averaged aggregation number for surfactant systems with and without calcium ions

The inner core and micellar radii of the systems are given in Figure 6-44, Figure 6-45, and Figure 6-46.

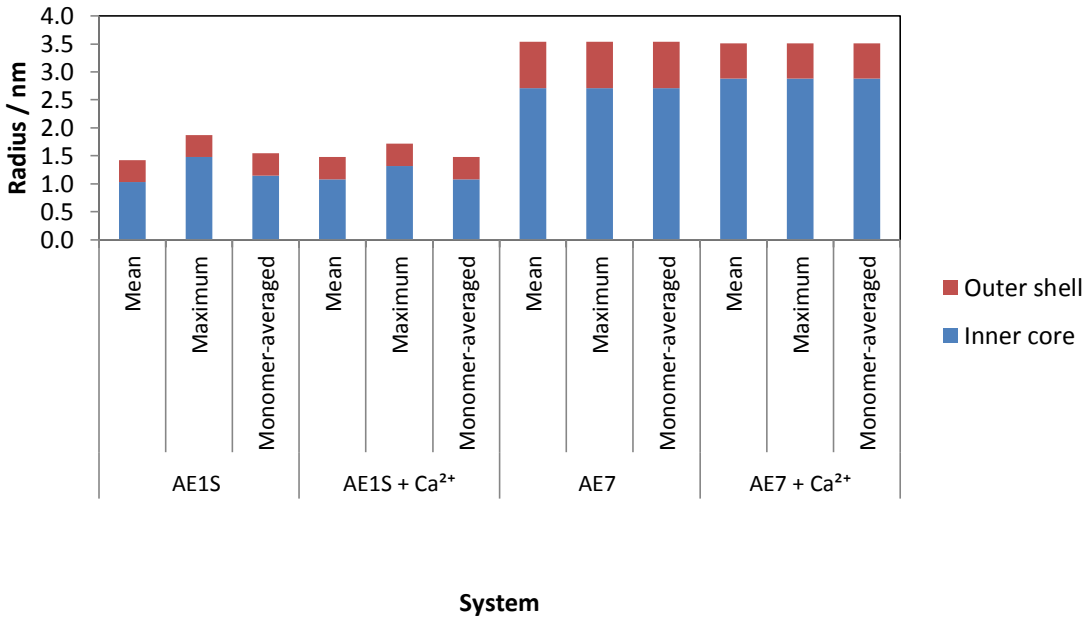

Figure 6-44: Micellar radii of the AE1S and AE7 systems, before and after the addition of calcium ions

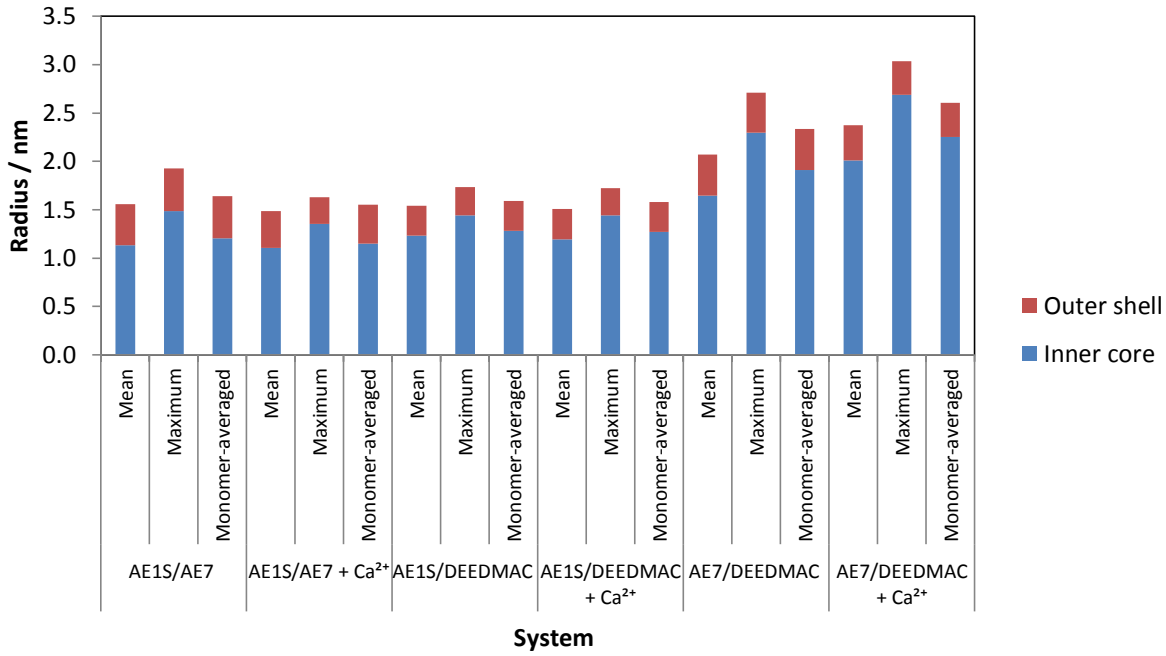

Figure 6-45: Micellar radii of the AE1S/AE7, AE1S/DEEDMAC, and AE7/DEEDMAC systems, before and after the addition of calcium ions

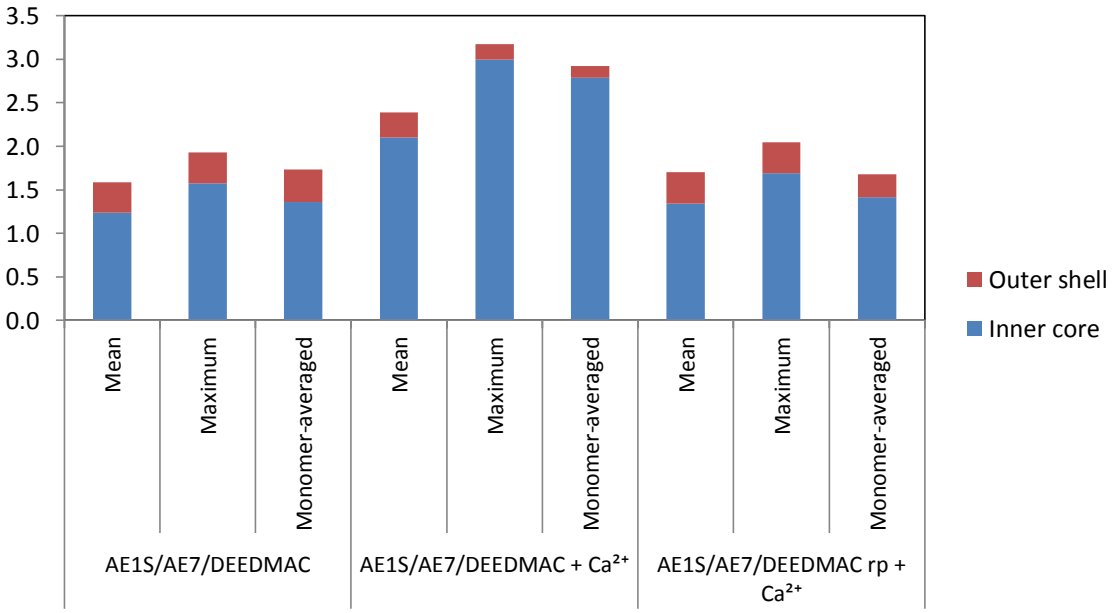

Figure 6-46: Micellar radii of the AE1S/AE7/DEEDMAC system, before and after the addition of calcium ions

The AE1S/DEEDMAC system, and the repeated AE1S/AE7/DEEDMAC sample, gave several occasions where two distinct micelles were close enough that the program identified them as one; to avoid this, frames were inspected visually to identify the number of micelles present. Frames misidentifying the number of micelles present were excluded from the calculations of average micelle size.

With the exception of the first AE1S/AE7/DEEDMAC system, there was no major difference in size and aggregation number between systems with and without calcium ions. When this sample was re-run, it gave a size and aggregation number closer to that seen in the system without calcium. This suggests that the calcium ions were not having a large effect on the micelle structure.

To look at the effect of the micelle on the ion position, the distance of the ions from their nearest micelle was tracked.

Table 6-17: Distance of Ca^{2+}, Na^{+}, and Cl^{-} ions from the surface of the micelles

System	**Ca^{2+} distance from micelle / nm**	**Standard deviation for Ca^{2+} / nm**	**Na^{+} distance from micelle / nm**	**Standard deviation for Na^{+} / nm**	**Cl^{-} distance form micelle / nm**	**Standard deviation for Cl^{-} / nm**
AE1S	n/a	n/a	0.8	0.7	n/a	n/a
AE1S + Ca^{2+}	0.0	0.2	0.8	0.8	n/a	n/a
AE7	n/a	n/a	n/a	n/a	n/a	n/a
AE7 + Ca^{2+}	3.9	2.3	n/a	n/a	3.7	2.3
AE1S/AE7	n/a	n/a	1.1	1.0	n/a	n/a
AE1S/AE7 + Ca^{2+}	0.0	0.6	1.3	1.0	n/a	n/a
AE1S/DEEDMAC	n/a	n/a	1.1	1.0	n/a	n/a
AE1S/DEEDMAC + Ca^{2+}	0.0	0.5	1.5	1.1	n/a	n/a
AE7/DEEDMAC	n/a	n/a	n/a	n/a	1.6	1.2
AE7/DEEDMAC + Ca^{2+}	3.2	1.7	n/a	n/a	2.1	1.9
AE1S/AE7/DEEDMAC	n/a	n/a	1.2	1.0	n/a	n/a
AE1S/AE7/DEEDMAC + Ca^{2+}	0.0	1.3	1.7	1.6	n/a	n/a
AE1S/AE7/DEEDMAC + Ca^{2+} (repeat)	0.0	0.8	1.6	1.3	n/a	n/a

In Table 6-17, the distance given for each ion from the micelle was the mean distance from each ion to the surface of its nearest micelle. The standard distribution was reflective of the broadness of the distribution, rather than error in the data in this instance. The ions are assumed to have been normally distributed such that $P(r) = \frac{e^{-(r-\mu)^2/2\sigma^2}}{\sigma\sqrt{2\pi}}$, where r is the distance from the micelle-solvent interface i.e. the mean distance of the ions from the micellar centre minus the micellar radius, μ is the mean distance of the ions from the micelle-solvent interface, σ is the standard deviation, and $P(r)$ is the probability distribution. It can be assumed that approximately 68% of the ions fell within 1 standard deviation of the mean, and 95% fell within 2 standard deviations of the mean.

The most obvious trend seen was for Ca^{2+} ions in samples containing AE1S, as shown in Figure 6-47. In these samples, the Ca^{2+} ions were at approximately 0.0 nm from the micelle – i.e. as close to the surface of the micelle as possible. This was as expected, due to the negative charge on this surfactant. The standard deviation in this sample was 0.2 nm, reflecting the narrow band within which the ions were found. For ions where the distance from the outer shell was negative, this represented the low head group density of the micelle, and thus potentially entry of the calcium ions into this region, along with the elliptical nature of the micelle, rather than deep penetration of the ions into the tail group region of the micelle. It can be seen that the Na^+ also had an attraction to the AE1S within the micelles, although this was weaker as indicated by its increased distance of 0.8 nm, and its more dispersed nature as indicated by its standard distribution of 0.8 nm. The weaker interaction of the Na^+ was expected due to its reduced charge compared to the Ca^{2+} ion.

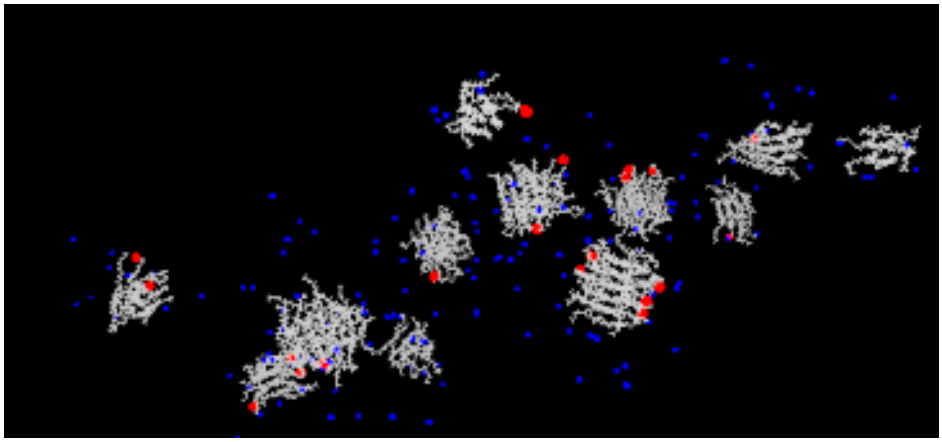

Figure 6-47: Position of calcium (red) and sodium (blue) ions in an AE1S (grey) system. Water molecules have been omitted for clarity.

It can be seen that, although in all samples containing the AE1S (i.e. AE1S, AE1S/AE7, AE1S/DEEDMAC, and AE1S/AE7/DEEDMAC) the Ca^{2+} had a mean distance of 0 nm from the outer shell, the standard deviation of these samples increased in the order AE1S < AE1S/DEEDMAC < AE1S/AE7 < AE1S/AE7/DEEDMAC. This indicated that the ions became more dispersed as this series progresses. The positions of the AE1S and the AE1S/AE7/DEEDMAC in this series were as expected; the system containing the highest proportion of anionic surfactant had the greatest affinity for the cationic ion, whereas the system with the lowest proportion of the anionic surfactant had the least affinity for the ion. It is perhaps unexpected that the system containing both anionic and cationic surfactants had a greater affinity for the cationic ion than the system containing both anionic and nonionic surfactants; however, this was likely due to the higher proportion of AE1S in the AE1S/DEEDMAC system (83%) than in the AE1S/AE7 system (71%). It can be noted that the standard deviation was very close for these systems: 0.5 nm for the AE1S/DEEDMAC system, compared to 0.6 nm for the AE1S/AE7 system.

It can be seen that, as the proportion of nonionic and cationic surfactants increased, the mean distance between the Na^{+} and the surface of the micelle increased in the order AE1S/AE7 < AE1S/DEEDMAC < AE1S/AE7/DEEDMAC. This was as expected given the like-charge repulsion between the DEEDMAC and the Na^{+}.

The AE7 showed little to no affinity for the Ca^{2+} ions, as indicated by the high average distance, low standard deviation in comparison to the mean distance, and similarity in distance between the mean Ca^{2+} distance and the mean Cl^{-} distance. Assuming the ions were normally distributed, there would be a 4.5% chance that any given Ca^{2+} ion would

be found at 0 nm or less from the micelle-solvent interface, and a 5.4% chance that any given Cl^- ion would be found at 0 m or less from this interface. Again, negative distances from the interface indicated penetration into the micelle head group region. This system is shown in Figure 6-48 below.

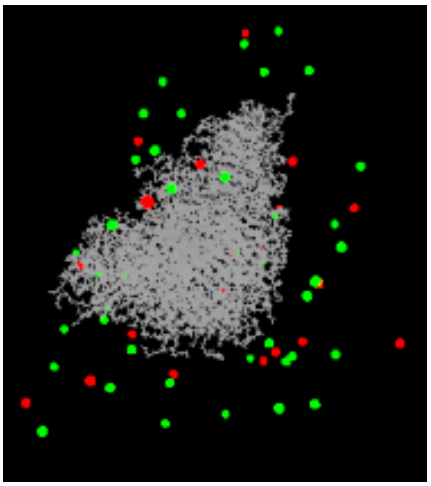

Figure 6-48: Position of calcium (red) and chlorine (green) ions relative to an AE7 (grey) micelle. Water molecules have been omitted for clarity.

The AE7/DEEDMAC sample showed significantly more affinity for the Cl^- ions than for the Ca^{2+} ions, as indicated by the lower mean distance from the shell (2.1 nm for the Cl^- ions, and 3.2 nm for the Ca^{2+} ions) and similar standard deviations (1.9 nm for the Cl^- ions, and 1.7 nm for the Ca^{2+} ions). This was expected due to the opposite-charge attraction and like-charge repulsion from the cationic head group.

In every case except the AE1S system, the addition of Ca^{2+} ions increased the mean distance of the Na^+ or Cl^- counterion from the micelle. In the AE1S system, the mean distance of the Na^+ ions did not change when calcium ions were added. In addition, the standard distribution of the Na^+ or Cl^- ions increased or was unchanged in every system studied. For the systems containing AE1S, where Na^+ is the counterion, this showed that the calcium is displacing the Na^+ ions from the micelles. For the AE7/DEEDMAC system, where Cl^- is the counterion, the increased distance of the Cl^- ions from the micelles when Ca^{2+} ions were added may have indicated charge shielding of the Ca^{2+} ions by the Cl^- ions.

6.3. Conclusions

6.3.1. Preformed micelles

Surfactants preformed in a micelle configuration, with additional hexane added to their centre, were shown to stabilise rapidly. When brightener molecules were added to these systems, the primary factor affecting the final position of the brightener molecule was the initial position of the brightener, suggesting that the system did not reach a true equilibrium.

6.3.2. Randomised micelles

6.3.2.1. Surfactant only systems

It was seen that the randomised surfactant solutions self-aggregated into micelles. The smallest aggregation numbers were seen in the AE1S-only surfactant systems, and the highest aggregation numbers and micellar radii were seen in the AE7-only surfactant systems. The proportion of AE7 in the system was correlated with micelle size and aggregation number, whereas the proportion of AE1S in the system was inversely correlated with micelle size and aggregation number.

6.3.2.2. Addition of brightener

When 10 brightener molecules were added to the surfactant systems, this generally had little effect on the micellar radii and aggregation number of the system. The brightener molecules were incorporated into the micelles with their hydrocarbon chains along the core-shell interface and their sulfate groups in the shell of the micelle.

6.3.2.3. Varying composition of solution

The number of brightener molecules added to the AE1S, AE7, and AE1S/AE7/DEEDMAC systems was varied. The number of brightener molecules added did not greatly affect the micellar radii and aggregation numbers of the AE1S and AE1S/AE7/DEEDMAC systems, but increased brightener concentrations acted to reduce the aggregation numbers and micellar radius of the AE7 system, when a sufficiently high number of brightener molecules, greater or equal to 15, were added. When AE1S was added to the AE7 system in small quantities, this had a similar but weaker effect on the aggregation number and micellar radius of the AE7 system.

6.3.2.4. Addition of calcium ions

It was seen that the addition of calcium ions did not significantly affect the micelle aggregation number or micellar radii. However, several trends in the placement of the calcium ions could be seen.

The calcium ions interacted strongly with the anionic AE1S surfactant. As the proportion of AE1S was decreased, the strength of this interaction was decreased, as shown by an increase in the mean distance to the micelle and the standard deviation. The calcium ions did not interact significantly with the nonionic surfactants, and repulsive effects were seen in systems containing cationic surfactants but no nonionic surfactants.

In systems where Na^+ ions were present, the Ca^{2+} ions displaced these from their position around the micelle. Where Cl^- ions were present, they acted to screen the cationic/nonionic micelle from the Ca^{2+} ions.

7. Conclusions

7.1. Effect of micelle composition on size and shape

The micelles with the largest radii were given by the AE7-only system. This was confirmed by the inner core radius of 2.3 nm and micellar radius of 3.3 nm given by GIFT analysis in Chapter 5, and by the inner core radius of 2.7 nm and micellar radius of 3.5 nm given by MD simulations detailed in Chapter 6. The smallest micelles were those in the AE1S system, again confirmed by the inner core radius of 2.0 nm and micellar radius of 2.6 nm given by GIFT analysis, and the mean inner core radius of 1.0 nm and mean micellar radius of 1.4 nm given by randomised MD simulations. It was shown in Chapter 6 that increasing the proportion of AE1S in a system decreased its micellar radii and aggregation number, with a mean aggregation number of 15 for an AE1S-only system, whereas increasing the proportion of AE7 in the system increased the radii and aggregation number, with a mean aggregation number of 200 for an AE7-only system.

Differences in the micellar shape could be seen in these two systems. The spherical nature of the AE7 micelles was seen from the good agreement obtained between DECON results and the modelled form factor, with an inner core electron density of 0.215 $e^{-}Å^{-3}$ and outer shell electron density of 0.371 $e^{-}Å^{-3}$ obtained from DECON, and inner core electron density of 0.26 $e^{-}Å^{-3}$ and outer shell electron density of 0.385 $e^{-}Å^{-3}$ obtained from the form factor model, and from the spherical appearance of the final configuration of the simulation. The micelle was seen to have a dense outer shell, as a result of the long-chain head groups folding.

The AE1S micelles were not spherical; instead they seemed to have a stacked cylindrical shape, particularly at lower aggregation numbers. This was seen most clearly in the simulation outputs, but could also be seen in the physically unrealistic results obtained from DECON analysis of this system, with the inner core electron density given as -0.031 $e^{-}Å^{-3}$, and the outer shell electron density given as 0.611 $e^{-}Å^{-3}$. Its outer shell region was shown to be sparse, with sulfate ions ‘dotting the surface’ but providing a large amount of space for water penetration.

For the mixed AE1S/AE7 system, results from DECON were still unrealistic, but less so than for the AE1S alone, with an inner core electron density of 0.05 $e^{-}Å^{-3}$ and an outer

shell electron density of 0.50 $e^{-}Å^{-3}$. The simulation results showed that this system had a more spherical shape than that of AE1S alone.

7.2. Placement of brightener within micelle

The brightener was shown to interact with all surfactant systems tested. However, in some systems, this interaction was more marked than in others.

The SAXS scattering given by the AE7 system with brightener showed a significant shift to higher *q*, from 1.1 to 1.4 nm^{-1}, with increasing brightener concentration, corresponding to an increase in electron density from 0.371 – 0.385 $e^{-}Å^{-3}$ to 0.433 – 0.44 $e^{-}Å^{-3}$ in the outer shell of the micelle. While a shift in *I*(*q*) was seen in the AE1S system, from approximately 1.5 to 1.6 nm^{-1} , and a corresponding increase in the electron density was seen from 0.40 $e^{-}Å^{-3}$ to 0.42 $e^{-}Å^{-3}$ as calculated using the modelled form factor, this was significantly less than that seen in the AE7 system.

This result can be explained by the trends seen in micelle structure shown in Chapter 6. When the brightener was added to AE1S, its hydrocarbon backbone was aligned with the tail groups of the AE1S, with its head groups oriented outwards. Further evidence for this configuration of the brightener molecule was seen in the crystal structure for the Brightener 49 methanol solvate obtained in Chapter 4. The addition of brightener had no effect on the overall size and aggregation number of the micelle. In this way, the brightener could be said to be replacing an AE1S molecule in the micelle.

When the brightener was added to the AE7, it was incorporated into the dense outer shell of the micelle, with its hydrocarbon chain at the boundary with the inner core and the outer shell, and its sulfate groups oriented into the outer shell. The most striking effect, however, was on the aggregation number of the AE7 system seen in the simulations. As the number of brightener molecules added to the simulation increased from 10 to 20 molecules, the mean aggregation number decreased from 210 to 55, and the mean micellar radii decreased from 3.7 nm to 2.2 nm. This was not seen in the AE1S and AE1S/AE7/DEEDMAC simulations, and could be seen as analogous to the decrease in aggregation number and radii caused by increasing the proportion of AE1S in the system (strengthening the comparison between the brightener molecule and the AE1S molecule).

7.3. Effect of surfactants on brightener deposition

The main trend seen in the deposition experiments in Chapter 3 was for the addition of AE1S to promote brightener deposition, and for the addition of AE7 to inhibit deposition. In addition, the addition of AE1S did not affect the emission and excitation structure of the brightener, whereas the addition of AE7 increased the number of peaks seen and shifts them to lower wavenumber, from 6927 cm^{-1} to approximately 5600 cm^{-1}, in the emission spectrum. This suggested that the brightener experienced the same amount of hydrogen bonding in the AE1S solution as in water alone, but experienced less hydrogen bonding when in AE7 solution.

These results can be interpreted in line with the output configurations of the simulations in Chapter 6 thus: when the brightener was added to the AE7 system, it was incorporated deep within the head group of the molecule. This hindered its ability to move freely, and to leave the surfactant micelle in order to be deposited onto the fabric. It also experienced less hydrogen bonding due to the low degree of water penetration into the head group of this micelle. However, when the brightener was added to the AE1S system and incorporated into micelles, it was less sterically hindered and could be deposited more easily. As there was a greater degree of water penetration into the head group region of this micelle, the brightener could also experience more hydrogen bonding.

7.4. Effect of calcium ions on surfactant micelles

The data presented in both Chapter 5 and Chapter 6 showed that the calcium ions had little to no affinity for the nonionic surfactant micelles. There was no change seen in the SAXS scattering data when calcium ions were added, and in the computational work, the mean distance of calcium ions to nonionic surfactant micelles was high (3.9 nm), suggesting that they were not attracted to the micelles. This was to be expected given the lack of a charged group on the nonionic surfactant micelle. Chapter 4 showed that, at low concentrations, increasing the concentration of AE7 from 2.49 g L^{-1} to 4.98 or 7.44 g L^{-1} decreased the time taken for $CaCO_3$ precipitation from 8 – 13 minutes to 4 – 6 minutes or 3 – 5 minutes respectively, but that at high concentrations, increasing the concentration of AE7 to 9.90 or 12.3 g L^{-1} increased the time taken for $CaCO_3$ precipitation to 10 – 47 minutes or 1 hour – 1 day respectively.

The data from these chapters also showed that the calcium ions had an affinity for the AE1S-containing micelles, as indicated by the very low distance between the micelle and the Ca^{2+} ions of 0.0 nm, and the increase in intensity of the peak in $I(q)$. However, this did not correspond to a change in the aggregation number or micellar radius of the micelles. Increasing the concentration of AE1S in a calcium carbonate system from 2.05 g L^{-1} to 8.14 g L^{-1} was also shown in Chapter 4 to increase the time taken for $CaCO_3$ precipitation from 2 minutes to up to 4 days, suggesting either that Ca^{2+} ions were adsorbing onto the micelle, or that the surfactant was adsorbing onto the face of the crystal.

7.5. Suggestions for future work

7.5.1. Fluorescence work

To expand upon this work, a greater range of surfactants, fabrics, and initial concentrations could be examined. During the fluorescence studies in Section 3.2.2.1, in which the effect of the addition of surfactant on the fluorescence emission and excitation spectra of Brightener 49 was studied, only two surfactant systems were used: AE1S and AE7. During the brightener deposition studies in Section 3.2.2.3, only two sets of surfactant systems were used due to time constraints: 2.05 g L^{-1} AE1S, and 2.49 g L^{-1} AE7. In addition, only two types of fabric were used in this section.

To improve upon this work, future studies would use a wider range of surfactants and surfactant mixtures of varied proportions, at various concentrations above and below their CMC. Firstly, the fluorescence spectra of Brightener 49 in these solutions would be collected, and any solvatochromic shift determined, allowing the hydrophilic environment of the brightener in these solutions to be studied. Fabric deposition testing could then be run on these solutions, to determine the effect that this change in environment has had on the deposition rate of the brightener. Using this method, it may be possible to determine a detergent composition which will optimise brightener deposition.

In addition, the calibration curve created in Section 3.2.2.2 could be recalculated using a wider range of data points, to improve the accuracy of results. Brightener fluorescence spectra could also be taken in a wider range of solvents, to gain a fuller picture of the effect of hydrogen bonding on the emission spectrum of this compound.

7.5.2. Crystallisation

Although attempts to produce a Brightener 49 or Brightener 15 crystal were unsuccessful in this work (with the exception of a Brightener 49 methanol solvate), it is possible that these crystals could be produced. Future work would study the effect of a wider range of solvents on the crystallisation of these brightener molecules, both through vapour diffusion methods and through reverse microemulsion crystallisation. Using these methods, a calcium-brightener precipitate could also be produced and characterised, showing the effect of hard water on this compound. The rate of this precipitation in standard wash conditions could also be studied, to determine the impact of this process on the detergent user.

7.5.3. SAXS

Due to time restraints, only one concentration of each surfactant was studied using SAXS, and only one composition of each mixed surfactant system was studied. Future studies would look at a variety of surfactant concentrations, and study the effect that concentration variance has on the radius and aggregation number of the surfactant micelles. The composition of the mixed micelles could also be varied, to determine the effect that changing the ratios of each surfactant has on the overall size of the micelle.

7.5.4. Molecular dynamics simulations

In the molecular dynamics simulations carried out in this project, the addition of ionic molecules to the simulation caused the aggregation number and micellar radii to decrease far beyond that seen in experiment. Future work would attempt to resolve this by repeating the simulations over longer timescales, to determine if these smaller micelles would aggregate over time. To reduce the computational impact of these longer timescales, coarse-grained models could be used to reduce the complexity of the simulation. This would show if the simulations seen previously had reached a true equilibrium, or merely a local equilibrium. The forcefield used to model the ionic molecules could also be varied, to find a system which can model ionic surfactants more accurately.

8. References

1 I. C. Reynhout, J. J. L. M. Cornelissen and R. J. M. Nolte, *Acc. Chem. Res.*, 2009, **42**, 681–692.

2 V. Kelley, *Soap and water: cleanliness, dirt and the working classes in Victorian and Edwardian Britain*, I B Taurus, London, 2010.

3 D. Bajpai and V. K. Tyagi, *J. Oleo Sci.*, 2007, **56**, 327–340.

4 R. A. Watson, in *Handbook of Detergents Part D: Formulation*, ed. M. S. Showell, CRC Press, Boca Raton, FL, 2006, pp. 51–104.

5 N. Homendra and C. I. Devi, *Indian J. Chem. Technol.*, 2004, **11**, 783–786.

6 K. L. Matheson, M. F. Cox and D. L. Smith, *J. Am. Oil Chem. Soc.*, 1985, **62**, 1391–1396.

7 M. F. Cox and K. L. Matheson, *J. Am. Oil Chem. Soc.*, 1985, **62**, 1396–1399.

8 J. M. Newsam, *Science (80-.).*, 1986, **231**, 1093–1099.

9 C. Fruijtier-Pölloth, *Arch. Toxicol.*, 2009, **83**, 23–35.

10 A. J. O'Lenick, Jr., *J. Surfactants Deterg.*, 1999, **2**, 553–557.

11 T. S. Espósito, I. P. G. Amaral, D. S. Buarque, G. B. Oliviera, L. B. Carvalho Júnior and R. S. Bezerra, *Food Chem.*, 2009, **112**, 125–130.

12 D. A. Basketter, J. S. C. English, S. H. Wakelin and I. R. White, *Br. J. Dermatol.*, 2008, **158**, 1177–1181.

13 V. Croud, in *Handbook of Detergents Part A: Properties*, eds. U. Zoller and G. Broze, Marcel Dekker, Inc, New York, 1999, pp. 597–618.

14 M. J. Rosen, *Surfactants and interfacial phenomena*, Wiley, New York, 2nd edn., 1989.

15 J. N. Israelachvili, D. J. Mitchell and B. W. Ninham, *J. Chem. Soc. Faraday Trans. 2 Mol. Chem. Phys.*, 1976, **72**, 1525.

16 R. Nagarajan, *Langmuir*, 2002, **18**, 31–38.

17 M. L. Chen, J. Penfold and R. K. Thomas, *Langmuir*, 2010, **26**, 17958–17968.

18 J. H. Clint, *J. Chem. Soc. Faraday Trans. 1 Phys. Chem. Condens. Phases*, 1975, **71**, 1327–1334.

19 P. Mukherjee, S. K. Padhan, S. Dash, S. Patel and B. K. Mishra, *Adv. Colloid Interface Sci.*, 2011, **162**, 59–79.

20 K. Shinoda, N. Yamaguchi and A. Carlsson, *J. Phys. Chem.*, 1989, **93**, 7216–7218.

21 M. Kahlweit and H. Reiss, *Langmuir*, 1991, **7**, 2928–2933.

22 P. A. Winsor, *Trans. Faraday Soc.*, 1948, **44**, 376–398.

23 A. C. John and A. K. Rakshit, *Langmuir*, 1994, **10**, 2084–2087.

24 E. Magennis and M. Jackson, 2012.

25 J. Penfold, R. K. Thomas, C. C. Dong, I. Tucker, K. Metcalfe, S. Golding and I. Grillo, *Langmuir*, 2007, **23**, 10140–10149.

26 P. Goon, S. Das, C. J. Clemett, G. J. T. Tiddy and V. V. Kumar, *Langmuir*, 1997, **13**, 5577–5582.

27 I. Adami, in *Handbook of Detergents Part F: Production*, eds. U. Zoller and P. Sosis, CRC Press, Boca Raton, FL, 2009, pp. 83–116.

28 P. Goon, C. Manohar and V. V. Kumar, *J. Colloid Interface Sci.*, 1997, **189**, 177–180.

29 C. Genova, U. Schoenkaes, D. Smith and M. Stolz, *J. Surfactants Deterg.*, 2003, **6**, 365–372.

30 M. Li, Y. Rharbi, M. A. Winnik and K. G. Hahn, Jr., *J. Colloid Interface Sci.*, 2001, **240**, 284–293.

31 M. F. Cox, *J. Am. Oil Chem. Soc.*, 1989, **66**, 1637–1646.

32 M. Aoudia, B. Al-Haddabi, Z. Al-Harthi and A. Al-Rubkhi, *J. Surfactants Deterg.*, 2010, **13**, 103–111.

33 M. J. Schwuger, *ACS Symp. Ser.*, 1984, **253**, 3–26.

34 S. T. Giolando, R. a. Rapaport, R. J. Larson, T. W. Federle, M. Stalmans and P. Masscheleyn, *Chemosphere*, 1995, **30**, 1067–1083.

35 *Human and Environmental Risk Assessment on ingredients of Household Cleaning Products Esterquats Environmental Risk Assessment Report*, 2008.

36 M. G. Basavaraj, N. L. McFarlane, M. L. Lynch and N. J. Wagner, *J. Colloid Interface Sci.*, 2014, **429**, 17–24.

37 E. R. Trotman, *Dyeing and chemical technology of textile fibres*, Arnold, London, 6th edn., 1984.

38 A. B. D. Cassie, *Trans. Faraday Soc.*, 1945, **41**, 458–464.

39 L. J. Lynch, I. C. Watt and K. H. Marsden, *Kolloid-Zeitschrift und Zeitschrift für Polym.*, 1971, **248**, 922–942.

40 J. D. Leeder and I. C. Watt, *J. Phys. Chem.*, 1965, **69**, 3280–3284.

41 I. C. Watt and J. D. Leeder, *J. Appl. Chem.*, 1968, **18**, 1–4.

42 Q. Li, T. Lin and X. Wang, *J. Text. Inst.*, 2012, **103**, 662–668.

43 J. Lyklema, *Chem. Phys. Lett.*, 2009, **467**, 217–222.

44 P. Lo Nostro, L. Fratoni, B. W. Ninham and P. Baglioni, *Biomacromolecules*, 2002, **3**, 1217–1224.

45 R. Samu, A. Moulee and V. G. Kumar, *J. Colloid Interface Sci.*, 1999, **220**, 260–268.

46 C. A. Miller and K. H. Raney, *Colloids Surfaces A Physicochem. Eng. Asp.*, 1993, **74**, 169–215.

47 C. Pakula and R. Stamminger, *Energy Effic.*, 2010, **3**, 365–382.

48 K. Laitala, I. G. Klepp and C. Boks, *Int. J. Consum. Stud.*, 2012, **36**, 228–237.

49 M. Albeck, A. Ben-Bassat, J. A. Epstein and M. Lewin, *Text. Res. J.*, 1965, **35**, 836–843.

50 R. M. A. Malek and I. Holme, *Iran. Polym. J.*, 2003, **12**, 271–280.

51 S. Perincek, M. İ. Bahtiyari, K. Duran and A. E. Körlü, *J. Text. Inst.*, 2009, **100**, 738–746.

52 S. Margutti, S. Vicini, N. Proietti, D. Capitani, G. Conio, E. Pedemonte and A. L. Segre, *Polymer (Guildf).*, 2002, **43**, 6183–6194.

53 K. R. Millington, A. L. King, S. Hatcher and C. Drum, *Color. Technol.*, 2011, **127**, 297–303.

54 G. Gryn'ova, J. L. Hodgson and M. L. Coote, *Org. Biomol. Chem.*, 2011, **9**, 480–490.

55 K. R. Millington and G. Maurdev, *J. Photochem. Photobiol. A Chem.*, 2004, **165**, 177–185.

56 O. D. Bangee, V. H. Wilson, G. C. East and I. Holme, *Polym. Degrad. …*, 1995, **50**, 313–317.

57 C. H. Choi and M. Kertesz, *J. Phys. Chem. A*, 1997, **101**, 3823–3831.

58 J. March, *Advanced organic chemsitry: reactions, mechanisms, and structure*, Wiley, New York, 4th edn., 1992.

59 N. J. Turro, *Modern molecular photochemistry*, University Science Books, Mill Valley, CA, Expanded p., 1991.

60 A. S. Holmes, D. J. S. Birch, A. Sanderson and G. G. Aloisi, *Chem. Phys. Lett.*, 1997, **266**, 309–316.

61 V. D. Vachev, J. H. Frederick, B. A. Grishanin, V. N. Zadkov and N. I. Koroteev, *J. Phys. Chem.*, 1995, **99**, 5247–5263.

62 A. Dorlars, C.-W. Schellhammer and J. Schroeder, *Angew. Chemie Int. Ed.*, 1975, **14**, 665–679.

63 S. M. A. Martins, P. C. S. Branco and A. M. D. R. L. Pereira, *J. Braz. Chem. Soc.*, 2012, **23**, 688–693.

64 W. R. Findley, *J. Am. Oil Chem. Soc.*, 1983, **60**, 1367–1369.

65 4,605,511, *US Pat. 4,605,511*, 1986.

66 B. Simončič and J. Špan, *Dye. Pigment.*, 1998, **36**, 1–14.

67 B. Simončič and F. Kovac, *Dye. Pigment.*, 1998, **40**, 1–9.

68 S. Göktürk and M. Tunçay, *Spectrochim. Acta Part A Mol. Biomol. Spectrosc.*, 2003, **59**, 1857–1866.

69 S. Fazeli, B. Sohrabi and A. R. Tehrani-Bagha, *Dye. Pigment.*, 2012, **95**, 768–775.

70 B. Simončič and J. Špan, *Dye. Pigment.*, 2000, **46**, 1–8.

71 Z. Xie, H. Wang, F. Li, W. Xie, L. Liu, B. Yang, L. Ye and Y. Ma, *Cryst. Growth Des.*, 2007, **7**, 2512–2516.

72 M. N. Miljković, M. M. Purenović, M. K. Novaković and S. S. Randjelović, *Hem. Ind.*, 2011, **65**, 61–66.

73 E. T. Iamazaki and T. D. Z. Atvars, *J. Appl. Polym. Sci.*, 2012, **124**, 4371–4380.

74 E. T. Iamazaki, M. A. Pereira-Da-Silva, A. J. F. Carvalho, R. B. Romero, M. C. Gonc and T. D. Z. Atvars, *J. Appl. Polym. Sci.*, 2010, **118**, 2321–2327.

75 J. Was-Gubala, *Sci. Justice*, 2009, **49**, 165–169.

76 J. Was-Gubala and E. Grzesiak, *Sci. Justice*, 2010, **50**, 55–58.

77 K. Maseka, *AATCC Rev.*, 2005, **5**, 35–38.

78 H. W. Zussman, *J. Am. Oil Chem. Soc.*, 1963, **40**, 695–698.

79 P. S. Stensby, *J. Am. Oil Chem. Soc.*, 1968, **45**, 497–504.

80 E. Wilkowska and L. Konopski, *QSAR Comb. Sci.*, 2008, **27**, 357–364.

81 M.-Y. Park, Y.-K. Lee and B.-S. Lim, *Dent. Mater.*, 2007, **23**, 731–735.

82 I. Hanyż, R. M. Ion, A. Nuta and D. Wróbel, *J. Mol. Struct.*, 2008, **887**, 165–171.

83 D. H. He, X. W. Li, C. Yang and J. Yang, *Spectrochim. Acta - Part A Mol. Biomol. Spectrosc.*, 2012, **95**, 184–187.

84 W.-C. Shu and W.-H. Ding, *J. Chinese Chem. Soc.*, 2009, **56**, 797–803.

85 S. T. Glassmeyer, E. T. Furlong, D. W. Kolpin, J. D. Cahill, S. D. Zaugg, S. L. Werner, M. T. Meyer and D. D. Kryak, *Environ. Sci. Technol.*, 2005, **39**, 5157–5169.

86 D. B. D. Simmons, V. L. Trudeau, V. L. Marlatt, T. W. Moon, J. P. Sherry and C. D. Metcalfe, *Environ. Toxicol. Chem.*, 2008, **27**, 442–451.

87 H. J. Kobus, E. Silenieks and J. Scharnberg, *J. Forensic Sci.*, 2002, **47**, 819–823.

88 I. M. Algaba, M. Pepió and A. Riva, *Ind. Eng. Chem. Res.*, 2007, **46**, 2677–2682.

89 M. R. Spiegel, *Schaum's outline of theory and problems of Fourier analysis with applications to boundary value problems*, McGraw-Hill, New York, 1974.

90 R. W. Ramirez, *The FFT : Fundamentals and concepts*, Prentice-Hall, Englewood Cliffs, N.J, 1985.

91 G. Porod, in *Small Angle X-ray Scattering*, eds. O. Glatter and O. Kratky, Academic Press, London, 1982, pp. 17–52.

92 P. Debye and A. M. Bueche, *J. Appl. Phys.*, 1949, **20**, 518–525.

93 O. Glatter, in *Small Angle X-ray Scattering*, eds. O. Glatter and O. Kratky, Academic Press, London, 1982, pp. 119–166.

94 O. Glatter, in *Small Angle X-ray Scattering*, eds. O. Glatter and O. Kratky, Academic Press, London, 1982, pp. 167–196.

95 S. Vass, J. Pleštil, P. Laggner, T. Gilányi, S. Borbély, M. Kriechbaum, G. Jákli, Z. Décsy and P. M. Abuja, *J. Phys. Chem. B*, 2003, **107**, 12752–12761.

96 Y. C. Liu, S. H. Chen and R. Itri, *J. Phys. Condens. Matter*, 1996, **8**, A169–A187.

97 O. Kratky and K. Müller, in *Small Angle X-ray Scattering*, eds. O. Glatter and O. Kratky, Academic Press, London, 1982, pp. 499–510.

98 L. A. Feigin and D. I. Svergun, *Structure Analysis by Small-Angle X-Ray and Neutron Scattering*, Springer US, 1987.

99 J. L. Lebowitz and J. K. Percus, *Phys. Rev.*, 1966, **144**, 251–258.

100 J. B. Hayter and J. Penfold, *Colloid Polym. Sci.*, 1983, **261**, 1022–1030.

101 A. Jusufi, A. Kohlmeyer, M. Sztucki, T. Narayanan and M. Ballauff, *Langmuir*, 2012, **28**, 17632–17641.

102 V. Aswal and P. Goyal, *Phys. Rev. E*, 2000, **61**, 2947–2953.

103 V. K. Aswal and P. S. Goyal, *Chem. Phys. Lett.*, 2002, **364**, 44–50.

104 V. K. Aswal and P. S. Goyal, *Chem. Phys. Lett.*, 2003, **368**, 59–65.

105 S. Vass, J. S. Pedersen, J. Pleštil, P. Laggner, E. Rétfalvi, I. Varga and T. Gilányi, *Langmuir*, 2008, **24**, 408–417.

106 C. Chen, O. Cook, C. E. Nicholson and S. J. Cooper, *Cryst. Growth Des.*, 2011, **11**, 2228–2237.

107 P. Dierckx, *Curve and surface fitting with splines*, Clarendon Press, Oxford, 1993.

108 O. Glatter, *J. Appl. Crystallogr.*, 1977, **10**, 415–421.

109 J. Brunner-Popela and O. Glatter, *J. Appl. Crystallogr.*, 1997, **30**, 431–442.

110 S. Kantorovitz, *Introduction to Modern Analysis*, Oxford University Press, 2003.

111 O. Glatter, *J. Appl. Crystallogr.*, 1981, **14**, 101–108.

112 O. Glatter and B. Hainisch, *J. Appl. Crystallogr.*, 1984, **17**, 435–441.

113 E. Lindahl, B. Hess and D. van der Spoel, *J. Mol. Model.*, 2001, **7**, 306–317.

114 H. J. C. Berendsen, D. van der Spoel and R. van Drunen, *Comput. Phys. Commun.*, 1995, **91**, 43–56.

115 D. Van Der Spoel, E. Lindahl, B. Hess, G. Groenhof, A. E. Mark and H. J. C. Berendsen, *J. Comput. Chem.*, 2005, **26**, 1701–1718.

116 B. Hess, C. Kutzner, D. van der Spoel and E. Lindahl, *J. Chem. Theory Comput.*, 2008, **4**, 435–447.

117 S. Pronk, S. Páll, R. Schulz, P. Larsson, P. Bjelkmar, R. Apostolov, M. R. Shirts, J. C. Smith, P. M. Kasson, D. Van Der Spoel, B. Hess and E. Lindahl, *Bioinformatics*, 2013,

29, 845–854.

118 U. Essmann, L. Perera, M. L. Berkowitz, T. Darden, H. Lee and L. G. Pedersen, *J. Chem. Phys.*, 1995, **103**, 8577–8592.

119 D. A. Case, J. T. Berryman, R. M. Betz, D. S. Cerutti, I. Cheatham, T. E., T. A. Darden, R. E. Duke, T. J. Giese, H. Gohlke, A. W. Goetz, N. Homeyer, S. Izadi, P. Janowski, J. Kaus, A. Kovalenko, T. S. Lee, S. LeGrand, P. Li, T. Luchko, R. Luo, B. Madej, K. M. Merz, G. Monard, P. Nedham, H. Nguyen, H. T. Nguyen, I. Omelyan, A. Onufriev, D. R. Roe, A. Roitberg, R. Salomon-Ferrer, C. L. Simmerling, W. Smith, J. Swails, R. C. Walker, J. Wang, R. M. Wolf, X. Wu, D. M. York and P. A. Kollman, 2015.

120 K. B. Koziara, M. Stroet, A. K. Malde and A. E. Mark, *J. Comput. Aided. Mol. Des.*, 2014, **28**, 221–233.

121 A. K. Malde, L. Zuo, M. Breeze, M. Stroet, D. Poger, P. C. Nair, C. Oostenbrink and A. E. Mark, *J. Chem. Theory Comput.*, 2011, **7**, 4026–4037.

122 J. J. Gray, *Arch. Hist. Exact Sci.*, 1980, **21**, 375–385.

123 M. Walker, 2014.

124 A. D. MacKerell Jr., *J. Phys. Chem.*, 1995, **99**, 1846–1855.

125 T. Wymore, X. F. Gao and T. C. Wong, *J. Mol. Struct.*, 1999, **485-486**, 195–210.

126 S. Jalili and M. Akhavan, *Colloids Surfaces A Physicochem. Eng. Asp.*, 2009, **352**, 99–102.

127 E. M. Piotrovskaya, A. A. Vanin and N. A. Smirnova, *Mol. Phys.*, 2006, **104**, 3645–3651.

128 J. Gao, W. Ge, G. Hu and J. Li, *Langmuir*, 2005, **21**, 5223–5229.

129 H. P. Schuchmann and C. von Sonntag, *J. Photochem.*, 1981, **16**, 289–295.

130 J. R. Lakowicz, in *Principles of Fluorescence Spectroscopy*, Springer US, 3rd Editio., 2006, pp. 27–61.

131 A. Tiki, A. Amin, A. Kanwal and A. V. M. C. Industries, 2010, 42–43.

132 *IARC Monogr. Eval. Carcinog. Risks to Humans*, 2010, **99**, 55–67.

133 Pliny, *Natural History: Volume X: Books 36-37. Translated by D. E. Eichholz*, Harvard University Press, Cambridge, MA, Loeb Class., 1962.

134 R. C. Newton and C. E. Manning, *Earth Planet. Sci. Lett.*, 2008, **274**, 241–249.

135 S. L. Morissette, S. Soukasene, D. Levinson, M. J. Cima and O. Almarsson, *Proc. Natl. Acad. Sci. U. S. A.*, 2003, **100**, 2180–2184.

136 C. E. Nicholson, C. Chen, B. Mendis and S. J. Cooper, *Cryst. Growth Des.*, 2011, **11**, 363–366.

137 T. Threlfall, *Org. Process Res. Dev.*, 2003, **7**, 1017–1027.

138 D. L. Graf, *Am. Mineral.*, 1961, **46**, 1283–1316.

139 A. Dal Negro and L. Ungaretti, *Am. Mineral.*, 1971, **56**, 768–772.

140 J. Wang and U. Becker, *Am. Mineral.*, 2009, **94**, 380–386.

141 F. Andersen and L. Brecevic, *Acta Chem. Scand*, 1991, **45**, 1018–1024.

142 G. Maurer, S. J. Portugal, I. Boomer and P. Cassey, *Reprod. Fertil. Dev.*, 2011, **23**, 339–345.

143 T. Baird and S. E. Solomon, *J. Exp. Mar. Bio. Ecol.*, 1979, **36**, 295–303.

144 S. E. Solomon and T. Baird, *J. Exp. Mar. Bio. Ecol.*, 1976, **22**, 145–160.

145 J. Zhao, X. Song, Y. Sun, B. Chen and J. Yu, *Cryst. Res. Technol.*, 2015, **50**, 277–283.

146 J. Wang, Q. Cheng and Z. Tang, *Chem. Soc. Rev.*, 2012, **41**, 1111.

147 W. V. Boynton, D. W. Ming, S. P. Kounaves, S. M. M. Young, R. E. Arvidson, M. H. Hecht, J. Hoffman, P. B. Niles, D. K. Hamara, R. C. Quinn, P. H. Smith, B. Sutter, D. C. Catling and R. V. Morris, *Science (80-.).*, 2009, **325**, 61–64.

148 A. Szcześ, *Colloids Surfaces A Physicochem. Eng. Asp.*, 2008, **320**, 98–103.

149 A. Szcześ, E. Chibowski and L. Hołysz, *Colloids Surfaces A Physicochem. Eng. Asp.*, 2007, **297**, 14–18.

150 H. K. Sung, I. Hirasawa, W. S. Kim and K. C. Chang, *J. Colloid Interface Sci.*, 2005, **288**, 496–502.

151 J.-H. Bang, Y. N. Jang, K. S. Song, C. W. Jeon, W. Kim, M. G. Lee and S.-J. Park, *J. Colloid Interface Sci.*, 2011, **356**, 311–5.

152 E. Chibowski, A. Szczes and L. Holysz, *Langmuir*, 2005, **21**, 8114–22.

153 H. Wei, Q. Shen, Y. Zhao, Y. Zhou, D. Wang and D. Xu, *J. Cryst. Growth*, 2005, **279**, 439–446.

154 H. Wei, Q. Shen, Y. Zhao, D. Wang and D. Xu, *J. Cryst. Growth*, 2004, **260**, 511–516.

155 H. Wei, Q. Shen, Y. Zhao, Y. Zhou, D. Wang and D. Xu, *J. Cryst. Growth*, 2004, **264**, 424–429.

156 Y. Zhao, S. Li, L. Yu, Y. Liu, X. Wang and J. Jiao, *J. Cryst. Growth*, 2011, **324**, 278–283.

157 V. Hurdon, R. Viola and C. Schroder, *J. Pain Symptom Manage.*, 2000, **19**, 130–6.

158 Ciba Specialty Chemicals Inc., *Human & Environmental Risk Assessment on ingredients of European household cleaning products. Substance: Fluorescent Brightener FWA-1 (CAS 16090-02-1)*, 2004, vol. 1.

159 *Human & Environmental Risk Assessment on ingredients of European household cleaning products. Substance: Fluorescent Brightener FWA-5 (CAS 27344-41-8)*, 2003.

160 B. M. Folmer and K. Holmberg, *Colloids Surfaces A Physicochem. Eng. Asp.*, 2001, **180**, 187–191.

161 *P&G Environ. Sci. data Fluoresc. whitening agents(Brighteners), https//www.scienceinthebox.com/en-UK/Assets/PDF/Glossary/brightners.pdf*.

162 M. Howarth, A. Riva, P. Marks and R. Williams, *Alcohol Alcohol.*, 2012, **47**, 688–696.

163 S. Soontravanich and J. F. Scamehorn, *J. Surfactants Deterg.*, 2010, **13**, 13–18.

164 B. J. Chun, J. Il Choi and S. S. Jang, *Colloids Surfaces A Physicochem. Eng. Asp.*, 2015, **474**, 36–43.

165 M. Tarek, S. Bandyopadhyay and M. L. Klein, *J. Mol. Liq.*, 1998, **7322**, 1–6.

166 A. Amani, P. York, H. de Waard and J. Anwar, *Soft Matter*, 2011, **7**, 2900–2908.

167 J. D. Rouse, D. A. Sabatini, R. E. Brown and J. H. Harwell, *Water Environ. Res.*, 1996, **68**, 162–168.

168 K. J. Smit and K. P. Ghiggino, *J. Polym. Sci. Part B Polym. Phys.*, 1991, **29**, 1397–1405.

9. Appendix 1: Data tables for Chapter 6

9.1. Preformed micelles containing hexane and brightener

Table 9-1: Inner core and micellar radii of preformed micelles containing hexane and brightener, and the positions of the centres of the five brightener molecules B1 - B5

System	Inner core radius / nm	Micellar radius / nm	B1 pos. / nm	B2 pos. / nm	B3 pos. / nm	B4 pos. / nm	B5 pos. /nm
AE1S	1.69	2.09	1.65	5.63	1.36	1.60	1.75
AE1S rp	1.71	2.12	1.44	1.68	1.64	4.38	1.48
AE7 (in heads)	2.80	3.60	3.56	5.65	3.18	3.75	2.89
AE7 (intermediate)	2.83	3.62	3.20	3.44	8.40	2.75	6.40
AE7 (in tails)	2.75	3.58	3.08	2.75	3.04	2.62	2.77
AE7 rp (in heads)	2.73	3.56	3.89	4.27	8.27	6.28	3.30
AE7 rp (intermediate)	2.78	3.62	3.15	6.58	2.97	3.24	3.61
AE7 rp (in tails)	2.81	3.62	2.73	2.88	2.64	3.42	2.85
AE1S AE7 (in heads)	2.46	2.93	7.62	7.97	7.24	7.05	8.42
AE1S AE7 (intermediate)	2.39	2.83	6.39	7.13	9.78	8.82	2.41
AE1S AE7 (in tails)	2.40	2.97	2.25	2.58	10.55	2.43	2.28
AE1S AE7 rp (in heads)	2.47	2.92	7.09	9.03	8.03	8.17	9.26
AE1S AE7 rp (intermediate)	2.46	2.95	7.34	7.99	7.18	2.54	8.32

AE1S AE7 rp (in tails)	2.50	2.96	2.48	2.28	2.56	6.20	2.68
AE1S DEEDMAC	2.10	2.43	1.99	1.70	2.55	2.07	1.94
AE1S DEEDMAC rp	2.07	2.38	1.90	2.00	2.39	2.07	2.15
AE7 DEEDMAC (in heads)	3.24	3.62	3.16	3.12	3.30	3.45	3.38
AE7 DEEDMAC (intermediate)	3.24	3.62	3.15	3.58	3.24	3.18	3.29
AE7 DEEDMAC (in tails)	3.23	3.64	3.13	3.02	3.05	3.12	3.11
AE7 DEEDMAC rp (in heads)	3.22	3.63	2.77	3.23	3.59	2.66	6.44
AE7 DEEDMAC rp (intermediate)	3.22	3.65	3.38	3.26	3.21	3.12	3.00
AE7 DEEDMAC rp (in tails)	3.22	3.65	3.37	3.27	3.21	3.12	3.01

9.2. Randomised surfactant systems with brightener

All values are presented to the nearest integer. For the column showing the number of monomers, the number of brightener monomers is given in the 'with bri' column, and the number of surfactant monomers is given in the 'without bri' column.

Table 9-2: Aggregation numbers for systems containing brighteners

Surfactant system	Conditions	No. of micelles	No. of monomers	Mean agg no	Max. agg. no.	Monomer average agg no.
AE1S	overall	14	0	15	26	17
	with bri	7	0	19	26	20
	without bri	7	0	11	21	14
AE7	overall	1	0	210	210	210
	with bri	1	0	210	210	210
	without bri	0	0	n/a	n/a	n/a
AE1S/AE7	overall	10	2	15	32	19
	with bri	7	2	18	32	21
	without bri	3	0	7	13	9
AE1S/ DEEDMAC	overall	11	0	12	22	14
	with bri	8	0	12	22	15
	without bri	3	0	11	12	11
AE7/ DEEDMAC	overall	2	0	80	80	80
	with bri	2	0	80	80	80
	without bri	0	0	n/a	n/a	n/a
AE1S/AE7/ DEEDMAC	overall	8	1	21	38	26
	with bri	5	1	28	38	29
	without bri	3	0	10	16	12

Table 9-3: mean inner core, micellar radii, and brightener positions

Surfactant system	**Conditions**	**Mean**			
		Inner core radius / nm	**Micellar radius / nm**	**Bri centre / nm**	**Bri sulfate / nm**
AE1S	overall	1.1	1.5	n/a	n/a
	with bri	1.2	1.6	1.1	1.6
	without bri	1.0	1.4	n/a	n/a
AE7	overall	3.0	3.7	n/a	n/a
	with bri	3.0	3.7	3.6	3.9
	without bri	n/a	n/a	n/a	n/a
AE1S/AE7	overall	1.1	1.5	n/a	n/a
	with bri	1.2	1.6	1.2	1.6
	without bri	0.9	1.4	n/a	n/a
AE1S/DEEDMAC	overall	1.1	1.5	n/a	n/a
	with bri	1.1	1.5	1.0	1.5
	without bri	1.1	1.4	n/a	n/a
AE7/DEEDMAC	overall	2.4	2.8	n/a	n/a
	with bri	2.4	2.8	2.3	2.6
	without bri	n/a	n/a	n/a	n/a
AE1S/AE7/DEEDMAC	overall	1.3	1.7	n/a	n/a
	with bri	1.4	1.8	1.5	1.9
	without bri	1.1	1.4	n/a	n/a

Table 9-4: Maximum inner core, micellar radii, and brightener positions

Surfactant system	Conditions	Maximum			
		Inner core radius / nm	Micellar radius / nm	Bri centre / nm	Bri sulfate / nm
AE1S	overall	1.4	1.7	n/a	n/a
	with bri	1.3	1.7	1.7	2.1
	without bri	1.2	1.6	n/a	n/a
AE7	overall	3.0	3.7	n/a	n/a
	with bri	3.0	3.7	3.6	3.9
	without bri	n/a	n/a	n/a	n/a
AE1S/AE7	overall	1.4	1.9	n/a	n/a
	with bri	1.4	1.9	1.6	2.0
	without bri	1.1	1.5	n/a	n/a
AE1S/ DEEDMAC	overall	1.3	1.7	n/a	n/a
	with bri	1.3	1.7	1.5	1.9
	without bri	1.1	1.5	n/a	n/a
AE7/DEEDMAC	overall	2.5	2.9	n/a	n/a
	with bri	2.5	2.9	2.5	2.9
	without bri	n/a	n/a	n/a	n/a
AE1S/AE7/ DEEDMAC	overall	1.6	2.0	n/a	n/a
	with bri	1.6	2.0	1.8	2.3
	without bri	1.2	1.6	n/a	n/a

Table 9-5: Monomer-averaged inner core, micellar radii, and brightener positions

Surfactant system	Conditions	Monomer-averaged			
		Inner core radius / nm	Micellar radius / nm	Bri centre / nm	Bri sulfate / nm
AE1S	overall	1.1	1.5	n/a	n/a
	with bri	1.2	1.6	1.1	1.6
	without bri	1.0	1.4	n/a	n/a
AE7	overall	3.0	3.7	n/a	n/a
	with bri	3.0	3.7	3.6	3.9
	without bri	n/a	n/a	n/a	n/a
AE1S/AE7	overall	1.2	1.6	n/a	n/a
	with bri	1.2	1.7	1.6	2.0
	without bri	1.0	1.4	n/a	n/a
AE1S/ DEEDMAC	overall	1.2	1.5	n/a	n/a
	with bri	1.2	1.5	1.1	1.5
	without bri	1.1	1.4	n/a	n/a
AE7/DEEDMAC	overall	2.4	2.8	n/a	n/a
	with bri	2.4	2.8	2.3	2.6
	without bri	n/a	n/a	n/a	n/a
AE1S/AE7/ DEEDMAC	overall	1.4	1.7	n/a	n/a
	with bri	1.4	1.8	1.5	1.9
	without bri	1.1	1.5	n/a	n/a

9.3. Randomised surfactant system with calcium ions

Table 9-6: Number of micelles, monomers, and aggregation numbers for surfactant systems with calcium ions

Surfactant system	Number of micelles	No. of monomers	Mean agg. no.	Maximum agg. no.	Monomer-averaged agg. no.
AE7	1	0	200	200	200
AE7/Ca^{2+}	1	0	200	200	200
AE1S	13	1	15	35	20
AE1S/Ca^{2+}	12	0	17	30	20
AE1S/AE7	8	0	18	33	20
AE1S/AE7/Ca^{2+}	9	0	16	29	18
AE1S/DEEDMAC	7	4	17	27	20
AE1S/DEEDMAC/Ca^{2+}	7	0	18	31	22
AE7/DEEDMAC	4	0	38	86	59
AE7/DEEDMAC/Ca^{2+}	3	0	50	85	64
AE1S/AE7/DEEDMAC	7	0	23	33	26
AE1S/AE7/DEEDMAC / Ca^{2+}	2	1	80	141	127
AE1S/AE7/DEEDMAC / Ca^{2+} (repeat)	6	1	27	44	33

Table 9-7: Inner core and micellar radii for systems with calcium

System	Mean		Maximum		Monomer-averaged	
	Inner core radius / nm	Micellar radius / nm	Inner core radius / nm	Micellar radius / nm	Inner core radius / nm	Micellar radius / nm
AE1S	1.1	1.5	1.3	1.7	1.1	1.5
AE7	2.9	3.5	2.9	3.5	2.9	3.5
AE1S/AE7	1.1	1.5	1.4	1.8	1.2	1.6
AE1S/DEEDMAC	1.2	1.5	1.4	1.7	1.3	1.6
AE7/DEEDMAC	2.0	2.4	2.7	3.0	2.3	2.6
AE1S/AE7/DEEDMAC	2.1	2.4	3.0	3.2	2.8	2.9
AE1S/AE7/DEEDMAC (repeat)	1.3	1.7	1.7	2.0	1.4	1.7

10. Appendix 2: Crystal data for Chapter 4

This appendix contains the data generated from X-ray crystallography of the Brightener 49 methanol solvate crystal obtained in Chapter 4. Data is presented as received from Dr Yufit of the departmental crystallography service on 2nd April 2014.

Table 10-1: Crystal data and structure refinement received from Brightener 49 methanol solvate

Empirical formula	$[C_{28}H_{20}O_6S_2]^{2-}$ x $2Na^+$ x $4CH_3OH$
Formula weight	690.71
Temperature/K	120.0
Crystal system	monoclinic
Space group	$P2_1/n$
a/Å	7.7472(4)
b/Å	23.2491(13)
c/Å	18.6186(10)
α/°	90.00
β/°	98.5411(18)
γ/°	90.00
Volume/Å^3	3316.3(3)
Z	4
ρ_{calc}mg/mm^3	1.383
m/mm^{-1}	0.243
F(000)	1448.0
Crystal size/mm^3	0.38 × 0.17 × 0.13
Radiation	MoKα (λ = 0.71073)
2Θ range for data collection	4.76 to 58°
Index ranges	$-10 \leq h \leq 10$, $-31 \leq k \leq 31$, $-25 \leq l \leq 25$
Reflections collected	50118
Independent reflections	8823 [R_{int} = 0.0694, R_{sigma} = 0.0497]
Data/restraints/parameters	8823/0/559
Goodness-of-fit on F^2	1.039
Final R indexes [I>=2σ (I)]	R_1 = 0.0459, wR_2 = 0.1052
Final R indexes [all data]	R_1 = 0.0701, wR_2 = 0.1156
Largest diff. peak/hole / e Å^{-3}	0.53/-0.27

Table 10-2: Fractional Atomic Coordinates and Equivalent Isotropic Displacement Parameters for Brightener 49 methanol solvate. U_{eq} is defined as 1/3 of of the trace of the orthogonalised U_{IJ} tensor.

Atom	*x*	*y*	*z*	U(eq) / Å^2 × 10^3
S1	0.71698(5)	0.441312(17)	0.55748(2)	12.49(10)
S2	0.47442(5)	0.862703(18)	1.16958(2)	15.53(10)
Na1	0.63004(9)	0.58028(3)	0.59601(4)	17.44(15)
Na2	0.106518(9)	0.54738(3)	0.56828(4)	17.34(15)
O1	0.89412(15)	0.46321(5)	0.55924(7)	17.8(3)
O2	0.61470(15)	0.47830(5)	0.59806(6)	17.2(3)
O3	0.63586(16)	0.43049(5)	0.48338(6)	19.8(3)
O4	0.61289(16)	0.86004(5)	1.12394(7)	19.5(3)
O5	0.32644(16)	0.82631(5)	1.14304(7)	22.8(3)
O6	0.41974(17)	0.92183(5)	1.17913(7)	21.7(3)
O7	0.45891(19)	0.60940(7)	0.67787(8)	32.6(4)
O8	0.79652(17)	0.59235(6)	0.50047(7)	19.9(3)
C1	0.7483(2)	0.36512(7)	0.67575(9)	17.2(3)
C1S	0.5159(3)	0.64294(11)	0.74029(12)	30.5(5)
C2	0.7349(2)	0.37272(7)	0.60022(9)	14.5(3)
C2S	0.7959(3)	0.64716(9)	0.46558(12)	28.4(4)
C3	0.7365(2)	0.32576(8)	0.5538(1)	20.7(4)
C4	0.7475(3)	0.27046(8)	0.58094(11)	26.7(4)
C5	0.7572(3)	0.26179(8)	0.65499(11)	30.2(5)
C6	0.7595(3)	0.30812(8)	0.70122(11)	26.4(4)
C7	0.7518(2)	0.41303(7)	0.72756(9)	17.8(3)
C8	0.7071(2)	0.40733(8)	0.79378(10)	19.7(4)
C9	0.7128(2)	0.45211(7)	0.84916(9)	18.1(4)
C10	0.7262(3)	0.51095(8)	0.83513(10)	23.0(4)
C11	0.7327(3)	0.55089(8)	0.8907(1)	21.9(4)
C12	0.7267(2)	0.53398(7)	0.96229(9)	17.0(3)
C13	0.7118(2)	0.47531(8)	0.97592(10)	20.8(4)
C14	0.7044(3)	0.43527(8)	0.92057(10)	20.7(4)
C15	0.7319(2)	0.57612(7)	1.02187(9)	16.7(3)
C16	0.8215(2)	0.56403(8)	1.09061(10)	20.9(4)
C17	0.8187(3)	0.60233(8)	1.14734(10)	20.8(4)

C18	0.7261(2)	0.65383(7)	1.13827(9)	18.2(4)
C19	0.6396(2)	0.66660(7)	1.06891(10)	18.5(4)
C20	0.6435(2)	0.62868(8)	1.0118.3(10)	18.6(4)
C21	0.7255(3)	0.69220(8)	1.20075(10)	21.1(4)
C22	0.6446(2)	0.74212(8)	1.20104(10)	20.5(4)
C23	0.6413(2)	0.78051(7)	1.26348(9)	17.6(4)
C24	0.5668(2)	0.83593(7)	1.25598(9)	16.6(3)
C25	0.5644(3)	0.87177(8)	1.31556(10)	21.8(4)
C26	0.6356(3)	0.85296(8)	1.38442(11)	27.9(4)
C27	0.7108(3)	0.79914(9)	1.39333(10)	28.0(4)
C28	0.7143(3)	0.76377(8)	1.33375(10)	24.6(4)
O9	0.2513(2)	0.71761(7)	1.08577(11)	45.3(4)
C3S	0.0704(3)	0.71696(13)	1.07578(16)	42.1(6)
O10	0.27221(18)	0.48031(6)	0.61900(7)	22.0(3)
C4S	0.2574(3)	0.45752(12)	0.68901(13)	36.7(5)

Table 10-3: Anisotropic Displacement Parameters for Brightener 49 methanol solvate. The Anisotropic displacement factor exponent takes the form: $-2\pi^2[h^2a^{*2}U_{11}+2hka^*b^*U_{12}+\ldots]$.

Atom	U_{11} /Å$^2\times10^3$	U_{22} /Å$^2\times10^3$	U_{33} /Å$^2\times10^3$	U_{23} /Å$^2\times10^3$	U_{13} /Å$^2\times10^3$	U_{12} /Å$^2\times10^3$
S1	13.3(2)	12.21(19)	12.03(19)	0.34(14)	1.95(15)	0.66(15)
S2	15.5(2)	15.8(2)	15.3(2)	1.96(15)	2.14(16)	1.24(15)
Na1	17.2(4)	18.1(3)	17.0(3)	-1.5(3)	2.1(3)	-0.1(3)
Na2	19.6(4)	16.5(3)	16.2(3)	-1.8(3)	3.5(3)	-0.4(3)
O1	15.1(6)	17.9(6)	20.9(6)	-0.9(5)	4.3(5)	-2.0(5)
O2	18.2(6)	15.3(6)	19.3(6)	0.9(5)	6.4(5)	4.8(5)
O3	23.5(7)	19.9(6)	14.2(6)	0.4(5)	-3.0(5)	0.5(5)
O4	17.8(6)	23.5(7)	17.7(6)	5.5(5)	4.6(5)	3.0(5)
O5	19.6(7)	25.3(7)	23.1(7)	-0.4(5)	1.6(5)	-4.7(5)
O6	25.3(7)	17.9(6)	21.2(7)	2.5(5)	1.2(5)	5.5(5)
O7	17.6(7)	52.3(10)	27.1(8)	-19.0(7)	0.9(6)	1.8(7)
O8	25.4(7)	18.1(6)	16.5(6)	0.6(5)	4.0(5)	1.5(5)
C1	18.9(9)	16.5(8)	15.8(8)	0.5(6)	1.0(7)	1.4(7)
C1S	25.5(11)	43.2(14)	22.1(10)	-11.3(9)	0.9(9)	3.7(9)
C2	14.9(8)	11.6(7)	16.9(8)	1.0(6)	1.7(7)	1.5(6)
C2S	38.5(13)	22.3(10)	25.3(10)	7.7(8)	7.3(10)	3.6(9)
C3	25.8(10)	17.8(8)	18.0(9)	-1.0(7)	2.2(8)	1.9(7)
C4	37.8(12)	17.0(9)	24.9(10)	-5.0(7)	2.9(9)	3.5(8)
C5	47.0(13)	13.5(9)	29.3(11)	4.7(8)	3.3(9)	4.9(8)
C6	41.6(12)	19.2(9)	17.5(9)	4.3(7)	1.8(9)	4.7(8)
C7	20.5(9)	15.1(8)	16.5(8)	0.8(7)	-0.9(7)	2.0(7)
C8	24.3(9)	16.2(8)	18.3(9)	-0.2(7)	2.7(7)	-0.5(7)
C9	20.1(9)	17.9(8)	16.5(8)	-1.3(6)	3.5(7)	-1.0(7)
C10	34.8(11)	21.0(9)	13.7(8)	1.9(7)	5.5(8)	-0.9(8)
C11	32.7(11)	14.9(9)	18.6(9)	2.9(7)	5.8(8)	-1.0(7)
C12	18.2(9)	17.5(8)	16.0(8)	-0.2(6)	4.1(7)	-0.1(7)
C13	29.1(10)	20.1(9)	14.7(8)	3.0(7)	8.5(8)	1.4(7)
C14	27.9(10)	14.9(8)	20.6(9)	2.6(7)	7.9(8)	-1.2(7)
C15	18.1(8)	16.9(8)	16.2(8)	0.1(6)	6.2(7)	-1.6(7)
C16	24.5(10)	18.5(9)	20.1(9)	3.1(7)	5.4(8)	6.4(7)

C17	26(1)	22.2(9)	13.6(8)	2.6(7)	0.7(8)	5.6(7)
C18	21.4(9)	17.4(8)	16.5(8)	1.6(7)	5.6(7)	-1.3(7)
C19	21.3(9)	15.0(8)	19.4(9)	1.6(7)	3.8(7)	2.2(7)
C20	22.1(9)	19.2(9)	14.2(8)	1.8(7)	1.6(7)	0.0(7)
C21	28.2(10)	20.1(9)	14.6(8)	0.9(7)	2.0(8)	2.6(7)
C22	27.4(10)	18.4(9)	14.9(8)	0.9(7)	0.8(8)	1.6(7)
C23	21.9(9)	16.0(8)	15.1(8)	0.8(6)	3.8(7)	-1.0(7)
C24	19.1(9)	16.2(8)	14.7(8)	1.9(6)	3.7(7)	-2.1(7)
C25	26.8(10)	17.9(9)	21.1(9)	-3.0(7)	5.2(8)	0.5(7)
C26	40.5(12)	26(1)	16.9(9)	-6.2(8)	3.2(9)	-2.1(8)
C27	42.8(12)	26.8(10)	13.1(9)	2.9(7)	-0.1(9)	-0.3(9)
C28	36.0(11)	17.7(9)	19.5(9)	3.0(7)	2.2(8)	3.1(8)
O9	29.7(9)	30.7(9)	73.0(13)	-12.6(8)	-0.5(8)	-4.5(7)
C3S	26.2(12)	49.2(16)	50.4(16)	-8.4(13)	4.6(11)	-9.6(11)
O10	16.7(7)	29.0(7)	20.5(7)	4.4(5)	3.2(6)	-2.1(5)
C4S	28.4(12)	56.1(15)	25.1(11)	15.7(11)	2.2(9)	0.3(11)

Table 10-4: Bond lengths for Brightener 49 methanol solvate

Atom	Atom	Length/Å		Atom	Atom	Length/Å
S1	Na2[1]	3.0942(8)		O7	C1S	1.415(2)
S1	O1	1.4596(12)		O8	C2S	1.430(2)
S1	O2	1.4546(12)		C1	C2	1.406(2)
S1	O3	1.4506(13)		C1	C6	1.406(2)
S1	C2	1.7785(16)		C1	C7	1.471(2)
S2	Na1[2]	3.1090(8)		C2	C3	1.394(2)
S2	Na2[2]	2.9690(8)		C3	C4	1.380(3)
S2	O4	1.4655(13)		C4	C5	1.384(3)
S2	O5	1.4512(13)		C5	C6	1.377(3)
S2	O6	1.4571(12)		C7	C8	1.336(2)
S2	C24	1.7733(18)		C8	C9	1.461(2)
Na1	S2[3]	3.1090(8)		C9	C10	1.400(2)
Na1	Na2	3.5683(10)		C9	C14	1.397(2)
Na1	O2	2.3745(13)		C10	C11	1.386(3)
Na1	O3[4]	2.3636(14)		C11	C12	1.397(2)
Na1	O5[3]	2.7207(15)		C12	C13	1.395(2)
Na1	O6[3]	2.5304(14)		C12	C15	1.476(2)
Na1	O7	2.2670(15)		C13	C14	1.384(2)
Na1	O8	2.3638(14)		C15	C16	1.391(3)
Na2	S1[1]	3.0942(8)		C15	C20	1.400(2)
Na2	S2[3]	2.9691(8)		C16	C17	1.384(3)
Na2	Na2[1]	3.4025(13)		C17	C18	1.393(2)
Na2	O1	2.3554(13)		C18	C19	1.396(2)
Na2	O1[1]	2.4535(14)		C18	C21	1.467(2)
Na2	O3[1]	2.6862(14)		C19	C20	1.384(2)
Na2	O4[3]	2.3937(13)		C21	C22	1.319(3)
Na2	O6[3]	2.5946(14)		C22	C23	1.469(2)
Na2	O8	2.4977(15)		C23	C24	1.410(2)
Na2	O10[5]	2.3336(15)		C23	C28	1.401(2)
O1	Na2[1]	2.4535(14)		C24	C25	1.390(2)
O3	Na1[4]	2.3636(14)		C25	C26	1.389(3)
O3	Na2[1]	2.6862(14)		C26	C27	1.380(3)

O4	Na2[2]	2.3936(13)		C27	C28	1.384(3)
O5	Na1[2]	2.7206(15)		O9	C3S	1.386(3)
O6	Na1[2]	2.5304(14)		O10	Na2[6]	2.3336(15)
O6	Na2[2]	2.5946(14)		O10	C4S	1.427(2)

[1]2-X,1-Y,1-Z; [2]-1/2+X,3/2-Y,1/2+Z; [3]1/2+X,3/2-Y,-1/2+Z; [4]1-X,1-Y,1-Z; [5]1+X,+Y,+Z; [6]-1+X,+Y,+Z

Table 10-5: Bond angles for Brightener 49 methanol solvate

Atom	Atom	Atom	Angle/°		Atom	Atom	Atom	Angle/°
O1	S1	Na2[1]	50.99(5)		O4[3]	Na2	O6[3]	57.65(4)
O1	S1	C2	106.99(7)		O4[3]	Na2	O8	84.61(5)
O2	S1	Na2[1]	138.01(5)		O6[3]	Na2	S1[1]	158.22(4)
O2	S1	O1	111.41(7)		O6[3]	Na2	S2[3]	29.39(3)
O2	S1	C2	108.07(7)		O6[3]	Na2	Na1	45.14(3)
O3	S1	Na2[1]	60.19(5)		O6[3]	Na2	Na2[1]	131.09(4)
O3	S1	O1	110.78(7)		O6[3]	Na2	O3[1]	137.00(5)
O3	S1	O2	113.83(7)		O8	Na2	S1[1]	95.11(4)
O3	S1	C2	105.31(8)		O8	Na2	S2[3]	76.60(4)
C2	S1	Na2[1]	113.56(6)		O8	Na2	Na1	41.34(3)
Na2[2]	S2	Na1[2]	71.86(2)		O8	Na2	Na2[1]	76.15(4)
O4	S2	Na1[2]	114.63(5)		O8	Na2	O3[1]	115.91(5)
O4	S2	Na2[2]	53.03(5)		O8	Na2	O6[3]	81.89(5)
O4	S2	C24	106.25(8)		O10[5]	Na2	S1[1]	86.77(4)
O5	S2	Na1[2]	61.03(5)		O10[5]	Na2	S2[3]	115.26(4)
O5	S2	Na2[2]	116.34(6)		O10[5]	Na2	Na1	133.79(4)
O5	S2	O4	112.77(8)		O10[5]	Na2	Na2[1]	88.83(4)
O5	S2	O6	111.24(8)		O10[5]	Na2	O1	79.59(5)
O5	S2	C24	107.23(8)		O10[5]	Na2	O1[1]	98.34(5)
O6	S2	Na1[2]	53.53(5)		O10[5]	Na2	O3[1]	72.27(5)
O6	S2	Na2[2]	60.91(5)		O10[5]	Na2	O4[3]	111.90(5)
O6	S2	O4	111.21(7)		O10[5]	Na2	O6[3]	102.48(5)
O6	S2	C24	107.81(8)		O10[5]	Na2	O8	162.80(6)
C24	S2	Na1[2]	138.89(6)		S1	O1	Na2[1]	101.47(6)
C24	S2	Na2[2]	136.19(6)		S1	O1	Na2	143.96(7)
S2[3]	Na1	Na2	52.251(17)		Na2	O1	Na2[1]	90.05(5)
O2	Na1	S2[3]	117.41(4)		S1	O2	Na1	123.34(7)
O2	Na1	Na2	80.73(3)		S1	O3	Na1[4]	145.83(8)
O2	Na1	O5[3]	144.96(5)		S1	O3	Na2[1]	91.87(6)
O2	Na1	O6[3]	90.73(5)		Na1[4]	O3	Na2[1]	120.93(5)
O3[4]	Na1	S2[3]	158.73(4)		S2	O4	Na2[2]	97.68(6)
O3[4]	Na1	Na2	129.88(4)		S2	O5	Na1[2]	91.15(6)

O3^{4}	Na1	O2	82.14(5)		S2	O6	Na1^{2}	98.89(7)
O3^{4}	Na1	O5^{3}	132.82(5)		S2	O6	Na2^{2}	89.70(6)
O3^{4}	Na1	O6^{3}	172.70(5)		Na1^{2}	O6	Na2^{2}	88.25(4)
O3^{4}	Na1	O8	93.68(5)		C1S	O7	Na1	125.08(13)
O5^{3}	Na1	S2^{3}	27.82(3)		Na1	O8	Na2	94.41(5)
O5^{3}	Na1	Na2	73.88(3)		C2S	O8	Na1	118.82(12)
O6^{3}	Na1	S2^{3}	27.58(3)		C2S	O8	Na2	123.30(13)
O6^{3}	Na1	Na2	46.62(3)		C2	C1	C6	116.59(16)
O6^{3}	Na1	O5^{3}	54.25(4)		C2	C1	C7	123.52(15)
O7	Na1	S2^{3}	97.22(4)		C6	C1	C7	119.89(16)
O7	Na1	Na2	145.15(5)		C1	C2	S1	123.34(12)
O7	Na1	O2	104.57(6)		C3	C2	S1	115.61(13)
O7	Na1	O3^{4}	84.82(5)		C3	C2	C1	121.05(15)
O7	Na1	O5^{3}	84.28(5)		C4	C3	C2	120.58(17)
O7	Na1	O6^{3}	98.55(5)		C3	C4	C5	119.45(18)
O7	Na1	O8	155.43(6)		C6	C5	C4	120.15(18)
O8	Na1	S2^{3}	75.67(4)		C5	C6	C1	122.14(18)
O8	Na1	Na2	44.26(4)		C8	C7	C1	123.23(17)
O8	Na1	O2	99.48(5)		C7	C8	C9	126.57(17)
O8	Na1	O5^{3}	78.81(5)		C10	C9	C8	124.05(16)
O8	Na1	O6^{3}	85.93(5)		C14	C9	C8	118.12(16)
S1^{1}	Na2	Na1	136.42(3)		C14	C9	C10	117.83(16)
S1^{1}	Na2	Na2^{1}	67.92(2)		C11	C10	C9	120.74(17)
S2^{3}	Na2	S1^{1}	128.92(2)		C10	C11	C12	121.41(16)
S2^{3}	Na2	Na1	55.891(17)		C11	C12	C15	121.95(15)
S2^{3}	Na2	Na2^{1}	149.16(4)		C13	C12	C11	117.65(16)
Na2^{1}	Na2	Na1	93.73(3)		C13	C12	C15	120.39(15)
O1	Na2	S1^{1}	112.38(4)		C14	C13	C12	121.17(16)
O1^{1}	Na2	S1^{1}	27.53(3)		C13	C14	C9	121.19(16)
O1	Na2	S2^{3}	116.52(4)		C16	C15	C12	120.76(16)
O1^{1}	Na2	S2^{3}	139.64(4)		C16	C15	C20	117.82(16)
O1	Na2	Na1	69.81(3)		C20	C15	C12	121.39(16)
O1^{1}	Na2	Na1	114.93(4)		C17	C16	C15	120.66(17)
O1	Na2	Na2^{1}	46.14(3)		C16	C17	C18	121.77(17)

O1[1]	Na2	Na2[1]	43.81(3)		C17	C18	C19	117.57(16)
O1	Na2	O1[1]	89.95(5)		C17	C18	C21	119.28(16)
O1	Na2	O3[1]	129.74(5)		C19	C18	C21	123.14(16)
O1[1]	Na2	O3[1]	55.33(4)		C20	C19	C18	120.84(16)
O1	Na2	O4[3]	145.80(5)		C19	C20	C15	121.28(17)
O1[1]	Na2	O6[3]	158.57(5)		C22	C21	C18	126.58(18)
O1	Na2	O6[3]	88.85(4)		C21	C22	C23	127.01(17)
O1[1]	Na2	O8	76.71(5)		C24	C23	C22	122.12(16)
O1	Na2	O8	83.90(5)		C28	C23	C22	121.21(16)
O3[1]	Na2	S1[1]	27.94(3)		C28	C23	C24	116.66(16)
O3[1]	Na2	S2[3]	113.00(4)		C23	C24	S2	120.97(13)
O3[1]	Na2	Na1	153.39(4)		C25	C24	S2	117.54(13)
O3[1]	Na2	Na2[1]	91.86(4)		C25	C24	C23	121.49(16)
O4[3]	Na2	S1[1]	100.65(4)		C26	C25	C24	119.84(17)
O4[3]	Na2	S2[3]	29.29(3)		C27	C26	C25	119.95(18)
O4[3]	Na2	Na1	80.39(4)		C26	C27	C28	120.03(18)
O4[3]	Na2	Na2[1]	156.27(5)		C27	C28	C23	122.02(18)
O4[3]	Na2	O1[1]	118.39(5)		C4S	O10	Na2[6]	118.29(13)
O4[3]	Na2	O3[1]	84.08(4)					

[1]2-X,1-Y,1-Z; [2]-1/2+X,3/2-Y,1/2+Z; [3]1/2+X,3/2-Y,-1/2+Z; [4]1-X,1-Y,1-Z; [5]1+X,+Y,+Z; [6]-1+X,+Y,+Z

Table 10-6: Bond lengths and angles of hydrogen bonds in Brightener 49 methanol solvate

D	H	A	d(D-H)/Å	d(H-A)/Å	d(D-A)/Å	D-H-A/°
O7	H7	O4[1]	0.80(3)	2.01(3)	2.811(2)	179(3)
O8	H8	O10[2]	0.72(2)	2.07(2)	2.781(2)	171(2)
O9	H9	O5	0.90(3)	1.88(3)	2.771(2)	169(3)
O10	H10A	O2	0.76(3)	1.99(3)	2.7389(18)	167(3)

[1]-1/2+X,3/2-Y,-1/2+Z; [2]1-X,1-Y,1-Z

Table 10-7: Examples of torsion angles in Brightener 49 methanol solvate

A	B	C	D	Angle/°		A	B	C	D	Angle/°
C1	C2	S1	Na2[1]	139.30(13)		C13	C12	C15	C20	-139.74(19)
C1	C2	S1	O1	85.09(15)		C17	C18	C21	C22	-179.95(19)
C1	C2	S1	O2	-34.98(17)		C18	C21	C22	C23	179.16(18)
C1	C2	S1	O3	-156.99(14)		C19	C18	C21	C22	0.9(3)
C1	C7	C8	C9	177.72(17)		C21	C22	C23	C24	172.73(19)
C2	C1	C7	C8	157.12(18)		C21	C22	C23	C28	-6.6(3)
C3	C2	S1	Na2[1]	-40.19(15)		C23	C24	S2	Na1[2]	129.34(13)
C3	C2	S1	O1	-94.40(14)		C23	C24	S2	Na2[2]	-109.97(14)
C3	C2	S1	O2	145.53(13)		C23	C24	S2	O4	-56.92(16)
C3	C2	S1	O3	23.52(15)		C23	C24	S2	O5	63.91(16)
C6	C1	C7	C8	-23.2(3)		C23	C24	S2	O6	-176.22(14)
C7	C8	C9	C10	16.0(3)		C25	C24	S2	Na1[2]	-51.32(18)
C7	C8	C9	C14	-163.97(19)		C25	C24	S2	Na2[2]	69.37(17)
C11	C12	C15	C16	-142.88(19)		C25	C24	S2	O4	122.42(14)
C11	C12	C15	C20	38.9(3)		C25	C24	S2	O5	-116.75(15)
C13	C12	C15	C16	38.5(3)		C25	C24	S2	O6	3.12(16)

[1]2-X,1-Y,1-Z; [2]-1/2+X,3/2-Y,1/2+Z

Table 10-8: Hydrogen Atom Coordinates and Isotropic Displacement Parameters for Brightener 49 methanol solvate

Atom	*x* / Å×10^4	*y*/ Å×10^4	*z*/ Å×10^4	U(eq) / Å×10^3
H1SA	5020(30)	6836(12)	7306(14)	51(8)
H1SB	4530(30)	6326(10)	7799(13)	40(7)
H1SC	6430(30)	6358(9)	7546(12)	31(6)
H2SA	6850(40)	6568(10)	4409(14)	46(7)
H3	7270(30)	3320(8)	5024(11)	23(5)
H4	7440(30)	2376(9)	5464(11)	28(6)
H5	7610(30)	2249(9)	6731(11)	27(6)
H6	7690(30)	3025(10)	7506(13)	41(7)
H7	3610(40)	6185(12)	6626(15)	49(8)
H7A	7930(30)	4486(9)	7125(10)	20(5)
H8A	6690(30)	3703(9)	8094(11)	20(5)
H8	7760(30)	5709(10)	4725(13)	26(7)

H2SB	8770(30)	6480(9)	4287(13)	34(6)
H2SC	8290(40)	6761(12)	5015(15)	58(8)
H10	7300(30)	5233(9)	7873(11)	24(5)
H11	7430(30)	5899(9)	8806(11)	24(5)
H13	7010(30)	4620(8)	10234(11)	20(5)
H14	6900(30)	3956(9)	9324(11)	25(5)
H16	8890(30)	5307(8)	10970(10)	18(5)
H17	8830(30)	5948(9)	11906(12)	25(5)
H19	5730(30)	7014(9)	10620(11)	24(5)
H20	5760(30)	6366(8)	9658(11)	19(5)
H21	7930(30)	6800(11)	12432(14)	47(7)
H22	5830(30)	7543(10)	11548(13)	44(7)
H25	5160(30)	9098(10)	13093(11)	28(6)
H26	6260(30)	8780(9)	14240(12)	35(6)
H27	7640(30)	7873(9)	14382(12)	31(6)
H28	7650(30)	7276(9)	13407(10)	19(5)
H3SA	290(40)	6807(13)	10561(15)	60(8)
H3SB	150(40)	7298(15)	11195(19)	87(11)
H9	2810(40)	7506(14)	11097(17)	73(10)
H3SC	270(40)	7460(14)	10444(18)	77(11)
H4SA	3260(40)	4220(12)	6982(14)	52(8)
H10A	3690(30)	4840(10)	6172(13)	38(7)
H4SB	1310(40)	4494(12)	6875(15)	62(8)
H4SC	3020(40)	4845(12)	7265(15)	57(8)